



Issue  
**08**  
2023

# The Paton WELDING JOURNAL

Published Monthly Since 2000

ISSN 0957-798X

[www.patonpublishinghouse.com](http://www.patonpublishinghouse.com)

Welding and Related Technologies

## PLASMA-ARC WELDING AT A VARIABLE POLARITY ASYMMETRICAL CURRENT OF HIGH-STRENGTH ALUMINIUM ALLOYS

(see pp. 17-28)



■ Modern technologies of welding  
railway rails

■ Electron beam sintering of  
hard alloy billets

■ Plasma transferred arc surfacing with two  
powder feeding systems

# Universal automated PTA system PM-308

MADE IN  
UKRAINE

CE



Index 21971



**Plasma-Master Co., Ltd.**  
52, Popudrenko str.  
Kyiv, 02094, Ukraine

tel./fax: +38 044 537-31-44  
info@plasma-master.com  
www.plasma-master.com



facebook.com/PlasmaMasterCoLtd



instagram.com/plasma\_master\_co\_ltd



youtube.com/user/PlasmaMasterCoLtd



**THE LARGEST MANUFACTURER  
OF EUROPEAN QUALITY  
WELDING WIRE IN UKRAINE**



**Excellent**

**Welding Performance**

49000, Ukraine, Dnipro, Slobozhanskyi Avenue, 20  
<https://dneprometiz.com>, e-mail: [vg.petrovskij@dneprometiz.com](mailto:vg.petrovskij@dneprometiz.com)  
+38 (067) 693-38-76

**PATON**

# WELDING IS PATON



PATON-WELDING.COM



# International Center for Electron Beam Technologies (ICEBT)

## Electron Beam Physical Vapor Deposition (EB-PVD) equipment and technologies.

ICEBT has been carrying on systematic scientific investigations and developments of new materials and protective coatings produced using electron beam technologies and developed new samples of EB-PVD equipment:

- Available technologies for thermal barrier coatings (TBC) deposition and high-rate evaporation of MCrAlY alloys (11 patents);
- 40 years of experience in the development and manufacture of EB-PVD units (laboratory, pilot-production, industrial) with direct electron beam heating and with radiant heating;
- The EB-PVD units use the most modern components of Western production;
- 21 EB-PVD units have been delivered to customers (operated in the USA, Canada, China, India);
- Metal coatings and TBC have been applied to thousands of blades and vanes of various gas turbine engines;
- Conducting training for end-user specialists in the operation of EB-PVD units, develop coating parameters with ICEBT help.



Address: 68, Antonovicha street, Kyiv, 03150, Ukraine,  
phone +38 044 2873166, +38 044 2892176; <http://www.paton-icebt.kiev.ua>  
Contact person: Kostyantyn Yakovchuk, e-mail: [yakovchuk@paton-icebt.kiev.ua](mailto:yakovchuk@paton-icebt.kiev.ua).



# CONFIDENCE IN THE RESULT



PrJSC "PlasmaTec"

tel.: +38 (0432) 55-49-71  
+38 (067) 433-04-50

zbut@plasmatec.com.ua  
plasmatec-weld.com.ua



# LEADER IN THE PRODUCTION OF FLUX-CORED WIRES IN UKRAINE



for welding  
**SELF-SHIELDED**  
Ø 1,0 - 2,8

for welding  
**GAS-SHIELDED**  
Ø 1,0 - 2,5

for welding  
**UNDER FLUX**  
Ø 2,0 - 4,0

for surfacing  
**RECOVERY**  
Ø 1,2 - 4,0

for surfacing  
**HARDFACING**  
Ø 1,2 - 4,0

FOR SPRAYING  
Ø 1,6 - 2,4

EUROPEAN QUALITY - REASONABLE PRICE  
MORE THAN 70 GRADES OF FLUX-CORED WIRES

[www.weldtech-group.com](http://www.weldtech-group.com)



# MANUAL ELECTRON-BEAM TOOL FOR TECHNOLOGICAL WORK IN OPEN SPACE

**NEW GENERATION OF MANUAL AND AUTOMATED ELECTRON-BEAM TOOLS FOR WORK IN OPEN SPACE**



Designed for welding and cutting aluminum and titanium alloys, as well as stainless steel up to 6 mm thick in Space and on the surface of the Moon. It can work both manually and in an automated version.

## STAGES OF THE PATH



Experiment on electronic beam welding and cutting in the open space. «SALUT-7» station, 1984  
The experiment in open space lasted more than 3 hours.

Several series of ground tests of the «Universal» equipment were carried out, including flight tests at the flying laboratory NASA KS-135 in the mode of short-term weightlessness.  
George Marshall Space Flight Center, 2000.



A test stand installed in the flying laboratory.



A set of equipment for manual electron beam welding «Universal».



**Paton Welding Institute**  
<https://paton.org.ua>  
E-mail: [nadamova54@gmail.com](mailto:nadamova54@gmail.com)

# Non-Destructive Testing (NDT)



## COMPLEX EQUIPMENT FOR BUTT WELDS TESTING OF THE PIPING, TANKS...

- ✓ DEVELOPMENT AND MANUFACTURING OF NDT DEVICES
- ✓ NDT SPECIALISTS TRAINING AND CERTIFICATION

[www.oko-ndt.com](http://www.oko-ndt.com)



OKOndt GROUP

### TOFD MAN

complex wireless equipment for testing of the long welded joints with the aid of TOFD technique.



### TOFD PRO

equipment for full testing of the welded joints with the aid of TOFD technique.



OKOndt GROUP



[global-sales@oko-ndt.com](mailto:global-sales@oko-ndt.com)



[www.oko-ndt.com](http://www.oko-ndt.com)

# Electron Beam Welding

## Design and manufacturing machines for EBW



Small-size unit of SB 112 type  
Chamber volume – 0.3 m<sup>3</sup>

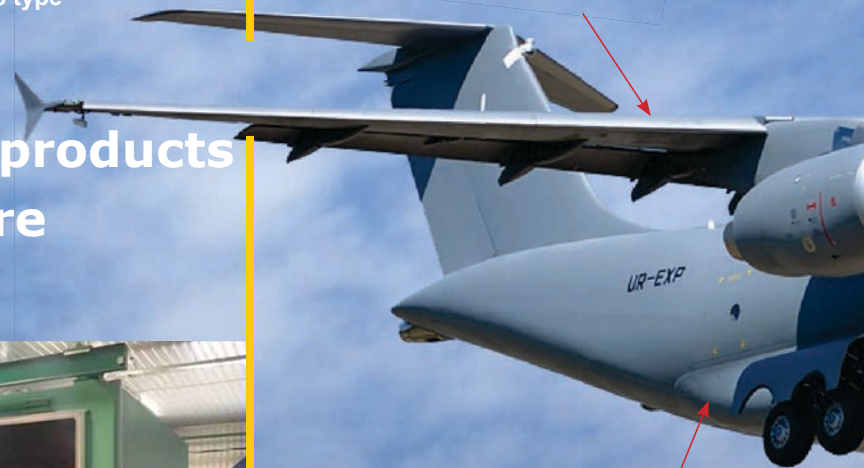


Mid-size unit of KL 138 type  
Chamber volume – 40 m<sup>3</sup>



Large-size unit of KL 118 type  
Chamber volume – 66 m<sup>3</sup>

## Electron Beam



## EB 3D prototyping of products using filler wire



Surfaced cylinder



Restored shaft

# Paton Welding Institute

www.paton.org.ua ♦ e-mail: office@paton.kiev.ua



# for Industry

# 65 years of innovation and development

## Welding for Aircraft



## EBW mashines for granular metallurgy



Mashines for granular metallurgy are designed for degassing, filling and vibration compaction of granules in capsules with a subsequent sealing applying electron beam welding (mashines KL168, KL114 and KL139).

## EB sintering of hard alloy billets



Mashine for EBS of hard alloy billets



Products manufactured by EBS method

SINCE 1988



**HUAYANG METALWORKING TECHNOLOGY (HMT)** is an official trademark presenting **Liaoning Xinhuyang Weiye Equipment & Manufacturing Co., Ltd.**

HMT enjoys more than **35 years'** experience in the field of explosion welding. Explosive welding allows to solve complex problems in the design of equipment in various industries.

HMT has the credible experts in explosion welding. We are ready to partner with customers to meet their demands by applying innovative methods to ensure our customers' long-term success and balance cost-efficiency, safety, and reliability when it matters most.

HMT utilizes two sites for conducting explosion welding works all the year round.

### PRODUCTS & CAPABILITIES

- Various sized dual-layer and multilayer plates obtained by explosion welding (up to 260 combinations of dissimilar metals).
- Multilayer plates obtained by rolling (up to 153 layers).
- Bimetal cylindrical rods and pipes; tube transition joint with smooth inner surface.
- Repair and restoration of products by explosion welding.
- Explosion welding and rolling combined.
- Producing equipment and pressure vessels by using corrosion-resistant bimetal.



Address: No.1 Road, Tieling High-Tech Industrial Development Zone, Tieling, Liaoning Province, China, 112611

Tel. +86 24 7883 1001

Mob. +86 139 4100 7017 (Russian)

Mob. +86 176 0410 3077 (English)

E-mail: [inquiry@hmt.clad.com](mailto:inquiry@hmt.clad.com)

Website: <https://hmtclad.com>

Linkedin: <https://lnkd.in/gSv6E>

## EDITORIAL BOARD

### Editor-in-Chief

I.V. Krivtsun E.O. Paton Electric Welding Institute, Kyiv, Ukraine

### Deputy Editor-in-Chief

S.V. Akhonin E.O. Paton Electric Welding Institute, Kyiv, Ukraine

### Deputy Editor-in-Chief

L.M. Lobanov E.O. Paton Electric Welding Institute, Kyiv, Ukraine

### Editorial Board Members

O.M. Berdnikova E.O. Paton Electric Welding Institute, Kyiv, Ukraine  
Chang Yunlong School of Materials Science and Engineering, Shenyang University of Technology, Shenyang, China  
V.V. Dmitrik NTUU «Kharkiv Polytechnic Institute», Kharkiv, Ukraine  
Dong Chunlin Guangzhou Jiao Tong University, Guangzhou, China  
M. Gasik Aalto University Foundation, Finland  
A. Gumenyuk Bundesanstalt für Materialforschung und –prüfung (BAM), Berlin, Germany  
V.V. Knysh E.O. Paton Electric Welding Institute, Kyiv, Ukraine  
V.M. Korzhyk E.O. Paton Electric Welding Institute, Kyiv, Ukraine  
V.V. Kvasnytskyi NTUU «Igor Sikorsky Kyiv Polytechnic Institute», Kyiv, Ukraine  
Yu.M. Lankin E.O. Paton Electric Welding Institute, Kyiv, Ukraine  
O.V. Makhnenko E.O. Paton Electric Welding Institute, Kyiv, Ukraine  
S.Yu. Maksymov E.O. Paton Electric Welding Institute, Kyiv, Ukraine  
Yupiter HP Manurung Smart Manufacturing Research Institute, Universiti Teknologi MARA, Shah Alam, Malaysia  
M.O. Pashchin E.O. Paton Electric Welding Institute, Kyiv, Ukraine  
V.D. Poznyakov E.O. Paton Electric Welding Institute, Kyiv, Ukraine  
U. Reisgen Welding and Joining Institute, Aachen, Germany  
I.O. Ryabtsev E.O. Paton Electric Welding Institute, Kyiv, Ukraine  
V.M. Uchanin Karpenko Physico-Mechanical Institute, Lviv, Ukraine  
Yang Yongqiang South China University of Technology, Guangzhou, China  
**Executive Director** O.T. Zelnichenko, International Association «Welding», Kyiv, Ukraine

### Address of Editorial Board

E.O. Paton Electric Welding Institute, 11 Kazymyr Malevych Str., 03150, Kyiv, Ukraine  
Tel./Fax: (38044) 205 23 90, E-mail: [journal@paton.kiev.ua](mailto:journal@paton.kiev.ua)  
<https://patonpublishinghouse.com/eng/journals/tpwj>

**State Registration Certificate** 24933-14873 ПП from 13.08.2021

ISSN 0957-798X, DOI: <http://dx.doi.org/10.37434/tpwj>

**Subscriptions**, 12 issues per year:

\$384 — annual subscription for the printed (hard copy) version, air postage and packaging included;

\$312 — annual subscription for the electronic version (sending issues in pdf format or providing access to IP addresses).

### Representative Office of «The Paton Welding Journal» in China:

China-Ukraine Institute of Welding, Guangdong Academy of Sciences

Address: Room 210, No. 363 Changxing Road, Tianhe, Guangzhou, 510650, China.

Zhang Yupeng, Tel: +86-20-61086791, E-mail: [patonjournal@gwi.gd.cn](mailto:patonjournal@gwi.gd.cn)

The content of the Journal includes articles received from authors from around the world in the field of welding, cutting, cladding, soldering, brazing, coating, 3D additive technologies, electrometallurgy, material science, NDT and selectively includes translations into English of articles from the following journals, published in Ukrainian:

- Automatic Welding (<https://patonpublishinghouse.com/eng/journals/as>);
- Electrometallurgy Today (<https://patonpublishinghouse.com/eng/journals/sem>);
- Technical Diagnostics & Nondestructive Testing (<https://patonpublishinghouse.com/eng/journals/tdnk>).

# CONTENTS

PREFACE .....	3
---------------	---

## ORIGINAL ARTICLES

### **ADVANCED TECHNOLOGIES OF WELDING AND JOINING OF MATERIALS**

<b>I.V. Ziakhor, Ye.V. Antipin, O.V. Didkovskiy, O.V. Kavunichenko, A.M. Levchuk, Yu.A. Shylo, Yan Truska</b> MODERN TECHNOLOGIES OF WELDING RAILWAY RAILS (REVIEW)* .....	4
-------------------------------------------------------------------------------------------------------------------------------------------------------------------------------	---

<b>V.M. Korzhyk, A.A. Grynyuk, V.Yu. Khaskin, E.V. Ilyashenko, S.I. Peleshenko, A.O. Aloshyn, I.O. Skachkov, O.V. Dolyanivska</b> INFLUENCE OF THE SPEED OF PLASMA-ARC WELDING AT A VARIABLE POLARITY ASYMMETRICAL CURRENT ON THE FORMATION OF JOINTS OF HIGH-STRENGTH ALUMINIUM ALLOYS** .....	17
----------------------------------------------------------------------------------------------------------------------------------------------------------------------------------------------------------------------------------------------------------------------------------------------------	----

<b>A.I. Ustinov, Iu.V. Falchenko, S.O. Demchenkov, L.V. Petrushynets</b> MANUFACTURING LIGHTWEIGHT HONEYCOMB PANELS ON THE BASE OF HIGH-ENTROPY $\text{CoCrFeNiSi}_{0.2}$ ALLOY FOIL PRODUCED BY EB-PVD METHOD** .....	29
---------------------------------------------------------------------------------------------------------------------------------------------------------------------------------------------------------------------------	----

<b>S.V. Maksymova, P.V. Kovalchuk, V.V. Voronov, I.I. Datsiuk</b> THE INFLUENCE OF IRON ON THE STRUCTURE AND TECHNOLOGICAL CHARACTERISTICS OF Cu–Mn–Co–Fe BRAZING FILLER METAL** .....	36
-------------------------------------------------------------------------------------------------------------------------------------------------------------------------------------------	----

### **MATHEMATICAL MODELING OF WELDING AND RELATED PROCESSES**

<b>I.V. Krivtsun, I.V. Krikent, V.F. Demchenko</b> INFLUENCE OF WELD POOL SURFACE DEPRESSION ON BURNING CONDITIONS OF AN ARC WITH A REFRACTORY CATHODE** .....	44
-------------------------------------------------------------------------------------------------------------------------------------------------------------------	----

### **STRENGTH, RELIABILITY AND LIFE OF WELDED STRUCTURES**

<b>L. Lobanov, M. Pashchyn, O. Mikhodui</b> MODERN TECHNOLOGIES OF ELECTROPHYSICAL TREATMENT FOR REGULATION OF STRESS-STRAIN STATES OF ELEMENTS OF WELDED STRUCTURES** .....	50
---------------------------------------------------------------------------------------------------------------------------------------------------------------------------------	----

### **ADDITIVE TECHNOLOGIES**

<b>S.V. Adzhamskyi, G.A. Kononenko, R.V. Podolskyi</b> INFLUENCE OF A STOP IN THE PROCESS OF MELTING ON MECHANICAL PROPERTIES OF SPECIMENS FROM THE Co–Cr–Mo ALLOY MADE BY SLM TECHNOLOGY** .....	56
------------------------------------------------------------------------------------------------------------------------------------------------------------------------------------------------------	----

### **TECHNICAL DIAGNOSTICS AND NON-DESTRUCTIVE TESTING**

<b>L.M. Lobanov, D.I. Stelmakh, V.V. Savitsky, V.P. Diadin, O.P. Shutkevych, A.G. Kozachek</b> REMOTE ASSESSMENT OF DAMAGES OF THE KYIV TV TOWER BASED ON THE USE OF AERIAL PHOTOGRAPHY AND THE METHOD OF PHOTOGRAMMETRY*** .....	60
--------------------------------------------------------------------------------------------------------------------------------------------------------------------------------------------------------------------------------------	----

### **EQUIPMENT FOR WELDING AND RELATED TECHNOLOGIES**

<b>V.M. Nesterenkov, K.S. Khripko, V.V. Lukyanov, M.O. Sysoev, V.V. Chernyavskiy</b> TECHNOLOGY AND EQUIPMENT FOR ELECTRON BEAM SINTERING OF HARD ALLOY BILLETS .....	65
--------------------------------------------------------------------------------------------------------------------------------------------------------------------------	----

<b>O.I. Som</b> PLASMA TORCH FOR PLASMA TRANSFERRED ARC SURFACING WITH TWO POWDER FEEDING SYSTEMS** .....	73
--------------------------------------------------------------------------------------------------------------	----

<b>S.O. Hlushak</b> EVOLUTION OF ELECTRON BEAM HARDWARE FOR WELDING IN SPACE** .....	78
-----------------------------------------------------------------------------------------	----

## INFORMATION

<b>V.V. Holovko, O.S. Kotelchuk, A.A. Golyakevych, L.M. Orlov</b> MODERN FLUX-CORED WIRES FOR ARC WELDING OF METAL STRUCTURES FROM LOW-ALLOYED STEELS, DEVELOPED AT THE E.O. PATON ELECTRIC WELDING INSTITUTE AND OJSC "TM.WELTEC" .....	85
---------------------------------------------------------------------------------------------------------------------------------------------------------------------------------------------------------------------------------------------	----

PATON INTERNATIONAL — EVOLUTIONS IN YEARS .....	88
-------------------------------------------------	----

\*Translated Article(s) from "Automatic Welding", No. 5, 2023.

\*\*Translated Article(s) from "Automatic Welding", No. 8, 2023.

\*\*\*Translated Article(s) from "Technical Diagnostics & Nondestructive Testing", No. 3, 2023.

---



*DEAR COLLEAGUES, READERS  
OF “THE PATON WELDING JOURNAL”!*

This is the August issue of “The Paton Welding Journal” of the current year 2023. The journal has been published since 1989 in UK with interruptions, and since 2000 it has been published monthly by the E.O. Paton Electric Welding Institute of the National Academy of Sciences of Ukraine (PWI). What is this issue noteworthy for?

First, it contains articles reflecting a wide range of relevant areas of activity of the PWI — the largest R&D centre in Ukraine in the field of welding and related technologies. On the pages of this issue you will also find works performed within the framework of scientific and technical cooperation of PWI with profile organizations of Ukraine and other countries as well as the articles by some of our numerous partners. In particular, this issue of the Journal provides readers the opportunity to learn about the results of research works, scientific and technical developments of Ukrainian scientists and specialists in such fields as: advanced technologies of welding and joining of materials; mathematical modeling of welding and related processes; strength, reliability and life of welded structures; additive technologies; technical diagnostics and non-destructive testing; equipment for welding and related technologies.

Secondly, most of the research results, published in this issue of the Journal, were obtained in the recent, very difficult time for Ukraine, in the conditions of a large-scale war unleashed by the Russian Federation. This means that Ukrainian scientists and specialists in the field of welding and related technologies continue to work actively, develop new technologies and equipment, introduce them into industrial production, including for the purpose of solving the problems of improving the defence capability of our country.

Finally, this issue of the Journal provides an opportunity to learn about the activities of some industrial enterprises, research institutes and organizations of both in Ukraine as well as in foreign countries, with which PWI is connected by many years of scientific and technical cooperation.

Prof. Igor Krivtsun  
Editor-in-Chief,  
Director of PWI



---

DOI: <https://doi.org/10.37434/tpwj2023.08.01>

## MODERN TECHNOLOGIES OF WELDING RAILWAY RAILS (REVIEW)

I.V. Ziakhor<sup>1</sup>, Ye.V. Antipin<sup>1</sup>, O.V. Didkovskiy<sup>1</sup>, O.V. Kavunichenko<sup>1</sup>, A.M. Levchuk<sup>1</sup>,  
Yu.A. Shylo<sup>1</sup>, Yan Truska<sup>2</sup>

<sup>1</sup>E.O. Paton Electric Welding Institute of the NASU  
11 Kazymyr Malevych Str., 03150, Kyiv, Ukraine

<sup>2</sup>SaZ s.r.o. Company Koupelní 3908/6, 69501 Hodonín, Czech Republic

### ABSTRACT

The known methods of welding railway rails in terms of their efficiency, productivity and ability to provide the quality of welded rails in accordance with the requirements of standards in force were analyzed. When evaluating the efficiency of different methods of welding, the technological features of formation of welded joints, values of mechanical properties, macro- and microstructure of the joints, the probability of defects formation, efficiency and possibility of automation of the welding process were taken into account. It is shown that such welding methods as thermit, automatic electric arc, gas-pressure and electric resistance found practical application. The varieties of the latter are flash-butt welding (FBW) using continuous flashing, FBW with resistance preheating and FBW with pulsed flashing. FBW technology with pulsed flashing allows providing optimal thermal cycles when welding steels with different chemical composition and properties and ensures compliance of welded joints with the requirements of standards in force. Scientific, technological and design developments of E.O. Paton Electric Welding Institute (PWI) were implemented in a series of stationary and mobile rail welding machines, which are equipped with mobile rail welding complexes, successfully introduced in many countries of the world.

**KEYWORDS:** thermit, electric arc, gas-pressure, flash butt welding of rails

### INTRODUCTION

Current state and service conditions of Ukrainian railways, necessity of their integration in the international system of transport corridors, necessity of increase of movement speeds, ensuring correspondence to international standards for smoothness and safety of traffic — all this requires permanent development and improvement of the whole railway complex. First of all it refers to track facilities that are one of the most important elements of the railways. Condition of upper structure of a track determines the speed and safety of train movement, allowable loads on axles of carriages and locomotives [1]. Analysis of productivity of freight and passenger traffic on European railway shows that increase of their efficiency is mainly achieved due to technical progress [2, 3].

One of the scientific and technical problems requiring continuous solution is improvement of the technology and equipment for welding of a continuous seamless track [4] from railway steels of modern manufacture [5–7]. Seamless track is the most progressive structure of upper track construction. Its main advantage lies in almost complete elimination of rail bolted connections which are the reason of additional dynamic impact of the wheels on the rails.

Joining of rails in manufacture of extended rail sections (200–800 m) in fixed plants, as well as in the field, when laying the rails on the track, is carried out by welding [3, 4]. Service characteristics of railway

rails and their welded butt joints are an important component of the life of railway networks, and they are regulated by current domestic and international standards [8–11]. Leading world manufacturers of railway rails constantly improve rail steels aimed to increase the hardness, brittle fracture resistance, and wear resistance, in particular in the rail head [12–17].

Methods of fusion [18–26] and pressure welding [3, 4, 27–35] are used for welding of rails in construction and repair of railway tracks. Methods of fusion welding have been used since 1920<sup>th</sup>, in particular, in repair and subsequently at construction of railway tracks. The methods used in practice are thermit [18–20], and electric arc (manual with stick electrodes, semi-automatic gas-shielded and flux-cored wire [21, 22], automatic electric arc bath welding, using a consumable nozzle [23–26]). Among the methods of pressure welding the efficient ones are gas-pressure [27–28], induction [29, 30], linear friction [31–34], and electric resistance welding [3, 4, 35–39]. The varieties of the latter are flash-butt welding (FBW) using continuous flashing, FBW with resistance preheating and FBW with pulsed flashing.

The works on development and investigation of the technology of electroslag welding of rails [40, 41] were conducted, but information on wide practical application of this method could not be found in available publications.

The aim of the review is analysis of well-known methods of welding of railway rails from the point of view of their efficiency, productivity and ability to pro-

vide the characteristics of welded rails quality in accordance with the requirements of standards in force.

Evaluation of the efficiency of different methods of welding the railway rails was based on technological peculiarities of formation of welded joints, values of mechanical properties, macro- and microstructure of the joints, probability of defect formation, suitability for testing (prediction) of butt joint quality, productivity and possibility of welding process automation.

Since thermit, electric arc, gas-pressure and flash-butt welding have found practical application in construction and repair of railway tracks, this review will be dedicated to analysis of exactly these methods.

### THERMIT (ALUMOTHERMIC) WELDING

Thermit welding (TW) is the method in which heating and melting of rail ends is carried out by the heat of chemical reaction of a powder-like thermit mixture. It consists of oxidized iron and metallic aluminum as reacting components and of alloying components. The composition of the thermit mixture is specified in such a way that the composition of weld metal is close to that of the rail steel.

Reliable fixing of rails [18] is provided for the purpose of elimination of possible weld defects. A thermit mixture is poured into a crucible installed above the mould and the reaction is started using a pyrotechnic reagent. The time of the reaction is 15–30 s, the temperature during TW reaches 2000 °C or higher and molten steel and alumina slag are formed. They remain molten and are separated in the crucible due to a difference in the specific weight. Molten steel produced in such a way is poured between the rail ends. The process from release to solidification takes approximately 4 min. The total time of performance of one rail joint is approximately 30 min. The equipment for TW includes

a torch for preheating, a crucible, a set of moulds and a flash-remover with a hydraulic drive.

As can be seen from the photo of TW weld macrostructure (Figure 1), the width of cast zone is up to 75 mm and the HAZ width is approximately 20 mm on both sides of the weld [19]. The values of hardness of the metal of the weld and HAZ in TW of thermally-hardened rails are significantly lower in comparison with the characteristics of base metal. To reduce the hardness gradient (Figure 2) in TW of high-strength rails, heat treatment is sometimes used, i.e. reheating of the weld to austenite region and accelerated cooling with compressed air.

Weld metal structure is characterized by grain size number 1 typical for overheated steel. Formation of defective structures with large grain size promotes a loss of steel ductility [20]. Presence in the weld of nonmetallic inclusions of manganese sulphide type can significantly influence formation of defects, which considerably decrease the ductility and strength values of welded joints at cyclic loads.

In TW the rail length during welding does not change, therefore this method is successfully used under field conditions for the final stage of rail installation. Quality of welding mainly depends on compliance with the conditions of preparatory works and quality of thermit mixture. This is responsible for low suitability of TW to automated control and prediction of weld quality. The necessary level of joint metal hardness depends on the rail grade, and it can be controlled by the quantity of alloying elements [20]. Despite the comparatively low productivity and impossibility of process automation, the TW technology due to high mobility and versatility has been used for more than 100 years for joining rails for various applications (on tram and railway tracks), as well as for welding railway crosses [18, 19, 23, 37].

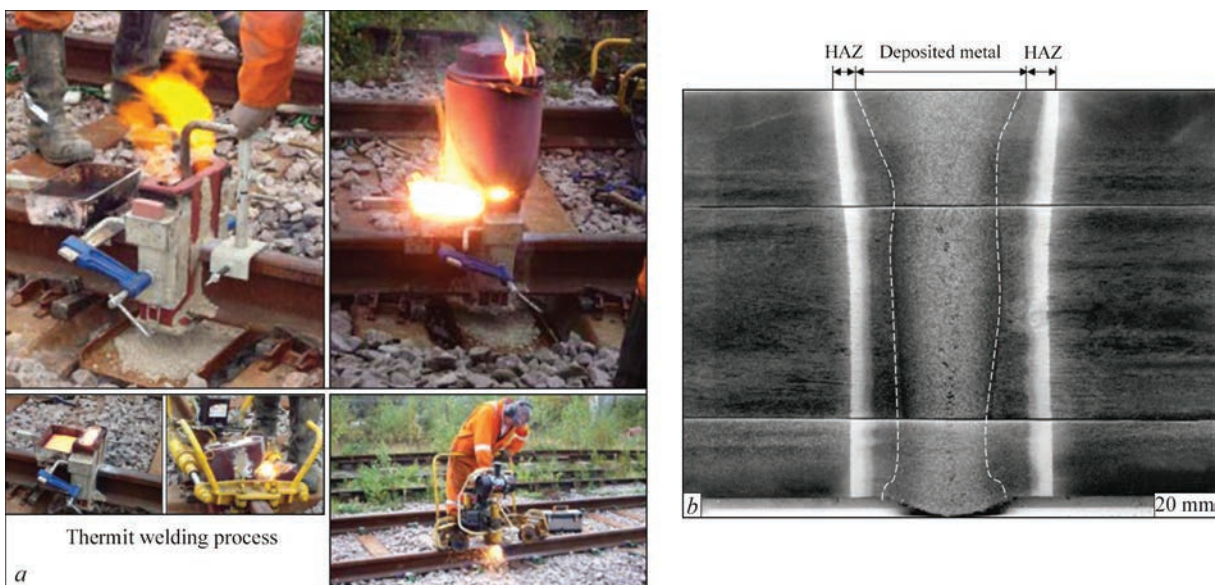
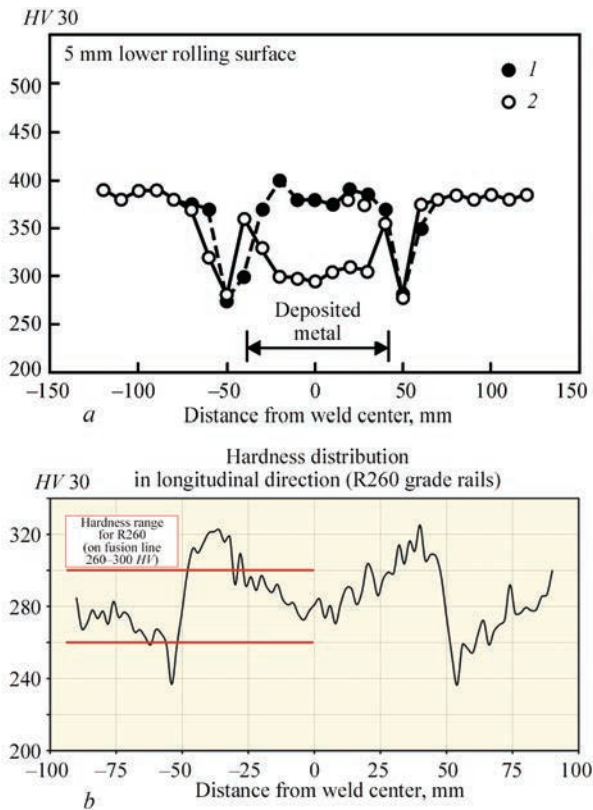


Figure 1. Sequence of technological operations at TW (a) [19], macrostructure of the weld (b) [23]



**Figure 2.** Hardness distribution in joining rails of R350HT (a) [23] and R260 (b) strength class [37]: 1 — after reheating and accelerated cooling; 2 — after welding

### ELECTRIC ARC WELDING (EAW)

The simplest variation, namely manual bath EAW using coated electrodes, is mainly applied for joining of tram and crane rails [21]. However, this method does not provide a satisfactory quality of joining the railway rails, it depends on welder's qualification and is significantly inferior to other welding methods in terms of productivity. Semi-automatic bath EAW has higher productivity. It was used, in particular, in repair of underground railway tracks [21]. Crack formation in the welded joint zone was eliminated using preheating to 300–350 °C temperature. Work [22] describes the experience of application of hidden arc EAW using high-carbon electrodes for joining high-strength steel rails. The technological cycle of welding included preheating and postweld heat treatment. Higher productivity was achieved at automatic fusion welding using a combination of consumable electrode gas-shielded EAW technology (for the rail foot) and narrow-gap electroslog welding [22].

There is experience of successful application of EAW in construction of a high-speed railway line in Japan, where the quality of welded joints [23] was dramatically improved due to upgrading of the technology and welding consumables, as well as application of special heat treatment. Process of EAW of rails includes deposition of a root bead with full penetration, multipass welding of the foot, continuous welding from web

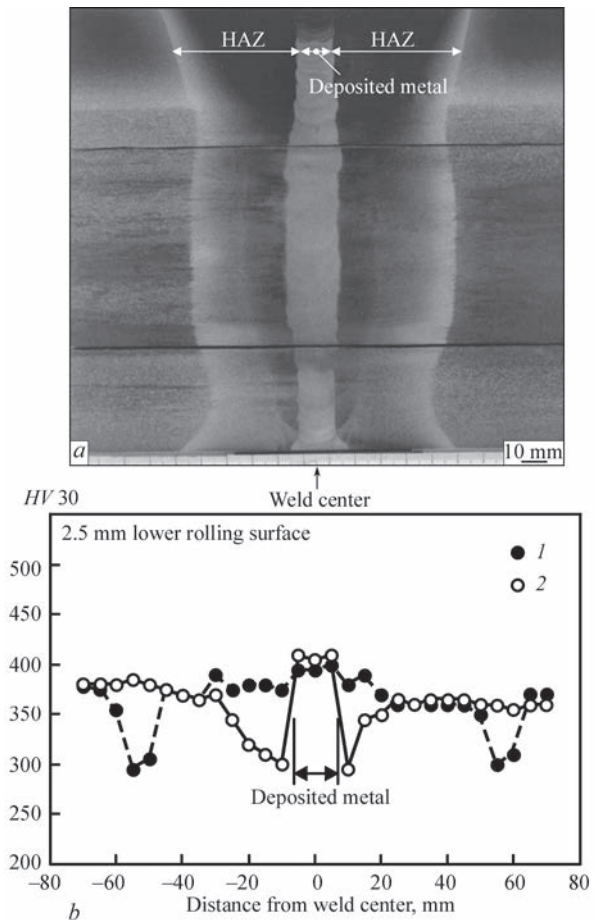


**Figure 3.** Macrostructure of weld (a), distribution of hardness in HAZ (b) of a joint of thermally-hardened rails [23]: 1 — after reheating and accelerated cooling; 2 — after welding

to head and multipass welding of the rail head. Welding wire of 800–1100 MPa class was used for standard carbon steel rails. Weld metal has a bainitic structure, due to a low content of carbon in the wire. High-carbon welding wire was used to produce a pearlitic structure in weld metal [23] that improves wear resistance and resistance to wear-out of weld metal of high-strength rails. Welding productivity (one butt joint in 60–75 min) is at a low level even under the conditions of modern equipment application.

Figure 3 shows weld macrostructure and hardness distribution in the zone of the joint of thermally-hardened rails. Weld width is approximately 20 mm and total HAZ width is approximately 100 mm. Weld metal hardness is close to base material hardness of 390 HV 30, but zones of lower hardness are present from both sides of the weld. Reheating and accelerated cooling of welded butt joint, carried out for reduction of hardness gradient, promote a shifting of lower hardness zones for 60 mm distance from the weld center [23]. Work [24] shows that in EAW of rails the HAZ metal is the most dangerous area of the joint in terms of cold crack nucleation. Elimination of cold cracking in the joints is problematic without application of preheating to the temperature of at least 250 °C. Increase

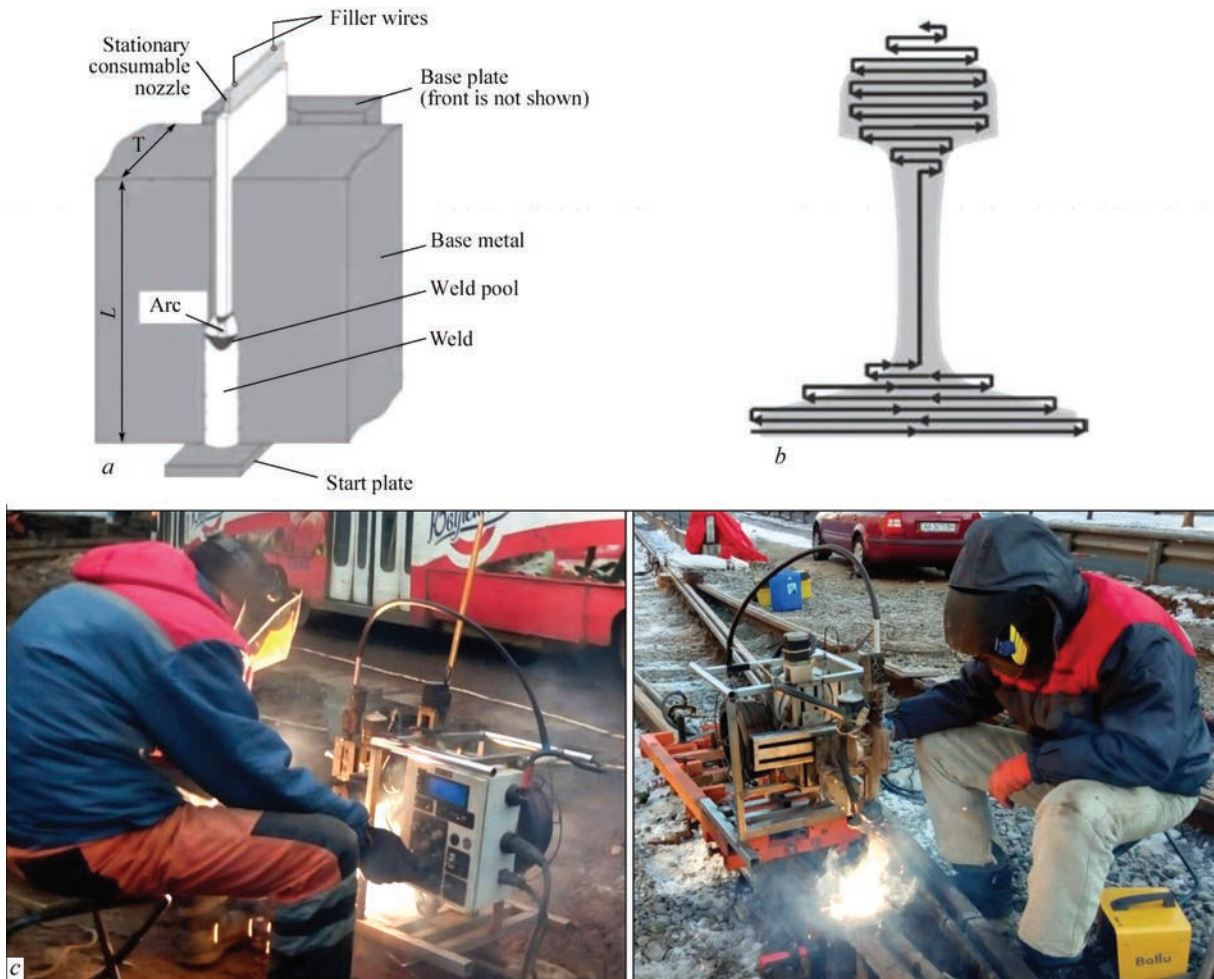


**Figure 4.** Scheme of the process (a), direction of nozzle movement (b) [25, 26], mobile equipment for EAW using a consumable nozzle (c)

of welding heat input promotes only deceleration of the processes of cold cracks development in the welded joints, but it does not prevent their nucleation.

Known EAW variations have low characteristics of efficiency in terms of guarantee of a defect-free weld, suitability for automated control (prediction) of welding quality, and process productivity.

PWI has developed a technology of automatic bath EAW using a consumable nozzle [25, 26]. Its peculiarity (Figure 4, a, b) is application of self-shielded flux-cored wire fed through a longitudinal channel in a flat nozzle being melted that allows welding performance at 12–16 mm gap and in some cases at 8–22 mm [25]. Owing to welding process mechanization, the developed EAW technology allows 2–3 times increase of work productivity and a considerable improvement of quality characteristics of welded joints, while preserving the high mobility and versatility of equipment (Figure 4, c). Special welding consumables and technology of automatic EAW provide satisfactory values of mechanical properties of the joints [25, 26]. Thus, weld metal hardness in welded joint of R65 rails is equal to  $HB$  2600–3200 MPa, yield strength is 800–900 MPa [25], fracture load at static bend testing is 1500–1650 kN at deflection of 16–22 mm. This tech-

nology is suitable for welding of rail tracks of industrial enterprises, tram and crane tracks, as well as for performance of urgent repair operations on railways in the future.

### GAS-PRESSURE WELDING (GPW)

GPW is a method of pressure welding, at which end faces of the rails are pressed together and a gas flame is used for heating [23, 27, 28]. GPW process (Figure 5) consists of the stages of heating, upsetting, forging and flash removal. The process of heating is carried out manually by a welding operator using an oxyacetylene mixture, so that the level of welding process automation is low. Since the tightness of contact of the ends being welded has a significant effect on the joint quality, the end faces are treated using special grinding devices which determines the corresponding requirements to the staff qualification and organization of preparation work.

During heating the end faces and adjacent areas of the weld are heated to 1200–1300°C temperature. Pressure on the ends is usually constant,  $P = 20\text{--}30$  MPa during the entire heating process. During GPW the rail ends are subjected to plastic deformation, the value of rail shortening is 20–40 mm. Convexity formed



**Figure 5.** Sequence of technological operations in GPW [19]: 1 — dressing of rail ends; 2 — setting up GPW unit; 3 — GPW process (heating stage); 4 — end of GPW process (upsetting); 5 — flash removal; 6 — welded part immediately after GPW

during forging is removed in the hot condition using flash-remover with a hydraulic drive. GPW provides sufficiently high productivity, namely time of welding of one butt joint is 6–7 min, depending on the rail profile. Equipment for GPW consists of a gas-heating device, a system for rail pressing together and a hydraulic flash-remover.

Width of the HAZ of a rail joint is about 100 mm (Figure 6), hardness value decreases approximately to 270–290 HV 30, therefore postweld heat treatment is used at GPW of thermally-hardened rails that significantly decreases the efficiency of operations. Typical defects, formed in GPW joints, are oxide films. In work [27] the GPW process using hydrogen as a heating gas was studied, in order to reduce oxide formation.

Regardless of the fact that the quality of welded joints in GPW depends on the level of operator training, quality of heating gas and preparation of rail end faces, suitability for control (prediction) of welded joint quality is higher in comparison with TW and EAW. Subject to qualified staff availability, correct organization of auxiliary and welding operations, GPW provides reliable welding of rails at relatively

low investments. It is proved by successful experience of application of this technology in Japan [23]. This method did not become widely used in the EU countries and the USA.

### FLASH-BUTT WELDING (FBW)

FBW can be carried out using continuous or pulsed flashing [36–39] and also flashing with resistance preheating [35, 43–47]. In FBW with continuous flashing (Figure 7, *a*) the rails are gradually brought closer at turned-on current source that leads to formation and melting of contact-bridges. This continuous process results in heating of rails to a set depth, and formation of a layer of liquid metal at the ends. After that the speed of drawing together is increased for a short time (intensive flashing stage) (Figure 8, *a*) and upsetting is carried out. The liquid metal with oxide films is pressed out from the joint outside and flash is formed at solidification, which is usually removed while hot.

FBW process with preheating includes the stages of resistance preheating (main preheating of rails), intensive flashing, upsetting and flash removal. In resistance preheating (Figure 7, *b*) the ends of rails are

periodically pressed together with a small axial force and current is switched on, then they are separated and withdrawn which causes equalization of temperature fields in the rail cross-section. In resistance preheating the source of energy emission and preheating zone almost completely cover the metal located between the clamping jaws of the welding machine. After heating of rail edges to the necessary temperature, flashing and upsetting are carried out. Until the middle of the 60s of the XX century the rails were joined by FBW method with preheating under stationary conditions in bulky equipment of 20–30 t weight with available powerful (600–700 kVA) power sources.

A known current developer of technology and equipment for FBW with preheating is Schlatter Company (Switzerland) [35], which manufactures rail welding complexes, in particular stationary machines (Figure 8, *b*) for operation under plant conditions. Significant limitations for application of this technology are the necessity to use power sources of considerable capacity, relative complexity, large dimensions and high cost of the equipment, in particular of mobile rail welding complexes.

In 1960s PWI for the first time in the world developed the technological fundamentals and designed highly efficient mobile equipment for welding of railway rails under field conditions. They are based on FBW technology with continuous flashing with a programmed change of the main parameters of the welding process. Programmed change of parameters is carried out together with application of feedbacks which automatically correct the set values of parameters at welding conditions change. Successful realization of this technology is due to development of an original design of welding transformers with lower short-circuit resistance, in particular the idea was realized of application of elements of power hydraulic drive as current-carrying elements of the secondary circuit of the transformers.

The disadvantage of FBW technology with continuous flashing of rails are sufficiently large values

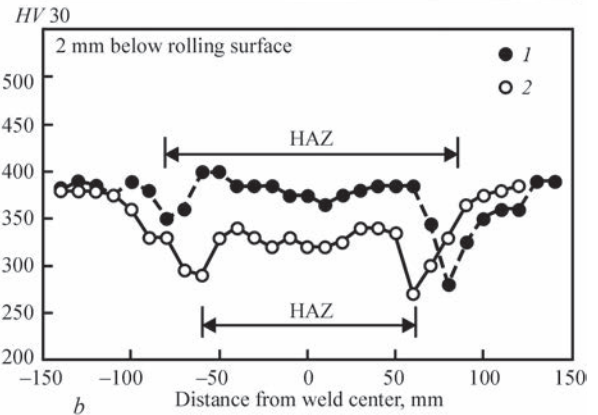
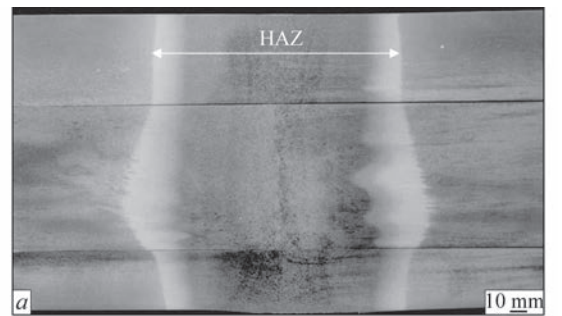


**Figure 6.** Macrostructure (*a*), hardness distribution in the HAZ (*b*) of the joint in GPW of thermally-hardened rails [23]: 1 — after reheating and accelerated cooling; 2 — after welding

of flashing allowance (around 40 mm) and total time of welding (180–240 s). FBW technology with pulsed flashing developed at PWI became a revolutionary improvement of the technology of FBW of rails [3, 4, 36, 38]. Multifactor regulation of flashing provides intensification of contact heating, reduction of metal consumption, and increase of thermal efficiency of the process. Due to highly concentrated heating, the total heat input, process duration and allowance for welding are reduced 1.5–2.0 times.

For evaluation of the efficiency of different FBW technologies it is necessary to consider the current standards of Ukraine and EU concerning welded joints of railway rails. Table 1 provides comparison of the requirements of current standards with quality characteristics of welded joints of rails during FBW.

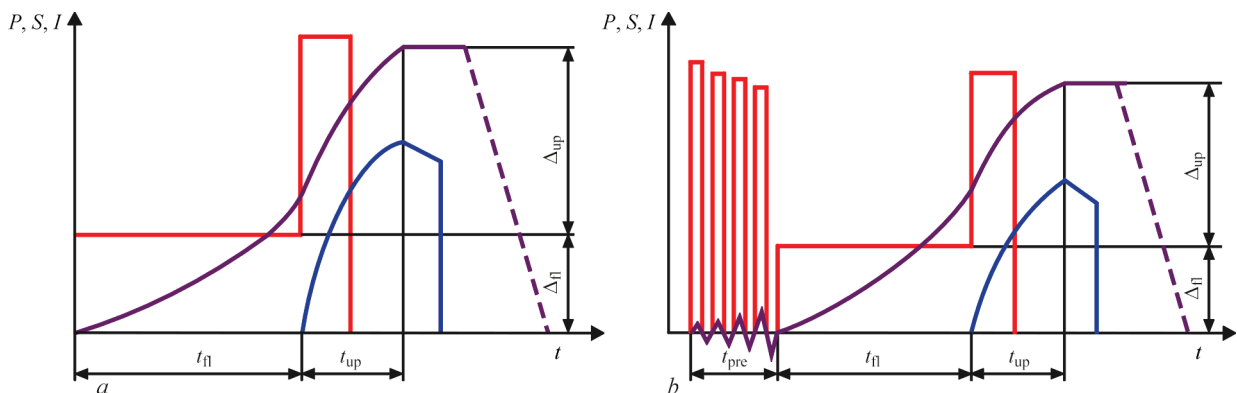


**Figure 7.** Typical cyclograms of FBW process with continuous flashing (*a*) and FBW with resistance preheating (*b*):  $t_{fl}$ ,  $t_{up}$ ,  $t_{pre}$  — duration of stages of flashing, upsetting, preheating;  $\Delta_{fl}$  and  $\Delta_{up}$  — allowance for flashing and upsetting;  $P$  — pressure;  $S$  — displacement;  $I$  — current

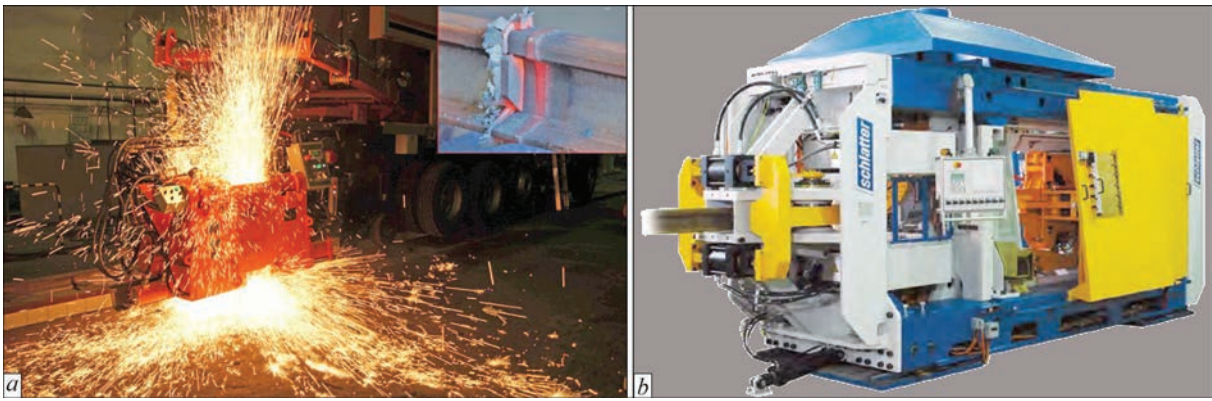


**Figure 8.** Mobile rail welding machine K922-1 during FBW with flashing (a), stationary rail welding machine Schlatter GAAS 80 (b) [35]

According to normative documents, namely domestic [8, 9] and European [10, 11] standards, the requirements to welded joints of railway rails can be conditionally divided into the following groups:

**Table 1.** Main requirements to quality characteristics of welded joints of rails at FBW

Parameter being controlled	EN 14587-1:2018	EN 14587-2:2009	TU U 24.1-40075815-002:2016
Mechanical properties at static bend testing			
Minimum fracture load at its application to rail head, kN	1600		1650
Sagging deflection, mm, not less than	20		30
Presence of defects at magnetic powder inspection			
Cracks	Unallowable		Unallowable
Presence of defects in the fracture of a joint after forced destruction of butt joints			
Lack of penetration	Unallowable		Unallowable
Flat spot (not lens)	Allowable $L < 10$ mm, $\delta < 0.7$ mm		Not more than 3 spots of the area of up to 15 mm <sup>2</sup>
Flat spot (lens)	Allowable $L < 4$ mm, $\delta < 0.7$ mm		
Defects and HAZ parameters at macrostructure analysis			
Presence of lacks of penetrations, inclusions, cracks, shrinkage	Unallowable		
Minimum HAZ width $H_{HAZmin}$ , mm	25	20	Not controlled
Maximum HAZ width $H_{HAZmax}$ , mm	45	45	Not controlled
Allowable difference of HAZ width $H_{HAZmax} - H_{HAZmin}$ , mm	10	20	Not controlled
Microstructure			
Presence of martensite and bainite at $\times 100$	Unallowable	Unallowable	Not controlled
Hardness distribution			
Non-thermally hardened rails (R260, R220, R260Mn, M76, HV 30)	Min: $P - 30$ HV 30 Max: $P + 60$ HV 30		Min: $P - 10$ % HV 30
Thermally-hardened rails (R350NT, K76F), HV 30	Min: $P = 325$ HV 30 Max: $P = 410$ HV 30		Min: $P - 15$ % HV 30
Fatigue tests			
Number of cycles, mln	5	5	Not controlled
Load, kN	190	190	Not controlled
<i>Note.</i> $P$ is the average value of hardness of the rail base metal.			

- values of mechanical properties — deflection and fracture loading in static transverse bending test of butt joints;
- presence of defects — types of unacceptable and maximum dimensions and number of acceptable defects;
- parameters of HAZ — its width and non-uniformity along the length and across the section of rails during analysis of welded joint macrostructure;
- distribution of hardness in the HAZ (minimum and maximum values);
- microstructure of metal in the joint zone and the HAZ — allowable pearlitic structure of different fineness (pearlite, sorbite, troostite), presence of areas with martensitic or bainitic structure is excluded;
- characteristics at fatigue testing of the joints.

Analysis of the data in Table 1 shows that there are considerable differences in the requirements of domestic and European standards, first of all, as regards the need to determine the strength values under cyclic loading of welded joints, and, secondly, quantitative evaluation of joint HAZ parameters. The information in the available foreign publications [43–47] indicates that the HAZ parameters (width, uniformity over rail section) and fatigue strength values are extremely important for prediction of wear resistance of welded joints and service life of the railway track (that is one of the defining criteria of evaluation of welding method efficiency).

That is why, it was a well-substantiated and timely decision of the Ministry of Infrastructure of Ukraine to approve the List of National Standards, correspondence to which gives a presumption of conformity to the requirements of Technical Regulations on Safety of Infrastructure of Railway Transport (Order dated 20.11.2019 No. 815). The mentioned List includes national standard DSTU EN 14587-2:2015 (EN 14587-2:2009, IDT), harmonized with the corresponding European regulatory document [11]. It means that in construction and repair of domestic railway tracks using rails of foreign manufacture the quality characteristics of the joints should be evaluated based on the requirements of the European standard.

Therefore, HAZ parameters, hardness distribution in the joint zone, microstructure (absence of hardening structures) are important criteria for evaluation of the efficiency of FBW technology. Available publications and many years of practical experience indicate that similar to any other method of welding of railway rails, a problem for FBW is formation of a hardness gradient in the HAZ (Figure 9): for thermally-hardened rails — zones of reduced hardness from both sides of the fusion line (Double Dip Hardness) [43–47], for non-thermally hardened rails — significant increase of hardness in overheating zone [4].

The main problem of FBW method with preheating is stabilization of the thermal field appearing during welding. Increase of cross-sectional area of the rails leads to a significant drop of the process energy efficiency and also a decrease of power coefficient. Practical experience indicates that appropriate development of the technology of FBW with preheating allows meeting the requirements to welded joint quality (Table 1). However, realization of this technology of welding is complicated under field conditions because of considerable dimensions of the mobile rail welding machines.

Technology of FBW with pulsed flashing allows regulating the thermal cycles in wide ranges in welding of steels of different composition and properties, and with optimization of the technological modes it provides specified by standards in force [10, 11] quality of rail joints made both by stationary and mobile rail welding machines [4, 39].

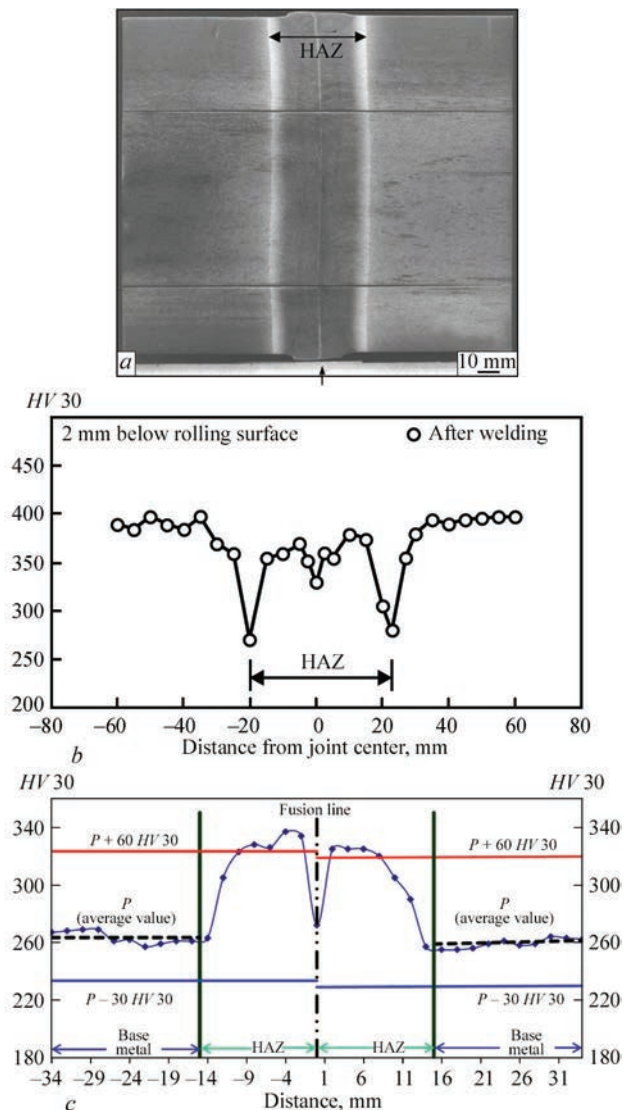


**Figure 9.** Macrostructure of welded joint of rails in FBW (a); distribution of hardness in the joint of rails of R350HT (b) and R260 grades (c)

**Table 2.** Comparison of the methods of railway rail welding [23]

Welding methods	Welding time, min	Equipment		Operator skills	Welding quality
		Initial investments	Mobility		
FBW	2–4	Considerable	Low	Not required	High
GPW	5–7	Considerable	Medium	Required	High
EAW	60	Low	High	Required	Satisfactory
TW	30	Low	High	Not required	Satisfactory

**Table 3.** Evaluative comparison of the methods of railway rail welding

Characteristic (value)	FBW	GPW	EAW	TW
Process metallurgy	Forging	Forging	Melting	Melting
Process automation	High	Medium	Medium	Low
HAZ width, mm	20–45	120–150	80–100	115–140
Suitability for control (prediction) of joint quality	High	Medium	Low	Low

### COMPARISON OF DIFFERENT METHODS OF RAIL WELDING

Table 2 provides evaluative comparison of the considered rail welding methods by several characteristics from reference [23] and Table 3 gives evaluation by other considered criteria.

Practical experience shows that despite a comparatively low productivity and complexity of process automation, fusion welding methods (TW and EAW) due to low initial investments, high mobility and versatility, have been used for more than 100 years for joining of rails for different applications on tram and railway tracks, and crane tracks of industrial enterprises, and TW is successfully used for welding of crosses on railway tracks.

Gas-pressure welding provides reliable welding of rails under the condition of availability of qualified staff and proper organization of the auxiliary and welding operations, despite a low level of automation of the processes of rail end preparation, heating and joint quality control. It was demonstrated by successful experience of application of this technology in Japan.

Practical experience of application of FBW with resistance preheating, in particular from Schlatter Company, indicates a correspondence of quality characteristics of rail welded joints to the requirements of standards in force. The main limitation for application of this technology is a relative complexity, large dimensions and high cost of rail welding equipment.

From 1960s till 2010s the technology of FBW with continuous flashing was successfully used in rail joining under stationary and field conditions, in particular for all types of rails of open-hearth production. The disadvantages of FBW technology with continuous flashing of rails are relatively high values of flashing allowance, total time of welding and complexity of provision of thermal cycles specified by the normative documents that are necessary for sound joining of modern wear-resistant rails.

FBW technology with pulsed flashing allows regulating in wide limits the thermal cycles when joining railway rails of different profiles or grade from steels of diverse composition and provides joint quality specified by standards in force. Production of mobile and stationary rail welding machines equipped with computer systems for control

**Figure 10.** Stationary rail welding units K1100 (a), K924 (b) designed at PWI



**Figure 11.** Mobile rail welding machines K920 (a), K922-1 (b) of the process and the main welding parameters was mastered in the 2000s. The base of the systems is the principles of controlling the pulsed flashing process [48–50]. A system for automatic control is based on application of fast acting hydraulic drive, industrial computer with a monitor for data visualizing, controller, and sensors of displacement, voltage and pressure. Welding of each joint includes

self-regulation of the parameters that provides optimization of the program of their change at all the stages of flashing and on the whole during welding. Computer control system registers all the welding parameters, determines their allowable deviations from set values and provides evaluation of the joint quality directly after welding in accordance with the established algorithms [49, 51].



**Figure 12.** Mobile machines K960 (a), K945 (b), rail welding complex with K945 machine (c) for FBW of rails with “tension”

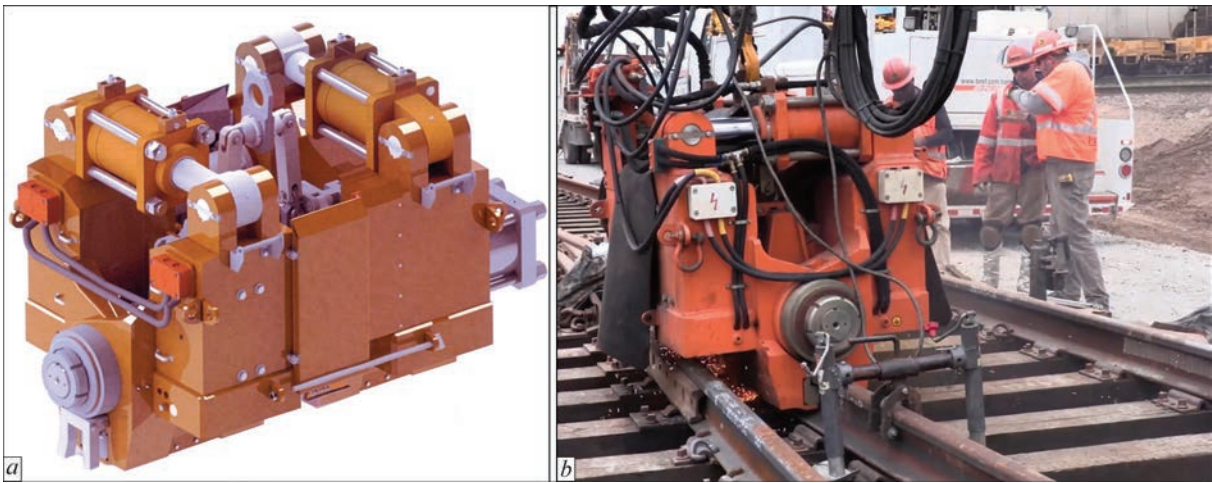


**Figure 13.** Prototype of machine K1045 (a) and welding complex with machine K1045 for FBW of rails in difficult-to-access locations (b)



**Figure 14.** Rail welding complex KCM 005 on a combined chassis equipped with machine K920 (a), K922-1 (b)

The scientific, technological and design developments of PWI were realized in a series of stationary (K1000, K1100, K924) and mobile machines (K900, K920, K921, K922-1, K930, K945, K950, K1045), which are included into the mobile rail welding complexes (Figures 10–14). The distinctive characteristics of these machines are the kinematic diagram, peculiarities of design of the clamping and axial displacement mechanism, upsetting force (650–2000 kN), etc. The advantage of most of the models of the machines is presence of a built-in flash remover with a separate drive for flash removing in the hot condition without unclamping the rails being welded.

These machines realize a series of internationally patented innovative technical solutions in the field of welding, control systems, designing the assemblies of welding machines, fast-acting hydraulic drives and principles of rail alignment. In recent years several hundred stationary and mobile rail welding machines were manufactured and delivered to different countries (USA, Canada, Austria, Great Britain, China, Singapore, Thailand, Malaysia, Taiwan, Kazakhstan, Slovakia, etc.).

Current scientific, technological and design developments of PWI are focused on maximum adaptation to the customer requirements from the point of view of efficiency of welding of rails of different categories,

grade and composition (in particular, of hypereutectoid class and those alloyed by Cr, Mn, Ti, V) [52, 53], design solutions and technical characteristics of the machines, increase of manufacturability of separate assemblies and mechanisms, and they are implemented in the design of new mobile rail welding machines.

## CONCLUSIONS

1. Permanent joints of railway rails are performed by fusion welding (thermit, electric arc, electrosag) and pressure welding methods (gas-pressure, electric resistance, induction, linear friction).

2. Thermit, electric arc, gas-pressure and flash-butt welding methods found practical application in construction and repair of railway tracks. The flash-butt welding method has the following variations, namely FBW with continuous flashing, FBW with resistance preheating and FBW with pulsed flashing.

3. Despite a comparatively low productivity, impossibility of process automation, thermit welding, due to its high mobility and versatility, has been used for more than 100 years for joining rails for different applications (on tram and railway tracks), as well as welding railway crosses.

4. Developed at PWI technology of automatic electric arc bath welding using a consumable nozzle is suitable for welding of rail tracks of industrial enterprises,

tram and crane tracks, as well as for performance of operative repair on the railways in the future.

5. Despite a comparatively low level of process automation, gas-pressure welding with availability of qualified staff and correct organization of auxiliary and welding operations provides reliable welding of rails. It is proved by successful experience of application of this technology in Japan.

6. Practical experience of application of FBW with resistance preheating, in particular from Schlatter Company, demonstrates the correspondence of quality characteristics of welded joints of rails to the requirements of current standards. The main limitation for application of this technology is a relative complexity, large dimensions and high cost of rail welding equipment.

7. Technology of FBW with pulsed flashing allows providing optimum thermal cycles in welding of steels of different composition and properties and guarantees joint quality specified by current standards. Scientific, technological and design developments of PWI were realized in a series of stationary and mobile rail welding machines, which are included into mobile rail welding complexes successfully introduced in many countries of the world.

8. Development of FBW technology and equipment is driven by the need for their maximum adaptation to modern requirements of efficient welding of rails of different categories, strength classes and composition, requirements to design solutions and technical characteristics of rail welding machines, increase of manufacturability of separate assemblies and mechanisms.

## REFERENCES

- Paton, B., Kostyuk, M., Kuchuk-Yatsenko, S. (2010) Innovative cluster «Velvet road» and scientific-technical breakthrough of Ukraine into world market of construction of high-speed railways. *Nauka ta Innovatsii*, 6(2), 69–86 [in Ukrainian].
- Cantos, P., Pastor, J., Serrano, L. (1999) Productivity, efficiency and technical change in the European railways: A non-parametric approach. *Transportation*, 26, 337–357. DOI: <https://doi.org/10.1023/A:1005127513206>
- Kuchuk-Yatsenko, S., Yakovlev, V., Didkovskiy, O. et al. (2016) Development of technologies and equipment of rail welding is the key for widening of all-welded seamless tracks in Ukraine. *Ukrainska Zaliznytsya*, 1, 56–59 [in Ukrainian].
- Kuchuk-Yatsenko, S. (2018) Technologies and equipment for flash-butt welding of rails: 60 years of continuous innovations. *The Paton Welding J.*, 11–12, 25–40. DOI: <https://doi.org/10.15407/tpwj2018.12.03>.
- DSTU 4344:2004: *Rails common to broad gauge railways. General specifications*. UkrNDIMet, Kyiv, Derzhspozhyvstandart [in Ukrainian].
- EN 13674-1:2011+A1:2017: *Railway applications – Track – Rail*. Pt 1: Vignole railway rails 46 kg/m and above. European Committee for Standardization.
- DSTU EN 13674-1:2018 (EN 13674-1:2011+A1:2017, IDT) (2018) *Railway transport. Track. Rails*. Pt 1: Vignole railway rails 46 kg/m and above. DP UkrNDNTs [in Ukrainian].
- TUU 24.1-40075815-002:2016: *New welded rails for railways. Specifications* [in Ukrainian].
- (2012) *Technical recommendations on technology of tension welding of rails*. VND UZ 32.7.02.012-2012 TsP-0280. Kyiv, Poligraphservis [in Ukrainian].
- EN 14587-1:2018 (E): *Railway applications — Infrastructure — Flash butt welding of new rails*. Pt 1: R220, R260, R260Mn, R320Cr, R350HT, R350LHT, R370CrHT and R400HT grade rails in a fixed plant.
- EN 14587-2:2009 (E): *Railway applications – Track – Flash butt welding of rails*. Pt 2: New R220, R260, R260Mn and R350HT grade rails by mobile welding machines at sites other than a fixed plant.
- Tachikawa, H., Uneta, T., Nishimoto, H. (2000) Steel welding technologies for civil construction applications. *Nippon Steel Techn. Rept.* 82(7), 35–41.
- Xiao-Fei, L.I., Langenberg, P., Münstermann, S. et al. (2005) *Recent developments of modern rail steels*. HSLA Steels. 2.
- Tatsumi, K., Mineyasu, T., Minoru, H. (2011) Development of SP3 rail with high wear resistance and rolling contact fatigue resistance for heavy haul railways. *JFE Technical Report*, 16.
- Pointner, P. (2008) High strength rail steels — The importance of material properties in contact mechanics problems. *Wear*, 265(9–10), 1373–1379.
- Kuziak, R., Zygmunt, T. (2013) A new method of rail head hardening of standard-gauge rails for improved wear and damage resistance. *Steel Res. Int.*, 84(1), 13–19. DOI: <https://doi.org/10.1002/srin.201200140>
- Morant, S. (2015) Next-generation super-premium rail steels hit the tracks. *Inter. Railway J.* <http://www.railjournal.com/index.php/track/next-generation-super-premium-rail-steels-hit-the-tracks.html?channel=531>
- Lonsdale, C. (1999) *Thermite rail welding: History, process developments, current practices and outlook for the 21<sup>st</sup> century*. Altoona, PA 16601: Conrail Technical Services Laboratory Altoona.
- Micenko, P., Muruganant, M., Huijun, L. et al. *Double dip hardness profiles in rail weld heat-affected zone literature and research review report*. CRC Project Report, R3.121. Brisbane, Australia.
- Wang, Y., Zhou, H., Shil, Y.-j. et al. (2012) Mechanical properties and fracture toughness of rail steels and thermit welds at low temperature. *Inter. J. of Minerals, Metallurgy and Materials*, 19(5), 409. DOI: <https://doi.org/10.1007/s12613-012-0572-8>.
- Dahl, B. (1995) Repair of rails on-site by welding. *Svetsaren*, 50(2), 10–14.
- Okumura, M. et al. (1995) Development of field fusion welding technology for rail-roadrails. *Nippon Steel Techn. Rept.*, 65(4), 41–49.
- Saita, K., Karimine, K., Ueda, M. (2013) Trends in Rail Welding Technologies and Our Future Approach. *Nippon steel and Sumitomo Metal Technical Report.*, 105, 84–92.
- Poznyakov, V., Kiriakov, V., Gajvoronsky, A. et al. (2010) Properties of welded joints of rail steel in electric arc welding. *The Paton Welding J.*, (8), 16–20.
- Kuzmenko, G., Kuzmenko, V., Galinich, V. et al. (2012) New technology of electric arc bath welding of rails on tram and crane tracks. *The Paton Welding J.*, 5, 33–36.
- Bajic, D., Kuzmenko, G., Samardzic, I. (2013) Welding of rails with new technology of arc welding. *Metallurgija*, 3, 399–402.
- Yamamoto, R. (2007) Advances in gas pressure welding technology for rails. *Railway. Technology Avalanche*, 17, 99–105.
- Yamamoto, R., Komizu, Y., Fukada, Y. (2014) Experimental examination for understanding of transition behaviour of oxide

- inclusions on gas pressure weld interface: Joining phenomena of gas pressure welding. *Welding Inter.*, **7**, 510–520. DOI: <https://doi.org/10.1080/09507116.2012.753237>.
29. *Induction rail welding plant*. [www.mirageservices.co.uk](http://www.mirageservices.co.uk)
  30. *Railway rail induction-welding device*: Pat. US2019330805: E01B29/46, B23K13/01, B23K37/04, E01B29/04, E01B29/44. Publ. on 06.12.2022.
  31. Maalekian, M (2007) *Friction welding of rails*. PhD Th., Graz University of Technology.
  32. Gould, J., Johnson, W. *Translational friction weld rail repair — Phase I final report*. EWI Project No. 52765GTH, FRA Contract No. DTFR53-11-C-00004.
  33. Shira, S. *The use of translational friction welding for constructing and repairing rail for high speed and intercity passenger rail — Phase II design report* EWI Project 54368GTH Task 1–3, FRA Contract No. DTFR53-13-C-00041.
  34. Zhang, H., Li, C., Zhu, Z. (2022) Influence of CDFW process parameters on microstructure and mechanical properties of U75V rail steel welded joint. *Metals.*, **12**(5), 711. DOI: <https://doi.org/10.3390/met12050711>
  35. *Schlatter Group. Rail welding systems* (2016) [www.schlatter.ch](http://www.schlatter.ch): [www.schlatter.ch/en/welding-machine](http://www.schlatter.ch/en/welding-machine)
  36. Kuchuk-Yatsenko, S., Krivenko, V., Didkovsky, A. (2012) Technology and new generation of equipment for flash butt welding of advanced high-strength rails for construction and reconstruction of high-speed railway lines. *The Paton Welding J.*, **6**, 22–26.
  37. *INNTRACK — Innovative track systems*. Concluding Technical Report. <http://www.innotrack.eu>
  38. Kuchuk-Yatsenko, S., Didkovsky, A., Shvets, V. (2016) Flash-butt welding of high-strength rails of nowadays production. *The Paton Welding J.*, **5–6**, 4–12. DOI: <https://doi.org/10.15407/tpwj2016.06.01>
  39. Kuchuk-Yatsenko, S., Didkovsky, A., Shvets, V. (2016) Flash-butt welding of high-strength rails. *Mining, Informatics, Automation and Electrical Engineering*, **528**, 4.
  40. Turpin, B., Danks, D. (2003) *Electroslag field welding of railroad rail — Final report for high-speed rail IDEA Project* [http://onlinepubs.trb.org/onlinepubs/archive/studies/idea/finalreports/highspeedrail/hsr-37final\\_report.pdf](http://onlinepubs.trb.org/onlinepubs/archive/studies/idea/finalreports/highspeedrail/hsr-37final_report.pdf)
  41. Danks, D., Turpin, B. (2005) Recent advances in field electroslag rail welding. In: *Proc. of AREMA 2005 Annual Conf.* [www.arena.org/files/library/2005\\_Conference\\_Proceedings/00049.pdf](http://www.arena.org/files/library/2005_Conference_Proceedings/00049.pdf)
  42. Grigorenko, G., Kostin, V., Zhukov, V. et al. (2016) Peculiarities of structural transformations in HAZ metal of rail steel M76 joint produced by flash-butt welding. *J. of Physical Sci. and Appl.*, **6**(5), 54–652. DOI: <https://doi.org/10.17265/2159-5348/2016.05.0>
  43. Weingrill, L., Krutzler, J., Enzinger, N. (2016) Temperature field evolution during flash-butt welding of railway rails. *Materials Sci. Forum.*, **879**, 2088–2093. DOI: <https://doi.org/10.4028/www.scientific.net/MSF.879.2088>
  44. Micheletto, A., Cookson, J., Pang, Y. et al (2020) The structural integrity of flash-butt welded premium rail steel — Evaluation of strength, microstructure and defects. *J. of Rail and Rapid Transit* (IF 1.87). DOI: <https://doi.org/10.1177/0954409720973138>
  45. Mousavizade, M., Farhangi, H. (2009) Characterization of surface defects associated with flash butt-welded pearlitic rails and their contribution to overload and fatigue failures. *Advanced Materials Research.*, **83–86**, 1262–1269.
  46. Porcaro, R.R., Faria, G.L., Godefroid, L.B. et al (2019) Microstructure and mechanical properties of a flash butt welded pearlitic rail. *J. Mater. Process. Tech.*, **270**, 20–27.
  47. (2008) D4.6.1: *The influence of the working procedures on the formation and shape of the HAZ of flash butt and aluminothermic welds in rails*. INNTRACK Project TIP5-CT-2006-031415. <http://www.innotrack.eu>
  48. Rudenko, P., Gavrish, V., Kuchuk-Yatsenko, S. (2017) Influence of flash butt welding process parameters on strength characteristics of railway rail butts. *The Paton Welding J.*, **5–6**, 75–78. DOI: <https://doi.org/10.15407/tpwj2017.06.14>
  49. Kuchuk-Yatsenko, S., Didkovsky, A., Antipin, E. (2017) Real-time operational control information management system for flash-butt welding of rails. *Mining — Informatics. Automation and Electrical Engineering*, **529**, 4. DOI: <http://dx.doi.org/10.7494/miag.2017.1.529.35>.
  50. Kuchuk-Yatsenko, S., Milenin, A., Velikoivanenko, E. (2018) Mathematical modeling of metal heating process in continuous flash-butt welding. *The Paton Welding J.*, **10**, 2–8. DOI: <https://doi.org/10.15407/tpwj2018.10.01>
  51. Kuchuk-Yatsenko, S. I., Rudenko, P. M., Gavrish, V. S. et al. (2016) Statistical control of process of flash-butt welding of rails. Two-level control system. *The Paton Welding J.*, **6**, 13–16. DOI: <https://doi.org/10.15407/tpwj2016.06.02>.
  52. Shvets, V.I., Didkovsky, O.V., Antipin, Y.V. et al. (2022) Features of microstructure of butt joints of hypereutectoid ARE-AL-136HE-X rail steel in flash-butt welding. *The Paton Welding J.*, **3**, 33–40. DOI: <https://doi.org/10.37434/tpwj2022.03.04>
  53. Shvets, V.I., Didkovsky, O.V., Zyakhor, I.V. et al (2023) Study of the structure of joints of rails of R260MN grade in flash-butt welding. *The Paton Welding J.*, **1**, 3–10. DOI: <https://doi.org/10.37434/tpwj2023.01.01>

## ORCID

I.V. Ziakhor: 0000-0001-7780-0688,  
 Ye.V. Antipin: 0000-0003-3297-5382,  
 O.V. Didkovskyi: 0000-0001-5268-5599,  
 O.V. Kavunichenko: 0000-0002-5164-9796,  
 A.M. Levchuk: 0000-0002-0361-7394,  
 Yu.A. Shylo: 0000-0002-6174-5925

## CONFLICT OF INTEREST

The Authors declare no conflict of interest

## CORRESPONDING AUTHOR

I.V. Ziakhor  
 E.O. Paton Electric Welding Institute of the NASU  
 11 Kazymyr Malevych Str., 03150, Kyiv, Ukraine.  
 E-mail: [zyakhor@paton.kiev.ua](mailto:zyakhor@paton.kiev.ua)

## SUGGESTED CITATION

I.V. Ziakhor, Ye.V. Antipin, O.V. Didkovskyi, O.V. Kavunichenko, A.M. Levchuk, Yu.A. Shylo, Yan Truska (2023) Modern technologies of welding railway rails (Review). *The Paton Welding J.*, **8**, 4–16.

## JOURNAL HOME PAGE

<https://patonpublishinghouse.com/eng/journals/tpwj>

Received: 10.04.2023  
 Accepted: 07.08.2023

DOI: <https://doi.org/10.37434/tpwj2023.08.02>

# INFLUENCE OF THE SPEED OF PLASMA-ARC WELDING AT A VARIABLE POLARITY ASYMMETRICAL CURRENT ON THE FORMATION OF JOINTS OF HIGH-STRENGTH ALUMINIUM ALLOYS

V.M. Korzhyk<sup>1</sup>, A.A. Grynyuk<sup>1</sup>, V.Yu. Khaskin<sup>1</sup>, E.V. Ilyashenko<sup>1</sup>, S.I. Peleshenko<sup>2</sup>, A.O. Aloslyn<sup>2</sup>, I.O. Skachkov<sup>3</sup>, O.V. Dolyanivska<sup>3</sup>

<sup>1</sup>E.O. Paton Electric Welding Institute of the NASU

11 Kazymyr Malevych Str., 03150, Kyiv, Ukraine

<sup>2</sup>LLC “Foreign Economic Representation of the E.O. Paton Chinese-Ukrainian Institute of Welding

11 Kazymyr Malevych Str., 03150, Kyiv, Ukraine

<sup>3</sup>National Technical University of Ukraine “Igor Sikorsky Kyiv Polytechnic Institute”

37 Peremohy Prosp., 03056, Kyiv, Ukraine

## ABSTRACT

The effect of change in the speed of movement of the heating source in plasma-arc welding of aluminium alloys of 2.0 mm thick of three Al–Mg–Mn (AMg5M, AMg6), Al–Cu–Mn (1201) and Al–Cu–Li (1460) alloying systems on the microstructure and hardness of the weld metal and near-weld zone, on the formation of inner pores and mechanical properties of welded joints was considered. Changes in the distribution of temperature fields and indices of the stress-strain state of welded specimens were analyzed. It was found that for each type of alloys there is a certain “peak” welding speed, with exceeding of which there is no significant reduction in residual deformations and stresses, as well as a decrease in the width of the base metal heating zone. Instead, mechanical properties of welded joints are deteriorated because of an increase in the number of pores in the weld metal and the formation of inadmissible undercuts in the upper part of the weld in the area of transition from the weld to the base metal. On the example of Al–Mg–Mn alloy it is shown that such regularities are also typical not only for the thickness of 2.0 mm, but also observed during welding of specimens with the range of thicknesses of 4–8 mm. This allows using these results to predict indices of strength of the welded joint and weld metal for these thicknesses when the speed of plasma-arc welding at a variable polarity asymmetrical current is increased higher than the “peak” value.

**KEYWORDS:** plasma-arc welding, variable polarity pulses, aluminium alloys, weld structure, pores, joint formation, strength, temperature distribution, stress-strain state

## INTRODUCTION

Structures manufactured of high-strength aluminium alloys are used in many fields of the modern industry, namely in the aerospace industry and in ground and water transport production [1]. In order to reduce the total weight of such structures, it is rational to use high-strength aluminium alloys (e.g., Al–Mg–Mn, Al–Cu–Mn and Al–Cu–Li). Aluminium alloys of alloying systems Al–Cu–Mn and Al–Cu–Li have high indices of specific strength, but these alloys are sensitive to excessive heating during welding. This causes a need in creating welding technologies to reduce the heat input into the base metal during welding, including due to the use of higher welding speeds. Traditionally, the joints of parts of Al–Cu–Mn and Al–Cu–Li alloys were produced with the help of a well-known process of argon tungsten-arc welding (TIG) at a variable polarity current [2]. This process is characterized by a low concentration of power in the heating spot. Here, wide and shallow welds are formed. Such low penetration capacity of the heating source in argon tungsten arc welding at a variable polarity current

necessitates the edge preparation in welding parts of more than 4 mm thickness. The heat released during TIG welding at a low power concentration in the heating spot causes softening of high-strength aluminium alloys in the heat-affected zone (HAZ) under the effect of arc heat [3]. In addition, aluminium alloys with the lithium content are prone to the formation of defects in the form of oxide inclusions in the process of argon-arc welding. To solve this problem, it is rational to use welding methods providing an increase in the concentration of power in the heating spot and allow increasing the welding speed, reducing the heat input into the base metal due to these factors, that will allow reducing the level of softening of the base metal in the HAZ of the heating source and improving the mechanical properties of welded joints.

Despite that the process of plasma-arc welding at a variable polarity asymmetrical current exists many years at the market (the first publications date back to the mid-1980s), this method of welding is relevant and in demand nowadays thanks to the use of welding sources on the basis of inverter technology of current conversion and a widespread use of welding robots [4–7].

## ANALYSIS OF LITERATURE DATA AND PROBLEM STATEMENT

It is rational to use plasma-arc welding at a variable polarity asymmetrical current for the formation of high-strength aluminium alloys welded joints, which provides a power density of at least 300 W/mm<sup>2</sup>, which is 5 times higher than this index compared to TIG, as well as up to 3 times increase in the speed of welding for parts of certain thicknesses [8]. Welding speed is one of the important factors to increase the efficiency of producing welded joint. At the same time, with an increase in the welding speed, an increase in the indices of strength of welded joints, as well as reducing the deformation of the structure during welding are observed. Despite the advantages of welding at high speeds, it is required to use more powerful power sources of welding current, plasmotrons with a more complex design and more complex and more accurate mechanisms for movement of plasmotrons. A logical question arises concerning the limit to which welding speed can be increased and whether there is such a limit in the welding speed, on reaching which, there is no longer a significant decrease in the level of deformation of a structure and a significant increase in strength indices. As the criteria for evaluating such welding speed, it is necessary to consider a significant decrease in the increment of strength indices, negative changes in the formation of welded joint geometry and arising of probable defects in the weld metal. It is rational to consider this issue both from the standpoint of the influence of speed on the formation of macrogeometry and microstructures of the weld, and from the standpoint of its influence on the residual stress-strain state of the structure.

The effect of plasma-arc welding speed on the produced joints from different materials was studied to some degree by various researchers. For example, such data were obtained by optimizing the process of plasma-arc welding (PAW) of duplex stainless 2205 steel of 2 mm thickness [9]. The parameters considered for experimentation and optimization include welding current, welding speed and length of the pilot arc, respectively. The experiment included the change in parameters and further registration of penetration depth and weld width. Welding current of 60–70 A, welding speed of 25.0–30.0 cm/min and pilot arc length of 1–2 mm is a range, in which the mode parameters were changed. During the experiments, a neural network with feedback was used. A genetic algorithm and Taguchi methods were used to predict the width and penetration depth. It was determined that the calculated forecasts are well confirmed by experimentally achieved results, and welding on optimized parametric values provides an increase in the strength of the weld with a reduction in consumables and time.

In [10] the issue of the effect of plasma-arc welding speed in the mode of a keyhole formation (K-PAW) on the quality of penetration and hot cracks formation in welding of the hastelloy X alloy was studied. K-PAW welding was carried out in one pass at speeds of 21.0, 19.0, 17.0 and 15.0 cm/min. Welding at a speed of 170 mm/min provided the best depth to width ratio in the weld compared to all other speeds, and hot cracks were detected at 15.0 cm/min due to a high heat input at a low speed. At welding speeds of 21.0 and 19.0 cm/min, insufficient penetration depth was detected as a result of a reduction in the heat input and the lack of keyhole penetration on the back side. The maximum Vickers microhardness was observed at a welding speed of 21.0 cm/min, and the lowest one at 15.0 cm/min, i.e. the value of the microhardness is inversely proportional to the welding speed. The speed of 170 mm/min provided the best welding quality in view of the depth/width ratio and almost the highest value of microhardness.

The comparison of plasma welding with conventional TIG welding showed [11] that in the case of using plasma process, it is possible to increase the welding speed, which causes an increase in the strength of joints during rupture tests, an increase in ductility indices, reduction of dendrites sizes, HAZ sizes and residual deformations. However, researchers in [12] have found that with a significant increase in welding speed (up to 150–200 cm/min), a constricted arc begins to burn unstable, and at even greater increase in welding speed, even the weld formation is stopped.

However, there were no comprehensive studies on determination of the limit of plasma-arc welding speed, after reaching which there is no more significant increment in strength indices, as well as reducing the width of HAZ and deformation of the structure.

## AIM AND TASKS OF RESEARCH

The aim of the work is to set reasonable limits for an increase in the speed of plasma-arc welding at a variable polarity asymmetrical current on the basis of determination of the effect of this parameter on the formation of welds, structure, change in mechanical properties of joints, distribution of temperature fields and stress-strain state of welded joints.

To achieve this aim, the following tasks were solved:

- determination of dependencies of formation, structure and change in mechanical properties of butt joints of alloys of the alloying systems Al–5Mg–Mn, Al–3Cu–1.8Li and Al–6Cu–Mn on the speed of plasma-arc welding at a variable polarity asymmetrical current;
- determination of distribution of temperature fields in welded plates from aluminium alloys, depending on the speed of plasma-arc welding;

**Table 1.** Chemical composition of aluminium alloys being welded, wt.%

Grade	Al	Cu	Mg	Mn	Zr	Ti	Zn	Fe	Si	Li
AMg5	Base	0.1	5.0	0.8	–	0.02		0.5	0.5	–
1201	–?–	6.0	–	0.4	–	0.06	0.2	0.4	0.4	–
1460	–?–	1.8	0.7	0.06	0.03	0.02	–	0.08	0.10	1.8

● investigation of residual deformation of welded joints produced by plasma-arc welding (by a constricted arc) at different welding speeds.

## MATERIALS, EQUIPMENT AND RESEARCH METHODS

As welded specimens, aluminium alloys of alloying systems Al–Mg–Mn, Al–Cu–Mn and Al–Cu–Li with the thickness of sheets of 2.0 mm were considered (Table 1).

The studies were performed using a robotic complex PLAZER PAW-R for plasma-arc welding at a variable polarity asymmetrical current with the smart automatic system for control and monitoring of welding equipment (LLC “Scientific and Production Centre

“PLAZER”, Ukraine) (Figure 1). In addition to plasma-arc welding at a variable polarity asymmetrical current, the robotic complex allows performing a combined and hybrid welding with a combination of plasma-arc welding at a variable polarity with consumable electrode inert gas welding both without the formation of a common pool between two processes (combined welding), as well as with the formation of one common pool (hybrid welding).

PD-174M2 plasmatron designed at PWI (Figure 2, *a, b*) was used to carry out studies of weldability of selected aluminium alloys in wide ranges of a variable polarity asymmetrical current [13]. This plasmatron includes a set of replaceable plasma-forming nozzles



**Figure 1.** General appearance of the robotic complex of equipment PLAZER PAW-R for plasma-arc welding of lengthy welded joints at a variable polarity asymmetrical current with an up to 2000 mm extension of the robot hand and a system of the robot movement to 3000 mm (*a, b*) and a rack with power sources of the robot, plasmatron, cabinet with adaptation of commands for the robot and smart automatic system for monitoring of welding equipment (*c*): 1 — anthropomorphic welding robot; 2 — welding plasmatron; 3 — smart system for control of robotic welding process; 4 — plasma module; 5 — power source of plasma welding; 6 — welding table with an assembly and welding device; 7 — system for linear movement of robot on rails; 8 — double-axial rotator-manipulator; 9 — mechanism for filler wire feed

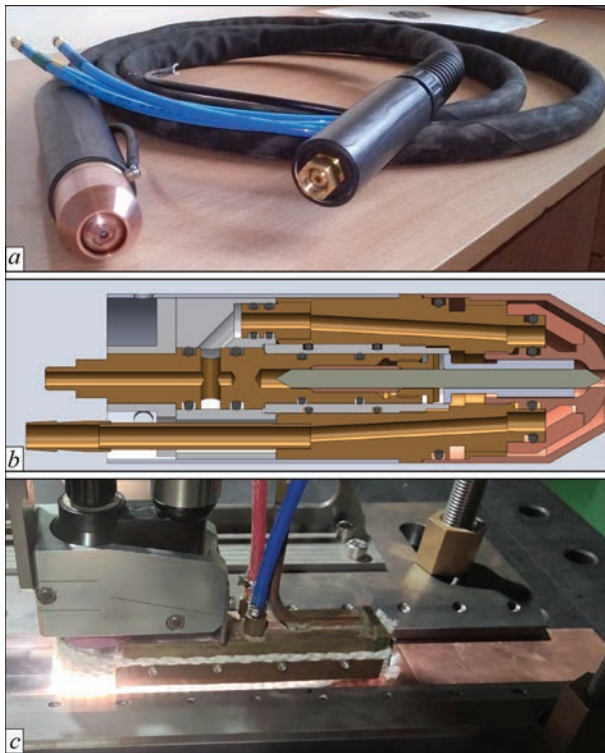


**Figure 2.** Appearance (a), cross-section of 3D-model (b) of welding plasmatron PD-174M2 for welding of aluminium alloys at a variable polarity asymmetrical current in the range from 80 to 350 A at DC 100 % and the process of robotic welding using an elongated gas protection nozzle (c)

with the holes of diameters from 2.0 to 4.5 mm with a step of 0.5 mm. For welding alloys with an increased fluidity of liquid metal, plasma-forming nozzles with 2 or 4 additional holes with a diameter of 1.0 mm are included in the set. The task of additional holes is to reduce the excessive gas pressure on the axis of a plasma-forming nozzle and to provide additional elongation of the plasma arc. Also, for the efficient operation of this plasmatron in the specified range of currents, there is an option of using tungsten electrodes with a diameter from 3.2 to 6.0 mm by replacing a collet



**Figure 3.** Appearance of welded joint of AMg5M alloy in the assembly and welding device immediately after plasma-arc welding at a variable polarity asymmetrical current at a speed of 200 cm/min

and a washer-current-lead for electrode unit, as well as a ceramic insulator-aligner, which is made of special thermal-resistant ceramics. For welding at high speeds (above 120 cm/min) using this plasmatron, a nozzle with elongated gas protection with a length of 200 mm and a width of 50 mm was used (Figure 2, c).

As a criterion “high-speed welding”, an excess of speed of the base process of arc welding of high-strength aluminium alloys (with the strength higher than 300 MPa) by 2 or more times, TIG welding at a variable polarity current was chosen. A limiting factor in plasma-arc welding at a variable polarity asymmetrical current in our case were the technological capabilities of welding plasmatrons, namely the maximum current load of up to 325 A.

The maximum speeds of plasma-arc welding at a variable polarity asymmetrical current in the flat position on the substrate with a forming groove and the use of a filler wire are shown in Table 2. Figure 3 shows the outer appearance of welded joint of AMg5M alloy in the assembly and welding device immediately after the end of plasma-arc welding at a variable polarity asymmetrical current of 200 cm/min speed. In welding, the change in the indices of strength of the welded joint and weld metal were taken into account. The following alloys were considered: AMg5M (Al–5 % Mg–8 % Mn), which is thermally unstrengthened and should be little sensitive to the loss of strength in the HAZ, thermally strengthened alloys 1201 (Al–6 % Cu–0.4 % Mn) and aluminium-lithium alloy 1460 (Al–3.0 % Cu–1.8 % Li). The base metal of 1201 and 1460 alloys tend to lose strength in the HAZ of the arc.

## RESULTS OF STUDYING THE EFFECT OF SPEED OF PLASMA-ARC WELDING AT A VARIABLE POLARITY ASYMMETRICAL CURRENT

### STUDYING THE EFFECT OF PLASMA WELDING SPEED ON WELDS FORMATION, THEIR STRUCTURE AND MECHANICAL PROPERTIES

An increase in the speed of plasma-arc welding of sheets of 1.8 mm thick 1201 alloy (Al–6Cu–Mn)

**Table 2.** Maximum welding speeds depending on thermophysical properties of aluminium alloys

Alloy	Thickness, mm	Maximum welding speed, cm/min
AMg5M (Al–5 % Mg–0.8 % Mn)	2.0	300
1201 (Al–6 % Cu–0.4 % Mn)	1.8	200
1460 (Al–3.0 % Cu–1.8 % Li)	2.0	300

from 30 to 300 cm/min causes a 40 % decrease in the amount of input energy (from 124 to 74 kJ/m), as well as a 33 % reduction in area of the base metal softening zone under the influence of heat action from the welding arc (Figure 4).

In welding at a high speed, dendrites are oriented clearly perpendicular to the weld axis, unlike the option with a low speed, where twisting of dendrites and their coupling along the weld axis at an acute angle is observed. Microstructure of welded joints of sheets of 1.8 mm thick from 1201 alloy produced by plasma-arc welding at a speed of 30 cm/min is shown in Figure 5.

In the weld metal of 1201 alloy of the alloying system Al-Cu-Mn produced by a constricted arc of a variable polarity asymmetrical current at a welding speed of 30 cm/min, the pores of up to 60 μm are observed. These pores are mainly localized on the boundaries of the fusion area with the base metal. In the weld metal dendrites are observed, the first-order axes of which are located mainly along the weld axis. On the boundaries of grains, coarse clusters of eutectic are observed. Zones of loosening are encountered.

Microstructure of joints of sheets of 1201 alloy of 1.8 mm thick, produced by plasma-arc welding at a variable polarity current at a speed of 300 cm/min in the flat position on the substrate without using filler, is shown in Figure 6. The comparison of welds produced at a speed from 30 to 300 cm/min showed that with an increase in plasma-arc welding speed, the

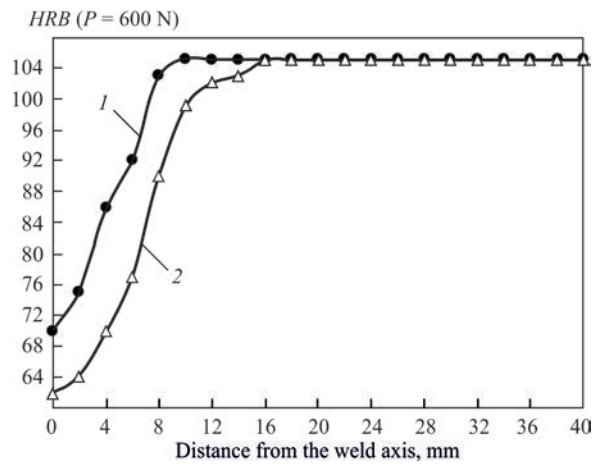


**Figure 4.** Distribution of hardness in the cross-sections of joints of sheets of 1201 (Al-Cu-Mn) alloy of 1.8 mm thick, produced by plasma-arc welding at a variable polarity current in the flat position at a speed of 30 and 300 cm/min; 1 — 18; 2 — 180 m/h

amount of pores in the weld metal increases, but their sizes decrease by 1.5–2.0 times.

In plasma-arc welding of sheets of 1.8 mm thick of 1201 alloy (Al-Cu-Mn) at a speed of 300 cm/min with the filler wire, the molten metal formed during melting of the wire, does not have time to mix with the molten metal of the welding pool. An excess of metal, which should form the upper bead of the weld, does not spread normally, the upper bead of the weld is formed unevenly and deep undercuts are formed along the boundary of the weld fusion zone with the base metal. The use of a filler in the form of an insert

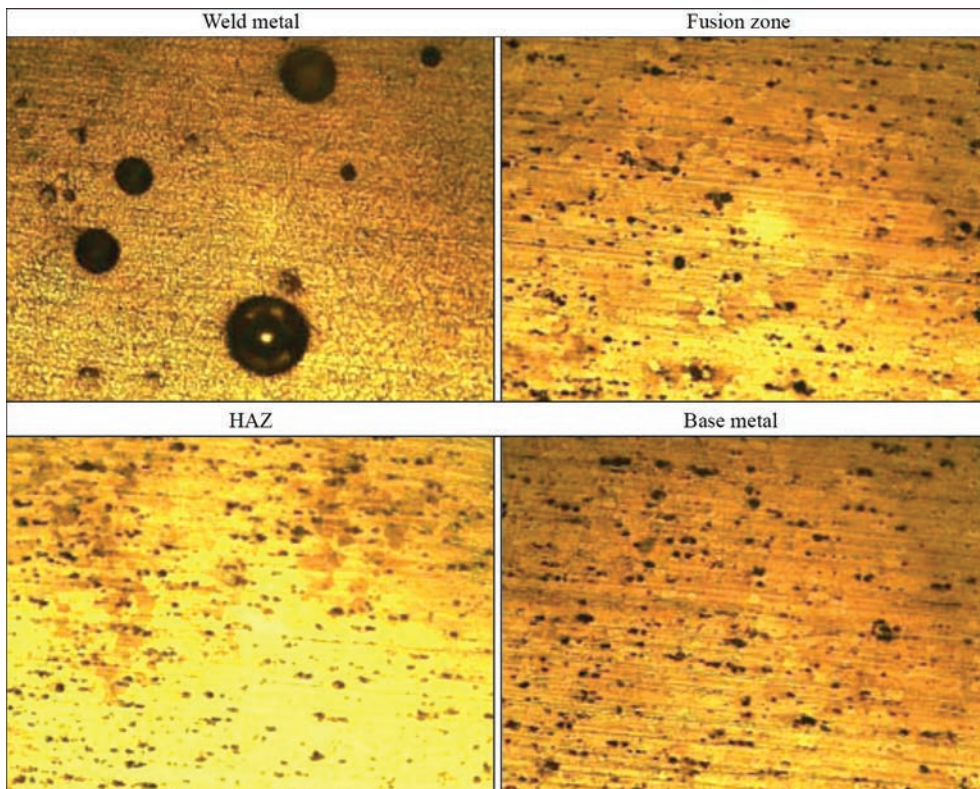


**Figure 5.** Microstructure (×150) of welded joint of sheets of 1.8 mm thick from 1201 (Al-6Cu-Mn) alloy produced by plasma-arc welding in the flat position without a filler at a speed of 30 cm/min

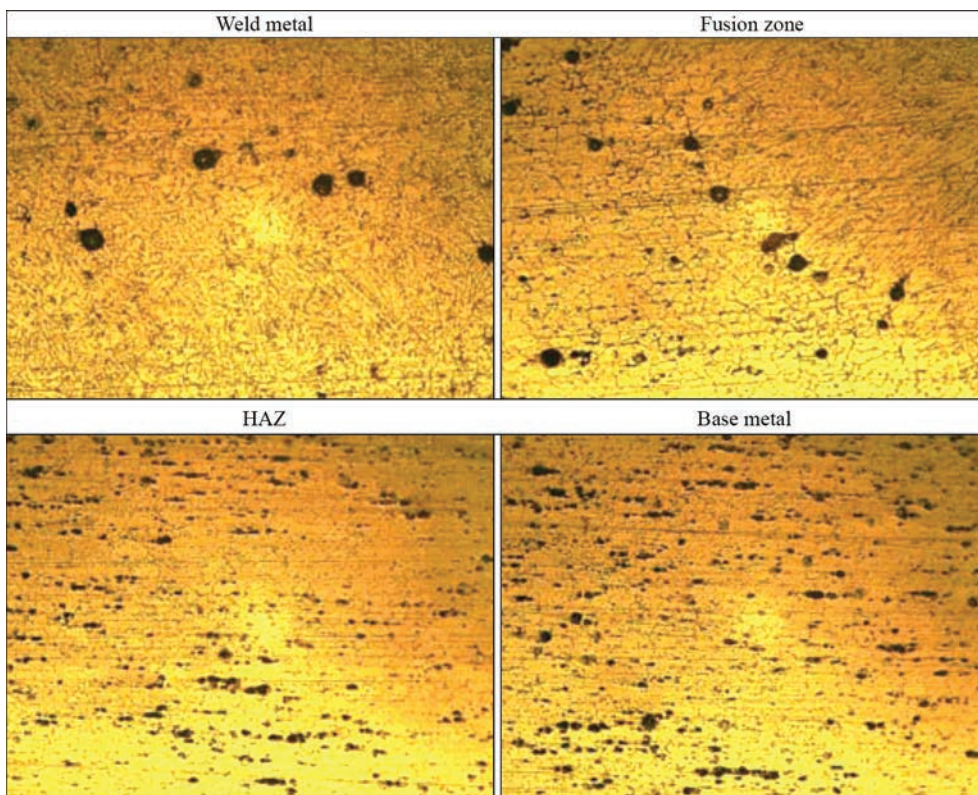


**Figure 6.** Microstructure ( $\times 150$ ) of welded joint of sheets of 1.8 mm thick from 1201 (Al–Cu–Mn) alloy, produced by plasma-arc welding in the flat position without a filler at a speed of 300 cm/min

from a strip cut out from the base metal also does not provide the qualitative formation of the weld surface. The strip melts unevenly. Splashing of the molten metal under the influence of a plasma jet is observed. On the surface at the center of the weld, a chain of pores coming to the surface remains.

The presence of deep undercuts (up to 0.5 mm or more) and the presence of pores over the whole weld metal, produced at a speed of 300 cm/min, cause not too high strength of the welded joint (249–251 MPa). As the welding speed is reduced to 200 cm/min, a clearly expressed chain of surface pores disappears from the surface, as well as the conditions of formation of the transition from the weld to the base metal are improved. In this case, the strength of the weld-

ed joint is 279–280 MPa, which exceeds the strength of the welded joint of 1201 alloy of 2.0 mm thick (246 MPa) produced by TIG welding at a speed of 20 cm/min (Figure 7).

The welds produced at a speed of 40 cm/min (24 m/h) have a cellular-dendritic structure typical of the cast state with the formation of a central crystallite. The structure of welds produced at speeds of 120 and 200 cm/min, is characterized by the absence of a central crystallite and a narrower region of columnar elongated small crystallites with a large number of cells and small equiaxial dendrites in the central part of the weld. An increase in crystallization rate at a welding speed of 120 cm/min provides the formation of branched dendrites of a solid solution and phases evenly located between them, which did not become a part of their composition, the shape and sizes of which are determined by the value of crystallization rate (Figure 8).

In the structure of welds produced at 120 cm/min, dendrites 3–4 times smaller are observed than in welding at a speed of 40 cm/min. The orientation of axes of the first-order dendrites is changed. Unlike welding at a low speed, these axes are directed perpendicularly to the longitudinal axis of the weld, which may be a consequence of not only high welding speed, but also a power concentration in the plasma jet and additional forced effect of plasma-forming gas.

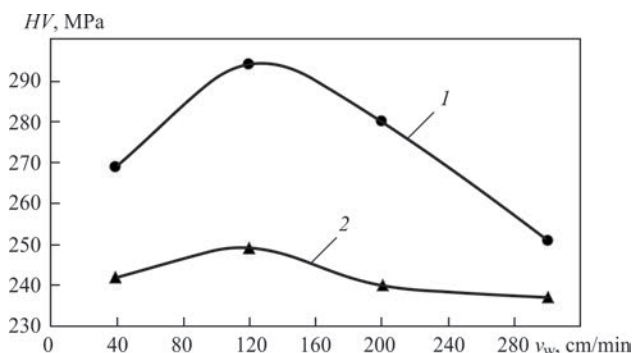


**Figure 7.** Diagram of change in strength of welded joints depending on speed of welding sheets of 1.8 mm thick from 1201 (Al–Cu–Mn) alloy produced by plasma-arc welding at a variable polarity current: 1 — welded joint; 2 — weld metal

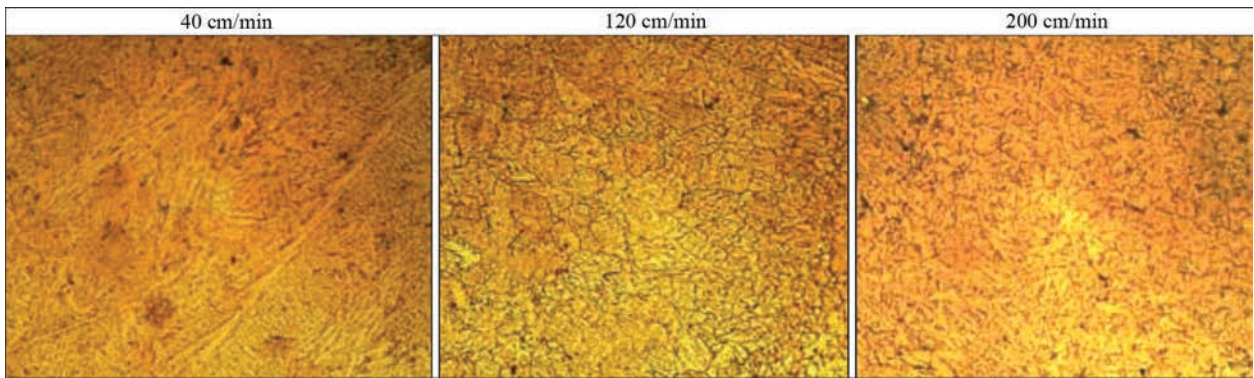


**Figure 8.** Microstructure ( $\times 150$ ) of weld metal produced by plasma-arc welding of sheets of 1.8 mm thick from 1201 (Al–Cu–Mn) alloy by a variable polarity current at different welding speeds

A change in the strength indices at different welding speeds is also observed in plasma-arc welding of a thermally strengthened 1460 alloy, which contains Cu and Li. The introduction of 1.9–2.3 % Li into the chemical composition of 1460 alloy allowed reducing the specific weight of 1460 alloy compared to 1201 alloy and increase its strength to 574 MPa (compared to 439 MPa for 1201 alloy).

An increase in the interval of increment of strength indices and their smooth decrease at a speed of 300 cm/min may be explained by a higher fluidity of the liquid metal of 1460 alloy compared to 1201 alloy by introducing Li. The reduction in strength at a welding speed of 300 cm/min is predetermined by the start of undercuts formation and deterioration of conditions of weld degassing (Figure 9).

In 1460 alloy, the process of reduction in strength begins after an increase in the welding speed above 200 cm/min. As in 1201 alloy, the process of reduction in strength is also predetermined by the formation of undercuts along the fusion line and an increase in porosity in the weld metal.

In plasma-arc welding of a thermally unstrengthened AMg5M (Al–Mg–Mn) alloy of 2.0 mm thick, also an increase in the growth of strength indices of welded joints with the growth of speed of plasma-arc welding is observed (Figure 10). However, unlike

1201 and 1460 alloys, which are thermally strengthened and more sensitive to heat input, in the mentioned alloy, the growth in strength indices occurs more slowly. At the same time, an increase in the welding speed above 200 cm/min, a decrease in the strength indices of the welded joint by the formation of undercuts in the fusion zone is observed. In this case, the size of undercuts is smaller compared to alloys containing Cu.

#### INFLUENCE OF PLASMA WELDING SPEED ON DISTRIBUTION OF TEMPERATURE FIELDS IN WELDED SPECIMENS

To calculate the regularities of temperature change, depending on the speed of plasma-arc welding, a procedure for calculating the temperature field in the plate at welding speeds of up to 20 cm/min (12 m/h) and from 30 to 300 cm/min (from 18 to 180 m/h) was used [14]. The calculation was performed by the finite element method. For welding speeds of up to 20 cm/min, the calculation scheme was chosen using a point moving heating source, and for welding speeds above 30 cm/min — a powerful linear heating source.

The maximum temperatures were determined from the temperature distribution diagrams for welding at a speed of up to 20 cm/min (Figure 11) and diagrams

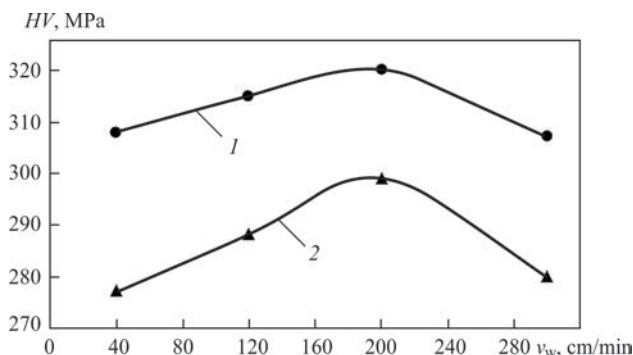


**Figure 9.** Diagram of change in strength of welded joints depending on speed of welding sheets of 2.0 mm thick from 1460 (Al–Cu–Li) alloy produced by plasma-arc welding at a variable polarity current: 1 — welded joint; 2 — weld metal

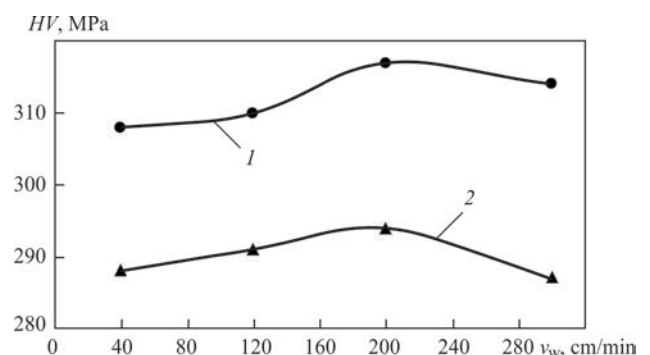


**Figure 10.** Diagram of change in strength of welded joints depending on speed of welding sheets of 2.0 mm thick from AMg5M (Al–Mg–Mn) alloy, produced by plasma-arc welding at a variable polarity current: 1 — welded joint; 2 — weld metal

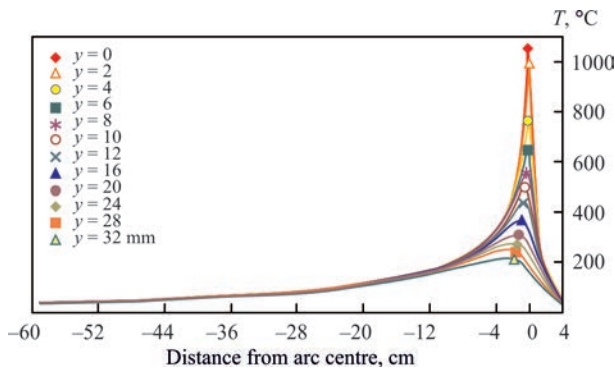


**Figure 11.** Diagram of temperature distribution in plasma-arc welding of aluminium 1201 (Al–Cu–Mn) alloy of 6.0 mm thick at a variable polarity current in the flat position at a speed of 20 cm/min (12 m/h)

of thermal cycles for the processes at a speed above 30 cm/min, for example, 200 cm/min (Figure 12).

Figures 13 and 14 show the diagrams of maximum temperatures in the cross-section of the welded joint obtained thanks to performed calculations.

When analyzing the diagrams of distribution of maximum temperatures (Figures 13, 14) in plasma-arc welding of sheets of 1.8 mm thick from 1201 alloy at a variable polarity asymmetrical current and welding speeds from 40 to 300 cm/min, it was found that at the same step between the speeds of 80 cm/min, the difference in the temperature between the curves of the distribution of maximum temperatures depends on the range of speeds changes (in the range from 40 to 120 cm/min, the differences in the temperature between the points at a distance of 5 mm from the weld axis are 3–4 times higher than in the speed range from 120 to 200 cm/min).

At a distance of more than 4 mm from the axis, in plasma-arc welding of aluminium 1201 alloy of 1.8 mm thick at a variable polarity asymmetrical current with a change in welding speed from 120 to 180 cm/min, the temperature changes on average by 50 °C, which does not significantly affect both the change of

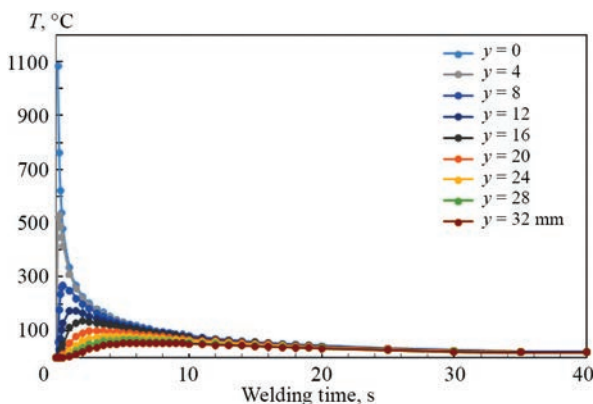


**Figure 12.** Thermal cycle in plasma-arc welding of sheets of 1.8 mm thick from 1201 (Al–Cu–Mn) alloy at a variable polarity current and a speed of 200 cm/min (120 m/h)

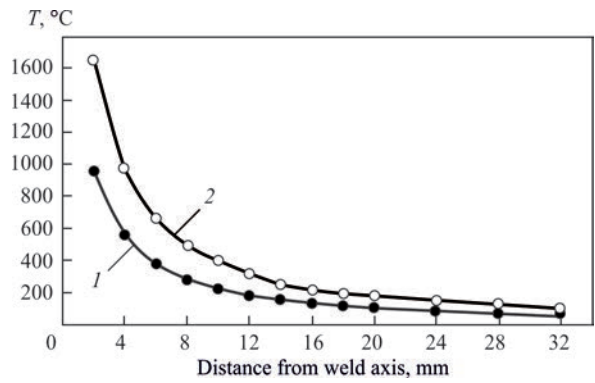


**Figure 13.** Distribution of maximum temperatures occurring in the sheets of 1201 alloy of 1.8 mm thick joined by plasma-arc welding at a variable polarity current at welding speeds of 40 (curve 1) and 120 cm/min (curve 2)

hardness, as well as the change of mechanical properties of welded joints.

#### STRESS-STRAIN STATE IN WELDED JOINTS PRODUCED BY WELDING USING CONSTRICTED ARC AT DIFFERENT WELDING SPEEDS

In order to improve the influence of plasma-arc welding speed on the obtained results, a study of a stress-strain state was conducted according to the procedure described in [15], making the necessary calculations with the use of the MatCAD software. The calculation was carried out on several indices of stress-strain state of plane specimens after welding. The calculations took into account the thickness of welded plates and their thermophysical and mechanical properties.

Figure 15 shows the features of changing the width of the plastic deformation zone depending on the speed of plasma-arc welding of aluminium alloys of specimens of 2.0 mm thick from AMg5M (Al–Mg–Mn) alloy and specimens of 1.8 mm thick from 1201 (Al–Cu–Mn) alloy at a variable polarity asymmetrical current. A similar regularity is observed for other indices, such as longitudinal reduction in area of the spec-

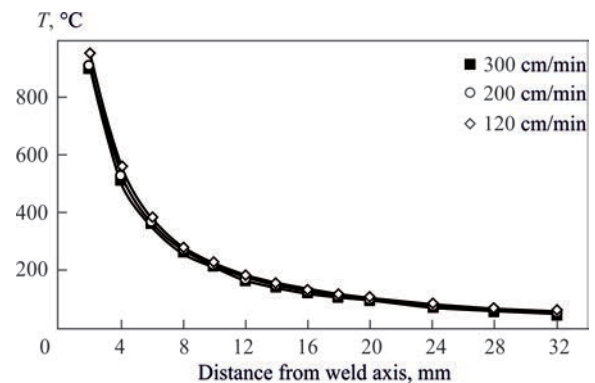


**Figure 14.** Distribution of maximum temperatures occurring in the sheets of 1201 alloy of 1.8 mm thick joined by plasma-arc welding at a variable polarity current at welding speeds from 120 to 300 cm/min

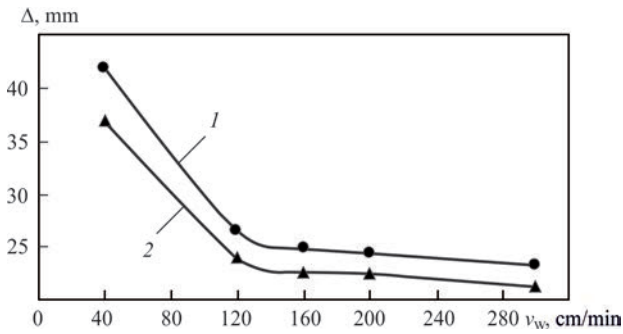


**Figure 15.** Change in the width of plastic deformation zone in welded specimens of 1.8–2.0 mm thick of AMg5M (Al–Mg–Mn) and 1201 (Al–Cu–Mn) alloys depending on speed of plasma-arc welding: 1 — Al–6Cu–Mn; 2 — Al–5Mg–Mn

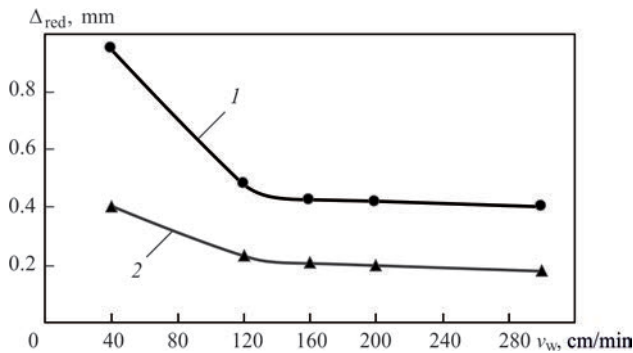


**Figure 16.** Change in the longitudinal reduction in area of the specimen of 1.8–2.0 mm thick of AMg5M (Al–Mg–Mn) and 1201 (Al–Cu–Mn) alloys depending on speed of plasma-arc welding: 1 — Al–6Cu–Mn; 2 — Al–5Mg–Mn

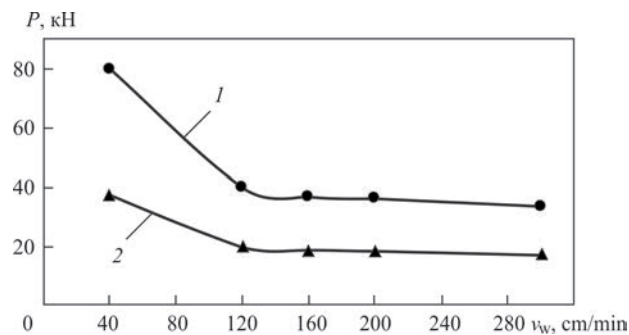


**Figure 17.** Change in the upsetting force of the specimen weld of 1.8–2.0 mm of AMg5M (Al–Mg–Mn) and 1201 (Al–Cu–Mn) alloys depending on speed of plasma-arc welding: 1 — Al–6Cu–Mn; 2 — Al–5Mg–Mn

imen (Figure 16) and the weld upsetting force during welding (Figure 17).

A more pronounced tendency of exponential decrease in the intensity of indices of stress-strain state with an increase in welding speed is observed in plasma-arc welding of specimens of 4.0 mm thick (Figures 18–20). As is seen from the abovementioned diagrams, there is a certain speed, after which the further increase in welding speed does not lead to a decrease in residual deformations and stresses in the studied alloys.

The regularity of rapid reduction in indices of stress-strain state in the specimens after welding is

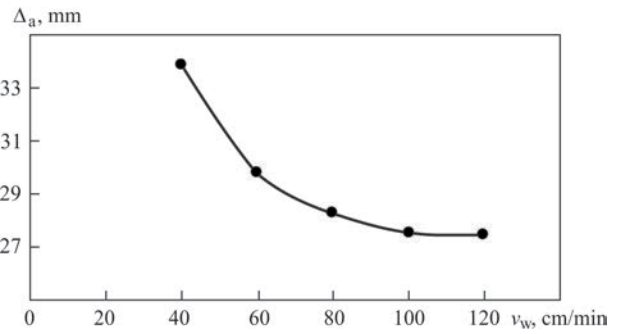


**Figure 18.** Change in the width of plastic deformation zone in welded specimens of 4.0 mm thick of AMg5M (Al–Mg–Mn) alloy depending on speed of plasma-arc welding

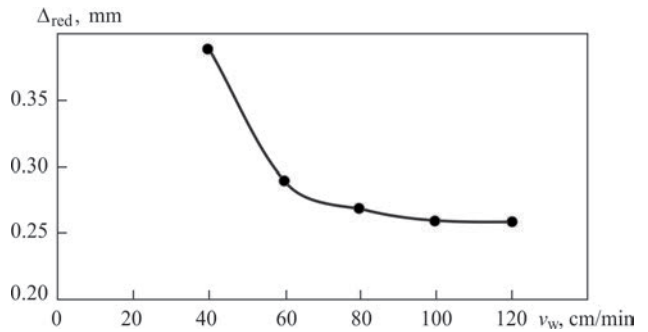


**Figure 19.** Change in the longitudinal reduction in area of the specimen of 4.0 mm thick of AMg5M (Al–Mg–Mn) alloy depending on speed of plasma-arc welding

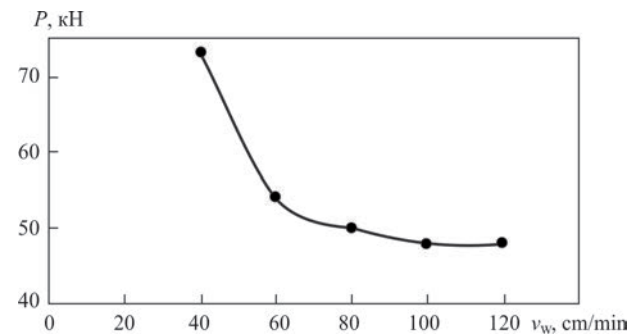


**Figure 20.** Change in the weld upsetting force of the specimen of 4.0 mm thick from AMg5M (Al–Mg–Mn) alloy depending on speed of plasma-arc welding

observed also in plasma-arc welding of sheets of Al–Mg–Mn alloying system in two delivery states of this AMg6M and AMg6N alloy. The alloys have a similar chemical composition, but differ in strength indices of the base metal and yield strength (Figures 21, 22). In AMg6N alloy due to plastic deformation (peening), the indices of strength and yield strength were increased compared to AMg6M alloy. Taking into account the similar chemical composition of alloys, plasma-arc welding was performed at the same modes of current, balance of variable polarity current, frequencies of variable polarity current and flow rate of plasma-forming gas.

Analyzing the regularities of change in the indices of stress-strain state in plasma-arc welding, it can be

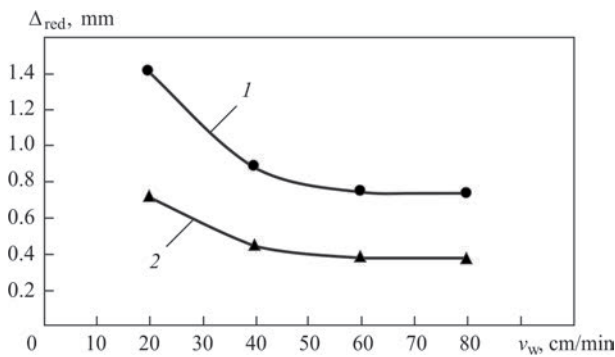


**Figure 21.** Change in the longitudinal reduction in area of 6.0 mm thick specimen of AMg6M (1) and AMg6N (2) alloys depending on speed of plasma-arc welding

concluded that welding speed, at which a rapid decrease in the indices of stress-strain state ends and changes begin by 1–2 %, first of all depends on the thickness of welded metal. Figure 23 shows a diagram of dependence of such speed on thickness of aluminium alloys.

#### DISCUSSION OF RESULTS OF STUDYING INFLUENCE OF TECHNOLOGICAL METHODS ON THE PECULIARITIES OF STRUCTURE FORMATION

According to metallographic analysis, the structure of the weld of 1201 alloy represents a solid solution with fine-dispersed  $\text{CuAl}_2$  phase inclusions and eutectics of type  $(\alpha + \text{CuAl}_2)$ . The inclusions of oxide films and microcracks are not observed, but in the places of location of precipitates of excessive phases, separate micropores of less than 0.1  $\mu\text{m}$  and microloosenings are encountered, the number and nature of whose location depends on the welding speed and crystallization rate.

The weld structure of 1201 alloy produced by plasma-arc welding at a speed of 40 cm/min contains crystallites differing in shape and direction. Near the fusion boundary, where the first stage of crystallization occurs, the structure is mostly fine crystalline. The processes of heat removal and crystallization overcooling occurring in the welding pool during cooling

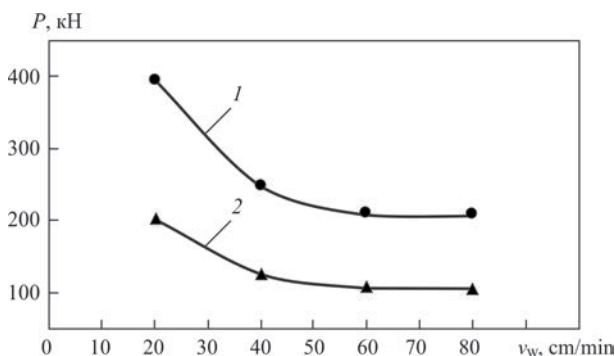


**Figure 22.** Change in the upsetting force of the specimen of 6.0 mm thick of AMg6M (1) and AMg6N (2) alloys depending on speed of plasma-arc welding

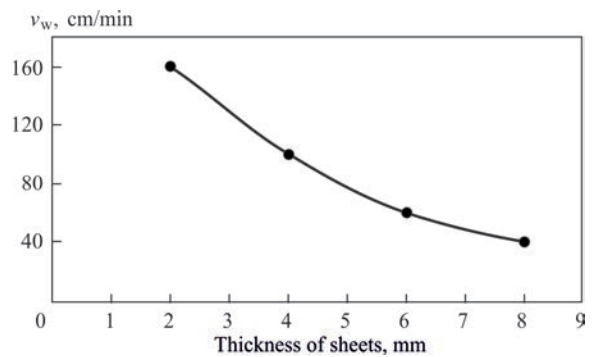


**Figure 23.** Dependence of welding speed on thickness of welded metal, at which a decrease in the indices of stress-strain state in welded specimens of aluminium alloys ends

of the metal and its crystallization, contribute to the formation of the columnar crystallites zone, which are oriented mainly to the vector of melting isotherm. In the centre of the weld, a central crystallite is observed, whose boundary is adjacent to the side crystallites. As the welding speed increases to 120 and 200 cm/min, the formation of central crystallite is not observed.

The microstructure of the welds of 1201 alloy with an increase in welding speed from 40 to 120 cm/min is featured by a decrease in the sizes of dendrites from 10–40 to 3–14  $\mu\text{m}$  and a number of intermediate phases  $\theta'$  ( $\text{CuAl}_2$ ) and  $S'$  ( $\text{Al}_2\text{CuMg}$ ) at a constant amount resistant to the thermal effect of the phase  $\theta'$  ( $\text{CuAl}_2$ ). An even greater tendency to reduce the sizes and number of mentioned phases is observed in the structure of welds produced at a speed of 200 cm/min.

The similar tendencies of structure formation are observed in welding of other studied alloys. The reduction in crystallization stage, at which phase embryos and a period of dendrites entanglement arises and develops, helps to increase the volume of solid solution, which can be the basis for increasing the strength of the weld metal. The gaps between the branches of dendrites are filled with liquid metal, the interfacial boundaries are stabilized. As a result, the solid phase becomes cellular and the sizes of crystallites in the welds decrease by about 3 times.

When welding speed 5 times increases (from 40 to 200 cm/min), the transformation processes occur more intensively, which causes the transition of microstructure of welds to a dendritic structure with a high density and dispersion of particles precipitates and strengthening phases. This is predetermined by the change in the size of the temperature gradient on the interface of the solid solution of liquid metal and phases, the rate of growth and distribution of the solution at the interfacial boundary of their growth (along the crystallization front).

Metallographic and microdurometric examinations showed that at a high welding speed (300 cm/min), dendrites are formed which are 3–4 times smaller than

at a welding speed of 30 cm/min. The orientation of the first-order dendrites is changed. Unlike welding at 30 cm/min, these axes of dendrites are directed perpendicular to the longitudinal axis of the weld. Refinement of dendrites may explain an increase in the microhardness of the weld (for example, by 5–25 % for 1201 alloy), produced at a speed of 300 cm/min, compared to the weld produced at a speed of 30 cm/min (Figure 4).

It was found that with an increase in the welding speed from 30 (Figure 5) to 300 cm/min (Figure 6), an increase in the number of pores with a decrease in their size (approximately by 1.5–2.0 times) occurs. This phenomenon may be explained by the fact that due to a higher welding speed, the pores did not have time to grow to large sizes, and a short time of existence of the pool in the liquid state deteriorates the conditions of weld degassing. The pores are localized mainly along the fusion zone of the weld with the base metal.

Mechanical tests showed a decrease in the strength of welded joints of aluminium alloys at an increase in the welding speed from 200 to 300 cm/min (Figures 7, 9, 10, 11). This is explained by the deterioration of the formation of the transition from the weld to the base metal and the formation of undercuts, as well as the formation of a chain of surface pores on the axis of the joint due to deterioration of the conditions of weld metal degassing. In the case of plasma-arc welding of AMg5M (Al–Mg–Mn) alloy at a variable polarity current (Figure 7), the effect of reducing the strength at an increase in the speed from 200 to 300 cm/min is not expressed so explicitly as for 1201 (Al–Cu–Mn) (Figure 4) and 1460 (Al–Cu–Li) alloys (Figure 6). This is caused by the fact that unlike 1201 and 1460 alloys, AMg5M alloy is not thermally strengthened, as well as the size of undercuts is smaller in the joints of AMg5M alloy compared to alloys containing Cu. It should be noted that in general the strength of plasma-arc welding of aluminium alloys is higher than the strength of TIG of these alloys. This is associated with an increase in the heat input in TIG, which leads to an increase in the sizes of dendrites and HAZ.

It was found that when the amount of copper in the composition of aluminium 1460 alloy (Al–3 % Cu–1.8 % Li) decreases, the speed of plasma-arc welding has a smaller effect on the change of the strength of welded joint (4–5%), a somewhat higher degree of copper on the strength of the weld metal (increases by 7 %) is observed at an increase in the welding speed from 40 to 200 cm/min. The further increase in speed leads to a decrease in strength indices, which is predetermined by the start of undercuts formation and deterioration of weld metal degassing.

Analysis of change in the temperature fields distribution in plasma-arc welding of 1201 alloy of 1.8 mm thickness showed a gradual decrease in HAZ size when welding speeds are changed from 40 to 120 cm/min and stabilization of this parameter with an increase in welding speed from 120 to 300 cm/min.

The studies of indices of stress-strain state in plasma-arc welding of specimens of the considered alloys showed that with an increase in speed, a tendency of almost exponential decrease in the value of these indices is observed (Figures 12–19). As is seen from the abovementioned diagrams, there is a certain speed (for example, 100 cm/min for the case of AMg5M alloy (Figures 15–17), after which the further increase in welding speed does not lead to a decrease in residual deformations and stresses in the studied alloys. Such speed depends not only on the grade of alloy, but also on its thickness (Figure 20).

## CONCLUSIONS

1. A tendency of at least 2–3 times reduction in the sizes of dendrites and a change in the orientation of axes of the first-order dendrites to the orientation of the perpendicularly longitudinal axis of the weld at an increase in the speed of welding high-strength aluminium alloys of Al–5Mg–Mn, Al–3Cu–1.8Li and Al–6Cu–Mn alloying systems from 40 to 120 cm/min was revealed. The effect of an increase in the indices of strength of welded joints reaching the welding speed extremum in the range of 120–200 cm/min with their subsequent decline caused by deterioration of the conditions of a welded joint formation due to the formation of undercuts and an increase of pores in the weld metal was determined. It is shown, that for aluminium Al–6Cu–Mn and Al–3Cu–1.8Li alloys, which are thermally strengthened, a rapid increase in the indices of strength is observed when the welding speed extremum is reached. Here, a decrease in the amount of copper in the base metal from 6.0 to 3.0 % allows increasing the index of welding speed extremum from 120 to 200 cm/min.

2. It was found that as the speed of plasma-arc welding of sheets of 1.8 mm thick from the Al–Cu–Mn alloy at a variable polarity asymmetrical current grows from 40 to 120 cm/min, the maximum temperature at a distance of 5 mm from the weld axis decreases from 850 to 450 °C. The further increase in the welding speed to 200 and 300 cm/min leads to a decrease in the maximum temperature at this point to 425 and 400 °C, respectively. Therefore, a decrease in the intensity of falling temperature at a point 5 mm from the weld axis with the growth of welding speed above 120 cm/min is observed.

3. It is shown that the value of residual deformations sharply decrease by 2 times when a certain welding speed extremum is achieved in the range of 120–200 cm/min, and the further growth in the welding speed does not cause a significant decrease in residual deformations, i.e. the change in the deformation value is not more than 5 %. On the example of Al–Mg–Mn alloy it is shown that such regularities are also typical not only for 2.0 mm thickness, but also observed in welding of specimens with the thickness range of 4–8 mm. This allows using these results to predict indices of strength and stress-strain state of welded joint, as well as weld metal for these thicknesses with an increase in the speed of plasma-arc welding at a variable polarity asymmetrical current higher than the “peak” value.

## REFERENCES

- Guan, R., Lou, H., Huang, H. et al. (2020) Development of aluminium alloy materials: Current status, trend, and prospects. *Strategic Study of Chinese Academy of Engineering*, 22(5), 68–75. DOI: <https://doi.org/10.15302/J-SSCAE-2020.05.013>
- Samiuddin, M., Li, J.-L., Taimoor, M. et al. (2021) Investigation on the process parameters of TIG-welded aluminium alloy through mechanical and microstructural characterization. *Defence Technology*, 17(4), 1234–1248. DOI: <https://doi.org/10.1016/j.dt.2020.06.012>
- Lis, A., Mogami, H., Matsuda, T. et al. (2018) Hardening and softening effects in aluminium alloys during high-frequency linear friction welding. *J. Materials Proc. Technology*, 255, 547–558. DOI: <https://doi.org/10.1016/j.jmatprotec.2018.01.002>
- Xu, B., Chen, S., Jiang, F. et al. (2019) The influence mechanism of variable polarity plasma arc pressure on flat keyhole welding stability. *J. of Manufacturing Processes*, 37, 519–528. DOI: <https://doi.org/10.1016/j.jmapro.2018.12.026>
- Xu, B., Tashiro, S., Jiang, F. et al. (2019) Effect of arc pressure on the digging process in variable polarity plasma arc welding of A5052P aluminium alloy. *Materials*, 12, 1071, 1–17. DOI: <https://doi.org/10.3390/ma12071071>
- Lang, R., Han, Y., Bai, X., Hong, H. (2020) Prediction of the weld pool stability by material flow behavior of the perforated weld pool. *Materials*, 303(13), 1–20. DOI: <https://doi.org/10.3390/ma13020303>
- Klett, J., Bongartz, B., Wolf, T. et al. (2023) Plasma welding of aluminium in an oxygen-free argon atmosphere. *Advances in Materials Sci.*, 23, 75(1), 5–18. DOI: <https://doi.org/10.2478/adms-2023-0001>
- Labur, T.M., Grinyuk, A.A., Poklyatsky, A.G. (2006) Mechanical properties of plasma welded joints on aluminium-lithium alloys. *The Paton Welding J.*, 6, 32–34.
- Selva Bharathi, R., Siva Shanmugam, N., Murali Kannan, R., Arungalai Vendan, S. (2018) Studies on the parametric effects of plasma arc welding of 2205 duplex stainless steel. *High Temperature Materials and Processes*, 37(3), 219–232. DOI: <https://doi.org/10.1515/htmp-2016-0087>
- Sathishkumar, M., Manikandan, M., Subramani, P. et al. (2020) Effect of welding speed on aspect ratio of hastelloy X weldment by keyhole plasma arc welding (K-PAW). *Materials Today*, 22(4), 3297–3304. DOI: <https://doi.org/10.1016/j.matpr.2020.03.291>
- Batool, S., Khan, M., Jaffery, S. et al. (2015) Analysis of weld characteristics of micro-plasma arc welding and tungsten inert gas welding of thin stainless steel (304L) sheet. Proceedings of the Institution of Mechanical Engineers, Pt L: *J. of Materials: Design and Applications*, 230(6). DOI: <https://doi.org/10.1177/14644207155592>
- Korzhyk, V., Khaskin, V., Grynyuk, A. et al. (2022) Comparison of the features of the formation of joints of aluminium alloy 7075 (Al–Zn–Mg–Cu) by laser, microplasma, and laser-microplasma welding. *Eastern-European J. of Enterprise Technologies*, 115 (1–12), 38–47. DOI: <https://doi.org/10.15587/1729-4061.2022.253378>
- Grinyuk, A.A., Korzhyk, V.N., Babich, A.A. et al. (2016) Unified plasmatron for consumable electrode constricted arc welding. *Tekhnologicheskie Sistemy*, 4, 86–89 [in Russian].
- Lobanov, L.M., Pashchyn, M.O., Mikhodui, O.L. et al. (2021) Modeling of stress-strain states of AMg6 alloy due to impact action of electrode-indenter in electrodynamic treatment. *The Paton Welding J.*, 6, 2–11. DOI: <https://doi.org/10.37434/tpwj2021.06.01>
- (2018) *Physical processes in welding and treatment of materials. Theoretical studies, mathematical modeling, computing experiment*: Collect. of articles and reports. Ed. by I.V. Krivtsun. Kyiv, IAW [in Russian].

## ORCID

V.M. Korzhyk: 0000-0001-9106-8593  
 A.A. Grynyuk: 0000-0002-6088-7980,  
 V.Yu. Khaskin: 0000-0003-3072-6761  
 E.V. Ilyashenko: 0000-0001-9876-0320,  
 S.I. Peleshenko: 0000-0001-6828-2110,  
 A.O. Aloslyn: 0000-0001-9696-6800,  
 I.O. Skachkov: 0000-0001-6933-1148  
 O.V. Dolyanivska: 0000-0001-8396-2894

## CONFLICT OF INTEREST

The Authors declare no conflict of interest

## CORRESPONDING AUTHOR

V.M. Korzhyk  
 E.O. Paton Electric Welding Institute of the NASU  
 11 Kazymyr Malevych Str., 03150, Kyiv, Ukraine.  
 E-mail: [vnkorzhyk@gmail.com](mailto:vnkorzhyk@gmail.com)

## SUGGESTED CITATION

V.M. Korzhyk, A.A. Grynyuk, V.Yu. Khaskin, E.V. Ilyashenko, S.I. Peleshenko, A.O. Aloslyn, I.O. Skachkov, O.V. Dolyanivska (2023) Influence of the speed of plasma-arc welding at a variable polarity asymmetrical current on the formation of joints of high-strength aluminium alloys. *The Paton Welding J.*, 8, 17–28.

## JOURNAL HOME PAGE

<https://patonpublishinghouse.com/eng/journals/tpwj>

Received: 19.06.2023

Accepted: 07.08.2023

# MANUFACTURING LIGHTWEIGHT HONEYCOMB PANELS ON THE BASE OF HIGH-ENTROPY $\text{CoCrFeNiSi}_{0.2}$ ALLOY FOIL PRODUCED BY EB-PVD METHOD

**A.I. Ustinov, Iu.V. Falchenko, S.O. Demchenkov, L.V. Petrushynets**

E.O. Paton Electric Welding Institute of the NASU  
11 Kazymyr Malevych Str., 03150, Kyiv, Ukraine

## ABSTRACT

The possibility of manufacturing thin foils of high-entropy alloys (HEA) of Co–Cr–Fe–Ni–Si system by the method of high-speed (up to 10  $\mu\text{m}/\text{min}$ ) electron beam physical-vapour deposition (EB-PVD) is shown in the work. It was established that silicon content in the alloy composition of approximately 5 wt.% improves the values of high-temperature resistance of basic CoCrFeNi HEA. It is shown that at soaking in air for 28 h at the temperature of 1000 °C the specific change in the weight of CoCrFeNiSi<sub>0.2</sub> sample is not more than 0.9 mg/cm<sup>2</sup>. A technological scheme was proposed of manufacturing by welding three-layer thermal protection honeycomb panels with a low specific weight based on thin foils of high-entropy CoCrFeNiSi<sub>0.2</sub> alloy. It was found that the produced by the proposed scheme three-layer thermal protection panels can stand multiple thermal cycling from 25 to 1000 °C in air without the structure failure. The derived results can be the base for development of the technology of manufacturing lightweight honeycomb structures, capable of ensuring thermal protection of aerospace equipment elements at their interaction with the atmosphere.

**KEYWORDS:** high-temperature resistance; high-entropy alloys; thin foils; electron beam deposition; three-layer honeycomb panels; thermal protection

## INTRODUCTION

Successful operation of modern flying vehicles, moving in the atmosphere at supersonic speeds and designed for multiple takeoff and landing cycles, necessitates reliable thermal protection of their skin from overheating and damage as a result of interaction with the atmosphere [1]. Experience of service of thermal protection structures based on ceramic materials, which were applied in Buran and Space Shuttle flying vehicles, showed their insufficient reliability and difficulty in maintenance. Technical problems of operation of such structures and their low cost-effectiveness make it necessary to carry on investigations aimed at creation of new systems, both in terms of development of the design of thermal protection panels, and high-temperature materials for their fabrication. Lightweight thermal protection honeycomb panels (LTPHP) are considered as one of the most promising and effective methods of solving the problem of protection of structural elements of aerospace equipment from heating at interaction with the atmosphere. Special attention is paid to three-layer honeycomb structures of thermal protection panels based on metal systems. Three-layer panel is a structure, consisting of two thin cover sheets with the core placed between them. The cover sheets take the in-plane longitudinal loads (stretching, compression and shear). The core takes the transverse forces in the bend of three-layer structure and ensures the redistribution of forces

between the cover sheets. Such a design of thermal protection panels can provide a combination of high strength and rigidity with the low specific weight, due to application of sheet metal materials [2, 3]. The sheet materials for LTPHP manufacturing should have a set of such properties as high-temperature resistance, strength and low specific weight. Alloys based on Ni–Cr, Ti–Al, Ti–Nb–Al systems and some other widely known high-temperature alloys are the most often used as materials for LTPHP cover sheets. Thin foils are usually produced by rolling bulk billets, which are formed from the melt or by powder metallurgy methods. Such an approach, however, significantly complicates the process of producing sheet materials. Moreover, thermodeformational treatment of the billets is accompanied by formation of a resistant oxide film on the foil surface, which greatly complicates producing permanent joints. In this connection, producing thin foil with the required set of properties and its joining methods remain relevant up to now.

On the other hand, we showed that thin foils based on high-temperature alloys can be produced directly during condensation of the vapour phase in vacuum at evaporation of an alloy of the specified chemical composition [4]. Such an approach allows producing sheet metal materials with a controlled structure and thickness, avoiding the limitations, which are inherent to the traditional metallurgical and thermomechanical treatment methods. It greatly enhances the possibilities of using a wide class of high-temperature alloys,

and allows prevention of dense oxide film formation on the foil surface which hinder application of welding in fabrication of structures from such materials.

At the same time, development of new alloys with the required set of properties is also important, when creating the technology of fabrication of thermal protection panels. From this viewpoint, so-called HEA attract considerable attention [5]. It is noted that these alloys are characterized by stability in a broad temperature range, and have relatively high values of strength and high-temperature resistance.

In the previous works, the authors [6–8] showed that the method of high-speed electron beam deposition allows producing thin foils from CoCrFeNiCu HEA with a rather wide range of micromechanical characteristics, high damping properties and weldability. It was also shown that at high-temperature resistance testing at the temperature of 900 °C in atmospheric air, foils from CoCrFeNi alloy demonstrate rather high values of high-temperature resistance due to formation of low-defect continuous scale based on  $\text{Cr}_2\text{O}_3$  oxide on the surface [9].

In view of that the objective of this work was development of scientific fundamentals of the technology of manufacturing lightweight thermal-protection honeycomb panels, using thin foils of high-entropy alloy based on Co–Cr–Fe–Ni system, produced by the method of vacuum electron beam deposition.

## EXPERIMENTAL

Foils of Co–Cr–Fe–Ni–Si system alloy were produced by the method of high-speed electron beam evaporation of the respective target-ingot with subsequent deposition of the vapour phase on a substrate

from stainless steel (AISI 302), heated to the specified temperature. Foils of 80–100  $\mu\text{m}$  thickness were deposited at the rate of approximately 8–10  $\mu\text{m}/\text{min}$  at substrate temperature of 550–600 °C. To ensure foil separation from the substrate, a thin layer of  $\text{CaF}_2$  salt was first deposited on it. Initial target ingots of 50 mm diameter were produced in an induction furnace.

Microstructural studies and local chemical analysis were conducted on transverse sections of the produced foils using scanning electron microscope (SEM) CamScan4, fitted with ENERGY 200 micro-analyzer. Total thickness of the foil was assessed by electron microscopy images of the transverse section. X-ray diffractometer DRON-4M (Cu- $K_\alpha$ -radiation) was used to conduct phase analysis.

Evaluation of heat resistance of the produced foils was conducted by the change of the sample specific weight during long-term annealing at temperatures of 900 and 1000 °C in shaft-type electric furnace of SShOL-2.4/12.5 type in atmospheric air.

Foil of AISI 304 stainless steel 100  $\mu\text{m}$  thick was used to produce the honeycomb core. Foil cutting up was conducted under the conditions of ensuring the required accuracy by sample length and prevention of appearance of tears or burrs. The profiled strip — honeycomb core was formed using the method of rolling in profiling rollers, which allows manufacturing corrugated strips with a high productivity [10].

The honeycomb core was manufactured by spot welding of the produced profiled strips, according to the scheme described in work [10]. The profiled strip surfaces were degreased with alcohol before their assembly into blocks. The strips were placed on a graphite electrode, which was manufactured, proceeding from overall dimensions of the honeycombs. The optimal process parameters for this foil thickness are current  $I = 300$  mA, voltage  $U = 5$  V at 2 mm diameter of copper electrode.

Joints of the honeycomb core with the cover sheets were produced by vacuum diffusion welding. Welding was performed using a specially designed fixture, which consists of the lower and upper flanges and limiting sleeve. The flanges provide pressing down to the honeycomb core over the entire cover sheet area during welding, and the limiting sleeve allows equalizing the temperature field in the product being welded. Figure 1 shows the schematic of the working chamber of the diffusion welding unit with the fixture installed in it. Welding temperature was monitored by the readings of chromel-alumel thermocouple mounted in the fixture. Pressure was applied to the parts being welded from the press through wedge 6 and lower rod 5. Pressure value was monitored by a dynamometer. Heating of the fixture with the honey-

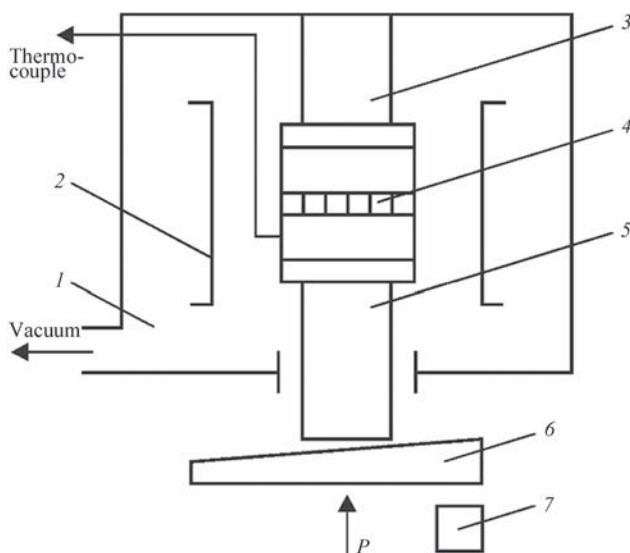


**Figure 1.** Scheme of the work chamber of diffusion welding unit; 1 — work chamber; 2 — molybdenum heater; 3 — upper rod; 4 — three-layer panel placed into a limiting sleeve; 5 — lower rod; 6 — wedge; 7 — press

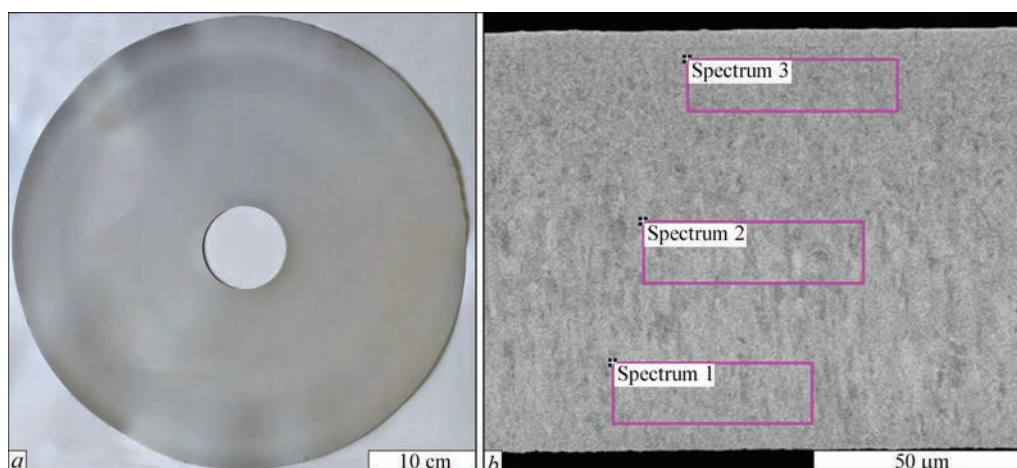


**Figure 2.** Appearance (a) and SEM image of the characteristic microstructure of the transverse section of deposited  $\text{CoCrFeNiSi}_{0.2}$  HEA foils

comb panel mounted in it was conducted with the rate of 25–30 °C/min; pressure was applied after welding temperature has been reached (800 °C). The time of soaking at the welding temperature was 15 min, and after that the pressure level was lowered to zero and cooling to room temperature was conducted under vacuum.

## RESULTS AND DISCUSSION

Earlier research established that copper content has an essential influence on the values of heat resistance of Co–Cr–Fe–Ni–Cu system alloys: with lowering of copper content in the alloy composition its heat resistance increases [9]. Also in works [11, 12] it was shown that alloying of  $\text{CoCrFeNi}$  base alloy by a small quantity of silicon may lead to a considerable increase of its heat resistance, as a result of formation of combined scale based on  $\text{Cr}_2\text{O}_3$  and  $\text{SiO}_2$  on the alloy surface. It was assumed that silicon content in the quantity of 5 wt.% will not influence the HEA structure, but will promote an increase in heat resistance at higher temperatures, due to formation of protective layers based on silicon oxides or chromium silicides on the foil surface. In view of that, the method of electron beam vacuum deposition was used to produce a series of foils of  $\text{CoCrFeNiSi}_{0.2}$  alloy 80 to 100 μm thick. Figure 2 shows the appearance and characteristic cross-sectional microstructure of the produced foils. Microstructural analysis showed that the optimized modes ensure formation of a homogeneous foil structure without macrodefects (cracks, pores, delaminations, etc.) with a uniform distribution of the

**Table 1.** Chemical composition (wt.%) of  $\text{CoCrFeNiSi}_{0.2}$  sections (Figure 2, b)

Section number	Cr	Fe	Co	Ni	Si
Spectrum 1	22.8	22.6	23.7	25.0	5.9
Spectrum 2	24.1	22.3	23.2	24.4	6.1
Spectrum 3	24.3	22.6	23.6	23.9	5.6

components over the thickness (Table 1). The average concentration of elements in the foils corresponds to their concentration in the initial target-ingot. Foil specific weight is  $8.1 \cdot 10^3 \text{ kg/m}^3$ .

Assessment of heat resistance of the produced foils showed that soaking at the temperature of 900 °C for 28 h is accompanied by only a slight increase of sample weight: less than  $0.2 \text{ mg/cm}^2$  (Figure 3, curve 2). At the temperature of 1000 °C the oxidation kinetics of foil of  $\text{CoCrFeNiSi}_{0.2}$  alloy obeys the parabolic law, which may be indicative of formation of a continuous protective oxide film on the surface. Here, the intensity of increase of the specific weight of  $\text{CoCrFeNiSi}_{0.2}$  foil samples at the temperature of 1000 °C is lower, even compared to foils of HEA without silicon at the temperature of 900 °C [9]. That is addition of silicon in the quantity of about 5 wt.% promoted an increase of heat resistance, and also allowed raising the potential service temperature of the material application up to 1000 °C (Figure 3, curve 1).

Analysis of the microstructure and chemical composition of  $\text{CoCrFeNiSi}_{0.2}$  foils showed (Figure 4, a, b) that after annealing in air at the temperature of 1000 °C scale layers of up to 10 μm thickness form on the foil surface, foil bulk structure remains poreless,

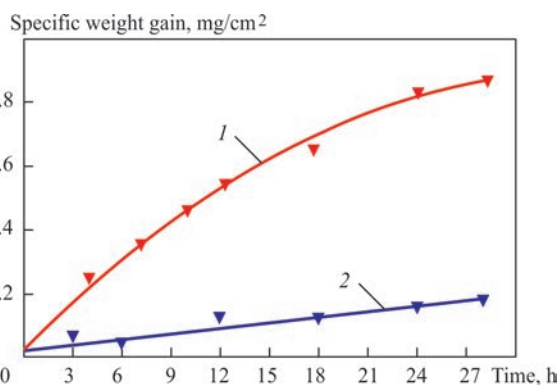


**Figure 3.** Oxidation kinetics of  $\text{CoCrFeNiSi}_{0.2}$  alloy foil at the temperature of 1000 °C (curve 1) and 900 °C (curve 2)

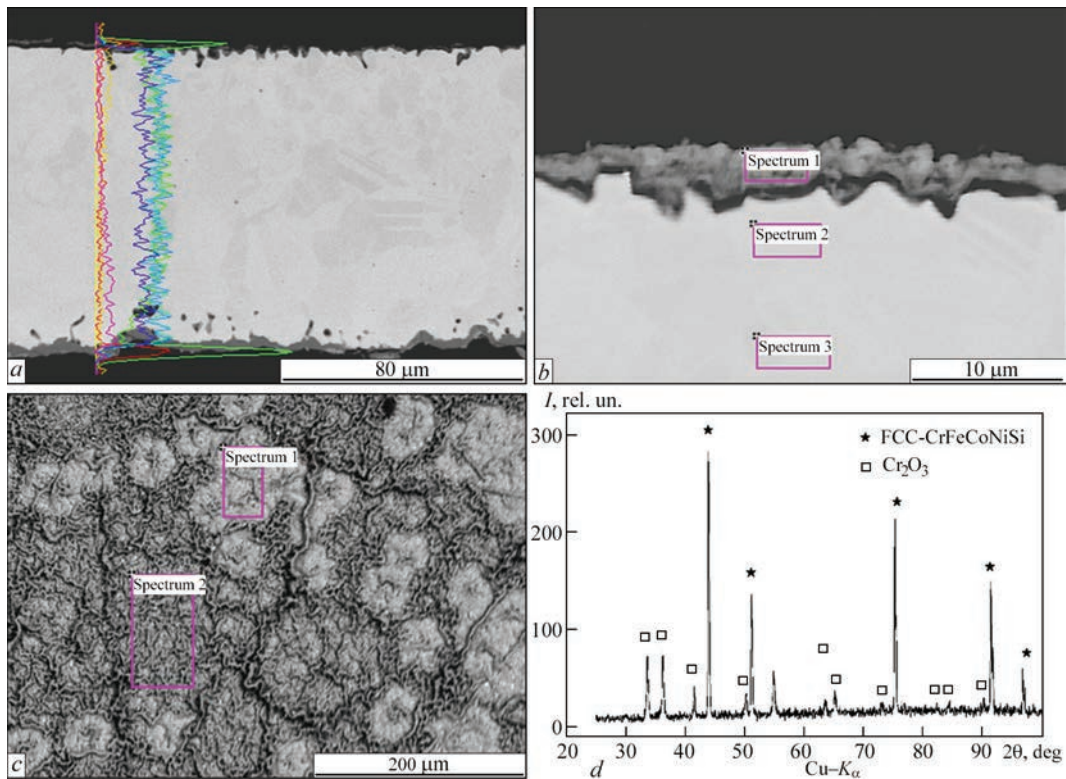


**Figure 4.** SEM images of cross-sectional microstructure (*a*, *b*) and surface (*c*) and diffraction pattern (*d*) of CoCrFeNiSi<sub>0.2</sub> HEA foils after heat-resistance testing at the temperature of 1000 °C

and formation of a small quantity of closed micropores located along the grain boundaries, is observed in the subsurface regions. At the same time, no oxygen was found in the subsurface regions of the foil. The scale surface is characterized by a sufficiently high level of continuity and low defect rate (Figure 4, *c*). Chemical analysis shows that scale consists predominantly of chromium, silicon and oxygen with a small content of the rest of the components (Table 2).

X-ray diffraction analysis revealed that the scale structure forms on the base of chromium oxide Cr<sub>2</sub>O<sub>3</sub> (Figure 4, *d*). In view of the fact that no diffraction signs of formation of silicides or other silicon compounds were observed, and by the data of energy-dispersive microanalysis the scale and foil surface layer contain silicon, it is assumed that silicon can promote inhibition of oxygen diffusion along the grain boundaries, thus preventing formation of unstable iron oxides and, consequently, rapid “burning out” of the foil material. At the same time, greater chromium affinity for oxygen in such a case promotes formation of a protective layer based on chromium oxide on the foil surface.

In keeping with published data, three-layer panels with hexagonal core, in which the cell walls are normal to the main layers (cover sheets), became the most widely applied. Wide application of such honeycomb cores is associated with their ability to ensure high specific strength and adaptability to manufacture [13].

Moreover, considering that the size of the thermal protection honeycomb panel is usually much smaller than that of the surface, which is to be “protected”, the shape of the three-layer panel proper has an important role. It is known that an area can be filled without gaps using three regular polygons: triangle, square and hexagon. A hexagonal panel has a number of advantages over a square or triangular one. First of all, a hexagonal panel can more effectively distribute the loads (for instance, at repeated entering of the dense layers of the atmosphere), as it has more neighbours, leading to a more uniform distribution of the load and smaller extreme values on any specific panel. Stresses are known to concentrate in acute angles, so that regular hexagons with angles of 120° have an obvious advantage over square panels with angles of 90° and

**Table 2.** Chemical composition (wt.%) of CoCrFeNiSi<sub>0.2</sub> sections (Figure 4)

Figure	Section number	Cr	Fe	Co	Ni	Si	O
Figure 4, <i>b</i>	Spectrum 1	39.3	8.5	6.8	4.7	8.4	32.3
	Spectrum 2	16.4	25.2	27.8	28.3	2.3	0
	Spectrum 3	14.2	25.1	28.9	29.6	2.2	0
Figure 4, <i>c</i>	Spectrum 1	44.9	6.3	7.0	6.7	7.4	27.7
	Spectrum 2	54.8	3.5	4.1	3.9	6.5	27.2

triangular panels with angles of  $60^\circ$ . Moreover, in the case of application of square panels straight regions of parallel welds can form along the rows, in which the heated gas flows will be accelerated, causing erosion wear of the panel materials, while application of a hexagonal panel will ensure distribution of the gas flows, as in this case extended continuous welds, parallel to the gas flow, will be absent. Another advantage of a hexagonal panel over a triangular or square one is a more uniform heating and cooling. Usually considerable overheating in the corners is noted in square and triangular parts, compared to the central areas of the parts.

In view of that, it was exactly the hexagonal shape of the thermal protection honeycomb panel, which was selected for making model samples. A sketch of a model sample of the three-layer honeycomb panel is given in Figure 5. Such a shape of the panel can ensure a more rational and effective covering of curvilinear surfaces or surfaces of the bodies of revolution, compared to panels of a square or rectangular shape.

The technological process of manufacturing a mockup of thermal protection honeycomb panel includes the following operations [14]: making skins (cover sheets); making blanks for honeycomb core; formation of profiled strips from the blanks; welding of the honeycomb core; manufacturing the honeycomb panels.

The procedure described above was used to manufacture honeycomb core elements of the required size and to join them to each other by spot welding. The appearance of the produced honeycomb core pack is shown in Figure 6. The outer frame is made from  $\text{CoCrFeNiSi}_{0.2}$  HEA foil strip, which was joined to the honeycomb core by spot welding. Frame welding mode was the same as in welding the honeycomb core.

To ensure uniform height for all the honeycomb core elements and eliminate the residual cutting, as-

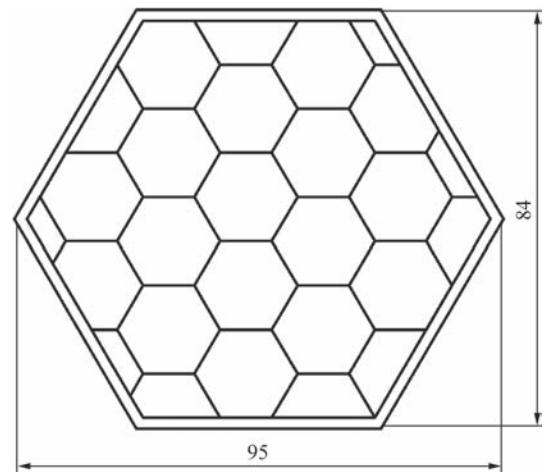


**Figure 5.** Sketch of the mockup of a three-layer thermal protection honeycomb panel

sembly and welding defects, the manufactured honeycomb cores were ground on a surface grinding machine from both sides. After grinding the honeycomb core height was 10 mm in all the cases.

The cover sheets in the form of a regular hexagon with side length of 48.5 mm were mechanically cut from the produced  $\text{CoCrFeNiSi}_{0.2}$  HEA foils according to pattern. In such a case the area of the cover sheet working surface is about  $60 \text{ cm}^2$ .

The manufactured elements of the three-layer panel (lower cover sheet, honeycomb core and upper cover sheet) were placed into the fixture, installed in the working chamber of the diffusion welding unit, and their joining was performed.

In such a way, a series of samples of three-layer honeycomb panels of a hexagonal shape were made (Figure 7) with dimensions according to the drawing given in Figure 5. The structure specific weight was  $3.3 \text{ kg/m}^2$ .

The made mockups of three-layer honeycomb panels were tested for structure resistance to cyclic thermal loads. Testing was conducted using electric



**Figure 6.** General view of the frame ( $\text{CoCrFeNiSi}_{0.2}$ ) with honeycomb core (AISI 304 stainless steel)



**Figure 7.** General view of the manufactured three-layer honeycomb panels



**Figure 8.** General view of the made mockup of the three-layer panel after 10 heat treatment cycles

furnace SShOL-2.4/12.5 of shaft type by a scheme, in which one cycle consisted of placing the panel into a furnace heated up to the temperature of 1000 °C, soaking for 30 min, removing from the furnace, and cooling to room temperature. Figure 8 shows the appearance of a mockup of a three-layer honeycomb panel after 10 heat treatment cycles. The integrity of the panel skin (cover sheets) and frame (honeycomb core) after thermal cycling should be noted.

Electron microscopy investigations revealed that the developed diffusion welding modes ensure formation of a sound joint of the honeycomb core and the cover sheets: one can see formation of the diffusion zone of up to 20 μm length with a smooth redistribution of elements between the material of the core and the cover sheets (Figure 9). Presence of a linear porosity of predominantly submicron size in the zone of the stainless steel and HEA joint is indicative of intensive

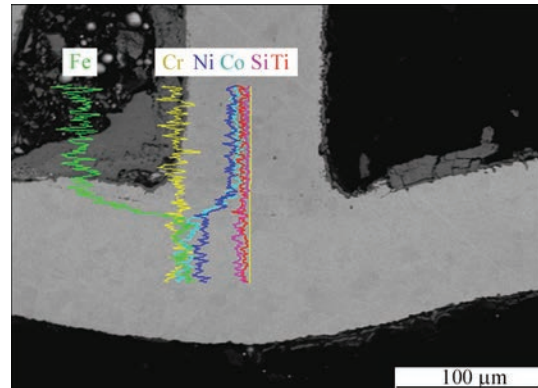


**Figure 9.** Electron image of the cross-sectional microstructure of the zone of core and cover sheet joint in the three-layer panel after testing at the temperature of 1000 °C

diffusion interaction between them with unbalanced flows of atoms, which causes the Kirkendall effect.

## CONCLUSION

1. Modes of high-speed EB-PVD process were optimized, which ensure producing thin foil of high-entropy alloy of Co–Cr–Fe–Ni–Si system with uniform structure across the thickness.

2. It was found that the proposed  $\text{CoCrFeNiSi}_{0.2}$  alloy ensures a combination of the required level of heat resistance with weldability in the solid phase.

3. Shown is the possibility of manufacturing by solid-phase welding of three-layer honeycomb panels based on thin  $\text{CoCrFeNiSi}_{0.2}$  HEA foils produced by the method of electron beam deposition, which can stand multiple thermal cycling from 25 up to 1000 °C in air without structure failure.

## REFERENCES

1. Takayuki, K., Hideyuki, T., Syunsuke, I. et. al. (2011) Conceptual study on heat resistant and cooling system of hypersonic airplanes. In: *Proc. of 17<sup>th</sup> AIAA Inter. Space Planes and Hypersonic Systems and Technologies Conf. (San Fran-*

- cisco, CA, USA, April 11–14, 2011), 1–12. DOI: <https://doi.org/10.2514/6.2011-2378>
2. Rakesh, K.K., Hazem, E.S., Summit, V. et al. (2008) Static Analysis of Sandwich Panels with Square Honeycomb Core. *AIAA J.*, **46**, 627–634. DOI: <https://doi.org/10.2514/1.28121>
  3. Boudjemai, A., Amri, R., Mankour, A. et al. (2012) Modal analysis and testing of hexagonal honeycomb plates used for satellite structural design. *Materials and Design*, **35**, 266–275. DOI: <https://doi.org/10.1016/j.matdes.2011.09.012>
  4. Semiatin, S.L., Gross, M.E., Matson, D.W. et al. (2012) Microstructure evolution and composition control during the processing of thin-gage metallic foil. *Metallurg. and Mater. Transact. A*, **43**, 4819–4834. DOI: <https://doi.org/10.1007/s11661-012-1255-9>
  5. Murty, B.S., Yeh, J.W., Ranganathan, S. (2014) *Chapt. 2 — High-entropy alloys: Basic concepts*. Eds by B.S. Murty, J.W. Yeh, S. Ranganathan. In: High entropy alloys. Butterworth-Heinemann, Oxford, UK, 13–35, DOI: <https://doi.org/10.1016/B978-0-12-800251-3.00002-X>
  6. Ustinov, A.I., Polishchuk, S.S., Demchenkov, S.A. et al. (2020) Formation of thin foils of high-entropy CrFeCoNiCu alloys by EB-PVD process. *Surf. and Coat. Technol.*, **403**, 126440. DOI: <https://doi.org/10.1016/j.surfcoat.2020.126440>
  7. Ustinov, A.I., Skorodzievskii, V.S., Demchenkov, S.O. et al. (2020) Effect of the structure of vacuum condensates of high entropy alloys of Cr–Fe–Co–Ni–Cu system on their mechanical properties. *Suchasna Elektrometal.*, **4**, 16–22. DOI: <https://doi.org/10.37434/sem2020.04.03>
  8. Ustinov, A.I., Demchenkov, S.A., Melnychenko, T.V. et al. (2021) Effect of structure of high entropy CrFeCoNiCu alloys produced by EB PVD on their strength and dissipative properties. *J. of Alloys and Compounds*, **887**, 161408. DOI: <https://doi.org/10.1016/j.jallcom.2021.161408>
  9. Ustinov, A.I., Demchenkov, S.O., Melnichenko, T.V. et al. (2022) The influence of copper on the heat resistance of thin foils of high-entropy alloys of the Cr–Fe–Co–Ni–Cu system obtained by the electron beam deposition method. *The Paton Welding J.*, **11**, 39–44. DOI: <https://doi.org/10.37434/tpwj2022.11.07>
  10. Gusarova, I.A., Parko, M., Potapov, A.M. et al. (2016) Evaluation of high-temperature resistance of three-layer honeycomb panel produced from YulPM-1200 alloy by vacuum diffusion welding. *The Paton Welding J.*, **12**, 29–33.
  11. Kai, W., Cheng, F.P., Liao, C.Y. et al. (2018) The oxidation behavior of the quinary FeCoNiCrSix high-entropy alloys. *Materials Chemistry and Physics*, **210**, 362–369. DOI: <https://doi.org/10.1016/j.matchemphys.2017.06.017>
  12. Li, Y., Zhang, P., Zhang, J. et al. (2021) Oxidation behavior of AlCoCrFeNiSix high-entropy alloys at 1100 °C. *Corrosion Sci.*, **190**, 109633. DOI: <https://doi.org/10.1016/j.corsci.2021.109633>
  13. Kobelev, V.N., Kovarsky, L.M., Timofeev, S.I. (1984) *Calculation of three-layer structures*. Moscow, Mashinostroenie [in Russian].
  14. Bitzer, T.N. (1997) *Honeycomb technology. Materials, design, manufacturing, applications and testing*. New York, Chapman & Hall.

### ORCID

A.I. Ustinov: 0000-0002-8855-3499,  
 Iu.V. Falchenko: 0000-0002-3028-2964,  
 S.O. Demchenkov: 0000-0002-2412-4214,  
 L.V. Petrushynets: 0000-0001-7946-3056

### CONFLICT OF INTEREST

The Authors declare no conflict of interest

### CORRESPONDING AUTHOR

A.I. Ustinov  
 E.O. Paton Electric Welding Institute of the NASU  
 11 Kazymyr Malevykh Str., 03150, Kyiv, Ukraine.  
 E-mail: [ustinov3g@gmail.com](mailto:ustinov3g@gmail.com)

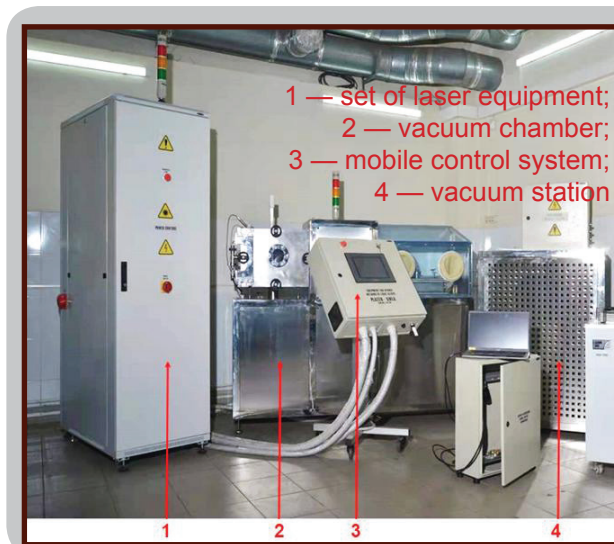
### SUGGESTED CITATION

A.I. Ustinov, Iu.V. Falchenko, S.O. Demchenkov, L.V. Petrushynets (2023) Manufacturing lightweight honeycomb panels on the base of high-entropy  $\text{CoCrFeNiSi}_{0.2}$  alloy foil produced by EB-PVD method. *The Paton Welding J.*, **8**, 29–35.

### JOURNAL HOME PAGE

<https://patonpublishinghouse.com/eng/journals/tpwj>

Received: 22.06.2023  
 Accepted: 07.08.2023



## DEVELOPED IN PWI



EQUIPMENT  
 FOR LASER WELDING  
 WITH INCREASED DEPTH  
 OF PENETRATION IN VACUUM



DOI: <https://doi.org/10.37434/tpwj2023.08.04>

# THE INFLUENCE OF IRON ON THE STRUCTURE AND TECHNOLOGICAL CHARACTERISTICS OF Cu–Mn–Co–Fe BRAZING FILLER METAL

S.V. Maksymova, P.V. Kovalchuk, V.V. Voronov, I.I. Datsiuk

E.O. Paton Electric Welding Institute of the NASU  
11 Kazymyr Malevych Str., 03150, Kyiv, Ukraine

## ABSTRACT

The results of complex studies on brazing filler metals of Cu–Mn–Co–Fe system alloyed with iron in the range of 1–5 wt.% are presented. The melting point was determined through calculation, and it was shown that increasing the concentration of iron from 1 to 5 wt.% leads to a slight (from 912 °C to 923 °C) increase in the solidus temperature and a significant increase in the liquidus temperature (from 931 °C to 1027 °C). At the same time, the melting temperature range expands to 104 °C. The results of experimental studies on spreading of brazing filler metals over Kovar and corrosion-resistant steel have established that an increase in the iron concentration from 1 to 5 % contributes not only to an increase in the liquidus temperature, but also to an increase in the spreading area, which is due to the melting temperature of a copper-based solid solution. Local X-ray microanalysis established a discrete distribution of constituent elements and showed that the brazing filler metal contains two solid solutions after spreading: copper-based and manganese-based. The research results on overlap brazed joints of Kovar - corrosion-resistant steel have demonstrated that addition of iron to Cu–Mn–Co–Fe alloy leads to an increase in microhardness and shear strength.

**KEYWORDS:** copper–manganese–cobalt–iron brazing filler metal, melting temperature range, structure, microhardness, wetting angle, solid solution

## INTRODUCTION

Joining dissimilar materials (Kovar–corrosion-resistant steel) is one of the most complicated tasks, faced by modern manufacturers. There exist different technologies of producing joints. In particular, brazing, diffusion, electron beam, laser welding, etc. have become the most widely applied [1–6]. Dissimilar joints are usually used in instrument-making, electrical engineering, chemical, petrochemical and nuclear industries, where it is necessary to ensure shape and dimensional stability at temperature change [7–11].

One of the main methods of producing this type of joints is brazing. Brazing technologies allow joining parts, if required, not around the contour, but simultaneously over the entire surface, while providing a high efficiency of the process, possibility of automation with preservation of the initial structure of the base metal, under the condition of correct selection of chemical composition of the brazing filler metal and melting temperature range [12].

Alloys based on binary copper–manganese system, characterized by solid solution structure, are widely used as filler metals for brazing dissimilar materials [13]. One can see on the state diagram of copper–manganese system the presence of a minimum on the liquidus curve, which corresponds to melting temperature of 870 °C and manganese concentration of approximately 37 at.% [14]. At lowering of heating temperature, the processes of solid solution ordering

run in the binary system. At the same time, it should be noted that two-component brazing filler metals are seldom used. One of the important factors is the possibility of manganese evaporation during heating that influences the chemical composition of the brazing filler metal and melting temperature. Additional doping of alloys of this system by other chemical elements is used to improve the technological characteristics of brazed joints [12]. The most common of them are nickel, iron, and cobalt, which improve the mechanical properties of not only the brazing filler metals, but also of the brazed joints.

## THE OBJECTIVE

of this work is investigation of iron influence on the technological properties of brazing filler metals of Cu–Mn–Co–Fe system, their melting temperature range, chemical heterogeneity, microhardness and wetting angle, which forms at Kovar spreading over corrosion-resistant steel.

## INVESTIGATION METHODS AND MATERIALS

Experimental alloys based on Cu–Mn–4.5Co–Fe system were produced by nonconsumable tungsten electrode argon-arc melting on a cold copper substrate in high purity argon (argon volume fraction of not less than 99.993 %). The uniformity of alloying element distribution through the ingot volume was achieved by fivefold remelting with ingot turning over.

**Table 2.** Composition and calculated solidus and liquidus temperatures of experimental brazing filler metals

Brazing filler metal No.	Composition, wt. %	Temperature, °C	
		$T_s$	$T_l$
1	Cu–Mn–4.5Co–1Fe	912	931
2	Cu–Mn–4.5Co–2Fe	915	946
3	Cu–Mn–4.5Co–2.5Fe	917	957
4	Cu–Mn–4.5Co–5Fe	923	1027

Used as the base material were plate samples of 20×20×2 mm size from Kovar and corrosion-resistant 12Kh18N10T steel (Figure 1, Table 1). The brazing filler metal was used in the cast condition.

Spreading of experimental brazing filler metals was conducted in a vacuum furnace (SGV 2.4-2/15-13) with radiation heating (working space rarefaction of  $1.33 \cdot 10^{-3}$  Pa) with the heating rate of 18–20 °C/min, and cooling rate of  $(10–15) \pm 5$  °C/min. Heating temperature ( $T_l + 20$  °C) was controlled using a thermocouple, which was fastened on the sample (soaking for 3 min).

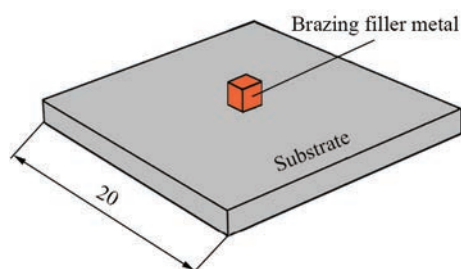
For thermodynamic calculations of the melting temperature range of the investigated alloys, a specialized program, JMatPro v.7.0, developed by “Sente Software” company, was used. This software package enables thermodynamic calculations for multi-component systems. These calculations are based on evaluation of Gibbs’ energy functions for each phase at the specified temperature [16–18].

Metallographic investigations and X-ray microanalysis of experimental brazing filler metals were conducted on cast samples of a polycrystalline structure (after melting). Here, all the alloys were cooled to room temperature at the same rate. A standard procedure was used to prepare microsections and conduct their microstructural studies with application of scanning electron microscope TescanMira 3 LMU. Local distribution of elements in individual phases was determined by X-ray microanalysis using energy-dispersive spectrometer X-max 80 of Oxford Instruments. The microsections were studied without chemical etching in BSE mode. Locality of measurements was up to 1  $\mu$ m.

Vickers microhardness ( $HV$ ) of brazing filler metals in the initial state was studied using a stationary hardness meter NOVOTEST TC-MKB-1M with

**Table 1.** Base material chemical composition [15]

Material grade	Chemical element, wt. %									
	Fe	Ni	Co	C	Si	Mn	Cr	Ti	Al	Cu
29NK Kovar	51.14–54.5	28.5–29.5	17–18	0.03	0.3	0.4	0.1	0.1	0.2	0.2
12Kh18N10T	67	9–1	–	0.12	0.8	2	17–19	0.4–1	–	0.3


**Figure 1.** Schematic image of substrate–brazing filler metal

0.05 N load ( $\tau = 15$  s), measurement error was 5 %. Image-Pro Plus 6.0 program was used to measure the spreading area. Application of this software allowed conducting accurate measurements and analysis of the obtained data on spreading. Moreover, the software provides a visualization of the results in a format convenient for further use. The shear strength of brazed overlap plate joints was determined at room temperature with application of testing machine ZDM 10 Zwick-1488.

## INVESTIGATION RESULTS AND DISCUSSION

Thermodynamic calculations determined the solidus and liquidus temperatures of the studied brazing filler metals of Cu–Mn–4.5Co–Fe system (Table 2).

Performed calculations showed that increase of iron concentration from 1 up to 5 % in Cu–Mn–Co–Fe system alloy leads to increase of the liquidus temperature from 931 up to 1027 °C. Solidus temperature changes only slightly (from 912 to 923 °C). Determined temperature results were used to plot a graph, which demonstrates iron influence on the alloy melting range, and shows that with increase of iron concentration the melting temperature range becomes much wider (Figure 2).

Further processing of the data by statistical analysis methods yielded the dependencies of the liquid phase on heating temperature for each alloy, which is indicative of a smooth increase of the quantity of the liquid phase at increase of iron concentration from 1 up to 2.5 % (Figure 3, a–c).

At heating of alloys containing 5 % of iron, the quantity of the liquid phase rapidly increases with temperature increase from 925 up to 937 °C (Figure 3, d). Further temperature rise (from 937 to 1027 °C) only slightly influences the increase in the liquid

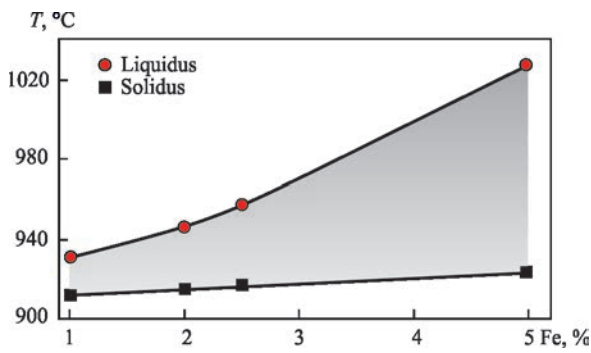


**Figure 2.** Influence of iron on melting range of alloys of Cu-Mn-4.5Co-Fe system

phase quantity (within 83–100 %). Obtained data agree well with the results of experiments on brazing filler metal spreading over the base metal (Kovar and corrosion-resistant steel), which will be given below.

Conducted metallographic investigations and results of X-ray microanalysis showed that Cu-Mn-4.5Co-(1–5)Fe alloys are characterized by a two-phase structure, which is formed by two solid solutions. Local X-ray microanalysis determined a discrete distribution of the constituent elements in individual phases.

In the case of investigations of Cu-Mn-Co-Fe system alloy with 5 % Fe it is shown that its structure is two-phase, and it consists of two solid solutions,

**Table 3.** Chemical composition of individual phases of Cu-Mn-4.5Co-5Fe alloy

Spectrum	Chemical elements, wt. %			
	Mn	Fe	Co	Cu
1	39.41	22.59	16.73	21.27
2	32.97	3.37	4.48	59.18

which are characterized by a pronounced segregation, inherent to alloys of Cu-Mn system [19]. The main phase is copper-based solid solution ( $\alpha$ -Cu) (Figure 4, Table 3, spectrum 2), along the grain boundaries of which dendrites of a manganese-based solid solution ( $\gamma$ -Mn) precipitate, which are enriched in iron, cobalt and copper (Figure 4, Table 3, spectrum 1).

Electronic images of the microstructure of Cu-Mn-Co-(1–5)Fe alloy (in the initial condition) are indicative of certain morphological changes, which are due to the influence of the alloying element — iron (Figure 5). Analysis of these structures leads to the conclusion that increase of iron concentration from 1 up to 5 % in alloys of Cu-Mn-Co-Fe system leads to refinement of the structural components and to formation of fine-crystalline structures (Figure 5).

X-ray microanalysis allowed establishing a connection between iron concentration in the brazing fill-

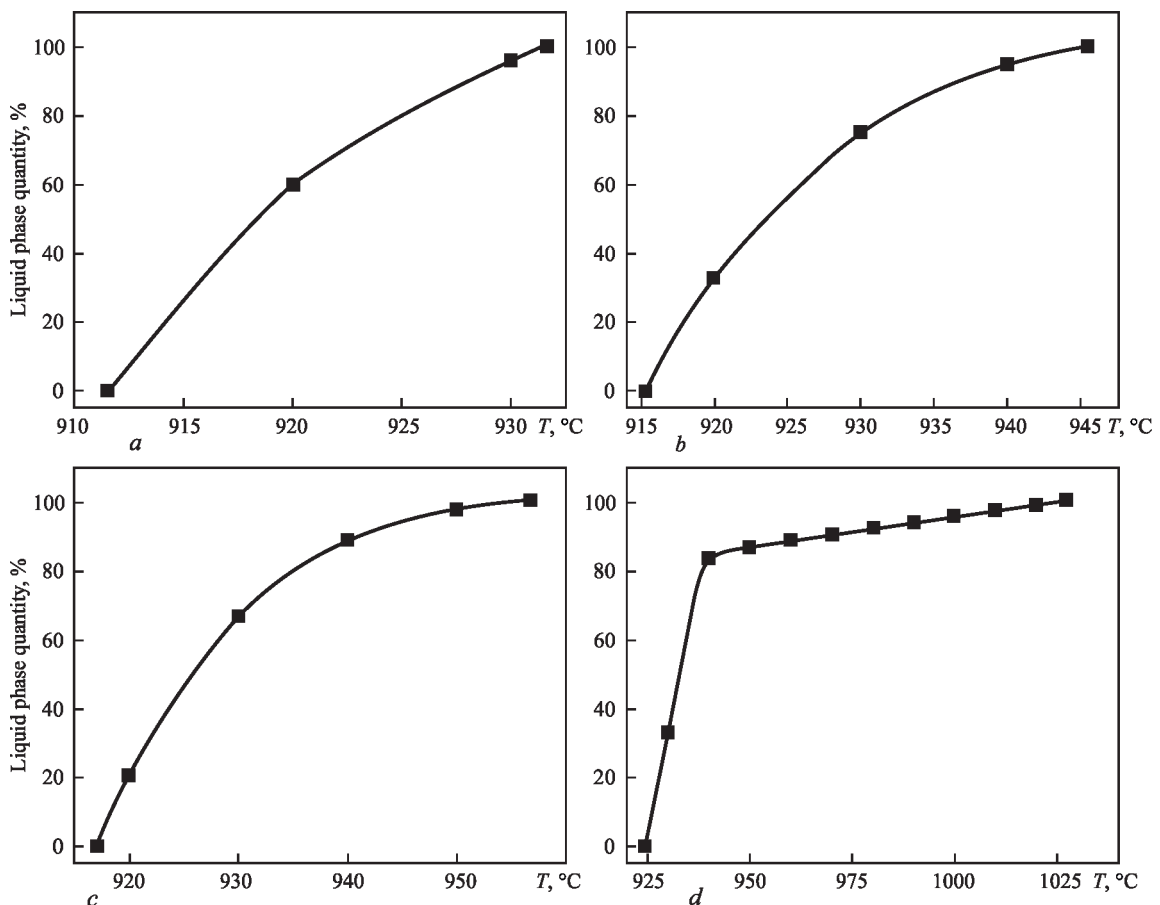


**Figure 3.** Quantity of the liquid phase in alloys of Cu-Mn-Co-Fe system, depending on temperature and Fe content in %: 1 (a); 2 (b); 2.5 (c); 5 (d)

er metal and in individual phases. So, increase of iron concentration from 1 to 5 % in experimental brazing filler metals leads to a slight increase in its quantity from 0.3 to 3.37 % in copper-based  $\alpha$ -solid solution. Here, a slight increase of iron concentration up to 22.59 wt.% (at alloying with iron in the quantity of 5 %) is found in  $\gamma$ -phase (based on manganese) (Figure 6). Such a structural heterogeneity is responsible for increase of brazing filler metal microhardness (Figure 7).

Results of experiments on spreading of experimental brazing filler metals over Kovar and corrosion-resistant steel (in keeping with the calculated melting temperatures) are indicative of satisfactory wetting of base metals under vacuum. Here, small wetting angles are formed: within  $4\text{--}22^\circ$  over Kovar and  $6\text{--}10^\circ$  over the corrosion-resistant steel. It should be noted that spreading is accompanied by certain kinetic peculiarities. The first to melt is the copper-based solid solution, which spreads over the base metal as a plane front to form a halo around the perimeter of the refractory component of the brazing filler metal, which is concentrated in the central zone of the plate sample (Figure 8).

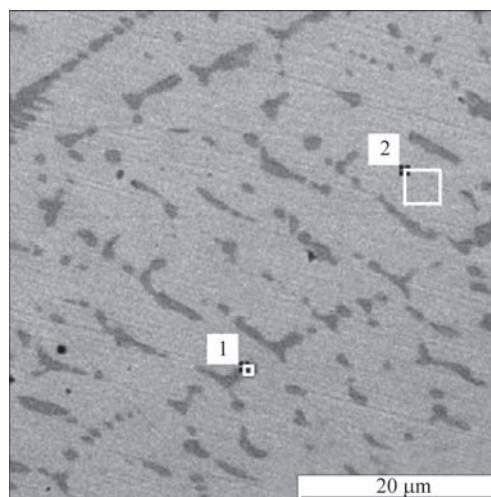


Figure 4. Microstructure of Cu–Mn–4.5Co–5Fe alloy

This is the result of partial evaporation of manganese taking place during heating [20], which is due to the high vapour pressure of the latter that is visually confirmed by the brazing filler metal colour after its spreading (Figure 8). Moreover, the concentration of refractory elements, namely iron and cobalt, increases considerably in  $\gamma$ -phase (manganese-based) that is confirmed by the results of X-ray microanalysis. In

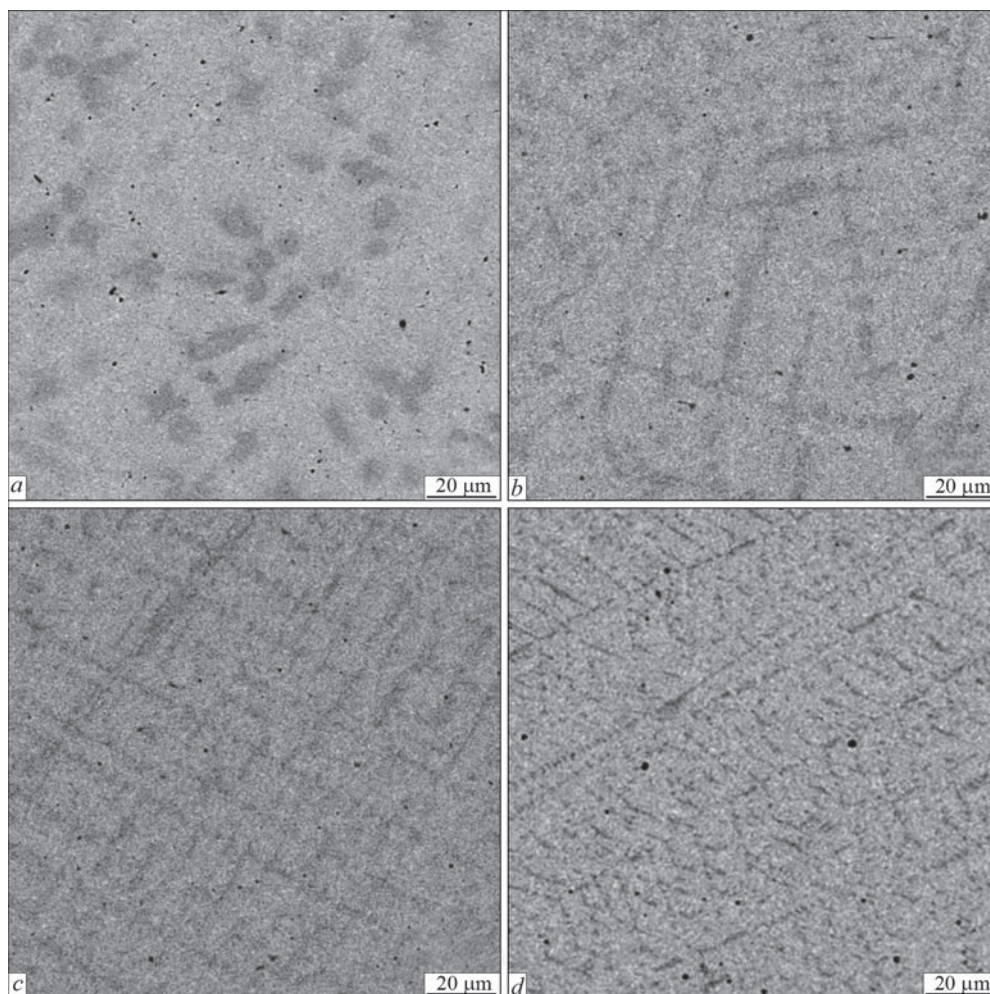
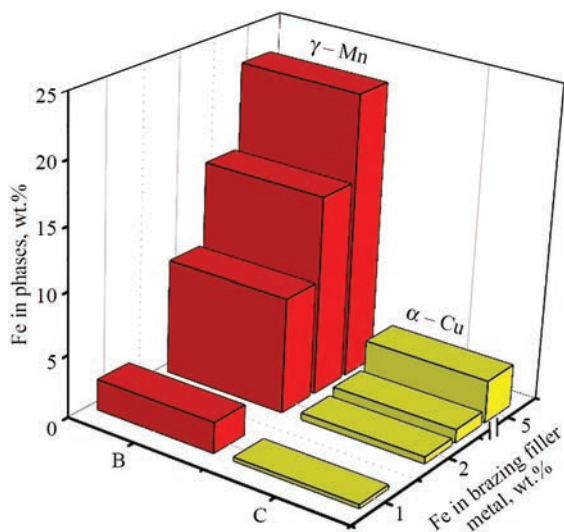


Figure 5. Microstructure of alloys of Cu–Mn–Co–Fe system with different Fe concentration in %: 1 (a); 2 (b); 2.5 (c); 5 (d)



**Figure 6.** Dependence of Fe concentration in individual phase on its content in the initial brazing filler metal

the copper-based solid solution, the iron quantity also increases, but only slightly, which was established by X-ray microanalysis of a drop of brazing filler metal after spreading. A significant heterogeneity of the brazing filler metal drop as to chemical composition (at spreading) leads to an increase in the difference between the melting temperatures of both the components. As the two solid solutions are characterized by different melting temperature, at base metal wetting the copper-manganese solid solution is the first to spread, which is exactly what forms a halo around the perimeter of the brazing filler metal drop. A schematic representation of the brazing filler metal after spreading is given in Figure 9.

Thus, at increase of iron concentration in brazing filler metals of Cu–Mn–Co–Fe system the liquidus temperature rises, requiring a corresponding increase of the heating temperature, when conducting the spreading experiments. It promotes better spreading of the low-melting component — the copper-based solid solution [21].

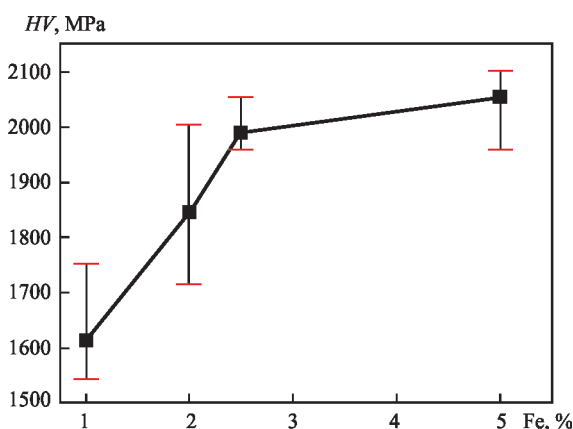


**Figure 7.** Influence of iron concentration on microhardness of brazing filler metals of Cu–Mn–Co–Fe system

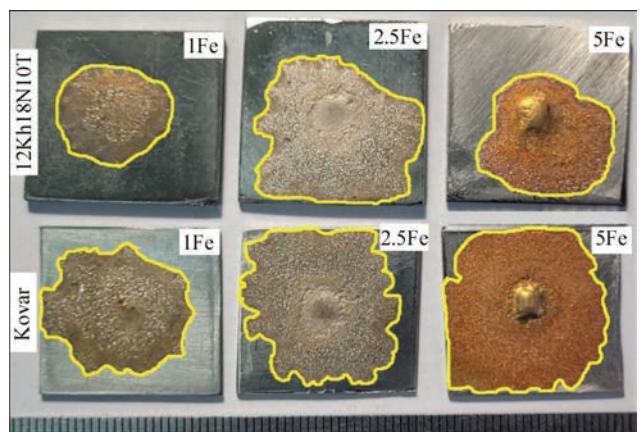


**Figure 8.** Appearance of samples after spreading of brazing filler metals with different quantity of iron over corrosion-resistant steel and Kovar

Analysis of the obtained results of X-ray microanalysis and local distribution of elements in a drop of brazing filler metal No. 1 (after spreading) points to a similar tendency of structure formation (as in the initial brazing filler metal). It was proved empirically that iron concentration in the copper-based and manganese-based solid solutions becomes higher with increase of its quantity in the brazing filler metal. It was determined, in particular, that the phase based on manganese-copper system is also enriched in iron up to 13.47 % and in cobalt up to 27.85 % (Figure 10, Table 4, spectrum 2). At the same time, manganese-based dendrites (86.06 % Mn) were revealed during investigations (Figure 10, a, Table 4, Spectrum 1).

Copper-based and manganese-based solid solutions also form at spreading of this brazing filler metal over corrosion-resistant steel (Figure 10, b). Iron concentration in grains of manganese- and copper-based phase practically does not change (Figure 10, b, Table 5).

After spreading of brazing filler metal No. 1 over corrosion-resistant steel a similar structure appears, which is also formed by the two solid solutions and manganese-based phase inclusions (Figure 10, b). Local X-ray microanalysis revealed that manganese-based grains, which solidify against the background of  $\alpha$ -Cu solid solution, contain the same quantity of iron (13.37 %), similar to spreading over Kovar. Iron concentration in the solid solution does not change, either.

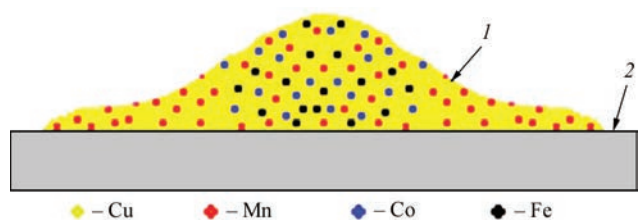


**Figure 9.** Schematic representation of brazing filler metal after spreading of brazing filler metal drop (1) and base metal substrate (2)

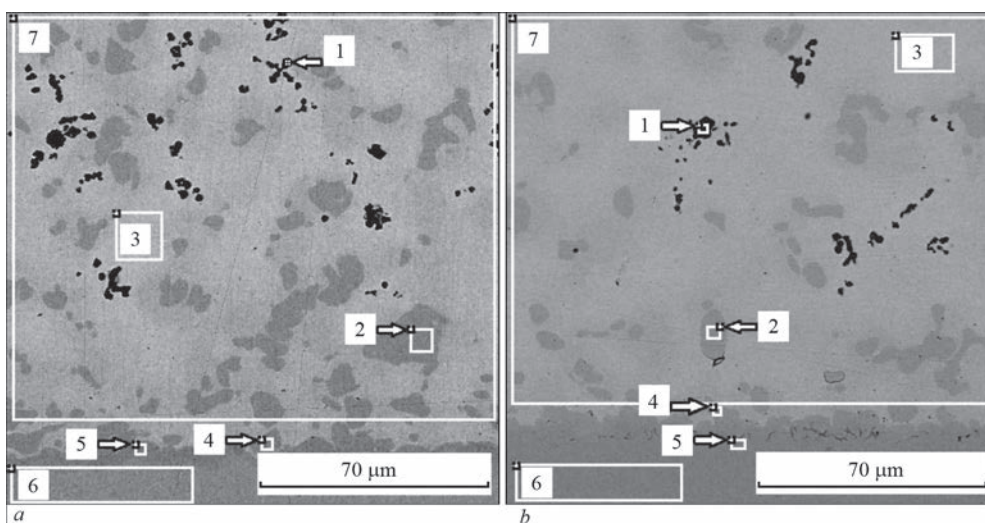


**Figure 10.** Microstructure of brazing filler metal No.1 after spreading over Kovar (*a*) and corrosion-resistant steel (*b*)

A somewhat higher concentration of alloying elements in individual phases after spreading of the brazing filler metal over the base metal is attributable to non-equilibrium thermokinetic conditions of brazing filler metal solidification, and presence of a gradient of constituent element concentration on the interface of the brazing filler metal with the base metal, leading to running of the diffusion processes and structural heterogeneity.

The derived investigation results proved that increase of iron quantity in the initial brazing filler metal from 1 up to 5 % leads to increase in its concentration in the structural components. So, in Cu–Mn solid solution (matrix) a slight increase in iron concentration from 1.1 to 3.0 % at spreading over Kovar and from 0.36 to 2.6 % over corrosion-resistant steel is observed (Figure 11, *a*).

It should be noted that in  $\gamma$ -Mn based solid solution a rapid increase in iron concentration (from 13.47 to 42.65 %) is observed after spreading of brazing filler metal No. 4 over Kovar (Figure 11, *b*). A similar increase in iron quantity (13.37 % to 44.82 %) is found also at spreading over corrosion-resistant steel

**Table 4.** Chemical composition of base metal and individual phases at spreading over Kovar

Spectrum	Chemical elements, wt.%				
	Mn	Fe	Co	Ni	Cu
1	86.06	0.83	1.15	0.27	11.70
2	40.71	13.47	27.85	0.52	17.47
3	27.15	1.10	3.92	0.39	67.44
4	39.51	14.91	27.97	0.78	16.73
5	34.50	24.52	24.94	3.34	12.60
6	0.51	52.97	17.58	28.61	0.33
7	3.93	3.66	9.76	0.50	54.15

(Figure 11, *b*). Results of electron microscopy and X-ray microanalysis correlated well with those of mechanical tests.

Preliminary studies [22] demonstrated that at brazing dissimilar overlap joints of Kovar-corrosion-resistant steel by Cu–Mn–4.5Co brazing filler metal the shear strength is equal to 434 MPa. Alloying of this brazing filler metal by iron in the quantity of 1 %

**Table 5.** Chemical composition of base metal and individual phases at spreading of brazing filler metal No.1 over corrosion-resistant steel

Spectrum	Chemical elements, wt.%							
	Si	Ti	Cr	Mn	Fe	Co	Ni	Cu
1	16.73	0.11	0.00	79.72	0.43	0.23	0.32	2.46
2	0.00	0.00	0.68	42.00	13.37	28.10	0.00	15.85
3	0.00	0.00	0.00	28.61	0.36	2.66	0.00	68.36
4	0.00	0.00	0.89	41.84	13.86	27.20	0.00	16.22
5	0.31	0.24	15.28	11.40	60.55	4.28	6.57	1.38
6	0.53	0.28	17.65	1.27	71.21	0.34	8.72	0.00
7	0.00	0.00	0.21	32.16	2.88	7.69	0.00	57.06

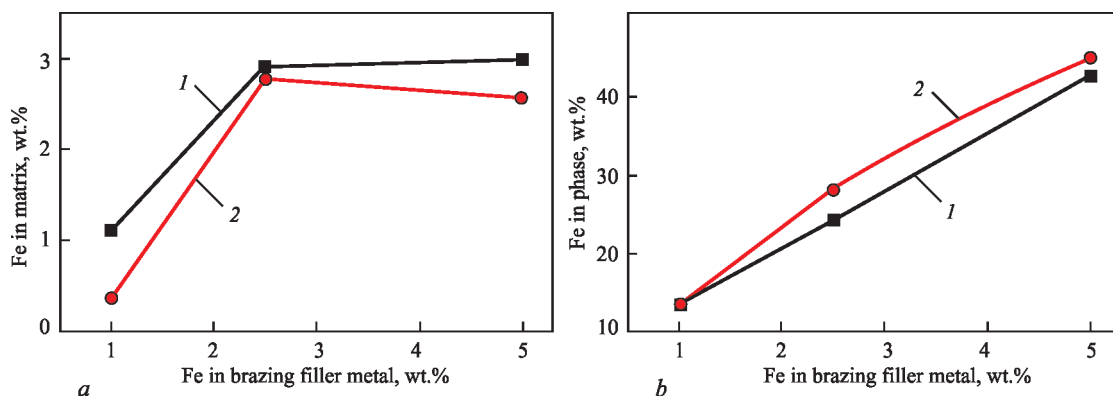


**Figure 11.** Fe content influence on its concentration in  $\alpha$ -Cu based solid solution (a) and  $\gamma$ -Mn based solid solution (b) after spreading of brazing filler metals over Kovar (1) and corrosion-resistant steel (2)

leads to strengthening of the two solid solutions by iron, and to increase of shear strength from 434 to 488 MPa, respectively.

Comprehensive results of the conducted studies open up additional possibilities of improving the technological properties of copper-manganese brazing filler metals which are applied in manufacture of brazed components from dissimilar materials.

## CONCLUSIONS

It was determined by calculations that increase of Fe content in alloys of Cu–Mn–Co–Fe system from 1 to 5 % leads to increase of liquidus temperature from 931 to 1027 °C, whereas the solidus temperature rises only slightly (from 912 to 923 °C). A significant (104 °C) widening of the melting range of the brazing filler metal is observed here.

Using the results of X-ray microanalysis studies and taking into account the shape of fusibility diagrams, it was proved that alloys of Cu–Mn–4.5Co–(1–5)Fe system are characterized by a two-phase structure, which consists of two solid solutions. The main phase is a copper-based solid solution, which contains dendrites of manganese-based solid solution, enriched in iron, cobalt and copper. Increase of iron concentration in the brazing filler metal promotes a considerable increase in its quantity in the manganese-based solid solution ( $\gamma$ -phase) and increase of its microhardness, respectively.

It is established that increase of iron quantity in the initial brazing filler metal from 1 to 5 % leads to increase of its concentration in the structural components after spreading. So, a slight increase of iron concentration (from 1.1 to 3.0 %) is found in Cu–Mn solid solution (matrix) at spreading over Kovar and from 0.36 to 2.6 % at spreading over the corrosion-resistant steel. In manganese-based solid solution, a rapid increase in iron concentration from 13.47 to 42.65 % is observed after spreading of the brazing filler metals over Kovar and from 13.37 to 44.82 % at spreading over the corrosion-resistant steel.

Mechanical testing of overlap brazed joints of Kovar–corrosion-resistant steel proved that alloying of brazing filler metal of Cu–Mn–Co–Fe system by iron in the quantity of 1 % promotes an increase of shear strength from 434 (basic brazing filler metal) to 488 MPa.

## REFERENCES

- Mai, T.A., Spowage, A.C. (2004) Characterisation of dissimilar joints in laser welding of steel–kovar, copper–steel and copper–aluminium. *Mat. Sci. and Engin., A*, 374(1–2), 224–233. DOI: <https://doi.org/10.1016/j.msea.2004.02.025>
- Fadhali, M.M. A., Zainal, S.J., Munajat Y., Jalil, A., Rahman, R. (2010) Laser welding characterization of kovar and stainless steel alloys as suitable materials for components of photonic devices packaging. *AIP Conference Proceedings*, 1217, 147–152. DOI: <https://doi.org/10.1063/1.3377802>
- Kaletina, Yu.V., Efimova, E.D., Romanov, M.K. (2014) Problems of weldability of parts made of austenitic steel 12Kh18N10T and precision alloy 29NK. *Metallovedenie i Termich. Obrab. Metallov*, 6, 26–29 [in Russian].
- Sun, Z., Moisiso, T. (1994) Melting ratio in laser welding of dissimilar metals. *J. Mater. Sci. Lett.*, 13, 980–982. DOI: <https://doi.org/10.1007/BF00701444>
- Xin, C., Jiazhen, Y., Li, N., Liu, W., Du, J., Cao, Y., Shi, H. (2016) Microstructural evolution during the brazing of  $Al_2O_3$  ceramic to kovar alloy by sputtering Ti/Mo films on the ceramic surface. *Ceramics Intern.*, 42(11), 12586–12593. DOI: <https://doi.org/10.1016/j.ceramint.2016.04.094>
- Baghjari, S.H., Gholambargani, M., Akbari Mousavi S.A. (2019) Application of the pulsed Nd:YAG laser welding to investigate the effect of laser beam position on weld characteristics of AISI 420 stainless steel to kovar alloy. *Lasers Manuf. Mater. Process.* 6, 14–25. DOI: <https://doi.org/10.1007/s40516-018-0078-y>
- Qiao, G.J., Wang, H.J., Gao, J.Q., Jin, Z.H. (2005) Brazing  $Al_2O_3$  to kovar alloy with Ni/Ti/Ni interlayer and dramatic increasing of joint strength after thermal cycles. *Mat. Sci. Forum*, 486–487, 481–484. DOI: <https://doi.org/10.4028/www.scientific.net/msf.486-487.481>
- Fang, Y.J., Jiang, X.S., Mo, D.F., Song, T.F., Shao, Z.Y., Zhu, D.G., Zhu, M.H., Luo, Z.P. (2018) Microstructure and mechanical properties of electron beam welded joints of titanium TC4 (Ti–6Al–4V) and kovar (Fe–29Ni–17Co) alloys with Cu/Nb multi-interlayer. *Advances in Mater. Sci. and Engin.*, 2018, 1–11. DOI: <https://doi.org/10.1155/2018/2042871>
- Sun, Z., Ion, J.C. (1995) Laser welding of dissimilar metal combinations. *J. Mater. Sci.*, 30, 4205–4214. DOI: <https://doi.org/10.1007/BF00361499>

10. Xiao, R., Dong, P., Chen, K. (2009) Laser beam welding of dissimilar materials. In: *28<sup>th</sup> Intern. Congress on Applications of Lasers and Electro-Optics – ICALEO 2009* (Orlando, FL, USA), **102**, 660–665.
11. Wang, J.L., Yang, Z.W., Wang, Y. et al. (2021) Microstructural stability and mechanical properties of Al<sub>2</sub>O<sub>3</sub>/kovar 4 J34 joint vacuum brazed using Ag–5Cu–1Al–1.25Ti (wt.%) filler metal. *J. of Manufacturing Processes*, **72**, 553–564. DOI: <https://doi.org/10.1016/j.jmapro.2021.10.057>
12. Ermolaev, G.V., Kvasnitsky, V.V., Kvasnitsky, V.F., Maksymova, S.V. et al. (2015) *Metal brazing: Manual*. Mykolaiv, NUK [in Ukrainian].
13. Sally, A. (1959) Manganese. Moscow, Metallurgizdat [in Russian].
14. Massalski, T.B. (1990) *Binary alloy phase diagrams*. American Society for metals. Ohio, Metals Park, ASM International, CD.
15. *Steel and alloy grades*. <http://www.splav-kharkov.com> <http://www.splav-kharkov.com>
16. *Practical software for materials properties*. <https://www.senteseoftware.co.uk/jmatpro>
17. Saunders, N., Guo, Z., Li, X., Miodownik, A.P., Schillé, J-Ph. (2003) Using JMatPro to model materials properties and behavior. *JOM*, **55**(12), 60–65. DOI: <https://doi.org/10.1007/s11837-003-0013-2>
18. Schillé, J-Ph., Guo, Z., Saunders, N., Miodownik, P.A. (2011) Modeling phase transformations and material properties critical to processing simulation of steels. *Mater. and Manuf. Processes*, **26**(1), 137–143. DOI: <https://doi.org/10.1080/10426910903153059>
19. (1997) *State diagrams of binary metallic systems*. Ed. by N.P. Lyakishev, Vol. 2, Moscow, Mashinostroenie [In Russian].
20. (2007) *Brazing Handbook*. 5<sup>th</sup> Ed., Miami. AWS.
21. Maksymova, S.V., Kovalchuk, P.V., Voronov, V.V. (2021) Vacuum brazing of kovar–molybdenum dissimilar joints. *The Paton Welding J.*, **7**, 13–18. DOI: <https://doi.org/10.37434/tpwj2021.07.03>
22. Maksymova, S.V., Kovalchuk, P.V., Voronov, V.V. (2021) Influence of Co on structure and mechanical properties of kovar–stainless steel brazed joints. *Metalofiz. ta Novitni Tekhnol.*, **43**(4), 553–566 [in Ukrainian]. DOI: <https://doi.org/10.15407/mfint.43.04.0553>

**ORCID**

S.V. Maksymova: 0000-0003-0158-5760,  
P.V. Kovalchuk: 0000-0002-2313-5982,  
V.V. Voronov: 0000-0002-0410-1154,  
I.I. Datsiuk: 0009-0008-1763-1382

**CONFLICT OF INTEREST**

The Authors declare no conflict of interest

**CORRESPONDING AUTHOR**

S.V. Maksymova  
E.O. Paton Electric Welding Institute of the NASU  
11 Kazymyr Malevych Str., 03150, Kyiv, Ukraine.  
E-mail: maksymova.svitlana15@ukr.net

**SUGGESTED CITATION**

S.V. Maksymova, P.V. Kovalchuk, V.V. Voronov, I.I. Datsiuk (2023) The influence of iron on the structure and technological characteristics of Cu–Mn–Co–Fe brazing filler metal. *The Paton Welding J.*, **8**, 36–43.

**JOURNAL HOME PAGE**

<https://patonpublishinghouse.com/eng/journals/tpwj>

Received: 08.06.2023

Accepted: 07.08.2023



**VII INTERNATIONAL  
CONFERENCE ON WELDING  
AND RELATED TECHNOLOGIES**

7-10 October 2024 Kyiv, Ukraine

[www.wrt2024.com.ua](http://www.wrt2024.com.ua)

DOI: <https://doi.org/10.37434/tpwj2023.08.05>

# INFLUENCE OF WELD POOL SURFACE DEPRESSION ON BURNING CONDITIONS OF AN ARC WITH A REFRACTORY CATHODE

I.V. Krivtsun, I.V. Krikent, V.F. Demchenko

E.O. Paton Electric Welding Institute of the NASU  
11 Kazymyr Malevych Str., 03150, Kyiv, Ukraine

## ABSTRACT

Results of mathematical modeling of an argon arc with refractory cathode in case of a deformed surface of the weld pool (arc anode) are described. It is assumed that there is a depression (crater) on the anode surface, the shape and size of which are preset; arc plasma has axial symmetry, and it is in a stationary state; metal evaporation from the anode surface is ignored. A mathematical model of the processes of energy, momentum, mass and charge transfer in the arc column and anode region is briefly described. A numerical study was conducted of thermal, electromagnetic and gas-dynamic processes in the arc column with a curved surface of the anode, as well as conditions of electric, thermal and force interaction of the arc with the anode surface, depending on the crater depth. Results of computational experiments are illustrated by the fields of isotherms, isobars and current lines in an arc with a curved surface of the anode, which are compared with similar fields in the case of an anode with a plane surface. A procedure for calculation of normal components of the vectors of electric current density and specific heat flux into the anode with a curved surface is described, and results of calculation of radial distributions of these characteristics, depending on the depth of the crater on the anode surface, are given. These results are complemented by numerical studies of the influence of the crater depth on arc pressure distribution over the anode surface. A conclusion was made that sagging of the weld pool surface in TIG welding can significantly change the conditions of electric and thermal interaction of the arc with the metal being welded, namely it can influence the thermal and hydrodynamic processes in the liquid metal, which determine the penetrability of the arc with the refractory cathode.

**KEYWORDS:** TIG welding, arc column, anode region, weld pool surface, anode, electric current density, specific heat flux into the anode, mathematical modeling

## INTRODUCTION

Technological results of TIG welding are largely determined by the conditions of electric arc interaction with the surface of the metal being welded. Such conditions include: distributions of the specific heat flux, electric current density, gas-dynamic pressure and stress of viscous friction of arc plasma on the weld pool surface. In their turn, these conditions determine the thermal, electromagnetic and hydrodynamic processes in the metal being welded, and the depth and shape of its penetration, respectively.

A large number of studies are devoted to investigations of plasma column and anode region of an electric arc with a refractory cathode, including the conditions of its interaction with the anode surface, depending on current, arc length, cathode shape and dimensions, shielding gas composition and pressure [1–14]. Experimental studies of the distributions of electric current density and specific heat flux over the anode surface in [1, 6, 10] were conducted using the method of split water-cooled anode with a plane working surface. A water-cooled anode with a plane surface was also used during spectrometric measurements of arc plasma temperature in [3, 7] and probe measurements of electron temperature and plasma po-

tential in the arc anode region [5]. Theoretical studies and numerical modeling of the processes in the column and anode boundary layer of an arc with a refractory cathode, performed in [2–4, 7–9, 11–14], were conducted with the assumption that the anode surface temperature is not higher than its material melting temperature, and the surface proper is plane. The thus obtained results do not allow fully taking into account the influence of weld pool surface deformation and its temperature on the thermal, gas-dynamic and electromagnetic characteristics of arc plasma, as well as on the processes in the metal being welded by a nonconsumable electrode arc.

Works [15–21] are devoted to studying the influence of the anode surface temperature on the above-mentioned characteristics, in particular on its material evaporation into arc plasma. In the majority of such theoretical works (see, for instance, reviews [17, 18] and references cited in them) the surface of the anode (weld pool) is also considered to be plane, and distribution of this surface temperature either is found by calculation using various models of the processes running in the anode body [15–19], or it is assigned *a priori* [20, 21].

Under the conditions of TIG welding, the pressure of arc plasma on the surface of the material be-

ing welded can considerably (depending on current and arc length) deform the melt surface. In this case, distribution of normal components of electric current density and specific heat flux into the anode, as well as distribution of gas-dynamic pressure of arc plasma along the weld pool surface can differ essentially from those determined during full-scale or numerical experiments for an anode with a plane surface. Eventually, it may lead to a change in the thermal or hydrodynamic situation in liquid metal and, consequently, it can influence the arc penetrability in TIG welding.

The works devoted to modeling the physical processes in welding by a constricted (plasma) arc and free-burning arc, with allowing for deformation of the weld pool free surface, appeared recently [22–24]. In these studies a unified mathematical model is used to describe a set of physical processes running in the arc column and anode region, as well as processes in the metal being welded. Such an approach allowed modeling the process of spot TIG welding at high values of arc current [23], i.e. under the conditions, when weld pool surface deformation turns out to be considerable, and studying the processes of plasma welding in the keyhole penetration mode in spot [22] and linear [24] plasma-arc welding. At the same time, the unified mathematical model used by the authors of [22–24], does not allow fully taking into account the specifics of the anode processes, which in the abovementioned works, were described using a diffusion approximation for the anode boundary layer plasma, which is assumed to be isothermal (local-thermal-equilibrium approximation) [25].

Thus, this work is devoted to computer modeling of the processes of transfer of energy, momentum, mass and charge in the plasma of the arc column and anode region of atmospheric pressure argon arc with a refractory cathode and an anode with a curved surface, based on a self-consistent mathematical model, which was proposed in [11, 12], used and verified in [13]. A computational experiment is used to study both the distributed characteristics of arc plasma, and the conditions of its interaction with the curved surface of the anode.

## CONDITIONS OF COMPUTATIONAL EXPERIMENT

The most adequate description of the process of TIG welding allowing for deformation of the weld pool surface, should be based on a conjugated model, which describes the thermal, electromagnetic and gas/hydrodynamic processes in “arc plasma–anode boundary layer–metal being welded” system. Computer realization of such a model involves considerable difficulties, and it requires significant computing

resources. In this work an approximate approach is used to study the influence of weld pool surface deformation on the conditions of burning of an argon arc with a refractory cathode. This approach is based on the following postulates:

1. The deformed surface of the weld pool is approximated by axially symmetric depression on the anode surface. The shape of this depression (crater) is assumed to be unchanged in time and *a priori* assigned as a surface of revolution with the generatrix described by the following equation  $z = ar^2$ . In this formula,  $z$  coordinate is calculated from the crater bottom;  $a = L/R^2$ ; where  $L, R$  are the depth and radius of the crater (Figure 1).

2. It is assumed that the processes of transfer of energy, momentum, mass and charge in the arc discharge are stationary, and distributions of arc plasma characteristics are axially symmetric.

3. The processes of energy, momentum, mass and charge transfer in the boundary arc column and anode layer are described using a self-consistent mathematical model [11–13], which includes two interrelated models:

- arc column model, describing the thermal, electromagnetic, and gas-dynamic processes in the arc column plasma, which is assumed to be quasineutral, isothermal and ionisationally equilibrium;
- anode boundary layer model, which describes the processes in near-anode plasma, allowing for its thermal and ionisational non-equilibrium, as well as presence near the anode surface of a space charge layer, and which allows formulation of boundary conditions on the interface of arc column plasma with the anode region and calculation of distributed character-

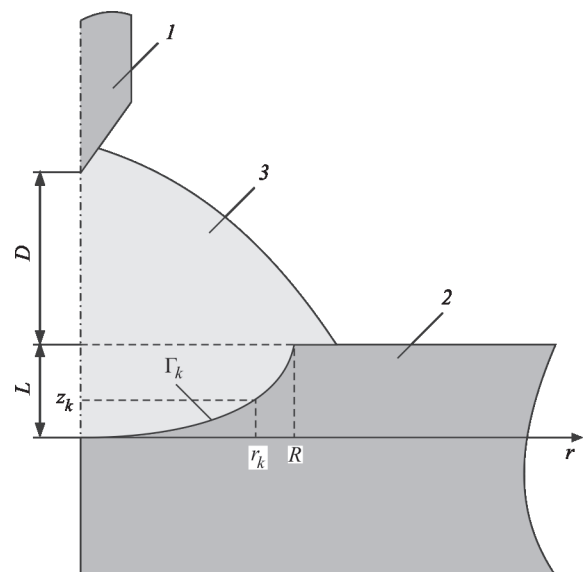
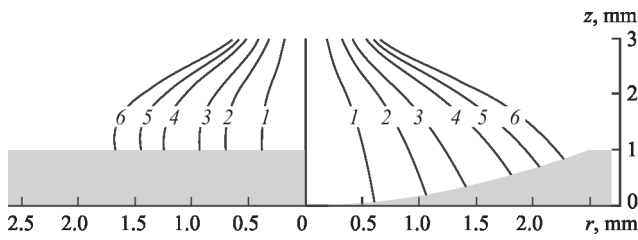


Figure 1. Schematic representation of arc-anode system: 1 — refractory cathode; 2 — anode; 3 — arc



**Figure 2.** Current lines in arc column: 1 —  $i = 10$ ; 2 — 30; 3 — 50; 4 — 80; 5 — 100; 6 — 120 A

istics of thermal, gas-dynamic and electromagnetic interaction of arc plasma with the anode surface.

4. Metal evaporation from the anode surface is not taken into account, which is valid, for instance, for a steel anode, if the maximum temperature of its surface does not exceed 2400 K [20].

Numerical realization of the mathematical model [11, 12] was performed on a rectangular mesh by finite difference method, using a compatible Lagrangian–Eulerian technique [26], adapted to the conditions of a compressive medium. In the mesh area the boundary between the plasma and metal was approximated by a stepped line. An argon arc of length  $D = 2$  mm (distance from the cathode to uncurved surface of the anode, see Figure 1) at current  $I = 200$  A was considered. Calculated data from [27, 28] were used to determine the thermodynamic and transport properties, as well as energy losses for radiation of atmospheric pressure argon plasma, depending on temperature.

During mathematical modeling the distributions of thermal, electromagnetic and gas-dynamic characteristics of plasma in the arc column were calculated, as well as distributed characteristics of arc interaction with anode surface, depending on the depth of the crater on this surface. During performance of calculation experiments  $R = 2.5$  mm was assumed, and  $L$  value was varied in the range of 0–1.4 mm.

### MODELING RESULTS

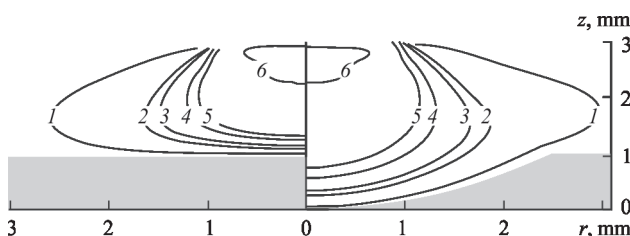
We will select  $L = 1$  mm as a characteristic value of crater depth on the anode surface, and will see how the curvature of the anode surface influences the electromagnetic, thermal and gas-dynamic processes in arc plasma. Figures 2–4 shows the current lines, isotherms and isobars of excess pressure  $\Delta p$  in arc column plasma, calculated for a plane (on the left in the

Figure) and curved (on the right in the Figure) surface of the anode. The current lines are understood to be the generatrices of the surfaces of revolution, which limit the arc plasma regions, through which the set fraction  $i$  of full arc current  $I$  flows.

The curved surface of the anode essentially changes the mode of current passage and the thermal and gas-dynamic situation in the arc column. Surface sagging has the greatest influence on the characteristics of the arc discharge near the anode, and it is still manifested in the middle of the interelectrode gap. In the near-cathode region the arc characteristics differ slightly from the case of an anode with a plane surface. This conclusion, which follows from analysis of the fields in Figures 2–4, is supported by the results of calculation of current density in two cross-sections of the arc column: in the plane of an uncurved surface of the anode (Figure 5, a); and in the plane located above this surface at 0.5 mm distance (Figure 5, b).

We will determine the distributions of normal components of the vectors of electric current density  $j_{an}$  and specific heat flux  $q_{an}$  on the curved surface of the anode, which are required at modeling of the thermal, gas-dynamic and electromagnetic processes in the metal being welded, allowing for deformation of the weld pool free surface. At numerical calculation, the vectors of current density and specific heat flux into the anode along the stepped mesh boundary, which approximates the curved surface of the anode  $\Gamma$ , have components both in the axial and in the radial directions (axial components on the horizontal lines of the mesh, and radial components on the vertical lines). This complicates calculation of the respective vector components, normal to the abovementioned surface.

We will use the following procedure to determine  $j_{an}$  and  $q_{an}$  distributions on the curved surface of the anode. Let  $\Gamma_k$  be a segment of the generatrix of crater surface, which begins from its bottom and ends with a point with coordinates  $\{r_k, z_k\}$  on generatrix  $\Gamma$  of the crater (see Figure 1). We will denote as  $I_a(r_k) = 2\pi \int_{\Delta_k} j_{an}(s)r(s)ds$  the electric current flowing into the plasma through part of the curvilinear surface of the anode with generatrix  $\Gamma_k$  and, accordingly, as  $Q_a(r_k) = 2\pi \int_{\Delta_k} q_{an}(s)r(s)ds$  the heat flux, which enters



**Figure 3.** Temperature field of arc column plasma: 1 —  $T = 13$ ; 2 — 17; 3 — 18; 4 — 20; 5 — 21; 6 — 25 K

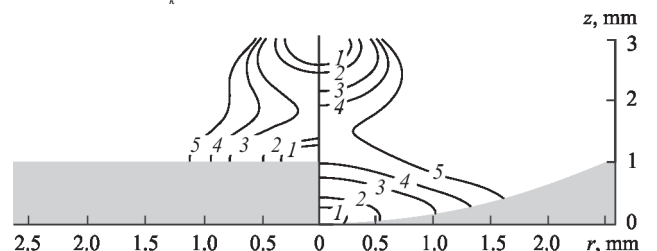


**Figure 4.** Field of isobars of excess pressure in arc column: 1 —  $\Delta p = 800$ ; 2 — 700; 3 — 500; 4 — 400; 5 — 300 Pa

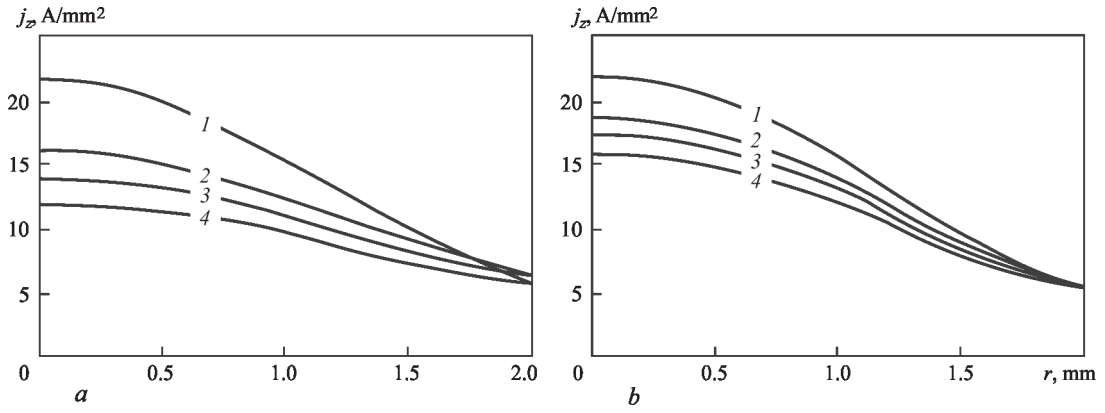


**Figure 5.** Radial distribution of axial component of current density in two cross sections of arc column at different  $L$  values: 1 —  $L = 0$ ; 2 — 0.7; 3 — 1.0; 4 — 1.4 mm

the anode through the abovementioned surface, where  $s$  is the current length of the generatrix  $\Gamma$ .

We will approximately assure:

$$j_{an}(r_k) \approx [(\tilde{I}_a(r_{k+1}) - \tilde{I}_a(r_k))] / S_k; \quad (1)$$

$$q_{an}(r_k) \approx [(\tilde{Q}_a(r_{k+1}) - \tilde{Q}_a(r_k))] / S_k, \quad (2)$$

where  $j_{an}(r_k)$ ,  $q_{an}(r_k)$  are the mean values of normal to the anode curved surface components of current density and specific heat flow in segment  $\Delta\Gamma_k$  of the generatrix between crater sections  $z = z_{k+1}$  and  $z = z_k$ ;  $S_k = 2\pi \oint_{\Delta\Gamma_k} r(s) ds$  is the surface area of the body of

revolution with generatrix  $\Delta\Gamma_k$  and  $\tilde{I}_a(r_k)$  and  $\tilde{Q}_a(r_k)$  are the summing analogs of  $I_a(r_r)$  and  $Q_a(r_r)$  distributions, respectively.

$\tilde{I}_a(r_k)$ ,  $\tilde{Q}_a(r_k)$  were calculated by numerical integration of discrete values of electric current density and specific heat flow along all (both horizontal and vertical) segments of broken mesh boundary  $\Gamma_k$ . Note that at numerical solution of the model equations on a rectangular mesh the mesh values of current and heat flow which are determined along the broken mesh boundary, develop small oscillations. In order to eliminate them, mesh functions  $\tilde{I}_a(r_k)$ ,  $\tilde{Q}_a(r_k)$  in

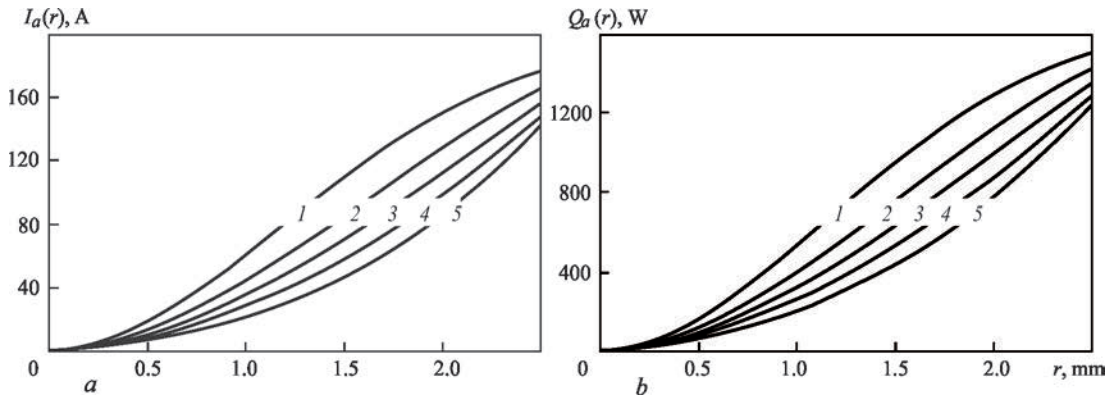


**Figure 6.** Radial distributions of electric current (a) and heat flux through the curved surface of the anode: 1 —  $L = 0$ ; 2 — 0.4; 3 — 0.7; 4 — 1.0; 5 — 1.4 mm

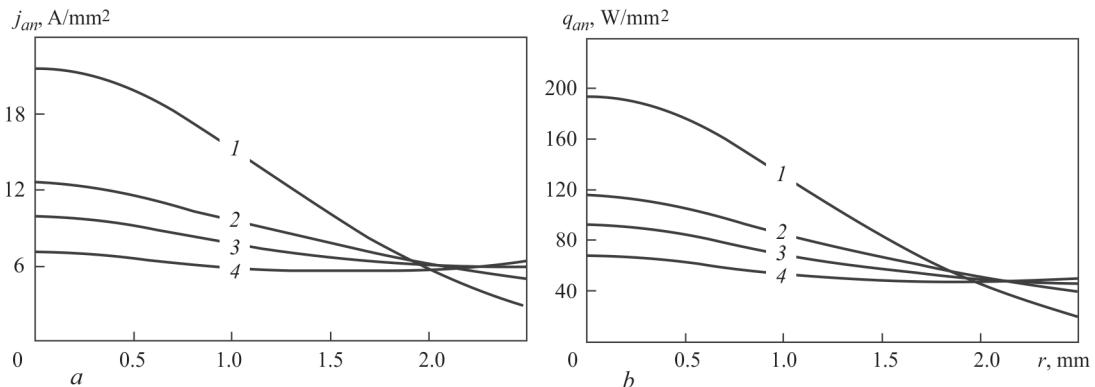


**Figure 7.** Radial distributions of normal components of vectors of current density (a) and specific heat flux (b) on anode surface: 1 —  $L = 0$ ; 2 — 0.7; 3 — 1.0; 4 — 1.4 mm

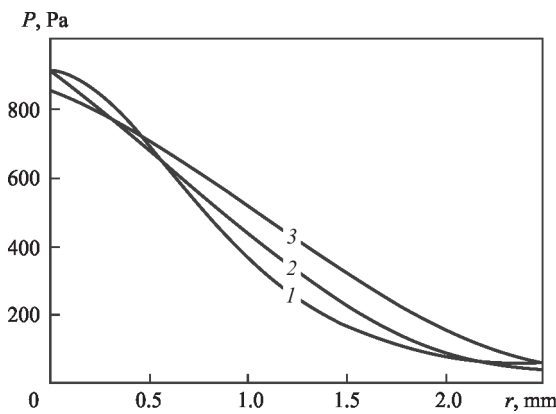


**Figure 8.** Arc plasma pressure on the curved surface of the anode: 1 —  $L = 0$ ; 2 — 0.4; 3 — 1.0 mm

$0 \leq r \leq 2.5$  mm segment are approximated by 3<sup>rd</sup> order polynomials, and the derived interpolation dependencies are used in (1), (2) at calculation of normal components of electric current density and specific heat flux on the curved surface of the anode.

The thus calculated radial distributions of  $I_a(r)$  and  $Q_a(r)$  values in the crater on the anode surface are shown in Figure 6. Respective distributions of  $j_{an}(r)$ ,  $q_{an}(r)$  for an argon arc with a refractory cathode and an anode with a deformed surface are shown in Figure 7.

With greater sagging of the crater, the area of the anode surface interacting with arc plasma becomes greater. As a result, both these parameters, which are responsible for the electric and thermal interaction of the arc with the anode having a curved surface, decrease with increase of this surface sag. The nature of their distribution along the anode surface also changes.

Unlike the density of anode current and specific heat flow into the anode (see Figure 7), pressure distribution along the curved surface of the anode only slightly depends on the value of its surface sagging (Figure 8). It should be noted that the gas-dynamic pressure, calculated by the method of mathematical modeling is excessive, compared to atmospheric pressure, and it includes two components: magnetic pressure and pressure of arc plasma velocity head, which results from the impact of a non-potential component of the Lorentz force [29].

## CONCLUSIONS

In straight polarity TIG welding:

1. Influence of weld pool surface deformation on the thermal, electric and gas-dynamic characteristics of arc plasma is the most pronounced in that part of the arc column, which is removed from the welded metal surface plane to a distance, which is comparable with the value of weld pool sag, and it becomes weaker when moving closer to the cathode.

2. Deformation of weld pool free surface may lead to an essential change of the conditions of thermal,

electric and dynamic interaction of the arc with the metal being welded, compared to the case, when the pool surface is plane. Depending on the value of pool surface sag, the axial values of normal components of electric current density and specific heat flux of the arc on the weld pool surface can decrease two times and more. The pressure, applied by the arc plasma flow to the weld pool surface, little depends on the extent of its surface deformation.

3. Influence of pool surface deformation on the arc penetrability consists not only in the heat source moving deeper into the metal being welded, but also in a radical change of the hydrodynamic flows in the weld pool, compared to those predicted by the models, which ignore the weld pool sagging. At pool surface deformation the characteristics of the electromagnetic field in the metal being welded undergo significant changes. These characteristics determine the value and distribution of the Lorentz force as an important force factor influencing the hydrodynamic processes in the weld pool and convective heat transfer in the molten metal.

## REFERENCES

1. Nestor, O.H. (1962) Heat intensity and current density distributions at the anode of high current, inert gas arcs. *J. Appl. Phys.*, 33(5), 1638–1648. DOI: <https://doi.org/10.1063/1.1728803>
2. Dinulescu, H.A., Pfender, E. (1980) Analysis of the anode boundary layer of high intensity arcs. *J. Appl. Phys.*, 51(6), 3149–3157. DOI: <https://doi.org/10.1063/1.328063>
3. Hsu, K.C., Etemadi, K., Pfender, E. (1983) Study of the free-burning high-intensity argon arc. *J. Appl. Phys.*, 54(3), 1293–1301. DOI: <https://doi.org/10.1063/1.332195>
4. Hsu, K.C., Pfender, E. (1983) Two-temperature modeling of the free-burning high-intensity arc. *J. Appl. Phys.*, 54(8), 4359–4366. DOI: <https://doi.org/10.1063/1.332672>
5. Sanders, N.A., Pfender, E. (1984) Measurement of anode falls and anode heat transfer in atmospheric pressure high intensity arcs. *J. Appl. Phys.*, 55(3), 714–722. DOI: <https://doi.org/10.1063/1.333129>
6. Tsai, N.S., Eagar, T.W. (1985) Distribution of the heat and current fluxes in gas tungsten arcs. *Metall. Transact. B*, 16, 841–846. DOI: <https://doi.org/10.1007/BF02667521>
7. Schmidt, H.P., Speckhofer, G. (1996) Experimental and theoretical investigation of high-pressure arcs. Pt I: The cylindrical arc column (two-dimensional modelling). *IEEE Transact. Plasma Sci.*, 24(4), 1229–1238. DOI: <https://doi.org/10.1109/27.536570>
8. Jenista, J., Heberlein, J.V.R. Pfender, E. (1997) Numerical model of the anode region of high-current electric arcs. *IEEE Transact. Plasma Sci.*, 25(5), 883–890. DOI: <https://doi.org/10.1109/27.649585>
9. Goodarzi, M., Choo, R., Toguri, J.M. (1997) The effect of the cathode tip angle on the GTAW arc and weld pool: I. Mathematical model of the arc. *J. Phys. D: Appl. Phys.*, 30, 2744–2756. DOI: <https://doi.org/10.1088/0022-3727/30/19/013>
10. Füssel, U., Schnick, M., Munoz, J.E.F. et al. (2007) Experimentelle möglichkeiten der WSG-lichtbogenanalyse. *Schweißen und Schneiden*, 59(7–8), 396–403.
11. Krivtsun, I., Demchenko, V., Lesnoi, A. et al. (2009) Model of heat-, mass- and charge-transfer in welding arc column and

- anode region. In: *Proc. of the 9<sup>th</sup> Int. Seminar on Numerical Analysis of Weldability, Graz-Seggau, Austria, 2009*.
12. Krivtsun, I.V., Demchenko, V.F., Krikent, I.V. (2010) Model of the processes of heat-, mass- and charge transfer in the anode region and column of the welding arc with refractory cathode. *The Paton Welding J.*, **6**, 2–9.
  13. Krivtsun, I.V., Krikent, I.V., Demchenko, V.F. (2012) Modelling of processes of heat-, mass- and electric transfer in column and anode region of arc with refractory cathode. *The Paton Welding J.*, **3**, 2–6.
  14. Semenov, I.L., Krivtsun, I.V., Reisgen, U. (2016) Numerical study of the anode boundary layer in atmospheric pressure arc discharges. *J. Phys. D: Appl. Phys.*, **49**, 105204. DOI: <https://doi.org/10.1088/0022-3727/49/10/105204>
  15. Lago, F., Gonzalez, J.J., Freton, P., Gleizes, A. (2004) A numerical modelling of an electric arc and its interaction with the anode: Pt. I: The two-dimensional model. *J. Phys. D: Appl. Phys.*, **37**, 883–897. DOI: <https://doi.org/10.1088/0022-3727/37/6/013>
  16. Yamamoto, K., Tanaka, M., Tashiro, S. et al. (2008) Metal vapour behaviour in gas tungsten arc thermal plasma during welding. *Sci. Technol. of Weld. Joining*, **13**(6), 566–572. DOI: <https://doi.org/10.1179/174329308X319235>
  17. Murphy, A.B., Tanaka, M., Yamamoto, K. et al. (2009) Modelling of thermal plasmas for arc welding: the role of the shielding gas properties and of metal vapour. *J. Phys. D: Appl. Phys.*, **42**, 194006. DOI: <https://doi.org/10.1088/0022-3727/42/19/194006>
  18. Murphy, A.B. (2010) The effect of metal vapour in arc welding. *J. Phys. D: Appl. Phys.*, **43**, 434001. DOI: <https://doi.org/10.1088/0022-3727/43/43/434001>
  19. Mougnot, J., Gonzalez, J.J., Freton, P., Masquere, M. (2013) Plasma-weld pool interaction in tungsten inert-gas configuration. *J. Phys. D: Appl. Phys.*, **46**, 135206. DOI: <https://doi.org/10.1088/0022-3727/46/13/135206>
  20. Krikent, I.V., Krivtsun, I.V., Demchenko, V.F. (2014) Simulation of electric arc with refractory cathode and evaporating anode. *The Paton Welding J.*, **9**, 17–24. DOI: <https://doi.org/10.15407/tpwj2014.09.02>
  21. Krivtsun, I.V., Demchenko, V.F., Krikent, I.V. et al. (2019) Effect of current and arc length on characteristics of arc discharge in nonconsumable electrode welding. *The Paton Welding J.*, **5**, 2–12. DOI: <https://doi.org/10.15407/tpwj2019.05.01>
  22. Jian, X., Wu, C.S. (2015) Numerical analysis of the coupled arc-weld pool-keyhole behaviors in stationary plasma welding. *Int. J. Heat Mass Transfer*, **84**, 839–847. DOI: <https://doi.org/10.1016/j.ijheatmasstransfer.2015.01.069>
  23. Wang, X., Luo, Y., Fan, D. (2019) Investigation of heat and fluid flow in high current GTA welding by a unified model. *Int. J. Therm. Sci.*, **142**, 20–29. DOI: <https://doi.org/10.1016/j.ijthermalsci.2019.04.005>
  24. Li, Y., Su, Ch., Wang, L., Wu Ch. (2020) A convenient unified model to display the mobile keyhole-mode arc welding process. *Appl. Sci.*, **10**, 7955. DOI: <https://doi.org/10.3390/app10227955>
  25. Lowke, J.J., Tanaka, M. (2006) LTE-diffusion approximation for arc calculations. *J. Phys. D: Appl. Phys.*, **39**, 3634–3643. DOI: <https://doi.org/10.1088/0022-3727/39/16/017>
  26. Demchenko, V., Lesnoi, A. (2000) Lagrange-Euler method of numerical solutions of multidimensional problems of convective diffusion. *Reports of the National Academy of Sciences of Ukraine*, **11**, 71–75 [in Russian].
  27. Cressault, Y., Murphy, A.B., Teulet, Ph. et al. (2013) Thermal plasma properties for Ar–Cu, Ar–Fe and Ar–Al mixtures used in welding plasma processes: II. Transport coefficients at atmospheric pressure. *J. Phys. D: Appl. Phys.*, **46**, 415207. DOI: <https://doi.org/10.1088/0022-3727/46/41/415207>
  28. Essoltani, A., Proulx, P., Boulos, M.I. et al. (1994) Volumetric emission of argon plasmas in the presence of vapours of Fe, Si and Al. *Plasma Chem. and Plasma Proc.*, **14**(4), 437–450. DOI: <https://doi.org/10.1007/BF01570206>
  29. Demchenko, V.F., Krivtsun, I.V., Krikent, I.V., Shuba, I.V. (2017) Force interaction of arc current with self-magnetic field. *The Paton Welding J.*, **3**, 15–24. DOI: <https://doi.org/10.15407/tpwj2017.03.03>

**ORCID**

I.V. Krivtsun: 0000-0001-9818-3383,  
I.V. Krikent: 0000-0002-4196-6800

**CONFLICT OF INTEREST**

The Authors declare no conflict of interest

**CORRESPONDING AUTHOR**

I.V. Krivtsun  
E.O. Paton Electric Welding Institute of the NASU  
11 Kazymyr Malevych Str., 03150, Kyiv, Ukraine.  
E-mail: [krivtsun@paton.kiev.ua](mailto:krivtsun@paton.kiev.ua)

**SUGGESTED CITATION**

I.V. Krivtsun, I.V. Krikent, V.F. Demchenko (2023) Influence of weld pool surface depression on burning conditions of an arc with a refractory cathode. *The Paton Welding J.*, **8**, 44–49.

**JOURNAL HOME PAGE**

<https://patonpublishinghouse.com/eng/journals/tpwj>

Received: 24.06.2023

Accepted: 07.08.2023



Electron beam unit UE-5812

**DEVELOPED IN PWI**

PRODUCTION  
OF TITANIUM ALLOY  
INGOTS  
AT "TITAN" CENTRE

All-purpose electron beam unit  
UE-5810



DOI: <https://doi.org/10.37434/tpwj2023.08.06>

# MODERN TECHNOLOGIES OF ELECTROPHYSICAL TREATMENT FOR REGULATION OF STRESS-STRAIN STATES OF ELEMENTS OF WELDED STRUCTURES

**L. Lobanov, M. Pashchyn, O. Mikhodui**

E.O. Paton Electric Welding Institute of the NASU  
11 Kazymyr Malevych Str., 03150, Kyiv, Ukraine

## ABSTRACT

The development of industry stimulates the development of modern approaches to the optimization of welded structures. The use of pulsed electromagnetic fields, plasma currents, electrodynamic forces and their combined effects is a new trend in engineering practice. Treatment with a pulsed electromagnetic field (TPEMF) is a promising direction for optimizing the stress-strain states (SSS) of welded joints (WJ) made of non-ferromagnetic metal materials. Using the method of electron speckle interferometry, the effect of TPEMF on the SSS of samples of circumferential WJ with a thickness of  $\delta = 1.0$  mm from aluminium alloy AMg6 was investigated. The kinetics of the action of the force  $P$  of the magnetic field pressure on the residual displacements  $f$  and SSS of the samples during their TPEMF were investigated. TPEMF of WJ samples was performed without and with the use of an additional screen ( $\delta = 5.0$  mm) contributes to the reduction of  $f$  values by 2 and 4 times, respectively, and residual SSS by 50 and 80 %. The advantages of using electrodynamic treatment (EDT) of butt 3.0 mm alloy AMg61 (1561) in the TIG welding process are substantiated. It was proved that EDT during TIG contributes to the formation of peak values of residual compressive stresses in the weld zone by 60 % more than EDT during room temperature ( $T_k$ ). The use of a pulsed barrier discharge (PBD), which generates a low-temperature plasma on the surface of the metal, contributes to the optimization of its structure. An increase in the hardness of  $HV$  structural steel 25KhGNMT as a result of its PBD treatment from 420 to 510 units was established.

**KEYWORDS:** treatment of welded joints, pulsed magnetic field, pulsed barrier discharge; electrodynamic treatment, aluminium alloy, structural steel, residual displacements, stress-strain state, hardness of steel

## INTRODUCTION

The development of modern industry requires the study of progressive energy-saving technologies to improve the service properties of metal structures. In this regard, the development of methods of treatment of metal materials and welded joints based on the effect of a pulsed electromagnetic field is challenging. These include electrodynamic treatment (EDT), treatment with a direct action (pressure) of a pulsed electromagnetic field (TPEMF) and a pulsed barrier discharge (PBD) [1–6]. Based on EDT and TPEMF, technologies for control of the stress-strain state of thin-sheet welded joints are developed. Taking into account the results [1], a promising technology of EDT in the process of welding has been developed, which provides the following advantages over EDT after welding:

- effect of the thermal cycle of welding contributes to more intensive relaxation of welding stresses as a result of EDT compared to treatment of weld metal at room temperature;
- reduction in the labour intensity of manufacturing welded structure due to the transition from successive to simultaneous performance of technological operations of welding and EDT. The use of PBD

opens up new opportunities to improve the hardness of structural steels for special equipment.

## AIM OF THE WORK

Is the study of TPEMF, EDT and PBD effect on residual stresses and mechanical characteristics of metal materials and welded joints.

## RESEARCH PROCEDURE AND MATERIALS

Electrophysical models, which form the basis of the action of TPEMF, EDT and PBD on metals, alloys and welded joints, are presented respectively in [4], [1] and [6]. Electrophysical characteristics of electrode systems and power sources for TPEMF, EDT and PBD are presented, respectively, in [2, 4, 5], [1, 3] and [6].

As a tool for TPEMF realization, a plane inductor (Figure 1, a) was used, and to evaluate the efficiency of treatment, plane specimens of AMg6 aluminium alloy in the form of a disc were used, whose thickness and diameter were respectively  $\delta = 1.0$  mm and  $D_{sp} = 90$  mm (Figure 1, b). During treatment, a current-conducting shield in the form of a disc from AMg6 alloy was used, its diameter and thickness were respectively 90 and 5.0 mm (Figure 1, c). Circumferential welds were produced by TIG method in Ar environment along the line of the circle with a diameter

Copyright © The Author(s)

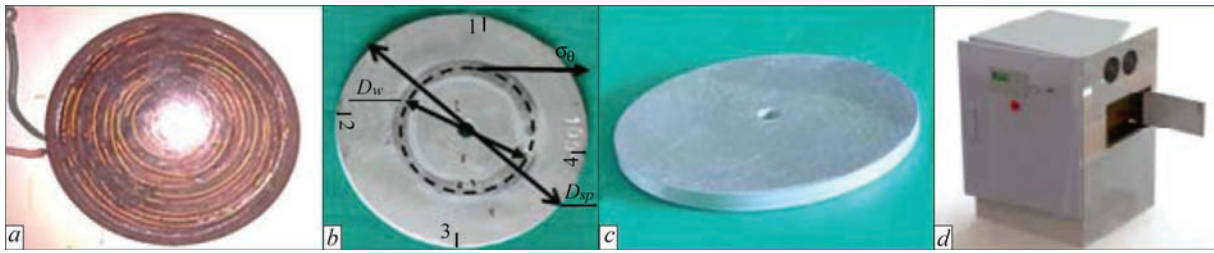


**Figure 1.** Appearance: *a* — plane inductor; *b* — specimen of circumferential welded joint of AMg6 alloy with a thickness  $\delta = 1.0$  mm, where  $D_{sp} = 90$  mm and  $D_w = 45$  mm are respectively the diameters of the specimen and the weld,  $\sigma_\theta$  is the component of residual stresses; *c* — current-conducting shield with a diameter of 90 mm and a thickness of 5 mm; *d* — PS for TPEMF

$D_w = 45$  mm. A tangent component  $\sigma_\phi$  (Figure 1, *b*) of residual stressed state of welded joints and vertical movements *f* of the discs' edges before and after TPEMF were evaluated by the method of electron and speckle-interferometry.

To realize the discharge cycles of TPEMF, the power source (PS) was used based on a capacitor system with a charging voltage  $U$  of up to 800 V and pulsed current amplitude of up to 10 kA (Figure 1, *d*). PS can perform TPEMF in an automatic mode with 1–5 s time periods between the pulses. The registration of time distributions of the pulsed current  $I$  and the power of electrodynamic pressure  $P$  at TPEMF of the specimens without and with the use of a shield was performed using a non-inductive shunt and an accelerometer Kistler Instrumente AG, respectively [7]. TPEMF was performed on the specimens with the thickness  $\delta = 1.0$  mm and on the assembly of the specimen  $\delta = 1.0$  mm with a current-conducting shield  $\delta = 5.0$  mm ( $\Sigma\delta = 6$  mm). Treatment was carried out by the series of EPC on the mode at a charging voltage  $U$  of up to 800 V. Residual stressed states of welded joints were studied using the electron and speckle-interferometry method [1].

The hardware complex for automatic welding of aluminium alloys in the EDT process has been developed and manufactured (Figure 2). The complex includes system for feeding filler wire 1, torch 2 for



**Figure 2.** Hardware complex for automatic TIG welding, which is compatible with EDT of a weld, where 1 — system for feeding filler wire; 2 — welding torch; 3 — electrode device; 4 — linear solenoid for movement of EDT electrode

TIG welding, electrode device for EDT 3 and linear solenoid for movement 4 of electrode for EDT. The components of the complex are structurally combined into a monoblock.

Mathematical modeling of stress-strain states of welded joints as a result of EDT was performed in the conditions of elevated temperatures (in the process of welding), with the use of a simplified two-dimensional (2D) planar formulation. The design diagram of the problem of the process of impact interaction of the electrode-indenter with plates [8] is presented in Figure 3. The solution of the problem was performed using ANSYS/LS-DYNA software.

PBD treatment of the surface of specimens of 25KhGNMT steel was performed using an electrode system (ES), the structural diagram of which is shown in Figure 4.

The diagram of the electrode system (ES) for PBD treatment is shown in Figure 4, *a*. ES consisted of studied specimen 1 of 25KhGNMT steel, high-voltage electrode 2 and glass (quartz glass) dielectric barrier 3 ( $100 \times 100 \times 1$  mm<sup>3</sup>). To reduce the edge effect, electrode 2 had rounded edges. The treatment was carried out at a gas gap  $\delta$  of 1 mm thickness between plate 1 and barrier 3. High voltage (HV) was supplied to electrode 2 from the pulse generator (PG), which provided unipolar pulses of a voltage with an amplitude of up to 30 kV at their rising rate  $\approx 3 \cdot 10^{11}$  V/s and a duration of about 150 ns. The appearance of the dis-

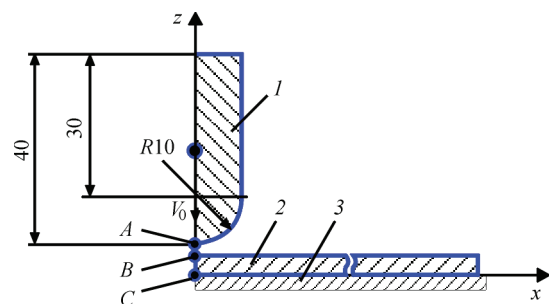


**Figure 3.** Design diagram of the process of dynamic loading of a plate at EDT: 1 — electrode-indenter; 2 — specimen being treated; 3 — absolutely rigid base, *A* — point on the outer surface of the electrode-indenter; *B* — point on the outer surface of a plate; *C* — point on the back surface of a plate;  $V_0$  — speed of movement of the electrode-indenter

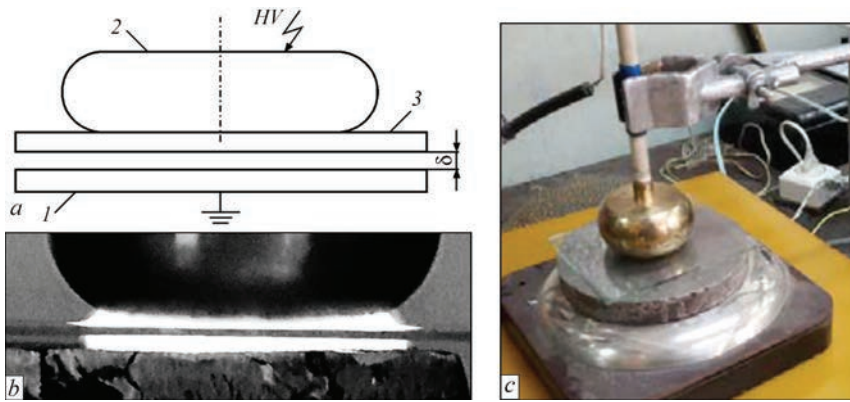


**Figure 4.** PBD treatment of 25KhGNMT steel, where: *a* — diagram of electrode system for PBD treatment of specimens of 25KhGNMT steel, where *l* — studied specimen 1 of 25KhGNMT steel; 2 — high-voltage electrode; 3 — dielectric barrier;  $\delta$  — gas gap; *HV* — high voltage; *b* — appearance of PBD; *c* — appearance of PBD treatment process of 25KhGNMT steel

charge, shown in Figure 4, *b* (exposure time is 0.1 s) indicates a homogeneous nature in the gap  $\delta$  rather than thredlike.

**DISCUSSION OF RESEARCH RESULTS**

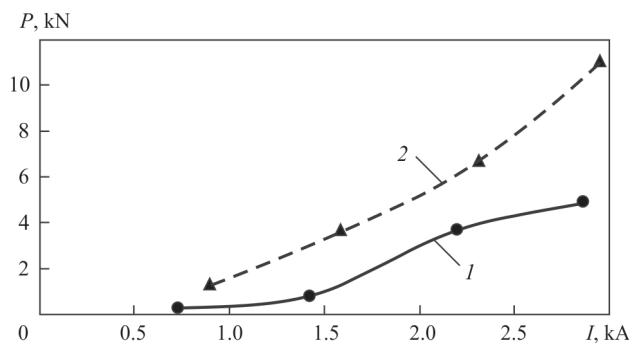
Dependence of pressure force *P* at TPEMF on current *I* for different thickness  $\delta$  of the specimens is shown in Figure 5. Based on its data, in the studied range of treatment modes, it is possible to see that with an increase in  $\delta$ , *P* will grow, because it is defined as an integral value in a certain volume of a current-conductive medium. At an increase in  $\delta$  to 6.0 mm as a result of using a shield (curve 2), the values *P* rise twice compared to TPEMF of the specimens  $\delta = 1.0$  mm without a shield (curve 1).

The efficiency of TPEMF effect on the residual forming of the specimens treated under the above-mentioned conditions confirm the data given in Figure 4, *a-c*. The values of vertical movements of the discs' edges *f* (Figure 6, *a*) were recorded at the points Nos 1–4 (Figure 6, *c*) with a fixed angular distance  $l_\alpha$  of 90° between the adjacent points. Performance of TPEMF without a shield (Figure 6, *d*, curve 2) and with its use (curve 3) allows reducing the values of movements *f* of the discs' edges relatively by up to

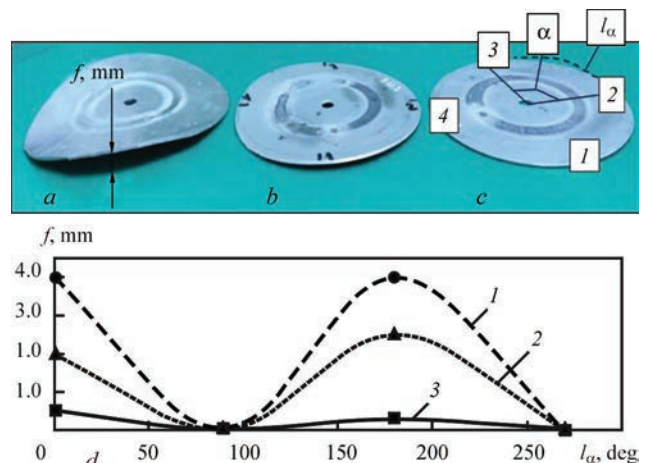
two or eight times compared to the specimens that were not subjected to TPEMF.

Figure 7 shows the results of TPEMF effect on the component  $\sigma_\theta$  of residual stresses in the centre of the weld (W) and in the area near weld zone (NWZ) at a distance of 10 mm from the weld line. Taking into account the bending of the discs (Figure 6), which results in the imbalance of the diagrams of residual stresses, as an evaluation of TPEMF effect on the stressed state, the peak values  $\sigma_\theta$  were determined in W and in NWZ in the specimens in the initial state and under the set treatment conditions. It is possible to see that in general TPEMF has a positive effect on the residual stressed state of the circumferential welded joints of AMg6 alloy with a thickness  $\delta = 1$  mm.

Though initial (before TPEMF) values  $\sigma_\theta$  during treatment without a shield (*a*) and with a shield (*c*) differ, which is associated with a low rigidity of the



**Figure 5.** Influence of amplitude EPC values — *I* on pressure force *P* at TPEMF of specimens of circumferential welded joints  $\delta = 1.0$  mm of AMg6 alloy; curve 1 — TPEMF without a shield; curve 2 — TPEMF with a shield



**Figure 6.** Residual forming of circumferential welded joints of AMg6 alloy, where: *a* — appearance (*A*) of the disc without treatment, where *f* is the movement of the disc's edges; *b* — *A* after TPEMF without a shield; *c* — *A* after TPEMF with a shield, where 1–4 is the number of point of movement measurement,  $\alpha$  and  $l_\alpha$  are respectively the angle and angular distance between the points 2–3; *d* — vertical movements *f* of the disc's edges, where curve 1 — without TPEMF; 2 — after TPEMF without a shield; 3 — after TPEMF with the use of a shield

discs, it can be seen that the use of a shield has a positive effect on relaxation of stresses in TPMEF. This is confirmed by comparing the diagrams between each other (*a*–*b*) and (*c*–*d*). Thus, the treatment without and with the use of a shield led to a decrease in the initial values  $\sigma_0$  in the active zone of tension (W) respectively by 36 and 56 %, and in the zone of reactive compression (NWZ) — by 50 and 80 %.

The results of mathematical modeling are shown in Figure 8, from which it can be seen that EDT in the conditions of heating the plate from AMg61 alloy to the temperature  $T = 150\text{ }^\circ\text{C}$  (thermoelasticity), provides larger values of longitudinal (along the axis  $X$  in Figure 3) compression  $\sigma_x$  stresses, than at  $T = 20\text{ }^\circ\text{C}$  (room) and at  $T = 300\text{ }^\circ\text{C}$  (thermoelasticity). This allows choosing the distance between welding torch 2 and electrode 3 for EDT (Figure 2) that provides the optimum level of residual compression  $\sigma_x$  in the weld joint.

Verification of modeling results was carried out on the specimens of butt joints from AMg61 alloy with the sizes of  $300 \times 200 \times 3\text{ mm}$  (Figure 9), where the Specimen No. 1 was not subjected to EDT, the Specimen No. 2 was subjected to EDT at  $T = 20\text{ }^\circ\text{C}$  and the Specimen No. 3 was subjected to EDT at  $T = 150\text{ }^\circ\text{C}$ . The values of residual longitudinal deflections  $f_x$  of the specimens and residual  $\sigma_x$  confirm both the efficiency of EDT, as well as its growth in the conditions of thermal deformation welding cycle. In the Specimen No. 2, the values  $f_x$  are reduced by 1.8 times compared to the Specimen No. 1, and in the Specimen No. 3 — by 3.7 (Figure 9, *a*). The values of the membrane tensile  $\sigma_x$  (curve 2 in Figure 9, *b*–*d*) in the weld centre on the Specimen No. 2 compared to the Specimen No. 1 are reduced by 95 % (Figure 9, *c*), and in the Specimen No. 3 they are transformed into compression and amount to about  $0.3\sigma_{0.2}$  for AMg61 alloy (Figure 9, *d*).

It was found that the maximum effect of PBD on the hardness of 25KhGNMT steel is achieved when duration of the specimens treatment is 15 minutes (at the optimal mode). In this case, the values of  $HV$  hardness after the treatment increase by 20 % from 420 to 505  $\text{kg/mm}^2$  (Figure 10, *a*). In depth from the treated surface (from 0 to 2200  $\mu\text{m}$ ) in the cross-section of the specimen, the changes in structural and phase composition, parameters of thin structure and dislocations density were revealed. In depth from the treated surface to 300  $\mu\text{m}$ , exclusively the structure of tempered martensite and lower bainite is formed during its refinement and a uniform distribution of dislocations density  $\rho = (2\text{--}8) \cdot 10^{10}\text{ cm}^{-2}$  (Figure 10, *b*). The obtained results indicate that PBD facilitates an improvement in the dynamic strength of welded

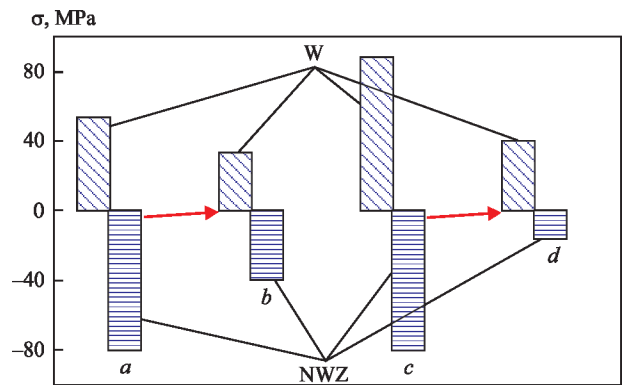


**Figure 7.** Influence of TPMEF on the component  $\sigma_0$  of residual stresses in the welds (W) and in the NWZ of circumferential welded joints of the specimens of AMg6 alloy with a thickness  $\delta = 1\text{ mm}$ : *a* — peak values  $\sigma_0$  of the specimens in the initial state; *b* —  $\sigma_0$  after TPMEF without the use of a shield; *c* —  $\sigma_0$  specimens in the initial state; *d* —  $\sigma_0$  after TPMEF with the use of a shield

structures of the mentioned steel during their contact interactions.

Analyzing the abovementioned results, it should be noted that TPMEF, EDT in the process of welding and local PBD treatment of metals, alloys and welded joints is the basis for the development of a number of

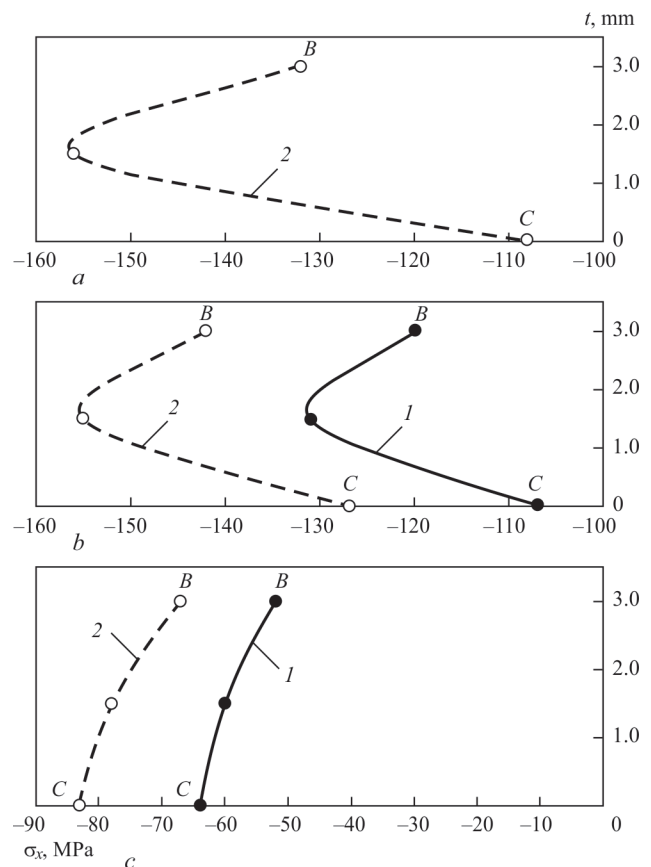


**Figure 8.** Results of modeling stresses  $\sigma_x$  along the line between the points B and C (Figure 3) of the plates of AMg61 alloy  $\delta = 3\text{ mm}$  after EDT at the temperature  $T$  and cooling to  $T = 20\text{ }^\circ\text{C}$ , where curve 1 —  $\sigma_x$  (instant) at the moment of completion of contact interaction at elevated temperatures; curve 2 —  $\sigma_x$  at room temperature: *a* —  $T = 20\text{ }^\circ\text{C}$ ; *b* —  $T = 150\text{ }^\circ\text{C}$ ; *c* —  $T = 300\text{ }^\circ\text{C}$

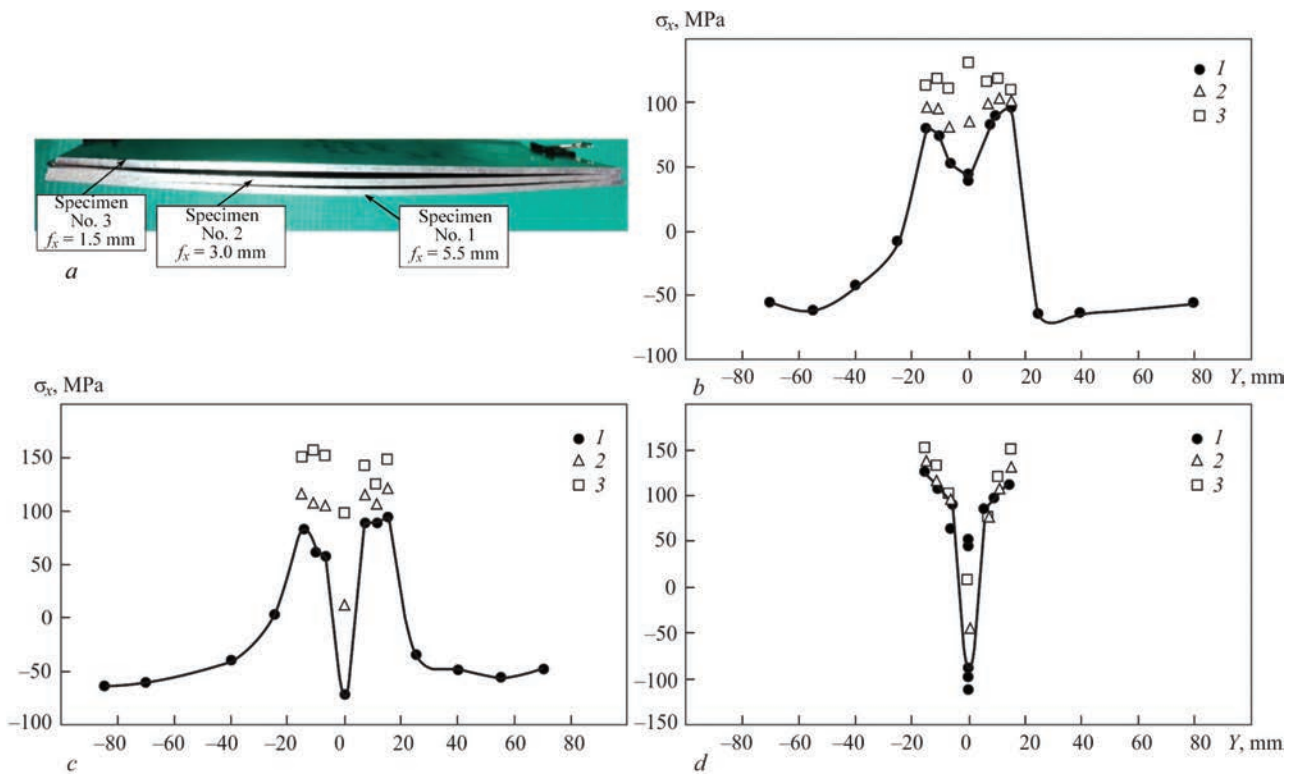


**Figure 9.** Longitudinal deflections  $f_x$  and residual stresses  $\sigma_x$  of the specimens of welded joints of AMg61 alloy of  $\delta = 3$  mm, where the Specimen No. 1 — no EDT, Specimen No. 2 — EDT at  $T = 20$  °C, Specimen No. 3 — EDT at  $T = 150$  °C: *a* — appearance and values of  $f_x$  of the Specimens Nos 1–3; *b* — distribution of  $\sigma_x$  at the central cross-section of the Specimen No. 1, where curve 1 — top (●) surface of the point B in Figure 3, curve 2 — membrane stresses; 3 — bottom (□) surface of the point B in Figure 3; *c* — similarly to (b) for the Specimen No. 2; *d* — similarly to (b) for the Specimen No. 3

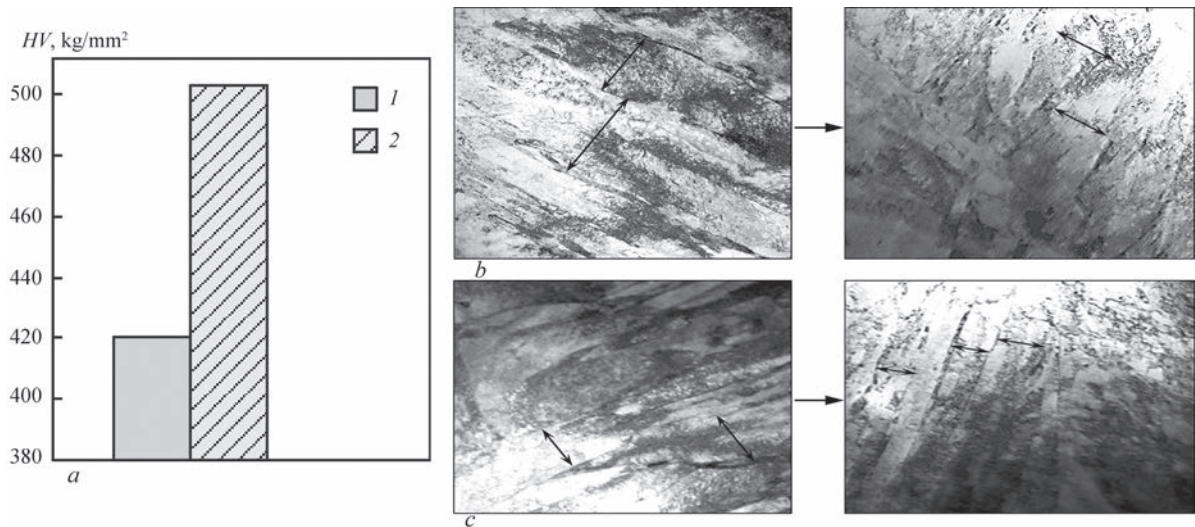


**Figure 10.** Influence of PBD treatment on the structure of 25KhGNMT steel: *a* — values of Vickers hardness ( $HV$ ) before and after PBD treatment; thin structure before and after PBD treatment; *b* — tempered martensite ( $M_{temp}$ ) before and after PBD treatment; *c* — lower bainite ( $B_l$ ) before and after PBD

technologies aimed at optimizing welded structures of new equipment.

### CONCLUSIONS

1. It was found that treatment with a pulsed electromagnetic field (TPEMF) allows reducing residual displacements and stresses of the specimens of circumferential welded joints from AMg6 alloy by up to eight times compared to untreated ones.

2. On the basis of mathematical modeling and experimental studies, it was proved that the use of electrodynamic treatment (EDT) of weld metal, which is performed in a single process synchronously with arc welding is more effective compared to separate EDT after welding, which is expressed in a more optimal residual stress-strain state of a finished welded joint of the aluminium AMg61 alloy.

3. It was found that as a result of treatment of 25KhGNMT steel with a pulsed barrier discharge (PBD), its Vickers hardness ( $HV$ ) is increased by 20 % — from 420 to 505 kg/mm<sup>2</sup>, which spreads to a depth of up to 2 mm and is accompanied by dispersion of the treated structure.

**REFERENCE**

1. Lobanov, L., Kondratenko, I., Zhiltsov, A. et al. (2018) Development of post-weld electrodynamic treatment using electric current pulses for control of stress-strain states and improvement of life of welded structures. *Mater. Performance and Charact.*, 7(4), 941–955. DOI: <https://doi.org/10.1520/MPC20170092>
2. Dubodelov, V.I., Goruk, M.S. (2018) The use of electromagnetic fields and magnetodynamic phenomena to intensify the effect on metal systems. World and Ukrainian experience. *Materials Science: Achievements and Prospects*, Vol. 2, Kyiv, Akadempriodyka, 24–50 [in Ukrainian].
3. Zhang, Jun, Liu, Ji-De, Zhang, Xin-Fang et al (2021) Effect of high density current pulses on microstructure and mechanical properties of dual-phase wrought superalloy. *Acta Metallurgica Sinica*, 34(12), 1635–1644. DOI: <https://doi.org/10.1007/s40195-021-01211-7>
4. Qin, Shuyang, Zhang, Xinfang (2022) Ultrafast regulation of nano-scale matrix defects using electrical property discrepancies to delay material embrittlement. *J. of Mater. Sci. and Technol.*, 119, 25–3620. DOI: <https://doi.org/10.1016/j.jmst.2021.11.070>
5. Guo, J.D., Wang, X.L., Dai, W.B. (2015) Microstructure evolution in metals induced by high density electric current

pulses. *Mater. Sci. and Technol.*, 31 (13a), 1545–1554. DOI: <https://doi.org/10.1179/1743284715Y.0000000001>

6. Zhang, Xinfang, Qin, Rongshan (2018) Exploring the particle reconfiguration in the metallic materials under the pulsed electric current. *Steel Research Intern. Open Access*, 89(12) Article number 1800062. DOI: <https://doi.org/10.1002/srin.201800062>
7. *Quartz Accelerometer 8042*. Kistler Instrumente AG. <https://www.datasheetarchive.com/kistler-datasheet.html>

**ORCID**

L.M. Lobanov: 0000-0001-9296-2335,  
M.O. Pashchyn: 0000-0002-2201-5137,  
O.L. Mikhodui: 0000-0001-6660-7540

**CONFLICT OF INTEREST**

The Authors declare no conflict of interest

**CORRESPONDING AUTHOR**

M. Pashchyn  
E.O. Paton Electric Welding Institute of the NASU  
11 Kazymyr Malevych Str., 03150, Kyiv, Ukraine.  
E-mail: [svarka2000@ukr.net](mailto:svarka2000@ukr.net)

**SUGGESTED CITATION**

L. Lobanov, M. Pashchyn, O. Mikhodui (2023) Modern technologies of electrophysical treatment for regulation of stress-strain states of elements of welded structures. *The Paton Welding J.*, 8, 50–55.

**JOURNAL HOME PAGE**

<https://patonpublishinghouse.com/eng/journals/tpwj>

Received: 16.05.2023  
Accepted: 07.08.2023

**SUPERHARD FUSED SPHERICAL TUNGSTEN CARBIDES**

**DEVELOPED IN PWI**



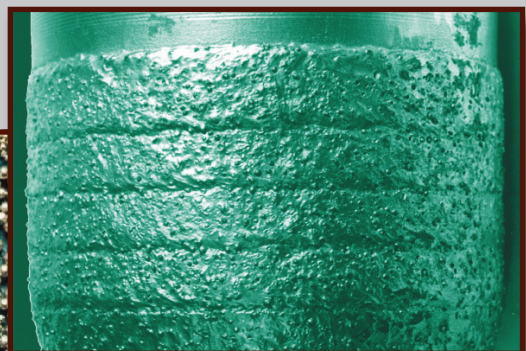
Drill pipe tool joint coated with spherical tungsten carbide



“Sfera-2500” machine for thermal centrifugal spraying



Appearance of spherical tungsten carbides



- Particle size, mm — 0.15–1.10
- Hardness,  $HV_{-0.1}$  — > 3000

Characteristic wear of drill bit teeth clad with tungsten carbide

DOI: <https://doi.org/10.37434/tpwj2023.08.07>

# INFLUENCE OF A STOP IN THE PROCESS OF MELTING ON MECHANICAL PROPERTIES OF SPECIMENS FROM THE Co–Cr–Mo ALLOY MADE BY SLM TECHNOLOGY

S.V. Adzhamskiy<sup>1,2</sup>, G.A. Kononenko<sup>1,3</sup>, R.V. Podolskiy<sup>1,3,4</sup>

<sup>1</sup>LLC “Additive Laser Technologies of Ukraine”

31 v Serhiy Podolynskiy Str., 49000, Dnipro, Ukraine

<sup>2</sup>Institute of Transport Systems and Technologies of NASU

5 Pisarzhevsky Str., 49000, Dnipro, Ukraine

<sup>3</sup>Iron and Steel Institute of Z.I. Nekrasov of NASU

Akademik Starodubov Sq., 49000, Dnipro, Ukraine

<sup>4</sup>Ukrainian State University of Science and Technologies

4 Haharina Prosp., 49000, Dnipro, Ukraine

## ABSTRACT

In the modern manufacturing of parts of metal powder, the method of Selective Laser Melting (SLM) has become widespread. In Ukraine, the LLC “Additive Laser Technologies of Ukraine” is engaged in the development of equipment for manufacturing parts of metal powders by SLM technology. Nowadays, for this equipment, the relevant task is the development of a procedure for choosing the parameters of the process of melting metal powder, providing the necessary mechanical and service properties of parts. For the investigations, three experimental cylindrical specimens of Co–Cr–Mo alloy were made in the vertical direction for tensile test according to ISO 6892:2019 — with a diameter of the working zone of 5 mm, with a controlled stop at a height of 18 mm from the beginning of the working zone, the total length of which is 28 mm. As a result of the analysis of the values of mechanical properties, it was found that the ultimate strength of the experimental specimens of Co–Cr–Mo alloy made by SLM technology with a controlled stop during 24 h decreases compared to the specimens made without a controlled stop — by ~13 %, relative elongation — by ~1 % and reduction in area — by ~17 %. It was found that for the experimental specimens with a stop in the manufacturing process, the deviation from the average values was: for ultimate strength ~11 %, relative elongation ~62 % and reduction in area of ~21 %. This is predetermined by failure of one of the specimens at the place of a stop. The use of parts with a production defect (stop) should be significantly restricted respective to a probable significant softening and embrittlement of a product.

**KEYWORDS:** selective laser melting, controlled stop, Co–Cr–Mo alloy, mechanical properties, density

## INTRODUCTION

In the modern manufacturing of parts of metal powder the method of Selective Laser Melting (SLM) has become widespread. This technology is based on layer-by-layer fusion of metal powder particles, in which the melting process is carried out by the movement of laser beam relative to the digital three-dimensional model of an object created.

At present, the main manufacturers of equipment for producing parts by SLM technology are located in Europe and America, for example, the companies 3D Systems (USA), Electro Optical Systems — EOS (Germany), Concept Laser GmbH (Germany) and in other countries of the world. The solutions offered at the market are expensive and require additional purchase of software for various materials, as well as purchase of powder from the manufacturer of equipment.

In Ukraine, the LLC “Additive Laser Technologies of Ukraine” is engaged in the development of equipment for creating parts of metal powders by SLM technology. The advantage of the equipment of the domestic manufacturer is the ability to independently

adjust the manufacturing parameters for different materials and to take into account the geometric features of a product (significant change in cross-section, sloping surfaces, etc.).

A large number of publications was dedicated to studying technological aspects of manufacturing parts by layer-by-layer deposition of the powder layer with the following melting [1–4]. The research data are aimed at obtaining high density [5–8], determination of rational parameters [9–12] and their use in parts manufacturing [13–15]. Based on the analysis of the mentioned works, it was found that in most cases a large number of factors play a significant role in the process of manufacturing parts for real printing conditions. But it should be noted that there are a number of reasons causing a stop in the process: reduction in the rate of surfacing a new layer, unevenness of powder surfacing, partial tear of a part due to the curvature, etc. This may play a significant role in changing the end mechanical properties due to different cooling rates and the influence of laminar inert gas flows on a printed layer.

Based on the preliminary studies of the heat-resistant Inconel 718 alloy [16] (used for parts and assem-

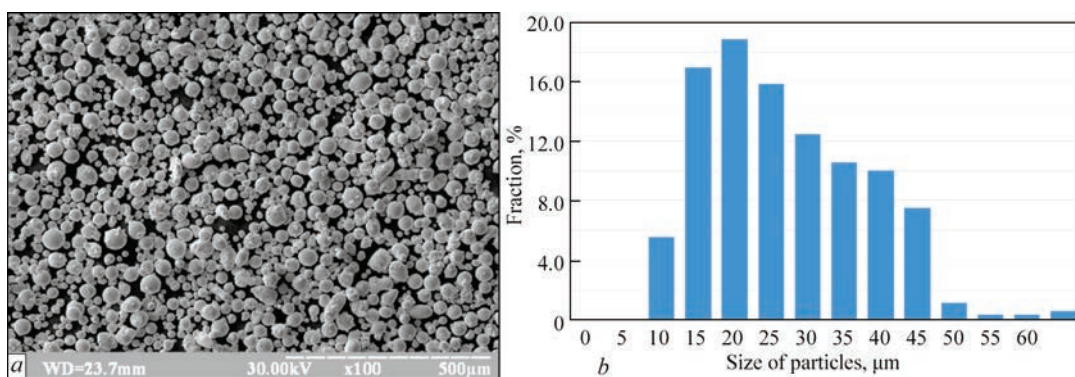


**Figure 1.** Particles of source material of Co–Cr–Mo at a magnification of 100 (a) and results of granulometric analysis (b)

blies of aircraft and space purpose), it was fairly clear noted that a stop in printing with the further resumption of the process has no significant influence on mechanical properties (deviation is approximately 5%), the average level of which corresponded to foreign analogues. Microstructure examinations helped the authors to find an area with a reduced material penetration, located in the zone of a stop.

The problem of the influence of a stop in the process of manufacturing parts by SLM method requires further study, including with the use of other materials in order to determine the level of deviations of mechanical properties and to predict the possibilities of operation of such products. The Co–Cr–Mo alloy is widely used in the dental industry, namely in orthopedics for the manufacture of dental prosthesis with the application of ceramic coating. The use of the Co–Cr–Mo alloy in the dental implantation is predetermined by a high level of values of mechanical properties and indices of wear resistance in combination with a low coefficient of temperature expansion and biocompatibility.

In the work, the studies of the cobalt-chromium Co–Cr–Mo alloy after a stop in the printing process and comparison of the characteristics of the alloy in the state obtained under rational printing conditions were carried out.

The aim of the work is to investigate the influence of a one-time stop in the process of manufacturing a part by SLM technology on mechanical properties of specimens from the Co–Cr–Mo alloy to establish the serviceability of parts that have such a feature.

## MATERIAL AND RESEARCH PROCEDURE

In the work, the tensile specimens were studied, manufactured in the 3D printing machine Alfa-150D of ALT Ukraine, produced of metal powder from the cobalt-chromium Co–Cr–Mo alloy with the following chemical composition, wt.%: 17.79 Cr; 12.63 Ni; 2.35 Mo; 0.78 Mn; 0.64 Si; C 0.016, granulometric analysis is presented in Figure 1.

Metallographic sections were made according to standard procedures with the use of diamond pastes. Metallographic examinations were performed with

the use of light microscopes Neophot 30 and Axiovert 200M MAT to determine the density of the specimens. The sizes and amount of pores and oxides were calculated using the ImageJ software module. Granulometric analysis was performed in a scanning electron microscope REM 106.

Three experimental cylindrical specimens were made for tensile tests according to ISO 6892:2019 with a diameter of the working zone of 5 mm. In the process of building, the specimens were arranged in the working space in a vertical position; a controlled stop during 24 h was carried out at a height of 18 mm of the working zone, the total length of which was 28 mm (Figure 2). The rational printing parameters were determined in [17]: deposited layer is 20 µm thick; distance between the tracks is 0.1 mm, power is 130 W, velocity of beam passing is 900 mm/s. Mechanical treatment of specimens to finished sizes was carried out with the use of the HAAS ST10 lathe.

Mechanical properties were determined during tensile tests in accordance with the standard procedure in the PHYWE machine.

## RESEARCH RESULTS

The studies of the specimens in a polished state showed that they all have a density of about ~99.97% (Figure 3), in most cases defects are represented by

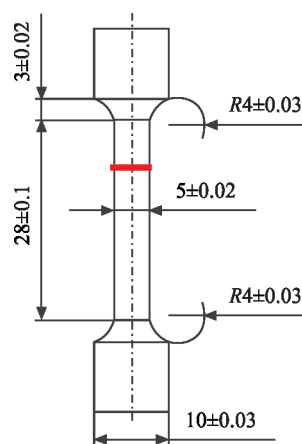


**Figure 2.** Scheme of location of a place of a controlled stop of printing an experimental specimen

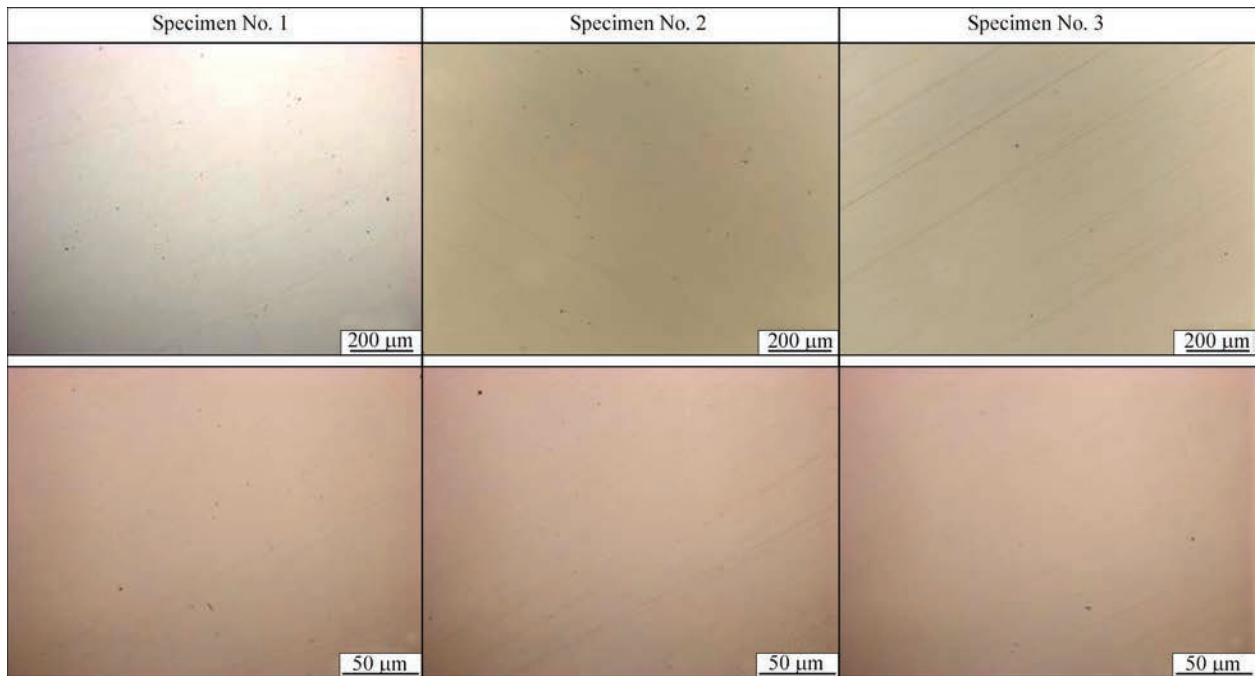


**Figure 3.** Microstructure of experimental specimens in the zone of stop

**Table 1.** Mechanical properties of experimental specimens manufactured from the Co–Cr–Mo alloy by SLM technology in the initial state with mechanical treatment of the working zone

Number	State	$\sigma_r$ , MPa	$\Delta\sigma_y$ , %	$\delta$ , %	$\Delta\delta_6$ , %	$\psi$ , %	$\Delta\psi_6$ , %	Source
1	With a stop	1067.6	+5.6	6.9	+0.5	13.9	+14.3	–
2		895.2	–11.1	2.6	–62	9.4	–21	–
3		1060.1	+4.9	11	+37.6	12.3	+3.25	–
Average		1007.6	0	6.86	0	11.9	0	–
4	Without a stop	1157	–0.19	1.8	–74.13	17.9	+23.78	[17]
5		1162	+0.23	8.7	+25	10.1	–30.15	[17]
6		1159	–0.02	10.4	+49.42	15.4	+6.50	[17]
Average		1159.3	0	6.96	0	14.46	0	[17]

separate globular pores with a diameter of 1–2  $\mu\text{m}$ . According to the results of studies, no defects of the influence of a stop on the continuity of the experimental specimens were found at the microstructure level.

According to the results of visual-optical inspection, failure of the experimental specimens Nos 1 and 3 occurred beyond the place of a controlled stop, and the surface of a fracture had a tough structure. It should be noted that failure of the experimental specimen No. 2 occurred in the zone of a controlled stop and had a brilliant fracture with the visible characteristic texture of the tracks (Figure 4).

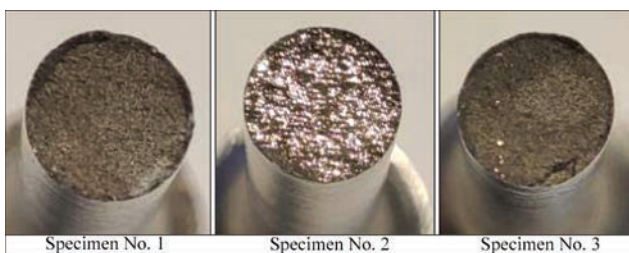


**Figure 4.** Failures of experimental specimens with a controlled stop

According to the results of the analysis of the values of mechanical properties (Table 1), it was found that the values of mechanical properties of the specimens with a controlled stop undergo changes compared to the initial state without a controlled stop [17].

The comparative analysis of the average values of ultimate strength of all the experimental specimens with a controlled stop allows setting a decrease in values by 13 % compared to the state without a stop in manufacturing. The average values of relative elongation of the experimental specimens with a stop undergo slight changes ( $\sim 1$  % compared to a state without a stop). While analysing changes in the average values of reduction in area, it was found that for the experimental specimens with a controlled stop, a decrease in this characteristic by  $\sim 17$  % is observed, compared to the specimens without a stop in the manufacturing process. It should also be noted that the experimental specimens with a controlled stop have large discrepancies in values within the framework of the study, namely: ultimate strength  $-11.1 - +4.9$  %, relative elongation  $-62 - +37.6$  %, reduction in area  $-21 -$

+14.3 % compared to the specimens made without a stop  $-0.19 - +0.23$  %,  $+1.8 - +10.4$  %,  $-30.15 - +23.78$  % accordingly. A small discrepancy in values indicates the stability of the process of manufacturing specimens and a heating-cooling cycle in manufacturing. A significant decrease in mechanical properties of the specimen No. 2, which was made with a stop and fractured along the place of its location indicates, that the use of parts with such a production defect should be significantly limited respective to a probable significant softening and embrittlement of a product.

## CONCLUSIONS

1. As a result of the analysis of the values of mechanical properties, it was found that the ultimate strength of the experimental specimens with a controlled stop from the Co–Cr–Mo alloy, made by SLM technology, is reduced compared to the specimens made without a controlled stop — by  $\sim 13$  %, relative elongation — by  $\sim 1$  % and reduction in area — by  $\sim 17$  %.

2. It was found that for the experimental specimens in the process of manufacturing, the deviation from the average values was: for ultimate strength  $\sim 11$  %, for relative elongation  $\sim 62$  % and for reduction in area  $\sim 21$  %. This is predetermined by the failure of one of the specimens at the place of a stop.

3. The use of parts with a production defect (stop) should be significantly limited, respectively to a probable significant softening and embrittlement of a product.

## REFERENCES

- Mahoney, M.W. (1989) *Superplastic Properties of Alloy 718*. In: *Superalloy 718 Metallurgy and Applications*. Eds by E.A. Loria, TMS, 391–405.
- Adjamskyi, S., Kononenko, G., Podolskyi, R., Badyuk, S. (2022) *Implementation of selective laser melting technology in Ukraine*. Kyiv, Naukova Dumka [in Ukrainian]. DOI: <https://doi.org/10.15407/978-966-00-1856-3>
- Conner, B.P., Manogharan, G.P., Martof, A.N. et al. (2014) Making sense of 3-D printing: Map of additive manufacturing products and services. *Additive Manufacturing*, **1–4**, 64–74.
- Viňáš, J., Brezinová, J., Brezina, J., Maruschak, P.O. (2019) Structural and mechanical features of laser-welded joints of zinc-coated advanced steel. *Mater. Sci.*, **55**.
- Dudda, W. (2019) Influence of high temperatures on the mechanical characteristics of 26H2MF and ST12T steels. *Mater. Sci.*, **55**.
- Frazier, W.E. (2014) Metal additive manufacturing: A review. *J. Mater. Eng. and Performance*, **23(6)**, 1917–1928.
- Kovalenko, V.S., Golovko, L.F., Merkulov, G.V., Strizhak, A.I. (1981) *Strengthening of parts by laser beam*. Kyiv, Tekhnika [in Russian].
- Kruth, J.-P., Leu, M.-C., Nakagawa, T. (1998) Progress in additive manufacturing and rapid prototyping. *CIRP Ann.-Manuf. Technol.*, **47(2)**, 525–540.

- Kamath, C. (2016) Data mining and statistical inference in selective laser melting. *Int. J. Adv. Manuf. Technol.*, **86**, 1659–1677.
- Adzhamskyi, S.V., Kononenko, G.A., Podolskyi, R.V. (2021) Influence of parameters of SLM-process on formation of boundary area of parts from heat-resistant nickel alloy Inconel 718. *Kosmichna Nauka i Tekhnologiya*, **27(6)**, 105–114. DOI: <https://doi.org/10.15407/knit2021.06.105>
- Williams, C.B., Mistree, F., Rosen, D.W. (2005) Towards the design of a layer based additive manufacturing process for the realization of metal parts of designed mesostructured. In: *Proc. of 16<sup>th</sup> Solid Free Fabr. Symp.*, 217–230.
- Loh, L.-E., Chua C.-K., Yeong W.-Y. et al. (2015) Numerical investigation and an effective modelling on the Selective Laser Melting (SLM) process with aluminium alloy 6061. *Int. J. Heat Mass Transf.*, **80**, 288–300.
- Adzhamskyi, S.V., Kononenko, G.A., Podolskyi, R.V. (2020) Influence of technological parameters of SLM-process on porosity of metal products. *The Paton Welding J.*, **10**, 13–18. DOI: <https://doi.org/10.37434/as2020.10.03>
- (2002) *ASM Metals Handbook*. Vol. 2: Properties and Selection: Nonferrous Alloys and Special-Purpose Materials. ASM Int.
- Callister, W.D., Callister, Jr W.D. (2000) *Fundamentals of Materials Science and Engineering: An Interactive Text*. 5<sup>th</sup> Ed. Wiley.
- Adjamskyi, S.V., Sazanishvili, Z.V., Tkachov, Y.V. et al. (2021) Influence of the time interval between the deposition of layers by the SLM technology on the structure and properties of Inconel 718 alloy. *Mater. Sci.* **57**, 9–16. DOI: <https://doi.org/10.1007/s11003-021-00508-3>
- Adjamskyi, S., Kononenko, G., Podolskyi, R., Badyuk, S. (2022) Studying the influence of orientation and layer thickness on the physico-mechanical properties of Co–Cr–Mo alloy manufactured by the SLM method. *Sci. and Innovation*, **18(5)**, 85–94. DOI: <https://doi.org/10.15407/scine18.05.085>

## ORCID

S.V. Adzhamskyi: 0000-0002-6095-8646,  
G.A. Kononenko: 0000-0001-7446-4105,  
R.V. Podolskyi: 0000-0002-0288-0641

## CONFLICT OF INTEREST

The Authors declare no conflict of interest

## CORRESPONDING AUTHOR

R.V. Podolskyi  
Ukrainian State University of Science  
and Technologies  
4 Haharina Prosp., 49000, Dnipro, Ukraine.  
E-mail: [rostislavpodolskij@gmail.com](mailto:rostislavpodolskij@gmail.com)

## SUGGESTED CITATION

S.V. Adzhamskyi, G.A. Kononenko, R.V. Podolskyi (2023) Influence of a stop in the process of melting on mechanical properties of specimens from the Co–Cr–Mo alloy made by SLM technology. *The Paton Welding J.*, **8**, 56–59.

## JOURNAL HOME PAGE

<https://patonpublishinghouse.com/eng/journals/tpwj>

Received: 16.06.2023

Accepted: 07.08.2023

DOI: <https://doi.org/10.37434/tpwj2023.08.08>

# REMOTE ASSESSMENT OF DAMAGES OF THE KYIV TV TOWER BASED ON THE USE OF AERIAL PHOTOGRAPHY AND THE METHOD OF PHOTOGRAMMETRY

L.M. Lobanov<sup>1</sup>, D.I. Stelmakh<sup>1</sup>, V.V. Savitsky<sup>1</sup>, V.P. Diadin<sup>1</sup>, O.P. Shutkevych<sup>1</sup>, A.G. Kozachek<sup>2</sup>

<sup>1</sup>E.O. Paton Electric Welding Institute of the NASU  
11 Kazymyr Malevych Str., 03150, Kyiv, Ukraine

<sup>2</sup>Broadcasting, Radiocommunications & Television Concern  
10 Dorogozhytska Str., 04112, Kyiv, Ukraine

## ABSTRACT

The article is devoted to the use of non-destructive testing and visual inspection methods using UAVs (drones) to assess damages of the TV tower structure. The methodology is described including the use of aerial photography and photogrammetry method to create a 3D TV tower model and localization of damages. With the use of 3DF Zephyr software, a 3D model was built, which allowed setting the sizes of defects and classifying them. On the basis of the carried out examination, recommendations for prompt repair and restoration of the TV tower were developed to provide the safety of its operation. The presented results confirm the high potential of combining traditional methods of non-destructive testing with remote diagnostics based on the use of drones and photogrammetry for inspection of large-sized structures.

**KEYWORDS:** UAV (drone), photogrammetry, non-destructive testing, 3D model, visualization, TV tower

## INTRODUCTION

Prevention of emergency situations and providing reliable operation of large-sized structures involves regular preventive measures to maintain their technical condition. The aim of examination of large-sized structures is to reveal possible drawbacks, defects or potentially problematic zones that require maintenance. In the case of large-sized structures, for effective detection of defects, specialized additional equipment should be used, which complicates the process, makes it long-term, labour-consuming and dangerous for performers [1]. In addition, for successful examination, professional climbers should be involved and it is necessary to obtain permits for their work. In many cases, there are also places with a limited view and a difficult access, which reduces the effectiveness of damage detection.

One of the possible methods to overcome the abovementioned limitations is the use of unmanned aerial vehicles (UAVs). However, the presence of qualified engineers on site continues to play a fundamental role in performing the examination task (for example, a pilot, a second pilot, an expert in the field of material diagnostics). In addition, to obtain objective results, it is important to eliminate the dependence of their checking on experience, physical aspects and skill set of UAV operator. The results cannot be achieved in real time and some defective places must be confirmed and examined repeatedly.

Therefore, experienced professional specialists in the field of non-destructive quality testing are required.

The article describes the procedure for examination of the Kyiv TV tower, which was damaged by an enemy missile strike on March 1, 2022 as a result of Russia's military aggression. The Kyiv TV tower, an all-welded metal spatial lattice high-rise 380 m tall erection, built in 1968–1973, was the highest lattice freely located erection in the world at the time of construction [2, 3]. Taking into account that PWI of the NAS of Ukraine and LLC “V.M. Shimanovskiyi Ukrainian Institute of Steel Construction” were the authors of the project of this unique engineering structure, examination and assessment of the technical condition of the tower metal structures was performed by these organizations.

The visual and instrumental inspection of the tower metal structures in the missile strike area from the mark +0.000 to + 80.000 was performed in four stages using the following methods of non-destructive testing:

- visual-measuring;
- magnetic flaw detection;
- ultrasonic testing of the base metal and welded joints of the tower elements;
- visual examination with the use of UAVs.

## METHODS OF INSPECTION OF LARGE-SIZED METAL STRUCTURES

Visual-measuring inspection consisted in external inspection of the tower pipe elements, assembly welded joints, facets and other elements of its metal struc-

tures. An inspection of the tower metal elements was performed from the marks 0; +5; +40; +72 and +80 m.

The main task of the visual-measuring method of testing was to detect and record all visually observed damages of the elements of the tower metal structures for their further assessment. Thus, depending on the exposure energy of fragments on the pipe walls, several types of damages of the elements of the structure can be distinguished:

- complete penetration of a fragment through a one wall of the pipe without influence on the other wall;
- complete penetration of a fragment through a one wall of the pipe with plastic deformation of the other wall;
- full penetration of a fragment through both walls of the pipe (shot through);
- partial penetration of a fragment into a one wall of the pipe to different depth (crater);
- presence of a dent in the pipe wall without penetration of a fragment;
- deformation of the element under the influence of debris and a shock wave;
- destruction of an element or an assembly of its fastening;
- presence of cracks in the places of exposure of fragments and in the assemblies of elements connection;
- destruction of shock absorbers between the elements.

The peculiarities of using magnetic and ultrasonic methods of testing consisted in the probable detection of hairline through, surface and subsurface cracks in the places of shock impact and penetration of missile fragments through the wall of the tower metal structure elements. In the places of detected damages, photographing with the record of their location place was made.

As a result of the performed inspection of different sections of the TV tower metal structures, it was found that:

1. In the places prone to significant force effect, there were no elongated hidden cracks, i.e., cracks extending on the inner surface or cracks inside the metal, which cannot be visually detected. Almost all of the detected and investigated cracks are a through thickness rupture of the metal. There are few deformed areas where traces of cracking are detected on the inner surface. The assessment of sizes of such cracking is only a few mm.

2. In instrumental inspection of metal in places with obvious plastics and ruptures, the quantitative estimates of cracking sizes are almost equal to visual-measuring estimates, the difference is not more than 2–3 mm.

3. No defects (including cracks) were detected in places distant from the zones of plastic deformation and traces of shock action.

Over the last decade, the widespread use of UAV (drones) has begun to perform a large range of tasks, including for non-destructive quality testing.

While studying damages of the TV tower, the use of this method of diagnostics was predetermined by several reasons. First, the accessible places for visual inspection of damaged structures did not allow inspecting the entire surface of spatial structures because of the restriction of the viewing angles from the places of observation. As a consequence, this significantly complicated the task of the overall assessment of the volumes of destruction of an object as a whole. Secondly, mapping of damages of the elements without their spatial review required considerable time and attracting a large number of climbers for their implementation. In addition to the mentioned reasons, it is also necessary to note the problem of defects identification on the results of visual inspection.

Examination of metal and reinforced concrete structures with the use of unmanned and robotic systems significantly reduces the cost and time of checking, simultaneously increasing the reliability and consistency of the obtained data. In addition, shortening the downtime helps to continue the work for a long period that leads to improving serviceability of critical objects. It should also be noted that in the case of examination of dangerous or difficult-to-access zones, the most effective method to diagnose structures in terms of operating risk, cost and capabilities is the use of drones [1, 4].

However, drones have some restrictions that need to be taken into account. One of the problems during the operation of a drone is vibration. UAVs are often exposed to various sources of vibration that may affect the reliability of the obtained data [5]:

- vibrations caused by external sources, for example, strong wind gust;
- vibrations caused by drone manoeuvres;
- vibrations caused by aerodynamic sources, for example, headwind;
- vibrations caused by the stabilization system itself;
- vibrations caused by engines and propellers.

In the process of examination of the TV tower, some influences of external factors were observed, namely:

- formation of shadows on pipe structures as a result of cloudy weather;
- violation of stabilization because of variable wind flows;
- changing the angle of object illumination;
- attraction to metal structures as a result of effect of electromagnetic equipment.

The specific time when the flight covering structures takes place, may significantly affect the accuracy

of the result. For example, shadows, daylight, weather conditions and solar radiation may have a negative impact that leads to inaccurate results [1].

### APPLICATION OF PHOTOGRAMMETRY METHOD FOR FINDING DAMAGES OF THE TV TOWER

Photogrammetry is a technology for obtaining reliable information about physical objects and the environment through the processes of recording, measuring and interpretation of photographic images. As the name of the technology implies, the methodology initially consisted of photo analysis, but the use of film cameras decreased significantly in favour of digital sensors. Photogrammetry was expanded to include an analysis of other records such as digital images, emitted acoustic energy, laser measurements and magnetic phenomena [6].

In recent years, photogrammetry with its capabilities of computer processing and attracting new data collection tools has opened many new areas of application: remote visualization, robotics, virtual reality, 3D animation, etc. [7]. In industrial inspection and quality testing, photogrammetric methods and systems have found their purpose in such areas as highways, bridges, pipelines, wind turbines, power lines.

There are two main types of photogrammetry: aerial (with a camera in the air) and terrestrial (camera handheld or on a tripod). Terrestrial photogrammetry dealing with object distances up to ca. 200 m is also termed close-range photogrammetry. Small-format aerial photogrammetry in a way takes place between these two types, combining the aerial vantage point with close object distances and high image detail [9].

The method of photogrammetry is based on geometrical–mathematical reconstruction of the paths of rays from the object to the sensor of a digital camera at the moment of exposure, which allows remotely determining defective areas, obtaining accurate geometric dimensions of damages and their location on the structure. In order to do that, first, orientation algorithms for determination of the inner and outer parameters of each image are used, such as focal length, point of the focus center, position and orientation of the camera and point of shooting. At the next stage, joint image processing is performed, they are aligned to provide a correct mutual position and the correspondence of the points in the photo. After alignment of the images, it is possible to determine 3D coordinates of the object's surface points using the methods based on their relative positions on the images. Based on 3D coordinates of the point cloud, a 3D model of the object is created. After receiving a 3D model based on photogrammetry, it is scaled.

To find the sizes of defects, a 3D model of the Kyiv TV tower was built using 3DF Zephyr software. A base from 2351th photography was used to build the model, 1292 photos were involved for the final result (Figure 1).

Before building the model, all available modes were analyzed in the 3DF Zephyr software and the best one among 6 variants was experimentally selected [9]:

- General;
- Aerial–Nadiral images;
- Urban;
- Human body;
- Surface scan;
- Vertical structure.

Urban and Human body modes were immediately rejected because they need to be used if there is a task of building a 3D model of city with its landscape and different facades of buildings or if 3D model of human with accurate sizes of its body is required.



**Figure 1.** Models of the lower tier of the Kyiv TV tower: *a* — full-scale model; *b* — place of explosion

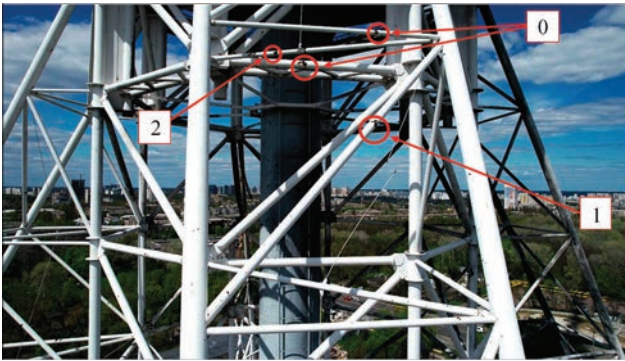


**Figure 2.** Photo of support element obtained with an unmanned aerial vehicle at aerial photography of the TV tower

General mode is universal and it can be used to complete the set task, but there is a problem with determination of sizes of defects. This mode does not provide a sufficient accuracy of sizes of the structural elements and makes it impossible to measure distance with the accuracy to mm.

Aerial–Nadiral images is the mode created to work with data provided by UAVs. When using this mode, there was a problem with doubling of elements and their indefinite orientation in space. Since the tower examination was conducted at different altitudes and at different angles, it was a major problem for the given mode, because for optimal construction of models in Aerial–Nadiral Images, the photos are required taken at the same altitude in a top-down direction to the object under examination.

Surface scan would fit if analysis of a small area of the structure was required. This also requires images from the closest distance to the object. A drone cannot fly closer than 1 m to the object, because protective built-in sensors are activated blocking its control. The problem with incorrect orientation of elements in space in this mode is also present.

It was determined, that Vertical structure is optimal for building a model of the Kyiv TV tower. With its help, it was managed to solve the set tasks.

To create a 3D model, a graphic station Dell Precision 3650 Tower was used with the following characteristics: Processor (11th Gen Intel(R) Core(TM) i7-11700 @ 2.50GHz), Memory (32 GB (4·8 GB)), Disc (512 SSD), Video card (Nvidia T1000 4 GB), Operating System (Windows 10 Pro).



**Figure 4.** Area of the TV tower at the epicentre of the explosion: *a* — photo; *b* — 3D model

The work with a large amount of data is labour-consuming, because the processes of creating models can take several days or even weeks. In our case, the final result required a continuous operation of the graphic station for about 36 h.

After building the rough version of the 3D model, the next stage of work began, namely its processing. Unnecessary graphic elements are filtered; optimal parameters are selected for the best inspection of the model and detecting defects. After that, the final 3D model (Figure 1) is obtained.

Figure 2 shows defects formed from a missile explosion. Defect 0 represents a destruction of the protective coating of the structural element and is not dangerous for the tower in the short term. Defects 1 and 2 are the holes formed as a result of penetration of a fragment through the wall of the pipe and through them water and moisture gets into the middle of the pipe elements, which leads to their corrosion and a significant decrease in strength characteristics.



**Figure 3.** Photos of damages in the structural element of the TV tower: *a* — defect 1; *b* — defect 2 (see Figure 2)

Based on the analysis of photographs and their projections on a digital 3D model obtained by the method of photogrammetry, the typical sizes of these defects were measured. Thus, for example, with the help of the Measures tool it was found that the diameter of the first defect is approximately 5 cm (Figure 3, *a*), and the second one is 2.2 cm (Figure 3, *b*). It is worth noting that these defects were found on the least damaged support of the TV tower.

The 3D model allowed successfully visualizing large damages with their real appearance and sizes (Figure 4).

The conducted works on examination of the Kyiv TV tower helped to assess defects and develop recommendations for repair.

## CONCLUSIONS

Damages of pipe structures of the Kyiv TV tower were examined using the methods of non-destructive testing and visual inspection with a drone with the subsequent use of the photogrammetry method. The built 3D model helps to detect locally the location of defects on the elements of the structure and visualize the results of diagnostics, determine the sizes of defects and classify them. Using a remote visual inspection with UAVs, it was possible to find damages that were not identified by non-destructive testing methods and critical defects that may pose a danger to safe operation of the object or lead to serious problems with its functioning and require urgent repair in order to reduce the risk of an emergency and provide the safety of the object operation. A built 3D model can be used for numerical calculations of the stressed-strain state of the Kyiv TV tower for the analysis of spatial stress distribution in assemblies and elements of its structure. The obtained data allowed developing recommendations for prompt repair and restoration of the TV tower. The presented results demonstrate the high potential of combining traditional methods of non-destructive quality testing with remote diagnostics technology based on the use of UAVs and photogrammetry for examination of large-sized structures of critical purpose.

## ACKNOWLEDGMENTS

The authors express gratitude to 3Dflow Corporation for the 3DF Zephyr digital support and technical support within the framework of the program 3D flow for the Ukrainian Crisis [10]. The authors are grateful for the opportunity to use this powerful tool in their research works and believe it helped to succeed with their work.

This research was conducted with the support of the project 022.01/0095 “Development of technology for remote diagnosis of damaged large-scale objects based on the use of unmanned aerial vehicles (UAVs) and photogrammetry” funded by the National Research Foundation of Ukraine in the framework of the

competition “Science for the Recovery of Ukraine in the War and Post-War Periods”.

## REFERENCES

1. Parham Nooralishahi, Clemente Ibarra-Castanedo, Shakeb Deane et al. (2021) Drone-based non-destructive inspection of industrial sites: A review and case studies. *Drones*, 5(4), 106. DOI: <https://doi.org/10.3390/drones5040106>.
2. Lobanov, L.M., Garf, E.F., Kopylov, L.N., Sineok, A.G. (2013) Welding at erection of Kyiv TV tower. *Promyslove Budivnytstvo ta Inzhenerni Sporudy*, 3, 16–20 [in Russian].
3. Demyanov, I.A., Murashov, A.P., Borisov, Yu.S. et al. (2005) Application of electric arc metallizing for anticorrosive protection of Kyiv TV tower. *Svarshchik*, 3, 19–21 [in Russian].
4. Nenad Gucunski, Hung Manh La, Kien Dinh, Mustafa Khudhair (2023) Advancing condition assessment of reinforced concrete bridge elements through automation, visualization, and improved interpretation of multi-NDE technology data. *Materials Evaluation*, 81(1); 56–66. DOI: <https://doi.org/10.32548/2023.me-04289>
5. Rok Cajzek, Uroš Klanšek (2016) An unmanned aerial vehicle for multi-purpose tasks in construction industry. *J. of Applied Engin. Sci.*, 14(2), 314–327. DOI: <https://doi.org/10.5937/jaes14-10918>.
6. Paul, R. Wolf, Bon A. Dewitt, Benjamin E. Wilkinson (2014) *Elements of Photogrammetry with Applications in GIS*. 4<sup>th</sup> Ed.
7. Zhilin Li, Jun Chen, Emmanuel Baltsavias (2008) *Advances in Photogrammetry, Remote Sensing and Spatial Information Sciences*. ISPRS Congress Book.
8. James, S. Aber, Johannes, B. Ries (2010) *Small-Format Aerial Photography*.
9. <https://www.3dflow.net/technology/documents/3df-zephyr-documentation/Copyright> © 2023 by 3Dflow srl.
10. <https://www.3dflow.net/3dflow-for-the-ukrainian-crisis/>(3 March 2022)

## ORCID

L.M. Lobanov: 0000-0001-9296-2335,  
D.I. Stelmakh: 0000-0002-0412-9747,  
V.V. Savitsky: 0000-0002-2615-1793,  
V.P. Diadin: 0000-0002-2061-8436,  
O.P. Shutkevych: 0000-0001-5758-2396

## CONFLICT OF INTEREST

The Authors declare no conflict of interest

## CORRESPONDING AUTHOR

V.V. Savitsky  
E.O. Paton Electric Welding Institute of the NASU  
11 Kazymyr Malevych Str., 03150, Kyiv, Ukraine.  
E-mail: viktor.savitsky@gmail.com

## SUGGESTED CITATION

L.M. Lobanov, D.I. Stelmakh, V.V. Savitsky, V.P. Diadin, O.P. Shutkevych, A.G. Kozachek (2023) Remote assessment of damages of the Kyiv TV tower based on the use of aerial photography and the method of photogrammetry. *The Paton Welding J.*, 8, 60–64.

## JOURNAL HOME PAGE

<https://patonpublishinghouse.com/eng/journals/tpwj>

DOI: <https://doi.org/10.37434/tpwj2023.08.09>

# TECHNOLOGY AND EQUIPMENT FOR ELECTRON BEAM SINTERING OF HARD ALLOY BILLETS

V.M. Nesterenkov<sup>1</sup>, K.S. Khripko<sup>1</sup>, V.V. Lukyanov<sup>1</sup>, M.O. Sysoev<sup>2</sup>, V.V. Chernyavskiy<sup>2</sup>

<sup>1</sup>E.O. Paton Electric Welding Institute of the NASU

11 Kazymyr Malevych Str., 03150, Kyiv, Ukraine

<sup>2</sup>Plasmatec LLC

18 Maksymovycha Str., 21036, Vinnytsia, Ukraine

## ABSTRACT

The paper studies application of electron beam in a technology of high-speed sintering of hard alloy billets made of secondary raw materials as well as high-performance equipment developed at the E.O. Paton Electric Welding Institute of the NAS of Ukraine for the implementation of this technology.

**KEYWORDS:** electron beam processing, hard alloy, sintering

## INTRODUCTION

High-power electron beam for many years has been used for commercial purposes as a tool of thermal influence on metals and their alloys. Firstly, it was used only for welding, surfacing and remelting of metals. Later on, with development of controlling equipment it was used for other tasks, for example, for local heat treatment [1, 2] (preheating, hardening, complete and incomplete annealing) as well as in additive manufacturing processes with application of surfacing wire as well as powder materials [3, 4]. This paper considers application of electron beam in sintering technology (conditionally) of cylinder billets of hard alloy as well as corresponding equipment for realization of this process on mass batches of such products.

## TECHNOLOGY OF SINTERING THE BILLETS FROM VK HARD ALLOY

Hard alloys are widely used for technical applications. At the same time, resources used for their manufacture are limited worldwide. Discovered and predicted world reserves of tungsten are estimated at 21 mln tons [5]. At that, tungsten ore reserves in Ukraine are concentrated mainly in the North-Western part of the Ukrainian Shield (the South-Western part of the foundation of the East European Platform) and are estimated at 105 thou tons of metal [6]. Whereas Ukraine's annual needs in tungsten products amount to 2.5 thou tons and are constantly growing. Therefore, today, tungsten carbide powder produced from secondary raw material (for example, from used cutting tools, stamps, molds, dies, etc.) is also used for manufacture of hard alloy products. The available technology of processing of hard alloy wastes is environmentally-friendly (i.e. it does not harm the environment) and

ensures the production of high-quality, that is, highly pure, raw material.

Change of parameters of the process of carbidization allows regulating the size of particles of tungsten carbide powder in a range from 50 nm to 10  $\mu\text{m}$  (Figure 1). Corresponding composition and grain-size of alloy is selected depending on area of application and conditions of specific part operation.

Manufacture of "raw" billet is carried out using traditional technology, namely mixing of components, mixing in plasticizer, formation of hard alloy billets on hydraulic presses in steel moulds, removal of plasticizer in course of previous sintering in hydrogen medium. Further these billets require final sintering.

It should be noted that a traditional furnace sintering of hard alloys provokes intensive growth of carbide grains at appearance of liquid phase. It is caused by the process of recrystallization of carbide through liquid phase as well as growth of neighbor grains due to prevailing growth of one grain at the expense of other ones. These phenomena can be prevented by application of growth inhibitors, namely carbides of vanadium, chromium and others.

In contrast to the traditional technology the electron beam technology, first of all, can provide high sintering speeds and, secondly, due to possibility of high-level regulation of the process itself, allows sufficiently "fine" regulation of alloy microstructure (Figure 2). In electron beam bombardment of "raw" billet at acceleration voltage of high-voltage power supply 60 kV, around 75 % of its power is transformed in heat in a surface layer of billet of thickness  $S$  of around 10  $\mu\text{m}$  [7]. From the surface layer heat spreads deep in the billet according to heat conductivity laws. After energy supply from electron beam is stopped the surface layer quickly cools down. Cooling time  $\tau$  is

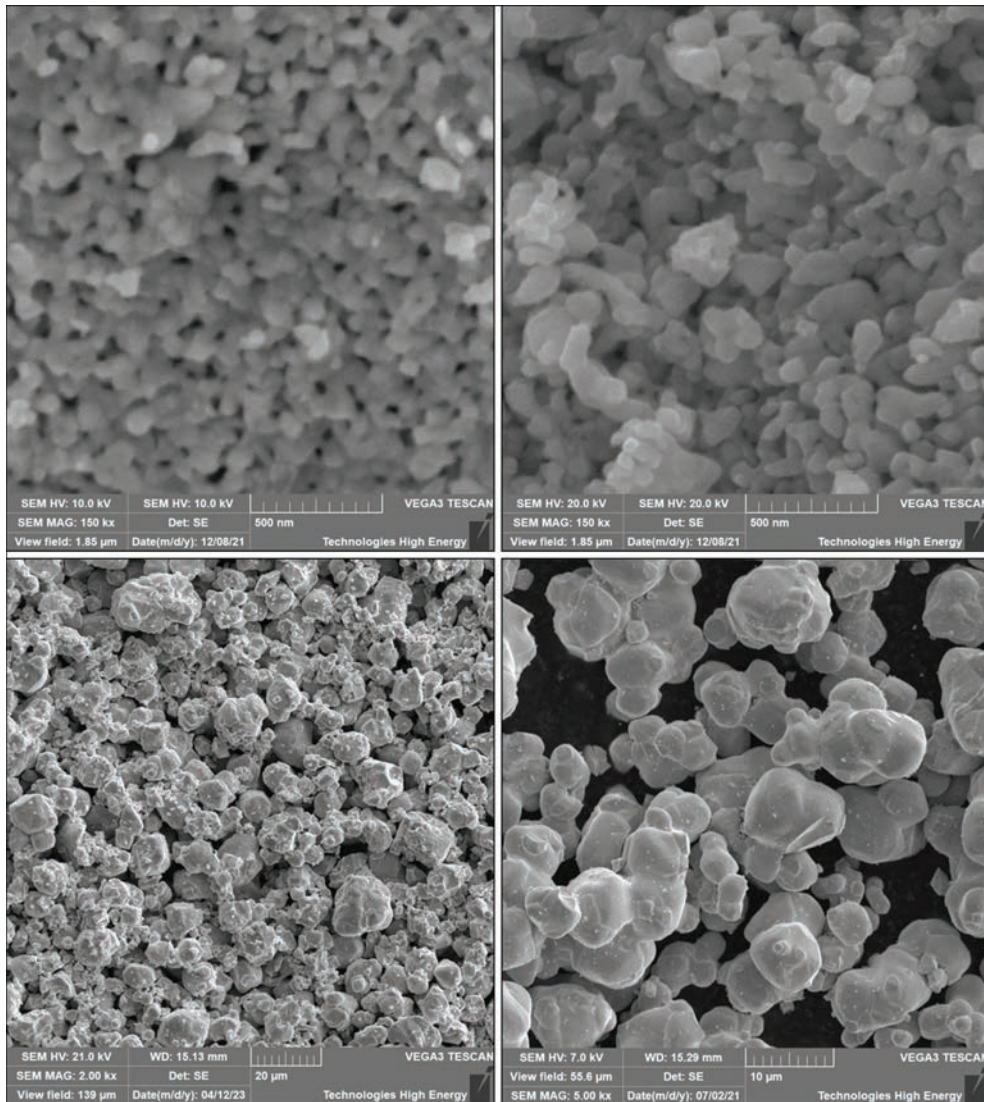


**Figure 1.** Morphology of particles of VK alloy powder

proportional to thickness  $S$  of the surface layer being irradiated and inversely proportional to temperature conductivity of material  $a$ , namely this time  $\tau \sim S^2/a$ . If, for example, for steels the temperature conductivity  $a = 0.05 \text{ cm}^2/\text{s}$  than cooling time makes  $\tau = 2 \cdot 10^{-5} \text{ s}$ . Such significant cooling rates allow eliminating intensive growth of carbide grains without growth inhibitors application.

Product mix produced using given technology includes metallurgical, rolling and guide rollers, rollers for straightening of wire in draw bench, various drawing tools, chipping knives, burrs, special products of military designation etc. (Figure 3).

#### UNIT FOR ELECTRON BEAM SINTERING OF HARD ALLOY BILLETS

The specialists of PWI together with the specialists of State enterprise “Engineering Center of Electron Beam Welding” developed and produced installation SV-229 for electron beam processing (EBP) of hard alloy preliminary sintered billets for the purpose of

their (final) sintering. General appearance of this installation is shown on Figure 4.

Except for innerchamber mechanisms this installation has a design mostly typical for electron beam welding equipment developed at the PWI with similar volume of vacuum chamber [8, 9]. A vacuum chamber (Figure 4, pos. 2) has a rectangular shape and inner volume approximately  $0.5 \text{ m}^3$ . Its door (Figure 4, pos. 3) moves left along the plane of front edge (flange) of chamber. Using movable screens the door is hanged on a longitudinal guide. The door is moved using a pneumatic cylinder. The chamber is fixed above rigid frame. A body of vertical pneumatic vacuum lock (Figure 4, pos. 4) is fixed using an arm to a hole on a back wall of the chamber. A running water trap and a diffusion pump are connected to it in series from the bottom. At some distance from them on the floor there is a mechanical forevacuum station which consists of the rotor and double-rotor pumps working in series. An electron beam gun (Figure 4, pos. 1) is dead fixed on a chamber roof and has strictly vertical orientation.

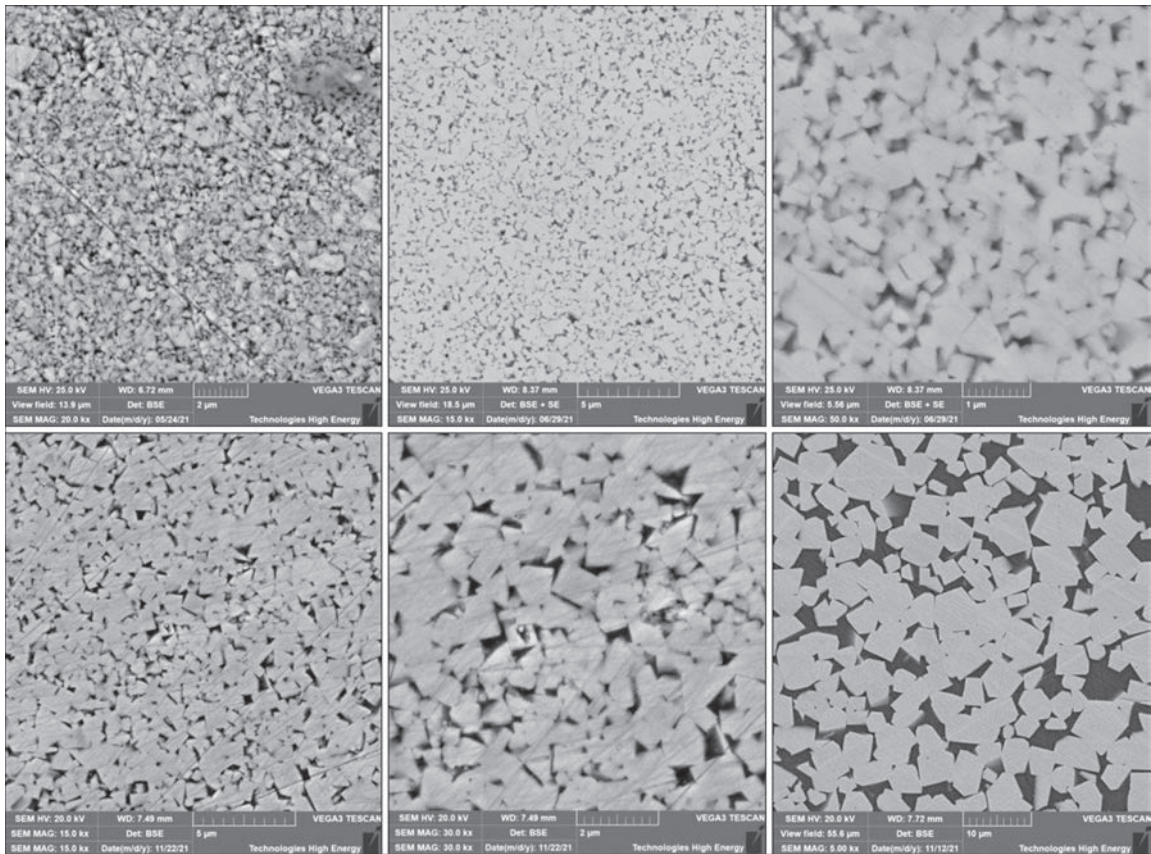


**Figure 2.** Microstructure of VK alloys produced by electron beam sintering

Usually it is a pneumatic gate valve isolating a source of gun electrons from the inner volume of vacuum chamber. Exhaust of a turbomolecular pump of the gun through a valve is connected with the volume of vacuum chamber, i.e. role of a step of prepumping of the gun is fulfilled by the volume of chamber itself. Productivity of the vacuum system of installation is sufficient for development of pressure of  $2 \cdot 10^{-4}$  mbar in the vacuum chamber and, respectively,  $5 \cdot 10^{-5}$  mbar in the gun for approximately 15 min.

Working place of installation operator is located on the right from the vacuum chamber before a control cabinet (Figure 4, pos. 5). Respectively, in the right wall of the chamber it is an inclined tube of the main window for visual observation of processes in the chamber (Figure 5).

A main display of the control cabinet is located at eye level of a person of average height standing on the floor. It displays the graphical interface of the installation control program (upper level for Windows OS), including the secondary emission monitoring system RASTR-6.

An additional display is fixed above the main display, which is designed for displaying the image from a camera (and also, if necessary, to display the operational information of the lower level control program for QNX OS). The video camera is installed on the roof of the vacuum chamber — opposite a small window.

On the front side of the control cabinet, there are also two industrial computers of the installation control system (upper and lower levels), a no-break power supply unit for these computers, an industrial keyboard and touchpad unit (for the upper level



**Figure 3.** Products manufactured by electron beam sintering method



**Figure 4.** Installation for EBP of hard alloy billets, where: 1 — electron beam gun; 2 — vacuum chamber; 3 — sliding doors; 4 — vacuum system; 5 — control cabinet; 6 — power cabinet; 7 — welding high-voltage power source cabinet; 8 — loading device for two feed drums of parts

computer), a converter of a turbomolecular gun of the pump, a control unit for the RASTR-6 secondary emission monitoring system, and a push-button control panel for welding high-voltage power source.

On the right of the control cabinet, close to it, there is a power cabinet (Figure 4, pos. 6) with a start-up control equipment of the vacuum system and control elements of the SIEMENS Sinamics S120 system. A cabinet of welding high-voltage power source 15 kW/60 kV, inverter type (Figure 4, pos. 7) is located a bit further to the right.

The installation is equipped with an autonomous water cooling system with an industrial chiller located to the left of the vacuum system.

In contrast to the above-described features, in fact, usual for electron beam equipment, the features of the installation related to the specifics of EBP are discussed below.

Both the vacuum chamber and the door of this installation have a hollow structure for cooling water circulation. This allows long-term EBP, including by ensuring the stability of the overall geometry of the

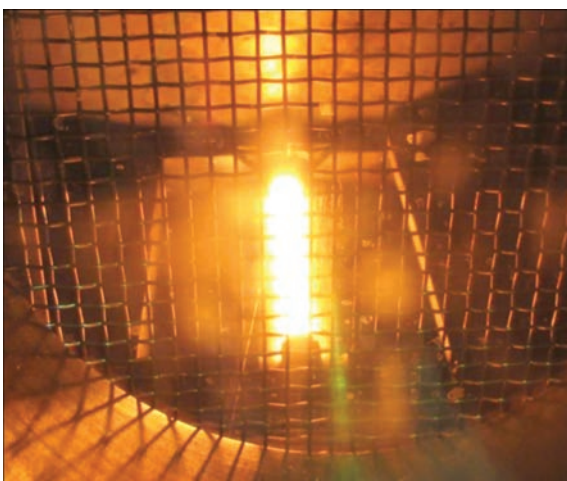


**Figure 5.** Observation of EBP process through main window

chamber, first of all spatial orientation of longitudinal axis of the electron beam gun.

To protect the main window from long-term thermal radiation and spraying in EBP process, there is a device on the inner wall of the chamber in the form of a pair of vertical metal flaps, the simultaneous opposite directed movement of which is provided by an external manual drive (its handle is located on the side of the window).

In addition to the above-mentioned window for the video camera, there is another small window on the roof of the vacuum chamber for the high-temperature pyrometer OPRIS CTratio 2M (which in two-color mode is designed for the temperature range from 550 to 3000 °C). Note that the proprietary pyrometer program is installed in the upper level computer and used in parallel with the installation main control program.

Both of the above-mentioned windows, for video camera and pyrometer, have a common manual shielding shutter, also for protection against heating and spraying during EBD. Thus, the installation provides only a relatively short-term visual observation (with a video camera or directly by eyes) of the EBP process as well as measurement of temperature of billets during processing. On the contrary, the secondary emission monitoring of the EBP process is constantly available.

These were auxiliary structural elements nevertheless related to the EBP process. Further the specific elements that directly participate in this process are considered.

First of all, it should be noted that this installation is intended for EBP of billets of only cylindrical outer surface, with *initial* diameter of 15–30 mm and length of up to 30 mm. Although in reality the design of installation allows for processing of a wider range billets, including those with a *final* diameter of only 6 mm, the basic configuration of installation provides equipment for only three dimension types of billets (initial diameter and length, respectively): 30×30 mm, 25×25 mm and 15×15 mm.

The following mechanisms are involved in the EBP technological cycle, namely a feed drum for parts to be processed; a mechanism of working rotation of parts (rotator), on which EBP is performed; a mechanism of line feed of parts at their loading on the rotator and unloading from it; a pallet for processed parts; as well as a loading device for two feed drums (Figure 4, pos. 8).

All billets that should be processed for one session of chamber pumping are located in the cells of the *feed drum* (Figure 6, pos. 4). In the chamber, the feed drum is hung on its left inner wall. For this two horizontal cylindrical guides (Figure 6, pos. 5) are attached to the wall, on which four support wheels

(rollers) of the feed drum base plate is tightly based on, so it can move freely along these guides to a limit stop. This stop, together with a clamp on the base plate, determines a working position of the feed drum in the chamber.

The installation has two identical feed drums. Each of them has a set of three replaceable inserts (Figure 6, pos. 7) with open cells along the outer perimeter, where the billets of three mentioned above dimension types are contained. The inserts are pushed on the outer diameter of the drum (Figure 6, pos. 8), and a guide key provides fixation against scrolling. The lateral dimensions of the cells in these inserts are different, therefore the number of cells in them is also different: 60 cells for “15 mm” dimension type, 40 — for “25 mm” and 36 for “30 mm”. The angular pitch between the cells is integer and equal to 6, 9 and 10°, respectively. The length of cells is the same and equal to 212 mm. The billets are kept from falling out of the open cells by an external immovable ring (Figure 6, pos. 9), that has a longitudinal gap from below (Figure 7, pos. 1). Close to this gap there is a pair of flaps (Figure 7, pos. 2), a longitudinal gap between which is set depending on billet dimension type. Thus, when the drum is rotated to a corresponding angular pitch, the billets fall down from a current lower cell into this gap (one of the successive loading operations of the rotator). The open ends of the cells are closed with a common cover (Figure 7, pos. 3), which is put on the drum edge and is quickly connected to it.

A base of drum rests through a pair of bearings on an immovable tubular shaft, which is attached normal to a base plate of the feed drum. To turn the drum, such a technical method as “carrier” is used. A bar connecting the edge flange on the drum base with a drive fork of this carrier passes through a hole of the tubular shaft. An outside slot of the fork is coupled (coupling/uncoupling is possible only at horizontal orientation of the fork) with a drive pin of electro-mechanical drive of drum rotation (Figure 6, pos. 6). Most of the elements of this drive are brought out through the vacuum chamber sealing. It is assumed that when the feed drum is uncoupled from the drive, in particular, when the feed drum is outside the vacuum chamber, to prevent spontaneous rotation of the drum, the operator must fix it manually with the help of a locking clamp. In the future, when the feed drum is next time coupled with the drive, this clamp is automatically removed.

Thus, an axis of feed drum rotation and, respectively, all the cells are oriented along the chamber longitudinal axis. Moreover, both axes, the axis of drum rotation and the axis of the drive of this rotation, co-

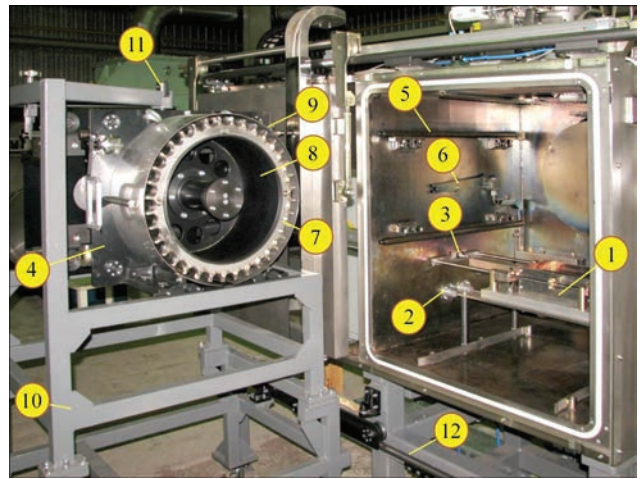


**Figure 6.** General appearance of most mechanisms related with EBP, where: 1 — mechanisms for rotation of parts; 2 — its drive; 3 — mechanism of line feed of parts; 4 — feed drum of parts; 5 — guides for its suspension in chamber; 6 — its drive; 7 — replaceable insert with cells for parts; 8 — rotating feed drum; 9 — outer ring of feed drum; 10 — frame of loading device; 11 — its swivel block of suspension for both feed drums; 12 — horizontal bearing guide of this device

incide and approximately intersect with longitudinal axis of the electron beam gun.

The feed drum is filled with billets outside the vacuum chamber and only then moved into it. A *loading device* is used for such operations. This is a frame structure (Figure 6, pos. 10), in the upper part of which there is a swivel block of rack suspension (Figure 6, pos. 11), which is designed for two feed drums. These are two pairs of racks that are similar to those installed in the chamber and located in two parallel

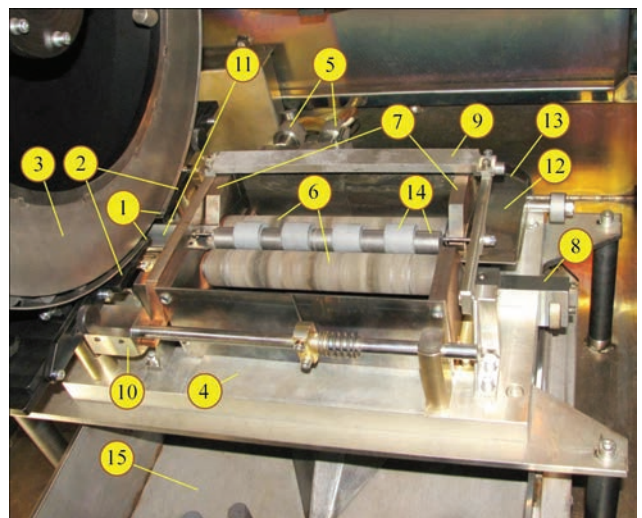


**Figure 7.** Inner elements of chamber for EBP (close-up), where: *a* — elements of feed drum: 1 — gap in outer ring; 2 — pair of low longitudinal flaps; 3 — edge cover of drum; *b* — rotator elements: 4 — base plate; 5 — its water cooling; 6 — working rolls; 7 — pair of bearing webs of one of rolls; 8 — template for rolls positioning; 9 — lift frame of part stoppers; 10 — block cam of its clamp; 11 — delivery tray; 12 — sloping uploading tray; 13 — screw tray; *c* — other: 14 — billets and graphite inserts; 15 — pallet for processed parts

planes equidistant from a vertical axis of rotation. The drums of suspended feed drums are turned outside in opposite directions and can switch positions when the suspension assembly is rotated by  $180^\circ$ .

The corresponding structural measures were used to move the feed drum in and out of the vacuum chamber. The loading device is placed in front of the chamber door (without interfering with its movement). From the end far from the door, the device rests on workshop floor by two swivel wheels. From the near end, it rests by two rollers on a horizontal guide (Figure 6, pos. 12) attached to the chamber frame parallel to plane of its door frame. Thus, the device can be manually moved along the guide from stop to stop. In the extreme left position, the device does not interfere with free access to the chamber door opening. Respectively, the rightmost position is a position of joining with the chamber guides, when the current right pair of device guides should be in the same plane with the pair of chamber guides. The spring-loaded clamp prevents willful longitudinal displacement of the device from this position. In addition, the parallelism of the guides of the device to the plane of the chamber guides provides a clamp of rotation angle of rack suspension assembly of this device. Finally, for the direct (manual) movement of the feed drum between the guides of the loading device and the chamber there is an easy to mount changeable guide bridge installed in a gap between them.

It is assumed that in the arranged production cycle, during each chamber pumping session (to perform EBP), the previously filled feed drum is located in the chamber, and the current right pair of guides of the loading device remains empty waiting for the return movement of this, already empty, feed drum from the chamber. Respectively the second feed drum is located on the left pair of guides of this device during pumping. It is usually empty, therefore, before the end of pumping, an operator should manually fill each feed drum cell with the appropriate number of billets (depending on dimension type). The cylindrical graphite inserts are located the extreme position from both ends of each cell. An intermediate chain of hard alloy billets and graphite inserts is placed between them. There should be 3 billets for dimension type "30", 4 — for "25" and 6 — for "15", respectively. In general, only billets can be placed between the last inserts, and this will increase the total number of billets treated at a time, however it is more reliable to use intermediate inserts. The first, lowest, cell is always left empty, because it is located above the longitudinal gap in the outer ring of the feed drum.

The main element of the *parts rotation mechanism* (rotator) is a pair of graphite rolls with a cylindrical

working surface of 208 mm long (Figure 7, pos. 6). Synchronous rotation of the rolls ensures uniform rotation of the billets (Figure 7, pos. 14) during EBP. The thinner ends of the rolls rest on bearing sleeves that are fixed in the holes of vertically located copper webs (Figure 7, pos. 7). The latter are attached by their lower edges to a massive horizontal base plate (Figure 7, pos. 4), which has internal channels for water cooling (Figure 7, pos. 5). The distance between the rolls is regulated depending on billets dimension type, so that the contact angle of the rolls with the raw billet and with it after sintering changes approximately from  $110$  to  $125^\circ$ . At that, the rolls should be symmetrical relative to the vertical longitudinal plane along which technological longitudinal oscillation of electron beam is performed (the maximum length of the electron beam scanning at this working distance is not less than 190 mm). A special movable template (Figure 7, pos. 8) facilitates setting a necessary distance in compliance with the above condition.

The drive end of each of the rolls (from the left side of the chamber wall) is connected with a joint electromechanical drive (Figure 6, pos. 2) through a double cardan joint. The drive is also brought outside through the vacuum chamber sealing.

The stoppers at both ends of rolls working surfaces (the distance between them is 210 mm) prevent axial displacement of billets from processing area. The rods of the stoppers are fixed in the side walls of U-shaped frame (Figure 7, pos. 9). The open side of this frame has a pivot connection with two vertical brackets attached to the base plate. In a free state, from the closed side, the frame rests on the stop on the far left web. When the frame is raised, the movable spring-loaded clamp with its cam (Figure 7, pos. 10) can block such a state of the frame and this allows passage of billets under it during loading of the rotator.

A V-shaped delivery tray (Figure 7, pos. 11) is located near the left edge of the working surface of the rolls — along the above-mentioned vertical longitudinal plane. The billets from the feed drum fall into it when turning the drum "per one cell". The height of the tray location is adjusted depending on billet dimension type so that the points of contact of billets with sloping walls of the tray are slightly higher than the points of contact with the rolls. This allows easy movement of billets from the tray to the working rolls.

On the right end of the rotator there is a sloping unloading tray (Figure 7, pos. 12) for receiving already treated parts from the rolls. The level of this transfer is regulated by the tray slop — depending on the size of the compacted billets. The opposite end of this tray passes into a screw tray (Figure 7, pos. 13), which ensures rolling of treated billets and inserts into a *pallet*

(Figure 7, pos. 15), which lies on the floor of vacuum chamber (which, as already mentioned, is cooled by water). Two identical pallets are provided — for quick replacement of a filled pallet with an empty one. To remove the filled pallet from the chamber (of course, after opening its door), there is a manual forklift hoist, which is made based on standard product. You can install an empty pallet into the chamber both with the help of this hoist and manually.

A *longitudinal feed mechanism* is, in fact, an industrial linear actuator (electric cylinder) with a rod working stroke of up to 600 mm. The actuator itself is located outside the vacuum chamber, and its elongated rod enters the chamber through a seal. A tip of a special shape is fixed at the end of the rod. It is of such shape because this mechanism performs several other related operations in addition to feeding raw billets to the rotator and unloading compacted billets from it. Firstly, at the stage of unloading the treated billets from the rotator rolls (after their EBP), the rod begins to move from a zero position in the direction to the billets; before reaching them, the tip of the rod, due to slope shape of its front part, lifts the frame of the rotator stoppers, and then the open side of the frame (the extended end of its left side wall) is blocked by the cam of the spring-loaded clamp — this condition is necessary for the next stage of billets loading on the rotator. Secondly, at the stage of this loading, after the rod feeds (shifts) a portion of untreated billets from the delivery tray of the rotator to its working rolls, the rod is returned to the zero position; at that, the tip of the rod with its rear edge catches and shifts the spring-loaded clamp to the left, pulling its spring; immediately near the zero position of the rod, the cam of the clamp releases the frame of the stoppers of rotator and it under its weight goes down to the state required for the next EBP.

The *algorithm of interaction* of all these mechanisms for EBP is described below. For example, let's take a condition of regulated production process, when the full EBP cycle is completed for all the billets placed in the feed drum at current chamber pumping session, atmospheric air is blown into the chamber and its door is opened. At that, in the (empty) feed drum, an initial cell is again located from the bottom and, respectively, the drive "carrier" stands horizontally and faces doorway with its fork. At this moment, second (already filled) feed drum is located on the left guides of the loading device, and the right guides are, respectively, empty. Then the operator performs the following actions.

He moves the loading device to the position of joining with the chamber guides and installs the guide bridge. After that, the operator unlocks the movement

of the feed drum (in the chamber), rolls it onto the rods of loading device (firmly) and fixes this position, as well as the feed drum. Then, the operator swaps the feed drums. For this he temporarily removes the guide bridge, unlocks a swivel block of rack suspension of the loading device, turns it by 180° and locks it again. Thus, the filled feed drum is already on the right rods. Then the operator again installs the guide bridge, unlocks the movement of this feed drum, rolls it into the chamber (firmly) and fixes this (working) position. At that, the "carrier" fork will already be coupled with the drive pin of rotation drive of feed drum, and the bolt clamp of the drum will be taken out. Next, the operator finally removes the rod bridge and moves the loading device away from the doorway (firmly).

In addition, with the help of a forklift hoist, the operator pulls out a pallet filled with treated billets (and graphite inserts) from the chamber and installs a second, empty pallet in its place.

The correct position of the internal chamber mechanisms at this time is as follows: the rod of line feed mechanism (actuator) is in a zero position, accordingly, the frame of the rotator stoppers is lowered. In addition, the rotator rolls are empty. Therefore, the operator should manually load the last batch of billets and graphite inserts on the rolls (because the bottom cell of the drum is empty).

After pumping the chamber and gun and turning on a high-voltage power source, the operator immediately starts the EBP program cycle. It repeats the same sequence of operations cyclically. The number of such repetitions is equal to the number of loaded portions of billets of a specific dimension type, i.e. portions in  $(n-1)$  cells of the feed drum plus one portion on the rolls. In other words, this is the total number of cells of the feed drum ( $n$ ).

The abovementioned repeated sequence of operations includes: firstly, direct EBP of a portion of the billets, secondly, operations of unloading a portion of treated billets from the rotator rolls, and, thirdly, operations of loading a portion of still untreated billets onto the rotator rolls.

EBP of a portion of billets starts with a programmed launch of working rotation of the rolls and longitudinal oscillation of the electron beam. The "length" of this technological scanning of the beam covers the entire chain of billets as well as about half of the length of the extreme graphite inserts contacting with the rotor stoppers (that is, it is not less than 190 mm). Only in the presence of these two factors, it is possible to turn on electron beam current. A defocused electron beam which performs scanning along a linear trajectory develops a heat source necessary to perform a thermal cycle of processing of all hard alloy

billets rotating on the rolls at the same time. It is necessary to note that the program that generates beam oscillation, including distribution of power density along its trajectory, can be adjusted by the user with the help of a special software interface. A time-programmed change of power of the electron beam determines a heating rate, holding time and cooling rate of the billets.

Unloading is performed in the following sequence: the actuator rod begins to move from a zero position in the direction of the rotor rolls; on this way, it firstly raises a frame of the rotator stoppers and then it is blocked with a cam of the spring-loaded clamp; then the actuator rod one by one pushes the treated billets (and graphite inserts) from the rolls onto a sloping tray, from which they roll onto the screw tray and down it into a pallet; after this, the rod is moved in the reverse direction, and stops at some distance from a zero position — when the tip of the rod no longer interferes with fall of a portion of billets from the feed drum into the delivery tray of the rotator, but the raised frame of its stoppers is still blocked.

Loading is performed in the following sequence: a drive of the feed drum turns the drum to the corresponding angular pitch and a portion of raw billets (and graphite inserts) from a feed drum cell through its lower gap falls into the delivery tray of the rotator; then the actuator rod shifts (feeds) this chain onto the rotator rolls (to the EBP position); finally, the rod moves back to the zero position, in which the raised frame of the rotator stoppers is unlocked and then lowered in a position necessary for next EBP.

Let's note the peculiarity of completion of EBP program cycle. After unloading the last ( $n$ -th) portion of treated (sintered) billets from the rolls of the rotator, in fact, there is nothing to load because the feed drum is already empty. But such an "empty" loading is necessary for the uniformity of the entire cyclic process. Then the feed drum will finally make a full revolution, i.e. it will be in the initial position, in which the drive "carrier" is oriented horizontally and faces the doorway. In addition, the actuator rod will be in a zero position and, respectively, the frame of the rotator stoppers will lower to a position necessary for EBP already in the next session of chamber pumping.

## CONCLUSIONS

1. An industrial technology has been developed for manufacture of WC–Co alloy powders from production wastes, their precision pressing into various

shapes and electron beam high-speed sintering of semi-finished products.

2. There was developed and produced a high-performance installation for electron beam processing of hard alloy previously formed billets used for sintering and obtaining the necessary service characteristics.

## REFERENCES

1. Shiller, Z. Gajzig, U., Pantser, Z. (1980) *Electron beam technology*. Moscow, Energiya [in Russian].
2. Dietrich v. Dobeneck (2007) *An International History of Electron Beam Welding*. Pro-beam AG & Co. KGaA.
3. (2017) *Electron beam additive manufacturing (EBAM)*. <http://www.sciaky.com/additive-manufacturing/electron-beam-additive-manufacturing-technology>
4. Nesterenkov, V.M., Matvejchuk, V.A., Rusynik, M.O. (2018) Manufacture of industrial products using electron beam technologies for 3D-printing. *The Paton Welding J.*, **1**, 24–28. DOI: <https://doi.org/10.15407/tpwj2018.01.05>
5. *Tungsten Statistics and Information by National Minera Information Center*. USGS. <https://www.usgs.gov/centers/national-minerals-information-center/tungsten-statistics-and-information>
6. *Tungsten ores*. VUE, URL. [https://vue.gov.ua/Вольфрамові\\_рудиди](https://vue.gov.ua/Вольфрамові_рудиди)
7. Rykalin, N.N. et al. (1985) *Laser and electron beam processing of materials*. Moscow, Mashinostroenie [in Russian].
8. Nesterenkov, V., Khripko, K. (2017) Recent achievements of E.O. Paton Electric Welding Institute in development of equipment for electron beam welding. *ZVÁRAČ Profesionál*, XIV(2), 9–13.
9. Nazarenko, O.K., Kajdalov, A.A., Kovbasenko, S.N. et al. (1987) *Electron beam welding*. Ed. by B.E. Paton. Kyiv, Naukova Dumka [in Russian].

## ORCID

V.M. Nesterenkov: 0000-0002-7973-1986,  
K.S. Khripko: 0000-0002-4893-5441,  
M.O. Sysoev: 0000-0001-7243-2388,  
V.V. Chernyavskiy: 0000-0001-9820-0809

## CONFLICT OF INTEREST

The Authors declare no conflict of interest

## CORRESPONDING AUTHOR

V.M. Nesterenkov  
E.O. Paton Electric Welding Institute of the NASU  
11 Kazymyr Malevych Str., 03150, Kyiv, Ukraine.  
E-mail: [nesterenkov@technobeam.com.ua](mailto:nesterenkov@technobeam.com.ua)

## SUGGESTED CITATION

V.M. Nesterenkov, K.S. Khripko, V.V. Lukyanov, M.O. Sysoev, V.V. Chernyavskiy (2023) Technology and equipment for electron beam sintering of hard alloy billets. *The Paton Welding J.*, **8**, 65–72.

## JOURNAL HOME PAGE

<https://patonpublishinghouse.com/eng/journals/tpwj>

Received: 21.07.2023

Accepted: 07.08.2023

# PLASMA TORCH FOR PLASMA TRANSFERRED ARC SURFACING WITH TWO POWDER FEEDING SYSTEMS

O.I. Som

Plasma-Master Co., Ltd.  
52 Popudrenko Str., 02094, Kyiv, Ukraine

## ABSTRACT

A new design of the PTA torch (PTA torch) for surfacing of nickel, cobalt and iron-based alloys was developed. It combines two systems of powder feeding into the arc: the internal and external one. Such a combination expands the technological capabilities of the PTA torch, and allows surfacing magnetic and nonmagnetic materials. These systems can be used both separately from each other and together for surfacing composite alloys with separate feeding of the matrix and reinforcing powder material. In order to increase the efficiency of powder heating at external feeding into the PTA torch, an auxiliary stabilizing gas flow is used, which allows reducing the powder losses by 10–15 % and improving the deposited bead formation. Optimal flow rates of stabilizing gas are 4–5 l/min. The PTA torch effectively operates in the current range of 50–300 A.

**KEYWORDS:** plasma transferred arc surfacing, PTA torch design, powder feeding systems, heating efficiency

## INTRODUCTION

The PTA torch is the main working tool of equipment for plasma transferred arc surfacing. The quality and stability of the surfacing process as a whole depends in many respects on its efficient and reliable operation. In its turn, the efficiency of PTA torch operation is determined by its thermal characteristics and effectiveness of heating and melting of powder in the arc, which greatly depends on the scheme and parameters of its feeding into the arc.

At present two schemes of powder feeding into the arc are the most widely used: internal and external [1–3]. In the first case (Figure 1, *a*), the powder is fed into the arc from inside the PTA torch in the form of a flow of particles uniformly distributed around a circle through a conical slot formed by the plasma and focusing nozzles. In the second case (Figure 1, *b*), it is

fed from outside the PTA torch through one or several openings in the end face of the plasma nozzle. In this case the focusing nozzle is not used.

Mathematical model [1] and experimental studies performed by the author [3, 4] show that the internal scheme of powder feeding is more efficient. It ensures lower powder losses, better formation of the deposited bead, and lower power consumption at the same deposition rate. This scheme, however, has two significant disadvantages. First, at long-term surfacing, particularly of low-melting materials, liquid metal drops can form at the outlet of the focusing nozzle, which leads to violation of the process stability, blocking of powder feed and deterioration of the deposited bead formation.

Secondly, surfacing of ferromagnetic materials with a large quantity of the ferrite phase in their struc-

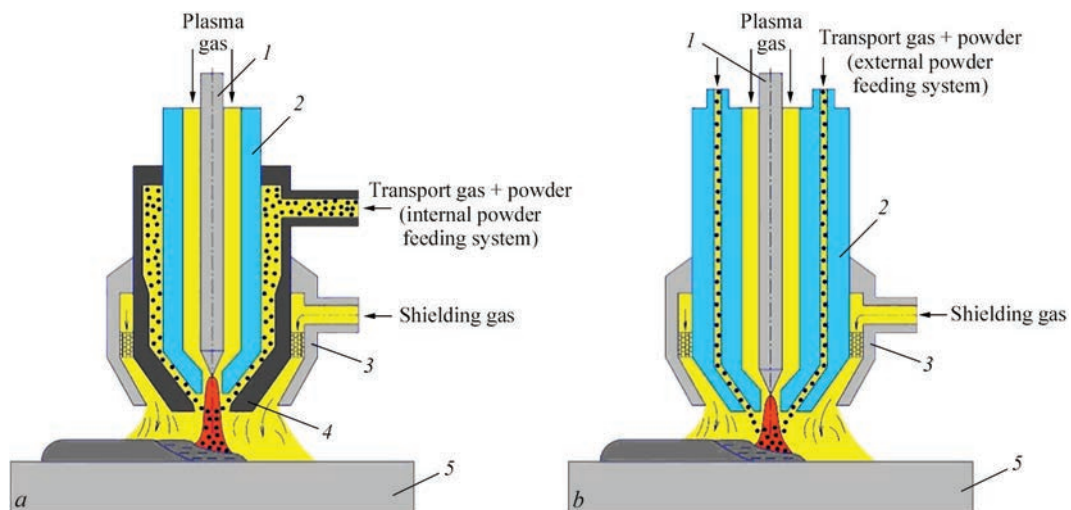


**Figure 1.** Schemes of powder feeding into the arc: *a* — internal; *b* — external (1 — electrode; 2 — plasma nozzle; 3 — shielding nozzle; 4 — focusing nozzle; 5 — part)

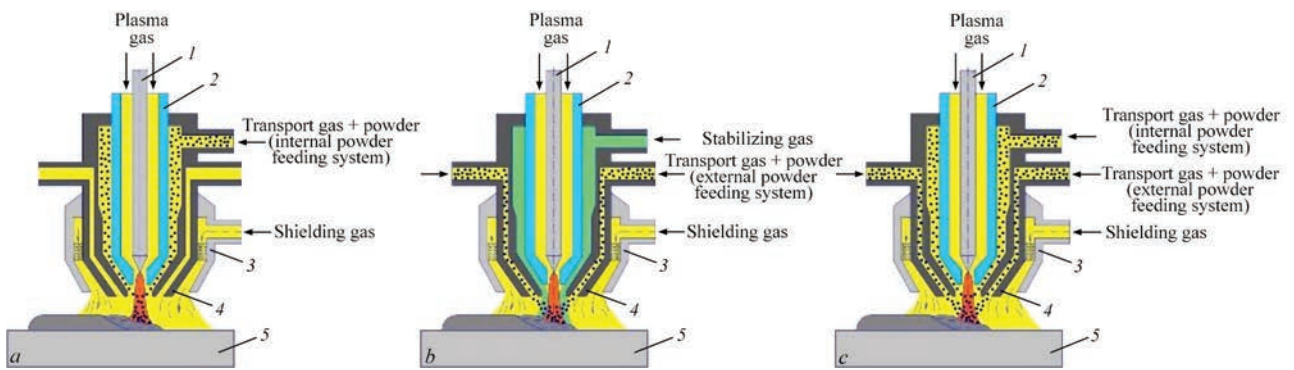


**Figure 2.** Scheme of PTA torch nozzle part with different variants of powder feeding into the arc: *a* — internal; *b* — external with stabilizing gas; *c* — combined (internal + external); 1 — electrode; 2 — plasma nozzle; 3 — shielding nozzle; 4 — focusing nozzle; 5 — part

ture is complicated. Under the impact of the magnetic field of the arc, the powder particles hang in the PTA torch distribution chamber, forming a kind of plugs. This is the most noticeable at current above 150 A. This drawback is absent with external scheme of powder feeding.

The objective of this work was to combine these two schemes in one PTA torch and to develop such a design of the nozzle part, which would expand its technological capabilities and improve the operation stability.

**FEATURES OF THE NEW PTA TORCH DESIGN**

Figure 2 shows the schematic of the PTA torch nozzle part, which combines the internal (Figure 2, *a*) and external (Figure 2, *b*) schemes of powder feeding. These schemes can be used both separately from one another and together (Figure 2, *c*; 5, *c*). The latter variant is highly effective at surfacing composite alloys with separate feed of matrix and reinforcing materials [5]. In this case, two separate powder feeders, operating synchronously, are used, as well as two separate flows of transport gas.

This idea was the base for development of two PTA torch variants: vertical (Figure 3, *a*) and horizontal (Figure 3, *b*) modifications. They have the same design of the nozzle part. Selection of either variant depends on the design features of surfacing equipment layout. The horizontal variant is more versatile, as it allows surfacing both the internal and external surfaces to different depth.

**Technical characteristics of the PTA torch**

Current of indirect (pilot) arc, A	30–50
Direct arc current at duty cycle of 100 %, A	50–300
Kind of current	direct
Polarity	straight
Working gas	argon
Deposition rate, kg/h	1.0–8.0
System of powder feeding into the arc	internal and external
Powder particle size, μm:	
internal system	63–200
external system	53–150
Powder losses, %:	
internal system	< 5
external system	5–10
Total gas flow rate, l/min	14.0–22.0
Cooling system	liquid
Cooling liquid flow rate, l/min	> 4.0

PTA torches allow surfacing nickel, cobalt and iron-based alloys and composite alloys based on tungsten carbides.

**POWDER FEED VARIANTS. INTERNAL POWDER FEED**

When the system of internal feeding is used, the powder through inlet nipple 1 (Figure 3, *a, b*) enters a special distribution chamber, where it is uniformly distributed around a circle by the transport gas and then is blown into the arc through a system of slots uniformly located on the conical surface of the plasma nozzle (Figure 4). The slots promote better cooling of the nozzle and direct the powder particles straight into the most heated central part of the arc. The angle of powder entering the arc is equal to 35° relative to the vertical. The focus of powder particles collision is located at 5 mm distance below the end face of the

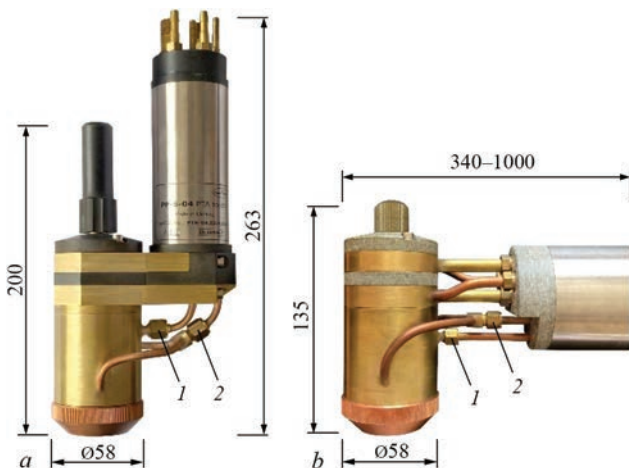


**Figure 3.** Appearance of PTA torches with two systems of powder feeding: *a* — vertical type PP-6-04; *b* — horizontal type PP-6-03M

focusing nozzle (Figure 5, *a*). This is done so as to eliminate powder particles hitting the focusing nozzle walls and thus to improve the reliability of PTA torch operation.

For effective heating of powder in the arc, the initial velocity of particles entering the arc should be as small as possible [1]. In this PTA torch, it was possible to bring this parameter to a minimal value, due to original design of the distribution chamber and optimization of transport gas flow rate. For a PTA torch of vertical type, it is equal to 1.5–2.0 m/s, for horizontal type it is 2.0–2.5 m/s, that is quite acceptable for heating powder particles of 50–160 μm diameter, which are widely used for PPS process [6]. To maintain such velocities of powder flowing out, the optimal flow rate of transport gas is 3.5–4.0 l/min for the vertical variant and 4.5–5.0 l/min for the horizontal one. Particle movement velocity was determined by photographic method of time-lapse photography [7].

**EXTERNAL POWDER FEED**

With this scheme the powder together with the transport gas is divided into two uniform flows through a special tee-nipple (Figure 3, *a*, *b*), and is then fed into the arc through two openings of 1.4 mm diameter, located on the focusing nozzle end face diametrically opposed to one another. The angle of powder entering the arc is the same as at internal feeding — 35°. The point of powder particle colli-



Figure 4. Appearance of plasma nozzle

sion is located at 8 mm distance below the focusing nozzle end face (Figure 5, *b*). The velocity of powder particles flowing out at the PTA torch outlet is noticeably higher than at internal feed both in the vertical and in the horizontal modification, and it is equal to 2.5–3.0 and 3.0–3.5 m/s, respectively. This is an essential disadvantage of this scheme of powder feeding into the arc, as increased velocity head of the cold transport gas flow penetrates deeply into the arc column, deforms it (Figure 6, *b*) and lowers the plasma temperature in the heating zone. Arc deformation leads to deterioration of powder heating, and, consequently, to increase of its losses and worse formation of the deposited bead.

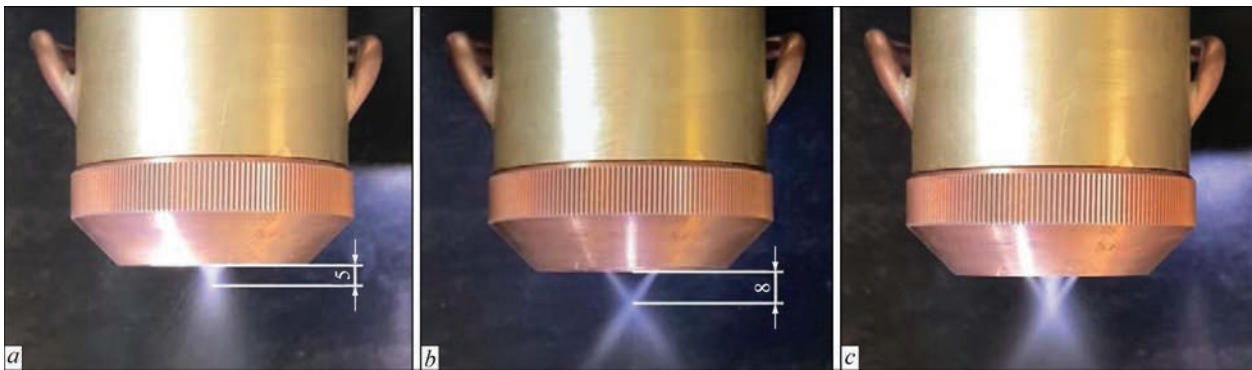


Figure 5. Appearance of plumes of powder flowing out of the PTA torch with internal (*a*), external (*b*) and combined (*c*) powder feeding schemes

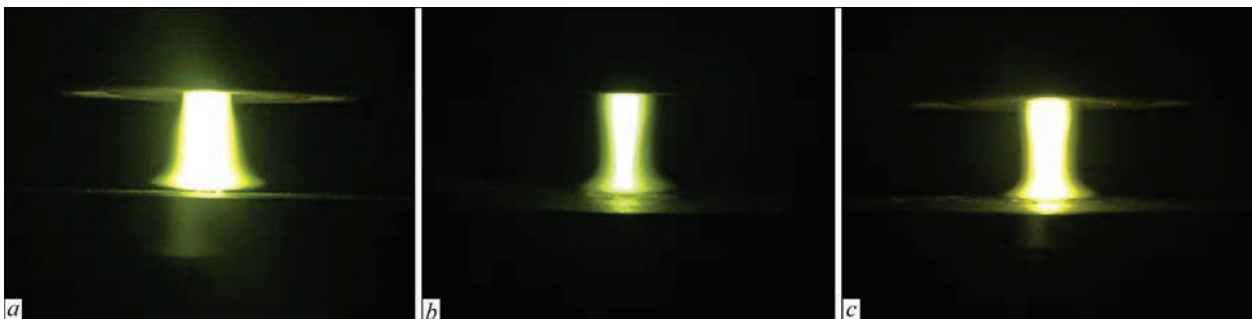
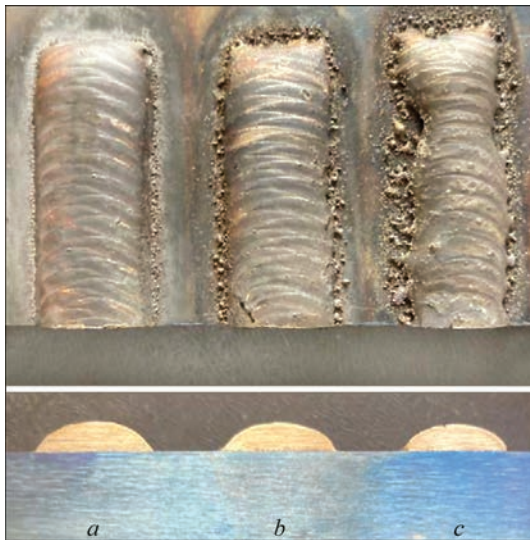
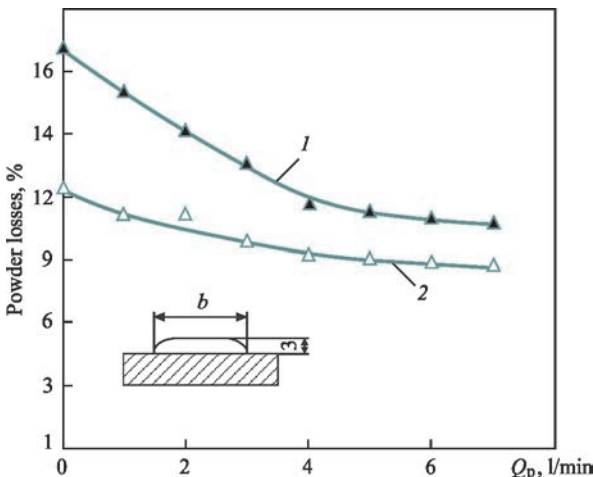


Figure 6. Appearance of arc columns at internal (*a*), external (*b*) and combined (*c*) schemes of powder feed



**Figure 7.** Appearance and cross-section of beads deposited in the same modes at different schemes of powder feeding into the arc: *a* — internal; *b* — external with stabilizing gas; *c* — external without stabilizing gas. Surfacing mode:  $I_a = 160$  A;  $V_d = 80$  mm/min;  $G_f = 16$  g/min;  $Q_{st.g} = 4$  l/min, deposited material is 304 stainless steel

In order to neutralize this harmful impact, in this PTA torch a gas flow is used, which is blown into the central orifice of the focusing nozzle, similar to transport gas feeding with internal system of powder feed. This flow has a stabilizing role. Concentrically washing the peripheral region of the arc from above, it is heated well, and ousts the cold flows of transport gas in the area of lateral entry of powder. The arc column is straightened, taking a more cylindrical shape (Figure 6, *c*), and it becomes close to the arc shape at internal powder feed (Figure 6, *a*). The spatial stability of the arc is improved, allowing increase of its length to 14–15 mm, and thus raising the powder heating temperature owing to its longer stay in the arc. Due to that, powder losses decrease by 10–15 % relative to external feed without the stabilizing gas, and deposited bead formation is improved. Figure 7 shows



**Figure 8.** Dependence of powder losses on stabilizing gas flow rate at different bead width *b*: 1 — 10; 2 — 20 mm

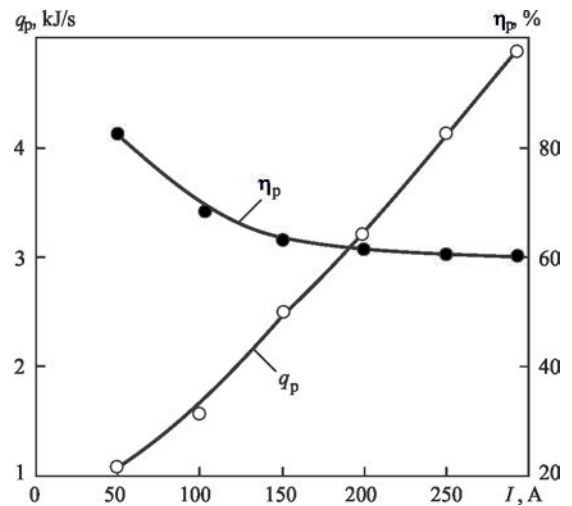


**Figure 9.** Dependence of effective thermal power  $q_p$  and effective efficiency of part heating  $\eta_p$  on arc current in the developed PTA torch

the appearance, as well as the cross-section of beads, deposited in the same modes with different schemes of powder feeding into the arc. In it one can clearly see that the additional (stabilizing) gas flow essentially improves bead formation (Figure 7, *b*), making it more similar to the appearance of the bead deposited with internal powder feed (Figure 7, *a*).

Bead fullness is also increased, which is a confirmation of smaller powder losses (Figure 7, *b*). As shown in Figure 8, the maximal effect is achieved at stabilizing gas flow rate of 4–5 l/min. This is valid both for narrow (curve 1), and for broad (curve 2) beads. A further increase of its flow rate no longer enhances the positive effect.

### THERMAL CHARACTERISTICS

Thermal characteristics of the developed PTA torch were studied by the method of flow calorimetry on a model sample by a procedure described in [3]. Attention was focused on investigation of effective thermal power and effective efficiency of part heating for the given design of the nozzle part of the PTA torch. Investigations were conducted without the indirect (pilot) arc.

Figure 9 showed that the dependence of effective thermal power  $q_p$  and effective efficiency of part heating  $\eta_p$  on arc current for a combination of plasma and focusing nozzles of 4/8 mm at flow rates of plasma (2 l/min), transport (4 l/min) and shielding (8 l/min) gases, characteristic for plasma surfacing.

One can see that with increase of arc current  $q_p$  grows practically linearly, but  $\eta_p$  decreases. In the range of currents of 50–250 A, it decreases from 80 to 60 %, which is related to increase of heat losses at the nozzle. On the whole, this index is sufficiently high, close to those for welding and cutting PTA torches [8].

**CONCLUSIONS**

1. Combination of internal and external schemes of powder feeding into the arc in one PTA torch significantly widens its technological capabilities, as it allows surfacing of magnetic and nonmagnetic materials with a high efficiency and productivity.

2. Additional flow of stabilizing gas with the external scheme of powder feeding reduces the harmful influence of cold flows of transport gas and lowers the powder losses by 10–15 % due to its more effective heating. Optimal flow rate of stabilizing gas is equal to 4–5 l/min.

3. Developed PTA torch ensures a high enough efficiency of part heating. It is not lower than 60 % at maximal currents.

**REFERENCES**

1. Gladky, P.V., Pavlenko, A.V., Zelnichenko, A.T. (1989) Mathematical modeling of heating of powder in arc during plasma surfacing. *Avtomatich. Svarka*, **11**, 17–21, 54 [in Russian].  
 2. Dilthey, U., Ellermeyer, J., Gladkij, P., Pavlenko, A.V. (1993) Kombiniertes Plasma-Pulver-Auftragschweißen. *Schweißen und Schneiden*, **5**, 241–244.  
 3. Som, A.I. (1999) New plasmatorches for plasma-powder surfacing. *Avtomatich. Svarka*, **7**, 44–48 [in Russian].

4. Som, A.I. (2015) Effect of scheme of powder feeding into arc on its losses and efficiency of plasma-powder surfacing process. *The Paton Welding J.*, **5–6**, 22–25.  
 5. Som, A.I., Halahuz, B.A. (2020) Plasma transferred arc surfacing of composite alloys with separate feed of tungsten carbides and matrix alloy. *The Paton Welding J.*, **12**, 34–39. DOI: <https://doi.org/10.37434/tpwj2020.12.05>  
 6. Gladky, P.V., Pereplyotchikov, E.F., Ryabtsev, I.A. (2007) *Plasma surfacing*. Kyiv, Ekotekhnologiya [in Russian].  
 7. Sidorov, A.I. (1987) *Restoration of machine parts by spraying and surfacing*. Moscow, Mashinostroenie [in Russian].  
 8. Stikhin, V.A., Patskevich, I.R. (1967) Determination of thermal characteristics of constricted arc. *Svarochn. Proizvodstvo*, **9**, 26–27 [in Russian].

**CORRESPONDING AUTHOR**

O.I. Som  
 Plasma-Master Co., Ltd.  
 52 Popudrenko Str., 02094, Kyiv, Ukraine.  
 E-mail: [info@plasma-master.com](mailto:info@plasma-master.com)

**SUGGESTED CITATION**

O.I. Som (2023) PTA torch for plasma transferred arc surfacing with two powder feeding systems. *The Paton Welding J.*, **8**, 73–77.

**JOURNAL HOME PAGE**

<https://patonpublishinghouse.com/eng/journals/tpwj>

Received: 28.06.2023  
 Accepted: 07.08.2023

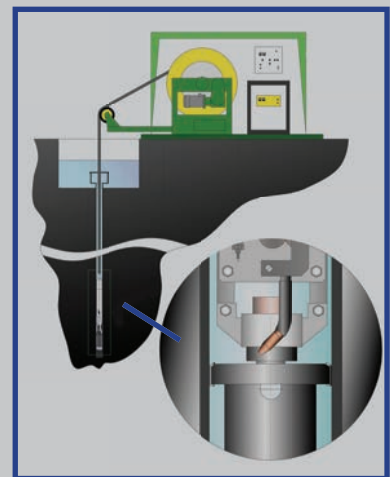
**UNDERWATER WELDING AND CUTTING**

**DEVELOPED IN PWI**



**Unique complex for automatic arc welding at great depth**

- The technology and equipment allows automatic welding of structural elements, which seal from the inside the lower part of heat exchanger column, using a method of wet arc welding with flux-cored wire.
- Work originality lies in development of automatic welding machine, which can operate when it is immersed in 119 mm diameter pipe at 200 m depth in liquid heat-carrying agent medium. The complex was successfully tested in GDE Company facility, London.
- Welding complex can be used in welding, surfacing and cutting of vertical steel product pipelines operating in water medium.



Automatic welding machine at 200 m depth

DOI: <https://doi.org/10.37434/tpwj2023.08.11>

# EVOLUTION OF ELECTRON BEAM HARDWARE FOR WELDING IN SPACE

**S.O. Hlushak**

E.O. Paton Electric Welding Institute of the NASU

11 Kazymyr Malevych Str., 03150, Kyiv, Ukraine

## ABSTRACT

The paper deals with application of welding and conducting repair-restoration operations in space, as well as evolution of the design of electron beam tool over several decades. Technical characteristics and technological capabilities of all the generations of hardware and requirements to it at different operation stages are described. Substantiation is provided for electron beam welding being the most suitable process for application under lower gravity conditions. Specification of “Vulcan” automatic unit is given, in which welding experiments were conducted for the first time in space. Specification of the versatile hand tool (VHT) is provided, and its capabilities are described during performance of operations of welding and other related technological processes, namely cutting, brazing, coating deposition and heat treatment, if required. Samples are shown, which were made when conducting the world’s first experiment in open space, when the cosmonaut-welders used VHT to perform the technological operations of welding, cutting, brazing and coating deposition. It is proved that generalization of investigation results and incorporating the experience of operation of all the previous samples of the hardware allowed development of the next “Universal” tool, which passed comprehensive testing at NASA, including in the KC-135 flying laboratory and in the space simulation test chamber. The paper presents new generation electron beam tool, which was developed and is manufactured at PWI.

**KEYWORDS:** space; hardware, electron beam welding, power source, automatic and manual welding

## INTRODUCTION

Performance of the operations of welding and related processes in open space, which are primarily associated with metal melting, presents risks and hazards [1]. At the same time, results of the first experiments on welding in space showed which criteria should be applied for evaluation of a particular welding process. Investigations conducted at PWI starting from 1964, demonstrate that the effectiveness of the available welding processes in the space environment should be assessed using additional criteria, compared to equipment which operates on the ground. One of the main criteria is the structure material to be joined in space, and its operating conditions. Another essential requirement to the hardware for welding in space is its high reliability, simplicity and versatility. Moreover, the hardware should also meet the criteria accepted for space hardware: it should have low power consumption, minimal weight and volume of the hardware and should be safe and efficient [2].

In earlier works [1, 3] it was proved that beam welding processes are the most promising for future application in space, primarily electron beam processes, which are more efficient and have a number of significant advantages.

High energy concentration, inherent to electron beam welding, is particularly necessary for work performance in space, as it ensures minimal heat input into the metal being welded and minimal power of the

entire unit. On the other hand, such a unit can be also used for cutting, brazing, and coating deposition, i.e. it has versatility highly important for space.

Investigations show that power of 1–3 kW at accelerating voltage of 10–20 kV is sufficient for performance of welding and cutting operations in space. Power to such a unit can be supplied from on-board mains of the space vehicle, or it can operate autonomously from storage batteries [3].

More over, technological hardware used in space, should have minimal overall dimensions and weight, dynamic strength, reliability, and serviceability under vacuum and at abrupt temperature changes from –120 to +120 °C [3].

## “VULCAN” EXPERIMENT

Owing to many years of investigations the first automatic “Vulcan” unit was created at PWI and in 1969 it was tested in “Soyuz-6” spaceship [1, 3]. It envisaged testing the following welding processes in space: consumable electrode low pressure electric arc, low pressure plasma arc, hollow cathode and electron beam welding.

“Vulcan” unit (Figure 1) consists of two containers: unsealed and sealed one. The first unit accommodates the devices for each welding process and a turntable, which carries the samples to be welded. Low pressure is maintained in this container during operation.

The second container accommodates the power sources: autonomous battery source, secondary power source (SPS), control modules and telemetry measur-

ing instruments. The unit is controlled from a remote panel [1].

“Vulcan” weight is approximately 50 kg. Duration of continuous operation was limited by the battery pack capacity.

Specification of “Vulcan” electron beam hardware is as follows [3]:

- electron energy of 10 keV;
- beam power of 0.6 kW;
- specific beam power of 1 kW/mm<sup>2</sup> at 40 mm distance from the gun edge;
- directly-heated tantalum cathode;
- diode projector;
- gun weight of 450 g; weight of high-voltage power unit with the gun of 6.5 kg.

Accelerating voltage of 10 kV was selected for performance of electron beam welding in “Vulcan” unit. A diode electron beam gun with direct heating of the cathode of 0.6 kW power and beam working current of up to 60 mA was used.

During experiment performance “Vulcan” was placed in the docking compartment of “Soyuz-6” spaceship, which was depressurized. Pressure of  $<1.33 \cdot 10^{-2}$  Pa was maintained in it. During the experiments, the crew with the remote panel stayed in the pressurized spaceship compartment, which was separated by a closed manhole from the docking compartment [1].

Studies of weldability of aluminium alloys at welding speed of 28–36 m/h were conducted when performing the experiments. Joints of AMg6 alloy produced as a result of the experiments had much greater porosity compared to those made on the ground.

The result of the conducted experiments on electron beam welding were butt joints with and without flanging of the edges, as well as overlap joints. The following materials were used for welding: 08Kh18N10T stainless steel, VT1-0 commercial titanium and AMg6 and D20 aluminium alloys 1.5–2.0 mm thick. Also cutting of aluminium and titanium alloys, and of 08Kh18N10T steel 1.0 mm thick was performed [1].

As a result of the conducted welding operations it was established that the electron beam welding and cutting processes are stable at long-term microgravity and space vacuum. The conditions necessary for normal formation of welded joints and cuts are provided.

Consumable wire low pressure arc welding was performed to study the processes of metal melting and transfer under low gravity. Butt joints of stainless steel sheets 1 mm thick were welded on 0.5 mm substrate from the same material. However, it was not possible to produce well-formed welds, as a result of nonuniform rotation of the welding table with the samples.



**Figure 1.** “Vulcan” automatic welding unit

As a result of experiment performance, it was found that the process of consumable wire low pressure arc welding in space at a high pumping down rate runs stably. A thorough study of the produced welded samples led to the conclusion that formation of a constricted low pressure arc in the vapours of the metal being welded is ensured both under the space and ground conditions. Despite certain drawbacks, experiments in “Vulcan” unit provided unique practical information, which was taken into account at development of new samples of space welding hardware.

#### **SPACE EXPERIMENTS ON WELDING AND RELATED TECHNOLOGIES USING VHT HAND ELECTRON BEAM TOOL**

The above-described hardware has remote or automatic program control. When working in open space, however, it may be necessary to perform a large number of operations (primarily, repair-restoration work or fixing large-sized structure fragments), for which it is complicated or impossible to prepare in advance. Moreover, development of emergency situations is probable, which require conducting urgent technological operations of cutting, welding or brazing, where the process and scope of the operation will be directly determined by the cosmonaut in the site of the required work performance [3].

Conducted technological experiments in “Vulcan” unit allowed developing and manufacturing a test sample of the first electron beam hand tool [3].

Experiments with the test sample for manual electron beam welding under earth gravity were conducted by PWI specialists in 1974 in space simulation test chamber using OB.1469 stand (Figure 2, a).

Before performance of open space experiments, the first prototype of electron beam hand tool was used to conduct numerous studies in the space simu-

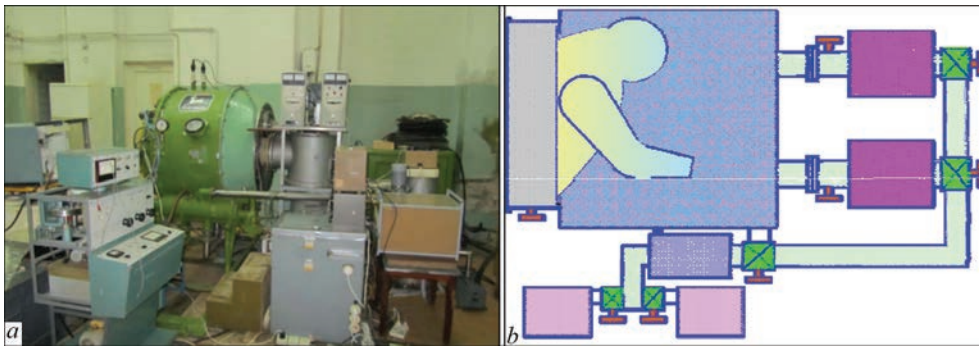


**Figure 2.** Hardware for conducting ground-based experiment on manual electron beam welding and cutting: *a* — OB.1469 testing stand; *b* — operator wearing a spacesuit, is under deep vacuum down to his waist

lation test chamber and in the flying laboratory under the conditions of microgravity and low temperatures.

When conducting the experiment in the chamber of OB.1469 stand, the vacuum required for electron beam operation ( $10^{-2}$ – $10^{-3}$  Pa) was created. For these experiments a diode electron beam gun of 1.5 kW rated power with up to 15 kV accelerating voltage was developed. The operator performing electron beam welding, was wearing a fragment of the spacesuit and was in deep vacuum down to his waist (Figure 2, *b*).

The results of the conducted experiments were used to produce a flight sample of versatile electron beam hand tool VHT (Figure 3). Considering the disadvantages revealed during trials of the first prototype, in VHT the accelerating voltage was lowered to 5 kV that allowed eliminating the rigid X-ray radiation. Such an accelerating voltage and power of 0.35 kW allow conducting the technological processes of welding, cutting and brazing of 1.0–1.5 mm thick samples, as well as coating deposition in open space.

All the technological processes with VHT tool are performed by electron beam method, which is the most suitable, adaptable-to-fabrication and versatile for conducting these operations. The vacuum environment on the low earth orbit is natural and convenient for implementation of this welding process. Here, the

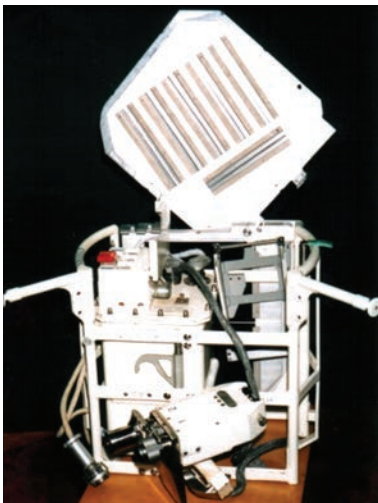


**Figure 3.** VHT electron beam hand tool

effective efficiency of electron beam welding process is equal to 85–90 %. It allows ensuring a reliable quality of welded joints, as well as the required tightness.

VHT tool is a monoblock, where the base element is a boxlike case with a special handle, made allowing for the anthropometry of the spacesuit glove. Mounted on the case front wall are two small-sized electron beam guns, each of which can form the electron beam and perform the processes of welding, cutting, brazing, as well as bombarding the crucible, while performing the coating deposition processes.

For convenience of transportation, all the functional components included into the VHT were arranged in one lattice container:

- sealed instrument compartment, containing the secondary power source, telemetry system and automatics module;
- control panel;
- cable communications.

At the container opposite side special replaceable cassettes can be fixed for performance of all the planned technological operations. Each of them carried six samples of VT1 titanium and 12Kh18N10T stainless steel for processing and joining.

VHT specification [6]:

- supply voltage of 23–34 V;
- power of up to 350 W;
- accelerating voltage of 5 kV;
- electron beam current of up to 70 mA;
- tantalum cathode of directly-heated type,  $2 \times 2$  mm,  $\delta = 0.06$  mm;
- VHT weight without the cassette of 30 kg;
- full weight of the cassette of 10 kg;
- weight of the tool proper of 3.5 kg.

On June 25, 1984, an experiment on performance of the technological processes of cutting, welding, brazing and coating deposition was held for the first time in the world in open space on board ‘Salyut-7’ orbital station, using VHT welding tool.

Samples of stainless steel and titanium alloy 0.5 mm thick were prepared for cutting. Welding and

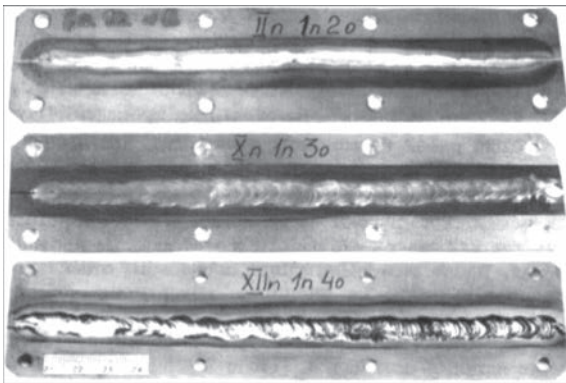


**Figure 4.** Samples of butt joints made in space using VHT hardware

brazing was conducted on samples from the same materials 1 mm thick. Silver coatings were deposited on blackened aluminium plates 2 mm thick of total area of 0.06 m<sup>2</sup> [1].

Titanium plate cutting was performed first, as the least complicated operation. This was followed by conducting the operations of welding, brazing and coating deposition. The first samples made in open space with the electron beam hand tool are shown in Figure 4. Experimental results were quite informative. First, the possibility proper of performing in open space the operations of welding and related technological processes, using the welding tool was shown; secondly, it was demonstrated that an operator wearing a spacesuit can safely conduct these technological operations and obtain good results.

After analysis of the investigation results, recommendations were developed on improvement of the procedure of ground-based training of cosmonaut-operators. The experiments were repeated in 1986, which were again performed in open space and were much more difficult. The cosmonauts conducted welding and brazing in open space of individual sections of girder structures, which were placed into special cassettes-manipulators (Figure 5). After completion of the work on deploying and folding the hinge-lever girders, the cosmonauts performed welding of the individual sections. All together, ten separate hinged sections from VT-4 titanium alloy were welded. This was followed by performance of a complex operation of welding-brazing the sections of a tube-rope girder. Each of the sections was a fragment of an open tube from 36NKhTYu steel, on which a ring from St30 steel filled with braze alloy was fitted.

Generalization of experimental results and analysis of the accumulated experience allowed formulation of the main principles of welding operations performance in space, and confirmed the need for modifying the tool, and introducing new engineering

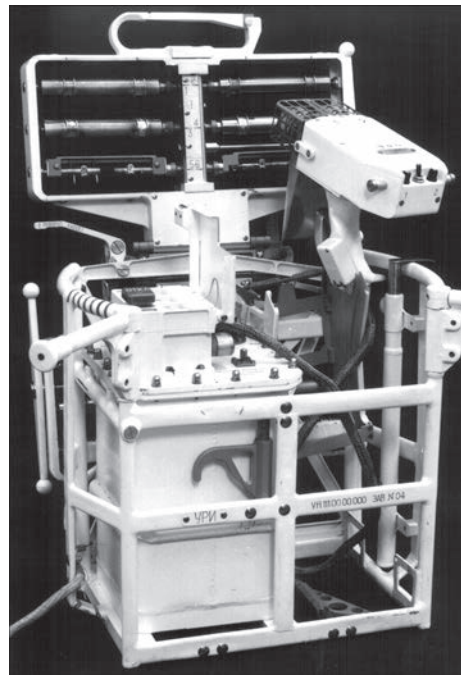


**Figure 5.** VHT and cassette-manipulator with installed samples of girder structure components

solutions, taking into account some essential corrections of the technological parameters.

The developers faced the following main tasks:

- bring the output power to 1 kW to work with aluminium and its alloys;
- fit the tool with wire feed mechanism;
- incorporate into the welding hardware a system of operational information and monitoring of the technological and technical parameters with the purpose of its transmission to the recording devices of the station.

#### **“UNIVERSAL” ELECTRON BEAM TOOL COMPLEX FOR REALIZATION OF WELDING AND RELATED TECHNOLOGIES IN OPEN SPACE**

Generalization of accumulated experience allowed development of a versatile set of “Universal” electron beam tool, designed for operation as part of future large-sized long-term orbital stations.

Compared to previous VHT hardware, the following changes were made in “Universal”:

- hardware output power was significantly increased (2.0–2.5 times);
- the tool proper is made as functional purpose, single gun, with cathode redundancy, which allows switching from one technological operation to another one by simple replacement of the required block or fixture;
- “Universal” is fitted with the basic tool for welding, brazing and cutting, filler material feed mechanism for welding and brazing, tool with a turret at-



**Figure 6.** “Universal” hardware

tachment which has four crucibles with evaporation materials for special coating deposition.

During development of this complex the task of unifying the main functionally important components was successfully solved. Here, the maximal possible useful application of on-board power at minimal weight and size characteristics of “Universal” hardware was achieved (Figure 6). The hardware set consisted of individual blocks, which can be assembled as specialized units of different purpose and required power, if necessary. For power supply to such a unit the complex incorporates the respective high-voltage blocks and secondary power source with forced heat removal [3].

The basic tool can independently perform welding, brazing and cutting, as well as welding and brazing with filler material, using the small-sized filler wire feed mechanism. The tool has a special mechanism for coating deposition by thermal evaporation of metals, as well as a drumlike attachment with four crucibles, which allows deposition of coatings from different materials. This tool can be also used for heating the surface being treated by a defocused electron beam.

If there is a need to apply robots or manipulators for performance of mounting-assembly and repair operations, an automatic welding unit can be put to-

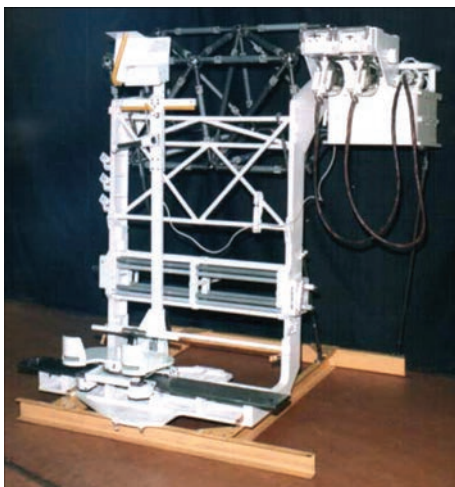


**Figure 7.** Cosmonaut-operator workplace

gether, which will include one or several (up to four) electron beam tools of up to 1.1 kW.

For performance of repair-restoration or mounting-assembly operations in previously unforeseen cases, a set of manual electron beam tools can be configured, which allows welding operations to be conducted directly by an operator wearing a spacesuit.

When performing this work, it is necessary to take into account the need to increase the hardware power, and to provide additional protection of the spacesuit and fitting of the cosmonaut-welder workplace, which ensures comfortable and safe working conditions for the operator (Figure 7). The workplace should be fitted with a container for storing the electron beam tool and operator panel, and it should be placed on the outer surface of the space vehicle in the area of work performance [3].

“Universal” specification:

- supply voltage of 23–34 V;
- power of up to 1110 W;
- accelerating voltage of 8–10 kV;
- electron beam current of up to 110 mA;
- tantalum cathode of directly-heated type,  $2 \times 2$  mm,  $\delta = 0.06$  mm.

After manufacture the “Universal” hardware was subject to multifunctional comprehensive testing. In 1991–1992 a series of tests under microgravity in KC-135 flying laboratory (L. Johnson Center, NASA, Houston), six immersions in the neutral buoyancy tank (J. Marshall Center, NASA, Huntsville) and five ascents to 6 km in the space simulation test chamber were conducted.

Qualification preflight tests of the manufactured hardware were performed with the purpose of its application during the experiment in the earth orbit [3]:

- testing for electromagnetic compatibility with the space vehicle systems;
- evaluation of hardware serviceability at long-term storage in the idle condition at temperatures of  $-113$ – $+80$  °C;
- thermal cycling tests ( $-40$ – $+60$  °C) by eight test cycles;
- toxicity tests (for toxic evolutions from space vehicle hardware);
- thermal tests;
- quantitative evaluation of spattering;
- vibration resistance testing;
- X-ray radiation measurements;
- evaluation testing for direct impact of the electron beam on materials.

After performance of comprehensive ground-based testing, “Universal” complex was recommended for use in the future orbital stations. However, in connection with problems in “Columbia” space vehi-



**Figure 8.** New generation manual electron beam tool and gun for welding and 3D printing for long-term operation: *a* — prototype of hand tool complex tested during performance of technological experiments; *b* — general view of electron beam gun for welding in space as part of a manipulator or robot; *c* — special 5-axes manipulator developed for performance of automatic welding; macrostructure of 8 mm AMg6 aluminium alloy

cle, the missions of these vehicles were discontinued, and the Program of the International Experiment with “Universal” tool was closed.

### NEW GENERATION ELECTRON BEAM EQUIPMENT FOR WELDING IN OPEN SPACE

Results of experiments on automatic and manual electron beam welding conducted in open space demonstrate that the earlier developed hardware allows welding stainless steels, titanium and aluminium alloys up to 1.5 mm thick. At the same time, the thickness of material used in manufacture of sheaths of manned space vehicles is up to 4–6 mm, and the length of welds can be up to several meters [4].

Another disadvantage of previous generation gun designs is the fact that the duration of their operation is not more than 7 min, because of absence of cathode block cooling. These factors did not influence the operation of the hand tool gun. However, these factors have a negative impact for operation in the automatic and long-term mode during performance of work on 3D-printing.

In this connection it was necessary to create a new generation gun, which would have the technical characteristics for welding thicker materials, which are used in modern aerospace engineering, as well as for conducting long-term 3D-printing technological processes [5, 6]. PWI performed work on development of a new generation small-sized electron beam gun of up to 2.5 kW electron beam power. Theoretical calculations with application of the method of trajectory analysis and synthesis allowed development of an electron-optical system of the gun with improved

electron beam density [7, 8], which solves the problem of welding up to 6 mm thick materials. New focusing and deflection systems were developed to enable performance of 3D-printing experiments.

Monolithic combination of the electron beam gun with the high-voltage power source was also eliminated, which promotes improvement of operating conditions of cosmonaut-operator at observation of the welding process, and allows the operator conducting the technological processes using 5 axes manipulator. The gun is connected to the power source (placed in the vacuum environment) by a flexible high-voltage cable with a high-voltage connector, and it enables the electromagnetic focusing system to form a sharp electron beam of 0.6 mm diameter. Application of such a gun design allows solving the problem of making welds of a great length.

The new electron beam gun for operation under the conditions of space has a combined system of the cathode block cooling [9]. Here, the gun duty cycle is 60 %, and the operating life is not less than 1 year, which is extremely important during performance of 3D-printing processes and conducting mounting and repair-restoration operations on the Moon surface.

Figure 8 shows a prototype of new generation electron beam gun for operation under high vacuum, temperature gradients and low gravity.

The gun design [10] also envisages use of monolithic insulators of a simplified configuration instead of brazed ones, which will be made from modern high-quality corundum materials, having higher insulation properties. Such a solution will eliminate the problems of breakdowns arising in the brazing points [11]. Filler wire feed mechanism is also envisaged [12].

## CONCLUSIONS

1. Over the years of working on creation of hardware for welding in space, a whole range of hardware for technological operations performance in space has been developed, manufactured and retrofitted during operation on the ground under the conditions simulating the space environment, using the flying laboratory and in the space simulation test chamber.

2. Generalization of the results of experiments and analysis of the accumulated experience allowed defining the main principles of development, manufacture and testing of the hardware, as well as performance of welding operations in space, which determined the need to modify the hardware, and introduce new engineering solutions, taking into account some essential corrections of the technological parameters.

3. Earlier developed “Vulcan” hardware for automatic welding and VHT hand tool, which were designed and manufactured at PWI, and were tested in the space orbit, as well as the “Universal” hand tool, have such drawbacks as the short operating life of the cathode (not more than 1 h), electrostatic focusing of the electron beam (beam diameter of not less 2.5 mm at 40–50 mm working distance).

4. Taking into account the experience of operation of the previous hardware modifications, it was determined what operations should be performed by modern level hardware.

5. So far, PWI has conducted work on development of a small-sized new generation electron beam gun of 2–2.5 kW power, which allows welding up to 6 mm thick aluminium alloys.

6. It was found that the new focusing and deflection systems enable performance of experiments on 3D printing. Modern electron-optical system of the gun allows generating an electron beam of higher specific power of not more than 1 mm diameter at the distance of 50–150 mm.

## REFERENCES

1. Paton, B.E., Lapchinskii, V.F. (1998) *Welding in space and related technologies*. Cambridge International Science Publishing.
2. (1987) *Cosmonautics of USSR*. Mashinostroenie, Planeta, 179–195 [in Russian].
3. (2002) *Space: Technologies, materials, structures*. Ed. by B.E. Paton. London, Taylor & Francis.
4. (2023) Prospects for the application of welding in Space. *Avtomatic Svarka.*, **3**, 46–60.
5. Lobanov, L.M., Asnis, Yu.A., Ternovyi, Ie.G. et al. (2020) *Method of ensuring high operational vacuum in electron beam gun and device for performance of welding and related technologies in open space*. Pat. 121773, Ukraine, Publ. 27.07.2020.
6. Fragomeni, J.M., Nunes, A.C. Jr. (2003) A study of the effects of welding parameters on electron beam welding in the space environment. *Aerospace Sci. and Technol.*, **7**(5), 373–384. DOI: [https://doi.org/10.1016/S1270-9638\(03\)00031-2](https://doi.org/10.1016/S1270-9638(03)00031-2)
7. Bondarev, A.A., Ternovoj, E. (2010) Features of weld formation and properties of aluminium and magnesium alloy joints under simulated space conditions. *The Paton Welding J.*, **11**, 16–20.
8. Paton, B.E., Lobanov, L.M., Asnis, Yu.A. et al. (2017) Equipment and technology for electron beam welding in space. *Kosmichna Nauka i Tekhnologiya*, **107**(4), 27–32 [in Ukrainian]. DOI: <https://doi.org/10.15407/knit2017.04.027>
9. Asnis, Yu.A., Zubchenko, Yu.V., Ternovyi, Ie.G. et al. (2018) *Method of electron beam formation in electron beam gun for welding and related technologies under open space conditions*. Pat. 17397, Ukraine, Publ. 25.07.2018.
10. Lobanov, L.M., Asnis, E.A., Ternovy, Ye.G. et al. (2020) *Some issues of repairing manned space vehicles in outer space using electron beam welding*. State Phenomena Submitted: 2020-07-07, 315, 101–105. DOI: <https://doi.org/10.4028/www.scientific.net/SSP.315.101>
11. Paton, B.E., Lobanov, L.M., Naidich, Yu. et al. (2019) New electron beam gun for welding in space. *Sci. and Technol. of Welding and Joining*, **24**(4), 320–326. DOI: <https://doi.org/10.1080/13621718.2018.1534794>
12. Paton, B.E., Lobanov, L.M., Asnis, Yu.A. et al. (2019) *Device for manual electron beam welding and related technologies in space*. Pat. 118896, Ukraine, Publ. 25.03.2019.

## ORCID

S.O. Hlushak: 0000-0003-4518-7262

## CORRESPONDING AUTHOR

S.O. Hlushak

E.O. Paton Electric Welding Institute of the NASU  
11 Kazymyr Malevych Str., 03150, Kyiv, Ukraine.  
E-mail: [electriber@ukr.net](mailto:electriber@ukr.net)

## SUGGESTED CITATION

S.O. Hlushak (2023) Evolution of electron beam hardware for welding in space. *The Paton Welding J.*, **8**, 78–84.

## JOURNAL HOME PAGE

<https://patonpublishinghouse.com/eng/journals/tpwj>

Received: 13.06.2023

Accepted: 07.08.2023



Short history  
of “The Paton Welding Journal”  
since 1989 via link:

<http://patonpublishinghouse.com/tpwj/pdf/2022/tpwj202201part.pdf>

## MODERN FLUX-CORED WIRES FOR ARC WELDING OF METAL STRUCTURES FROM LOW-ALLOYED STEELS, DEVELOPED AT THE E.O. PATON ELECTRIC WELDING INSTITUTE AND OJSC “TM.WELTEC”

V.V. Holovko<sup>1</sup>, O.S. Kotelchuk<sup>1</sup>, A.A. Golyakevych<sup>2</sup>, L.M. Orlov<sup>2</sup>

<sup>1</sup>E.O. Paton Electric Welding Institute of the NASU  
11 Kazymyr Malevych Str., 03150, Kyiv, Ukraine

<sup>2</sup>OJSC “TM.WELTEC”, 15 Kazymyr Malevych Str., Kyiv, Ukraine

Flux-cored wire arc welding is becoming more and more popular due to its efficiency and ease of use. PWI specialists, who initiated development of such an electrode material as flux-cored wire and its application technology, have more than sixty years of experience, both in the field of fundamental investigations on metallurgy of flux-cored wire welding, and of problems of its manufacture and use [1–4]. The accumulated experience shows that at selection of a specific technology of flux-cored wire welding all its advantages and disadvantages should be taken into account. Taking a correct well-balanced decision requires deep knowledge and extensive practical experience for evaluation of both the positive aspects of a particular technology or certain wire grade, and also the possible negative consequences. Choice made on the basis of previous experience, guarantees that the flux-cored wire welding technology will be the best variant in a specific situation.

The growth in the popularity of this technology of flux-cored wire arc welding was based on a number of essential advantages, inherent to the welding technology proper. Scientifically substantiated selection of the core composition opens up wide possibilities for controlling the kinetics of metallurgical processes in the welding arc. That is why the flux-cored wires can be used for welding practically any type of metal, making this technology more versatile, compared to other methods.

Flux-cored wires, which are released to the market by certified manufacturers, owing to their high efficiency and productivity allow reducing the labour costs for auxiliary operations, providing an economic substantiation for their application. The flux-cored wires themselves are a high-tech welding consumable, and their quality is guaranteed by a complex of special technological operations of their manufacture and quality control. High-quality flux-cored wires can only be produced by competent specialized companies. In Ukraine OJSC “TM.WELTEC” is the leading

manufacturer of flux-cored wires for welding and surfacing. PWI experience on development and use of flux-cored wires, gained over many years, is finding practical implementation in cooperation with such a manufacturer of welding consumables as OJSC “TM.WELTEC”. Flux-cored wire production is located in a specially designed for this purpose shop of more than 3 thou m<sup>2</sup> area in the city of Dnipro. This is one of the most technologically sophisticated enterprises on welding consumables manufacture in the country. In addition to several automated lines for wire manufacture, the production facility includes a laboratory, where engineers and technical specialists continuously monitor compliance with the technological parameters of equipment operation, and product quality indices. Research and development is continuously carried on, which is aimed at improvement of the technological operations of manufacture, and creation of new grades of flux-cored wires, in keeping with the user inquiries and needs.

OJSC “TM.WELTEC” and PWI specialists are constantly working to improve the currently available and develop new compositions of flux-cored wires, in order to guarantee the high quality of welded joints by increasing the stability indices of the arc process, as well as improving the technological and sanitary-hygienic characteristics of the wires.

Assessment of the danger of the generated welding fumes is conducted in the entire range of welding modes, as the toxic impact of the fumes depends not only on the particle composition and dispersity, but also on the degree of their agglomeration during emission and a number of other factors. The volumes of welding fumes emission are influenced both by the type of the flux-cored wire, and the composition of the shielding gas atmosphere, as well as the welding mode parameters.

In welding in an argon-based gas mixture the level of gross emissions of the fumes and of their toxic component is significantly lower. Use of flux-cored wires

of metal-core type allows lowering the total level of gross fume emissions to the level characteristic for solid wire application. The total level of gross emissions is higher in the case of application of flux-cored wires with slag-forming core, than at application of solid wires or wires filled with metal powder filler. When using such wires, it is necessary to particularly strictly follow the respective recommendations on

safety as regards cleanliness of the air in the working area of welding. However, presence of the slag melt leads to lowering of the overall level of burnout of deoxidizing and alloying elements, which eventually allows lowering the level of fume toxicity [5].

Presence of special stabilizers in the core composition allows significantly increasing the welding process efficiency, and lowering the level of molten metal

**Table 1.** Some characteristics of commercial flux-cored wires, proposed by OJSC “TM.WELTEC” for electric arc welding of low-alloyed steels

Wire grade, diameter and type, in keeping with the standards	Mechanical properties and chemical composition of weld metal	Purpose	Typical applications
FCWw-TMW1 ISO 17632-A: T 35 A Z N3 1.0–2.8 mm diameter	$UTS \sim 460\text{--}550$ MPa; $YS \sim 330$ MPa; $A_5 \geq 16$ %; $KCV_{+20^\circ\text{C}} \sim 40$ J/cm <sup>2</sup> $C \sim 0.08$ ; Si $\sim 0.1$ ; Mn $\sim 0.8$ ; S $\leq 0.035$ ; P $\leq 0.035$ wt. %	Semi-automatic arc welding of metal structures from general purpose low-alloyed steels, also of contaminated metal	Building metal structures, technological containers, parts of agricultural machinery, railway equipment and machines
FCWw-TMW3 ISO 17632-A: T 42 2 1Ni Y N 3 1.6–2.4 mm diameter	$UTS \sim 490\text{--}660$ MPa; $YS \sim 400$ MPa; $A_5 \geq 20$ %; $KCV_{+20^\circ\text{C}} > 80$ J/cm <sup>2</sup> ; $KCV_{-20^\circ\text{C}} > 35$ J/cm <sup>2</sup> $C \sim 0.12$ ; Si $\sim 0.2$ ; Mn $\sim 1.2$ ; Ni $\sim 1.0$ ; Al $\sim 0.85$ ; S $\leq 0.02$ ; P $\leq 0.02$ wt. %	Mechanized arc welding in the field of metal structures from general purpose low-carbon and low-alloyed steels	
FCWw-TMW -mk5A ISO 17632-A: T 42 2 M M 1 H10 AWS A5.18 E70T-6C 1.2–1.6 mm diameter	$UTS \geq 520$ MPa; $YS \geq 430$ MPa; $A_5 > 24$ %; $KCV_{+20^\circ\text{C}} \geq 160$ J/cm <sup>2</sup> ; $KCV_{-20^\circ\text{C}} \geq 110$ J/cm <sup>2</sup> ; $KCV_{-50^\circ\text{C}} \geq 40$ J/cm <sup>2</sup> $C \sim 0.06$ ; Si $\sim 0.45$ ; Mn $\sim 1.5$ ; S $\leq 0.02$ ; P $\leq 0.02$ (wt. %)	Automatic and semiautomatic high-speed single- and multipass gas-shielded welding of metal structures from carbon and low-alloyed structural and shipbuilding steels	Special-purpose structures, of which higher requirements are made to weld ductility characteristics at low temperatures (down to minus 60 °C)
FCWw-TMW29 ISO 17632-A: T 42 3 1.2 – 2.4 mm diameter	$UTS \geq 490$ MPa; $YS \geq 420$ MPa; $A_5 > 22$ %; $KCV_{+20^\circ\text{C}} \geq 80$ J/cm <sup>2</sup> ; $KCV_{-40^\circ\text{C}} \geq 35$ J/cm <sup>2</sup> $C \sim 0.12$ ; Si $\sim 0.4$ ; Mn $\sim 1.3$ ; S $\leq 0.03$ ; P $\leq 0.03$ wt. %	Welding of metal structures from low-carbon and medium-strength steels. Multipass welding without intermediate slag removal is possible, due to its small quantity and easy detachability of the crust. High efficiency of welding operations and good appearance of the welds	General mechanical engineering, metal structure plants, transport and lifting machinery
FCWw-TMW7 ISO 17632 A: T 42 4 P C 1 H5 AWS A5.18 E71T1- C1A4-CS2-H4 1.2–2.4 mm diameter	$UTS \geq 490$ MPa; $YS \geq 400$ MPa; $A_5 > 22$ %; $KCV_{+20^\circ\text{C}} \geq 120$ J/cm <sup>2</sup> ; $KCV_{-20^\circ\text{C}} \geq 90$ J/cm <sup>2</sup> ; $KCV_{-40^\circ\text{C}} \geq 70$ J/cm <sup>2</sup> $C \sim 0.08$ ; Si $\sim 0.3$ ; Mn $\sim 1.3$ ; S $\leq 0.03$ ; P $\leq 0.03$ wt. %	Gas-shielded welding of metal structures from low-carbon and low-alloyed steels, including D32-E40 shipbuilding steels, unalloyed S235, S355 structural steels. Excellent welding-technological properties. Deposited bead has a smooth surface with easily detachable slag crust	Manufacture of metal structures, with higher requirements to low-temperature ductility characteristics of weld metal
FCWw-TMW57 ISO 18276-A: T 55 2 R C 2 1.2 – 2.4 mm diameter	$UTS \sim 650\text{--}800$ MPa; $YS \geq 590$ MPa; $A_5 \geq 16$ %; $KCV_{+20^\circ\text{C}} \geq 65$ J/cm <sup>2</sup> ; $KCV_{-30^\circ\text{C}} \geq 35$ J/cm <sup>2</sup> $C \leq 0.12$ ; Mn $\sim 1.3$ ; Si $\sim 0.3$ ; Cr $\sim 0.30$ ; Mo $\sim 1.2$ ; V $\sim 0.3$ ; S $\leq 0.03$ ; P $\leq 0.03$	Gas-shielded welding of critical metal structures from low-alloyed high-strength steels, as well as alloyed structural steels with not less than 580 MPa yield limit	Repair welding of castings from higher-strength steels, repair of various-purpose equipment, building metal structures, mechanical engineering, metallurgical industry units
FCWw-TMW14 ISO 17634-A: T CrMo R C 1 1.2–2.4 mm diameter	$UTS \sim 500$ MPa; $YS \geq 430$ MPa; $A_5 \geq 22$ %; $KCV_{+20^\circ\text{C}} \geq 80$ J/cm <sup>2</sup> ; $KCV_{-20^\circ\text{C}} \geq 50$ J/cm <sup>2</sup> $C \leq 0.06$ ; Mn $\sim 0.8$ ; Si $\sim 0.3$ ; Cr $\sim 1.0$ ; Mo $\sim 0.5$ ; S $\leq 0.014$ ; P $\leq 0.012$	Mechanized gas-shielded welding of metal structures, building-up and repair of defects in castings from high-alloyed steels and corrosion-resistant, heat-resistant and high-temperature alloys operating at up to 545 °C temperature	Transport engineering, technological containers, vessels, tanks and pipelines, metal structures, etc.
FCWw-TMW11 ISO 17633-A: T55 2 R C 2 2.4–3.0 mm diameter	$UTS \sim 520$ MPa; $YS \geq 400$ MPa; $A_5 \geq 30$ %; $KCV_{+20^\circ\text{C}} \geq 80$ J/cm <sup>2</sup> ; $KCV_{-20^\circ\text{C}} \geq 50$ J/cm <sup>2</sup> $C \leq 0.12$ ; Mn $\sim 14.0$ ; Si $\sim 0.2$ ; Cr $\sim 10.0$ ; Ni $\sim 9.0$ ; S $\leq 0.025$ ; P $\leq 0.025$	Mechanized open-arc or gas-shielded welding and surfacing of low-carbon and low-alloyed steels, as well as welding alloyed structural steels to austenitic steels	Welding pearlitic steels to high-manganese steels, as well as welding and repair of mining excavator buckets

spatter [6]. The slag phase, forming at core melting, allows not only protecting the molten metal from undesirable interaction with the environment, but also realizing the necessary metallurgical reactions to improve the performance of the metal of the weld and the welded joint as a whole.

The main difference of the process of flux-cored wire welding in the spray transfer mode from solid wire welding consists in that the electrode metal transfer takes place on the wire edges (over the sheath cross-section), and not in the central zone, focused on the center of the arc burning. Presence in the flux-cored wire core of slag-forming materials and metal powders, as well as chemical compounds with a low ionization potential, influences the surface tension of molten metal of the weld pool, which allows regulation of the weld surface shape. For gas-shielded arc welding flux-cored wires with the following types of powder core are mainly used. Mineral-powder (slag-forming) core provides slag protection and performs metallurgical processing of the melt of the respective type (rutile or basic type). Metal-powder core, based on powders of iron and alloys with a small fraction of active chemical compounds (usually less than 1.5 % by weight), ensures active alloying and microalloying, as well as modifying of the weld metal structure. Here, the composition of the shielding gas atmosphere has a key role, determining the thermal conductivity of the arc gap, and degree of oxidizing process development at electrode metal transfer and in the weld pool.

As a rule, the cost of welding consumable for making a certain welded joint is higher in the case of using semi-automatic flux-cored wire welding, than in the case of coated-electrode manual arc welding or semi-automatic gas-shielded solid wire welding. However, even without allowing for a higher welding efficiency, the real cost of welding operations also includes the labour costs for postweld heat-treatment of the produced joint, and metal stripping along the weld. They take up from 50 up to 55 % of the total operation cost. The efficiency of the electric arc welding process, assessed by the quantity of the deposited metal, does not fully reflect the actual productivity of making the welds during metal structure fabrication. The influence of the possible deviation of weld dimensions from the design ones, in particular surface shape (reinforcement), and extent of the possible losses of electrode metal for spatter under the actual conditions should be also taken into account. For in-

stance, the time spent for making welds of equivalent design size increases by 5–15 % in the case of application of a gas mixture of M21 type instead of carbon dioxide gas in gas-shielded welding. This is achieved not only due to reduction of burnout and spattering losses, but also due to a more accurate correspondence of the reinforcement dimensions and shape to the design values, which influences the cost indices of fabrication of welded metal structures. Additional economic advantages can be also achieved at application of flux-cored wires instead of solid wires owing to reduction of the weld metal volume, for instance in welding single-pass fillet joints.

Higher cost of welding consumables (flux-cored wires, gas mixtures of argon with carbon dioxide gas) is compensated not only by increase of welding process efficiency, but also by lowering of overall costs for making the welded joints due to elimination of electrode metal losses, as well as improvement of the shape and more complete compliance of the weld shape and dimensions with the design values. All this allows lowering the cost of fabrication of welded metal structures and improving their quality.

The main properties of some commercial flux-cored wires, manufactured by “TM.WELTEC” are shown in the Table 1.

## REFERENCES

1. Pokhodnya, I.K., Suptel, A.M., Shlepakov, V.N. (1972) *Welding with flux-cored wire*. Kyiv, Naukova Dumka [in Russian].
2. Pokhodnya, I.K., Shlepakov, V.N. (1995) *Welding with flux-cored wire*. S.E., Harwood Academic Publishing.
3. Golovko, V.V., Kotelchuk, O.S., Naumeiko, S.M., Golyakevich, A.A. (2022) Development of self-shielded flux-cored wires for arc welding of low-alloy steels. In: *Innovative Technologies for Joining Advanced Materials XII. Selected Peer-Reviewed Full Text Papers from 12<sup>th</sup> Inter. Conf.: Innovative Technologies for Joining Advanced Materials (TIMA21, Switzerland. Baech)*. Trans. Tech. Publications Ltd., Vol. 4, Scientific Book Collection, 98–109.
4. Orlov, L.N., Novikova, D.P., Maksimov, S.Yu et. al. (2009) Investigation of microstructure correlation with properties of welded joints made with the rutile flux-cored wire. In: *Proc. of Inter. Sci. and Technical Conf. on The Petranovsky Readings. Welding Consumables Devoted to the 70<sup>th</sup> Anniversary of the Development of the UONI-13 Type Coated Electrodes, May 18–22, 2009*, 134–142.
5. Shlepakov, V.N., Kotelchuk, A.S. (2019) Improvement of technological and sanitary-hygienic characteristics of gas-shielded arc welding processes. *The Paton Welding J.*, **6**, 29–33. DOI: <http://dx.doi.org/10.15407/tpwj2019.06.05>
6. Golyakevich, A.A., Orlov, L.N., Maksimov, S.Yu. (2019). Peculiarities of welding process using metal cored wire of TMV5-MK grade. *The Paton Welding J.*, **6**, 50–53. DOI: <http://dx.doi.org/10.15407/tpwj2019.06.10>



## PATON INTERNATIONAL — EVOLUTIONS IN YEARS



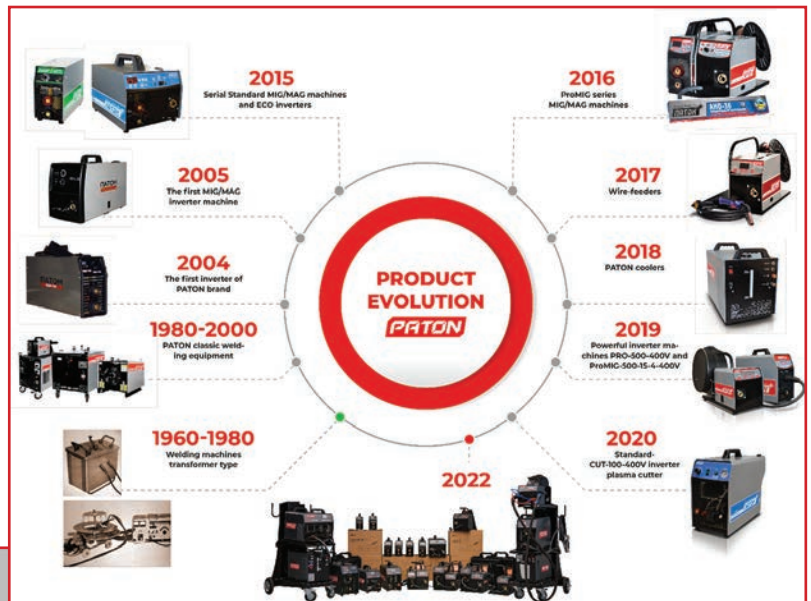
The history of development of welding equipment production in Ukraine has been almost hundreds of years. 64 years of them are closely related to the activities of the PATON INTERNATIONAL Company, which was created at the Electric Welding Institute in 1959 for the implementation of new developments of specialists from the Institute and EDTB. For the whole period from the date of its creation to this day, at the production facilities of the Company, hun-

dreds of thousands of units of welding equipment for various enterprises from almost all continents of the world have been manufactured. Today, PATON INTERNATIONAL is a leading manufacturer of welding equipment and materials in Ukraine and one of the leaders at the market of the CIS countries.

The Company has two production sites at the very heart of Ukraine — in Kyiv, which closely interact with the scientific potential of a leading institution in the field of welding — the E.O. Paton Electric Welding Institute. The own complex of design laboratories performs a full range of works related to the development of welding equipment, starting from bodies of machines and ending with the design of unique electronic circuits and software development. The mentioned design and production resources allow the Company to produce more than 60 models of equipment in such categories as:

- inverters for manual arc welding (MMA) with the current range from 150 to 630 A;
- MIG/MAG welding semi-automatic machines — from 150 to 630 A;
- argon-arc inverters (TIG) — from 200 to 350 A;
- machines for air-plasma cutting (CUT) — from 40 to 100 A;
- multimode welding inverters — from 250 to 350 A.

In the production, the most advanced components from such world's leading manufacturers as INFINEON, VISHAY, KENDEIL, NXP, TOSHIBA, TEXAS INSTRUMENTS etc. are used. The equip-



ment is completed with high-quality welding accessories of German and Ukrainian production. All this allows the Company to manufacture extra-class products, the high quality of which was reflected in an increased guarantee term — up to 5 years.

Except of welding equipment, PATON INTERNATIONAL develops and manufactures a wide range of

accessories for welding and 10 most popular grades of electrodes in such categories as AWS 5.1:E6013, AWS 5.1:E7015, AWS 5.1:E7018, AWS A5.4:E347-16, AWS 5.15:ESt and EN 14700: E Z Fe14. PATON electrodes are produced by improved modern recipes from raw materials of well-known Ukrainian and world manufacturers, they are featured by high quality and excellent consumer characteristics, meet the necessary requirements, which is confirmed by the presence of appropriate certificates from international certification companies.

Thanks to the own developments, high production culture and considerable experience of the Company, welding machines and electrodes under PATON brand are honoured by welding specialists both in Ukraine and far beyond its borders.

The development of export markets for products is one of the most priority directions of the Company development strategy. Today, PATON products are shipped in more than 50 countries around the world — from Latin America to the Far East and Australia.

A separate vector of development is the strengthening of PATON brand positions at the European market of welding equipment and materials. The Company offers European consumers a unique combination of high quality, functionality, efficiency and compactness of PATON welding equipment, whereby it can compete at the market with equipment from well-known European and world brands.

To provide deliveries and organize service for products, the official representation of the Company PATON Europe was created in Poland, whose team can respond promptly to the request from customers and provide delivery of products to consumers in the shortest possible term. And today, thanks to the work of the team, PATON welding equipment and materials are present at the market of almost every EU country and the United Kingdom. Due to the wide network of official dealers and partners of the Company, the work of the own local online stores and the availability of products at the largest European online marketplaces, each European consumer can get acquainted with PATON products and order them on the most favourable terms with the minimum delivery period.



PATON INTERNATIONAL Company has an impeccable reputation of a reliable manufacturer and a supplier of high-quality welding equipment and materials and makes everything necessary to maintain it at such a high level. The Company continues its movement to the set goals — providing the sustainable development of its research and production potential, increasing production of high-quality welding equipment and materials, promotion of PATON products among as many welding specialists from different countries as possible.

<https://paton-welding.com/en/>

# SUBSCRIPTION-2024



«The Paton Welding Journal» is Published Monthly Since 2000 in English, ISSN 0957-798X, doi.org/10.37434/tpwj.

«The Paton Welding Journal» can be also subscribed worldwide from catalogues subscription agency EBSCO.

If You are interested in making subscription directly via Editorial Board, fill, please, the coupon and send application by Fax or E-mail.

12 issues per year, back issues available.

\$384, subscriptions for the printed (hard copy) version, air postage and packaging included.

\$312, subscriptions for the electronic version (sending issues of Journal in pdf format or providing access to IP addresses).

Institutions with current subscriptions on printed version can purchase online access to the electronic versions of any back issues that they have not subscribed to. Issues of the Journal (more than two years old) are available at a substantially reduced price.

<b>Subscription Coupon</b>			
<b>Address for Journal Delivery</b>			
<b>Term of Subscription Since</b>	<b>20</b>	<b>Till</b>	<b>20</b>
<b>Name, Initials</b>			
<b>Affiliation</b>			
<b>Position</b>			
<b>Tel., Fax, E-mail</b>			

The archives for 2009–2021 are free of charge on [www://patonpublishinghouse.com/eng/journals/tpwj](http://www://patonpublishinghouse.com/eng/journals/tpwj)



## ADVERTISING

### in «The Paton Welding Journal»

**External cover, fully-colored:**

- First page of cover (200×200 mm) – \$700
- Second page of cover (200×290 mm) – \$550
- Third page of cover (200×290 mm) – \$500
- Fourth page of cover (200×290 mm) – \$600

**Internal cover, fully-colored:**

- First/second/third/fourth page (200×290 mm) – \$400
- Internal insert: (200×290 mm) – \$340 (400×290 mm) – \$500

- Article in the form of advertising is 50 % of the cost of advertising area
- When the sum of advertising contracts exceeds \$1001, a flexible system of discounts is envisaged
- Size of Journal after cutting is 200×290 mm

**Address**

11 Kazymyr Malevych Str., 03150, Kyiv, Ukraine  
 Tel./Fax: (38044) 205 23 90  
 E-mail: [journal@paton.kiev.ua](mailto:journal@paton.kiev.ua)  
[www://patonpublishinghouse.com/eng/journals/tpwj](http://www://patonpublishinghouse.com/eng/journals/tpwj)